The role of fusogenic vesicles in the regulation of nuclear envelope assembly

Gary Hong Chun CHUNG

A Thesis Submitted for the Degree of
Doctor of Philosophy
University College London

December 2014

Cell Biophysics Laboratory
Cancer Research UK London Research Institute
44 Lincoln's Inn Fields, London

Declaration

I, Gary Hong Chun Chung, confirm that the work presented in this thesis is my own. Where information has been derived from other sources, I confirm that this has been indicated in the thesis.

Acknowledgements

What an adventure in doing a PhD. This is almost a metamorphosis moving from marine biology to cell biology. First and foremost I am grateful that Banafshé Larijani, my supervisor, gave me a chance to be in Cell Biophysics Lab. I thank her for giving me time to adapt, directions about the interdisciplinary project, the reasonable pushing, the scientific and cultural lectures and most importantly a good team.

I would like to thank my thesis committee Peter Parker and Julian Downward for the scientific discussions, resources, and their British humour and wisdom. Also, thanks to Dominic Poccia for the findings he made in this field. Sincere gratitude to Lucy Collinson, really appreciate her for taking me in the EM unit when Banafshé moved, and also her patience, supervision and cakes! Special thanks to Sharon Tooze and Svend Kjaer for helping me in subcellular fractionation and protein purification; Jose Requejo-Isidro and Colin Rosser for teaching me optics and organic chemistry respectively.

Being a PhD actually has a different definition in the oriental culture, as illustrated in Figure 0. This may explain the random conversations I started during the daily life and part of my “Garylism”. I am still trying to find a balance between the two mentioned types of PhD.

Working in Cell Biophysics is really enjoyable. A remarkable thank to Richard Byrne for being my mentor, for he constantly provides excellent solutions to problems and guidance to the project. He also directs me with his “man card system” in order to get the best out of me. I hope I will earn a man card from him after finishing this thesis. Rich, you are the best mentor so “Ta!”. I thank Véronique Calleja for maintaining the smoothness in the lab, in addition to teaching me molecular cloning from zero. I really enjoyed the sci-fi conversations and movie time with you Vero. To Marie-Charlotte Domart, or MC, thank you for the supports in bench works and bearing my metaphoric way of delivering messages or concepts, and for “being French”. Moreover, advised me on bike and cycling. To Raju Veeriah, thanks for the daily reminder “No funny stuff” so that I am always serious at work. To Tina Hobday, thanks for being the senior student who established the framework of the project and brought us to dim sum restaurants. To Nirmal Jethwa, thanks for shadowing me in some bench works, for being critical, healthily sarcastic and skinny so that we did not have a problem to share a 2 m^2 working area. To Julien De Naurois, thanks for being the lab buddy, listening to my theories and providing medical advices from time to time. Applause to Christopher Applebee and Pierre Leboucher, the engineers in the lab, for they built practical machines and devices. In parallel, they shared their life experience, jokes, knowledge of beer and splendid champagnes.

The EM unit is my second home that gave me "high resolution". A big credit to Christopher Peddie, for being my EM guru and helped me with my project. I am always impressed by the calmness and the deep-wit of you Chris. To Anne Weston, Raffaella Carzaniga and Matt Russell, thanks for the helps in electron tomography, sample preparation, ordering and input in this thesis. Special thanks to Elisabeth Brama and Martin Jones, for their participation in my lab meeting.

To the students worked in the lab and collaborators from Bilbao, thanks and Gracias! To Gloria De Las Heras, thanks for being a role model of hardworking and hard-rock spirit, you will get your "home-car" eventually. To Charlotte Melia, Erica Lam, Mary Burkitt-Gray, Marta Gutierrez-Lete and Catherine MacLachlan (in chronological order of formal introduction), thanks for the helps in the project, the shared fun time and the insights you guys brought me such as "Arriba, Abajo, Adentro", "The Room", "The Big Lebowski" and "Scotchka".

To Sally Leevers, the administrative office and IT department, thank you very much for making things smooth. To the members of the Equipment Park: Graham Clark, Vicky Dearing, Olga O'Neil, Dave Phillips and Ramin Sadri, thanks for the professional service. Big thanks to Mark Dalton and other lab aides, for making a good working condition and ease my research life. Also, I would like to thank Coastal Marine Lab at Hong Kong University of Science and Technology, a starting point of my science career.

A very sincere and warm hug to my standard group of PhD buddies/allies/friends (in the order of surname): Alessandra Audia - Thanks for being my Salsa partner #1 and proofread my works. Thanks for sharing a southern Italian way of passion in most of the stuff especially the Rhino-Soul and being caring. Mariana Campos – Thanks for being my Salsa partner #2 and proofread my works, I am very grateful that you organised weekend events for the group many times and you are also a good travel buddy. Stefanie Derzsi – Thanks for sharing a sense of posh to look up to. Kinga Laszlo – Thanks for initiating the Cosy Science. It is really a meaningful and sustainable project. I have learned stuff from it. Rafal Lolo – Thanks for the time spending with us, especially the efforts you need to make coming from Clare Hall. Also thanks for making the "leisure walk" a special walk. Heike Miess – Thanks for being my Salsa partner #3 and participated in the Engineering Yes competition with me and Rafal. Thanks for being expressive and a good company to share the laughter and my sense and non-sense, appreciated. Special thanks to Tang Ngang Heok for inviting me and Eunice Chan (great travel buddy) to his family gathering so that I am not alone in festival times. To Jeroen Claus, Hannah Dooley, Richard Panayiotou and Yanxiang Zhou, thanks for being my writing buddies, especially Richard, thanks for your interest in Chinese medicine and related scientific discussion.

To the people above, thanks for listening to my dreams, hypothesis, statements of surrealism, conspiracy theories and my stories. Lastly, I would like to thank my parents for their love and supports no matter what. Thanks for all the understanding. 謝謝您們一直以來的信任和照顧。

I am truly happy to be here and I wish I can keep my curiosity to everything, to take risk and to make adventure.

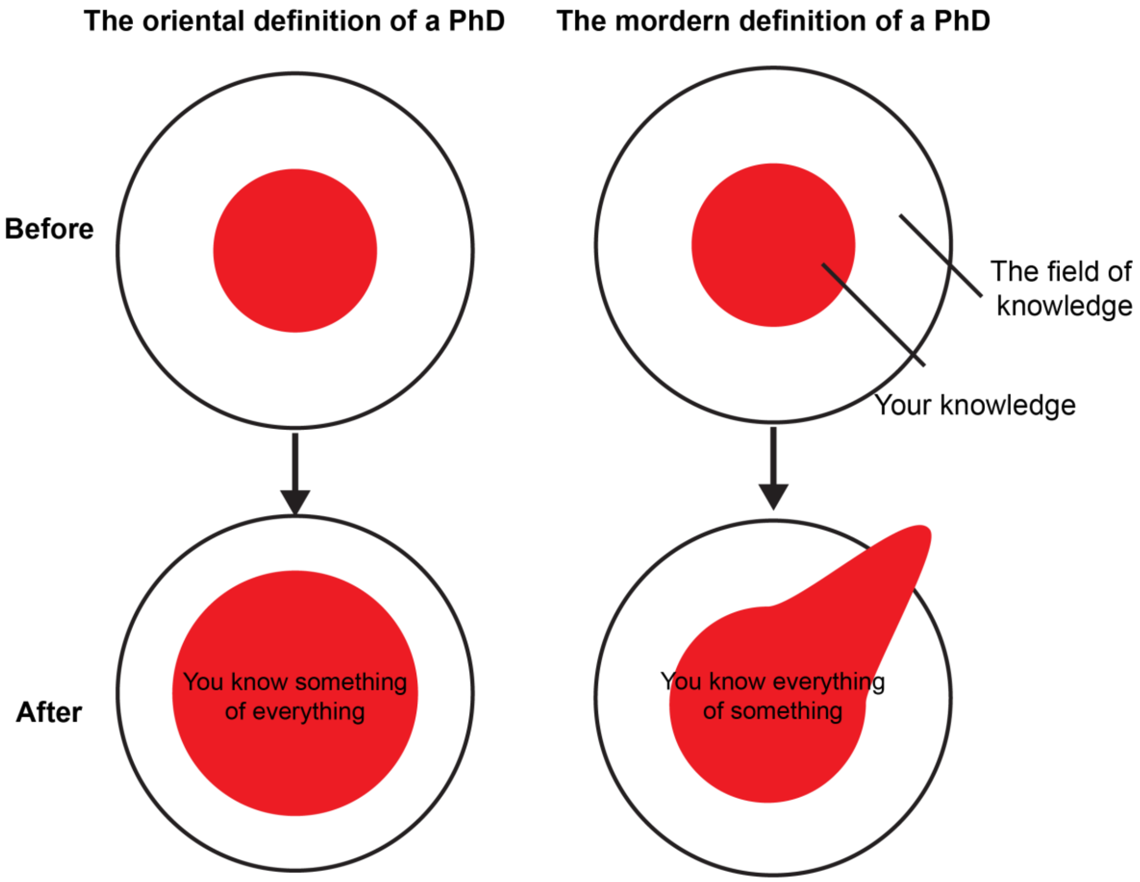

Figure 0 Definitions of a PhD

Abstract

Earlier studies of the male pronucleus (MPN) formation in echinoderms have isolated fusogenic vesicles, known as MV1, essential for nuclear envelope (NE) assembly. MV1 is a membrane compartment with elevated levels of phosphoinositides, a lipid-modifying enzyme PLCγ and its upstream regulator SFK1. These are responsible for production of localised diacylglycerol (DAG) which facilitates membrane fusion. The fusion mechanism in mammalian NE assembly is uncharacterised. We hypothesise MV1-like vesicles are responsible for completing the NE in mammalian cells by sealing the NE gaps at telophase.

To study the fusion mechanism in mammalian NE assembly, subcellular fractions analogous to MV1 were isolated from CHO and HeLa cells. However, these membrane fractions were rarely separated from the ER, Golgi and endosomes subfractions. Electron tomography confirmed the presence of membrane vesicles (MVs) in the vicinity of the NE gaps at telophase. Moreover, the quantity of these MVs was significantly higher in the regions of large gap versus regions without gap, suggesting a putative consumption of these MVs for gap closure. Furthermore, PtdIns(3,4,5)P_3 and class I PI3 kinase were detected in endomembranes at the vicinity of the mammalian NE implying the presence of MV1-like vesicles. DAG-enriched MVs were detected in interphase cells using a miniSOG-conjugated C1aC1b domain; they may be involved in house-keeping fusion events.

Using a chemically-induced dimerisation system and correlative light and electron microscopy, localised DAG production was demonstrated to be essential for mammalian NE assembly. Acute DAG depletion in the NE resulted in NE fragmentation. Fragmented NE was rescued by addition of exogenous DAG. Also, we show for the first time that Golgi-DAG depletion led to fragmented NE, signifying that the Golgi may produce fusogenic vesicles. Our findings show that the regulatory mechanisms involved in the MPN formation in fertilised echinoderm eggs are also conserved in mammalian NE assembly during mitosis.

Table of Contents

List of Abbreviations

AEBSF	4-(2-Aminoethyl)benzenesulfonyl fluoride hydrochloride
AKT/PKB	Protein kinase B
APEX	Engineered ascorbate peroxidase
ARNO	ARF nucleotide-binding site opener
ATP	Adenosine triphosphate
BDT	Big dye terminator
BiP	Binding immunoglobulin protein
BSA	Bovine serum albumin
BTK	Bruton's tyrosine kinase
CCD	Charge-coupled device
CLEM	Correlative light and electron microscopy
DAB	Diaminobenzidine
DABCO	1,4-diazabicyclo[2.2.2]octane
DAG	Diacylglycerol
DAB	Diaminobenzidine
DCS	Donor calf serum
DGK	Diacylglycerol kinase
$DiOC_6$	3,3’-dihexyloxacarbocyanine iodide
$DiOC_{18}$	3,3’-dioctadecyloxacarbocyanine perchlorate
DMEM	Dulbecco’s modified Eagle’s medium
DMSO	Dimethyl sulfoxide
DNA	Deoxyribonucleic acid
DTT	Dithiothreitol
ECL	Enhanced chemiluminescence
EDTA	Ethylenediaminetetraacetic acid
EGF	Epidermal growth factor
EM	Electron microscope/microscopy
ER	Endoplasmic reticulum
FA	Formaldehyde
FCS	Fetal calf serum
FKBP	FK506-binding protein
FLIP	Fluorescence loss in photobleaching
FRB	FKBP12-rapamycin associated protein 1
FRET	Förster resonance energy transfer
GA	Glutaraldehyde
GCNT1	Glucosaminyl (N-Acetyl) transferase 1, core 2
GFP	Enhanced green fluorescent protein
GRP1	General receptor of phosphoinositides 1
GST	Glutathione S-transferase
GTP	Guanosine triphosphate
HB	Homogenisation buffer
HBSS	Hank’s balanced salt solution
HRP	Horseradish peroxidase
HPLC	High pressure liquid chromatography
IP_4/Ins(1,3,4,5)P_4	Inositol 1,3,4,5-tetrakisphosphate
KD	Dissociation constant
K_{off}	Dissociation rate constant
K_{on}	Association rate constant
LB	Lysogeny broth
LBR	Lamin B receptor
LC-ESI-MS/MS	Liquid chromatography-electrospray ionisation-tandem mass spectrometry
MiniSOG	Mini singlet oxygen generator
MOPS	3-(N-morpholino)propanesulfonic acid
MPN	Male pronucleus
MV	Membrane vesicle
NE	Nuclear envelope
NMR	Nuclear magnetic resonance
NGF	Nerve growth factor
NPC	Nuclear pore complex
PAGE	Polyacrylamide gel electrophoresis

PB	Phosphate buffer
PBS	Phosphate buffered saline
PBST	0.2% (v/v) Tween-20 in PBS
PCR	Polymerase chain reaction
PDK	Phosphoinositide-dependent kinase
PFA	Paraformaldehyde
PH	Pleckstrin homology domain
PIs	Phosphoinositides
PIS	Phosphoinositides synthase
PI3K	Phosphatidylinositol 3-kinase
PKD	Protein kinase D
PLC	Phosphoinositide phospholipase C
PMSF	Phenylmethylsulfonyl fluoride
PNS	Postnuclear supernatant
PtdCho	Phosphatidylcholine
PtdIns	Phosphatidylinositol
PtdIns4P	Phosphatidylinositol-4-phosphate
PtdIns(4,5)P_2	Phosphatidylinositol-(4,5)-diphosphate
PtdIns(3,4,5)P_3	Phosphatidylinositol-(3,4,5)-triphosphate
PtdOH	Phosphatidic acid
PtdSer	Phosphatidylserine
PVDF	Polyvinylidene fluoride
rpm	Revolutions per minute
Ran	Ras-related nuclear protein
RFP	Red fluorescent protein
SBF SEM	Serial block-face scanning electron microscopy
SDS	Sodium dodecyl sulphate
SEM	Scanning electron microscope/microscopy
SKIP	Skeletal muscle and kidney enriched inositol phosphatase
SOC	Super optimal broth with catabolite repression
ST6GALNAC1	ST6 (alpha-N-acetyl-neuraminyl-2,3-beta-galactosyl-1,3)-N-acetylgalactosaminide alpha-2,6-sialyltransferase 1
T_m	DNA melting temperature, °C
TAE	Tris acetate EDTA buffer
TEM	Transmission electron microscope/microscopy
TGN	*Trans*-Golgi network
Tris	Tris(hydroxymethyl)aminomethane
WT	Wild type
2D/3D	two-dimensions/three-dimensions

List of Figures

List of Tables

List of Videos

Chapter 1 Introduction

1.1 Membrane structure and functions

All cells are confined by a membrane and eukaryotic cells have many membrane-enclosed organelles. A membrane is a lamellar bilayer of lipids associated with macromolecules such as carbohydrates and proteins. The fluid mosaic model (Singer and Nicolson, 1972) is traditionally used to describe the structure of a membrane. However, with the research advancement from different fields, the limitations of this model have been presented and today the model has been updated. A comprehensive review has discussed several novel aspects added to this model in order to describe membrane structure more accurately. For instance, the high density of proteins associated with the bilayer; the role of membrane curvature and its relation to lipid geometry; the existence of lateral heterogeneity in the membrane in addition to bilayer asymmetry (Goni, 2014). Membranes are well known for their selective permeability, however, apart from being barriers, membranes are involved in numerous cellular functions such as recognition and response to signal transduction, cell adhesion, cargo trafficking, and many others (Eyster, 2007, De Matteis and Godi, 2004, Murai, 2012).

Unlike nucleotides, amino acids and carbohydrates, lipid molecules do not form strong chemical bonds in their macromolecular assembly, and this gives them a unique "softness" and a conformational complexity compared to other organic molecules. The major components of membranes are phospholipids. Figure 1.1 illustrates a general chemical structure of a phospholipid. The formation of membranes is a self-assembly process under normal cellular conditions due to the amphipathic nature of phospholipids. In aqueous media, the hydrophobic effect drives the polar head groups of phospholipids to align along the lipid-water interface, minimising the exposure of the hydrophobic fatty acid chains to water. This is the most energetically favourable arrangement for the lipid molecules (Figure 1.2).

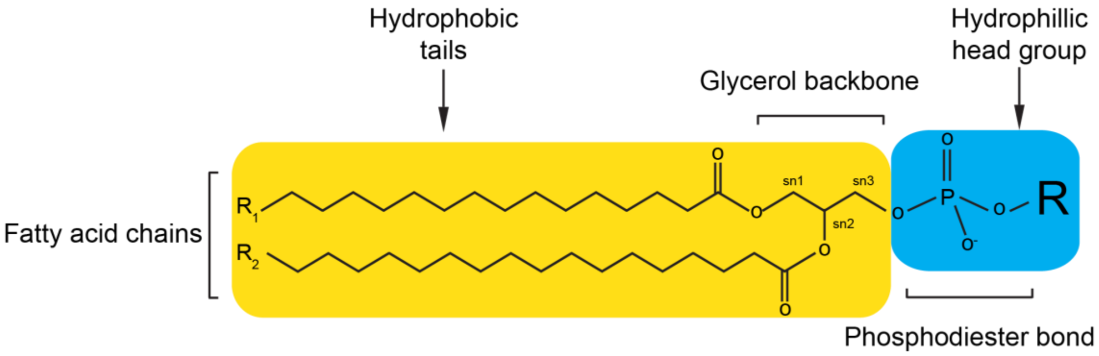

Figure 1.1 The amphipathic property of phospholipids

A glycerol backbone is bonded to two fatty acid molecules (R_1 and R_2) at the sn-1 and sn-2 positions. The sn-3 position of the glycerol is bound to a hydrophilic head group (R) though a phosphodiester bond. The physical properties of the lipids depend on the head groups and fatty acid chains.

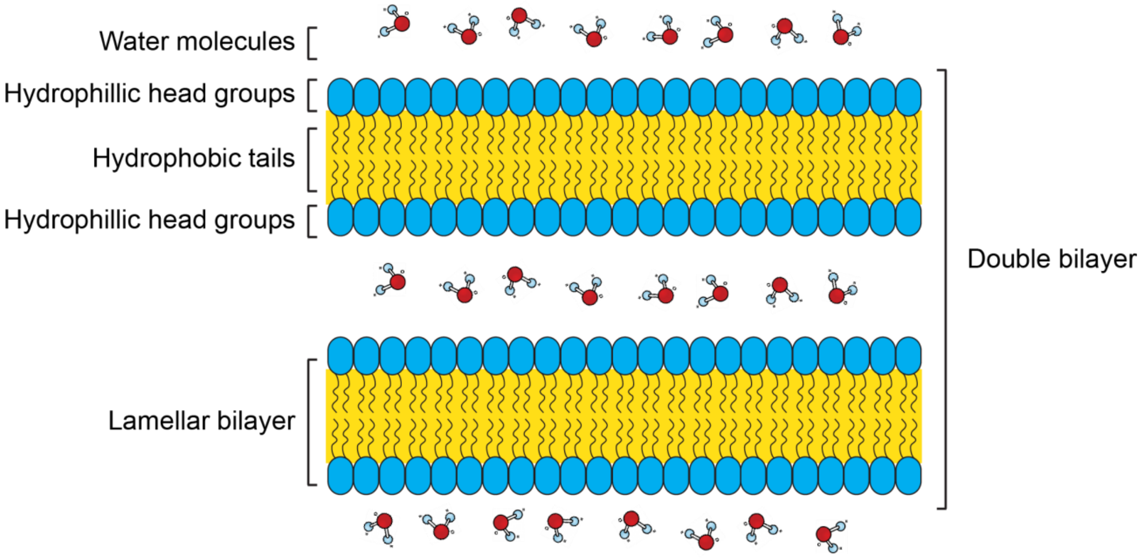

Figure 1.2 The structure of a double lipid bilayer

The hydrogen bonding of water molecules repels the hydrophobic tails of lipids. To reduce the exposure of fatty acid chains in aqueous solution, lipids are aligned into a bilayer though dipole-dipole interactions. Some cellular compartments are enclosed by a double lipid bilayer, such as mitochondria, chloroplasts and the nucleus. Size of molecules not in scale.

The effective shapes of lipids are highly diverse therefore they are able to form various structures. Figure 1.3 displays the possible macromolecular assemblies of lipids. Lamellar bilayer is the most energetically favourable structure at normal physiological conditions. Other macromolecular assemblies occur at specific lipid concentrations and thermodynamic conditions. The effective shape of a lipid is defined by the cross section area of the head group and the length and volume of the fatty acid chain(s), also known as the packing parameter (P). Hence, the effective shape of a lipid can be approximated as a cylindrical/conical shape.

To form a lamellar layer without any curvature, the effective shape of the lipids should be cylindrical. When the effective shape of lipids deviates from a cylindrical volume to a cone/inverted-cone, voids appear in the lamellar layer and this is energetically unfavourable. Therefore, the lamellar layer has to compensate the voids in the structure, resulting in bending of the membrane. The tendency of membranes to bend and relax in a specific direction is known as spontaneous curvature, and will be introduced in section 1.4.

In reality a biomembrane is a highly organised structure composed of proteins, polysaccharides and various lipid species with different packing parameters. Moreover, membrane compartments have distinctive morphologies and they are niches of different cellular functions. The cellular membranes *per se* act as sites for hundreds of enzymes to synthesise lipids. The newly synthesised lipids are then transported to their designated membrane through different mechanisms. Figure 1.4 summarises the biosynthesis and trafficking of some major lipids. These highly regulated events reflect the necessity of the “right lipid composition” within a membrane in order to maintain the correct membrane structure and function.

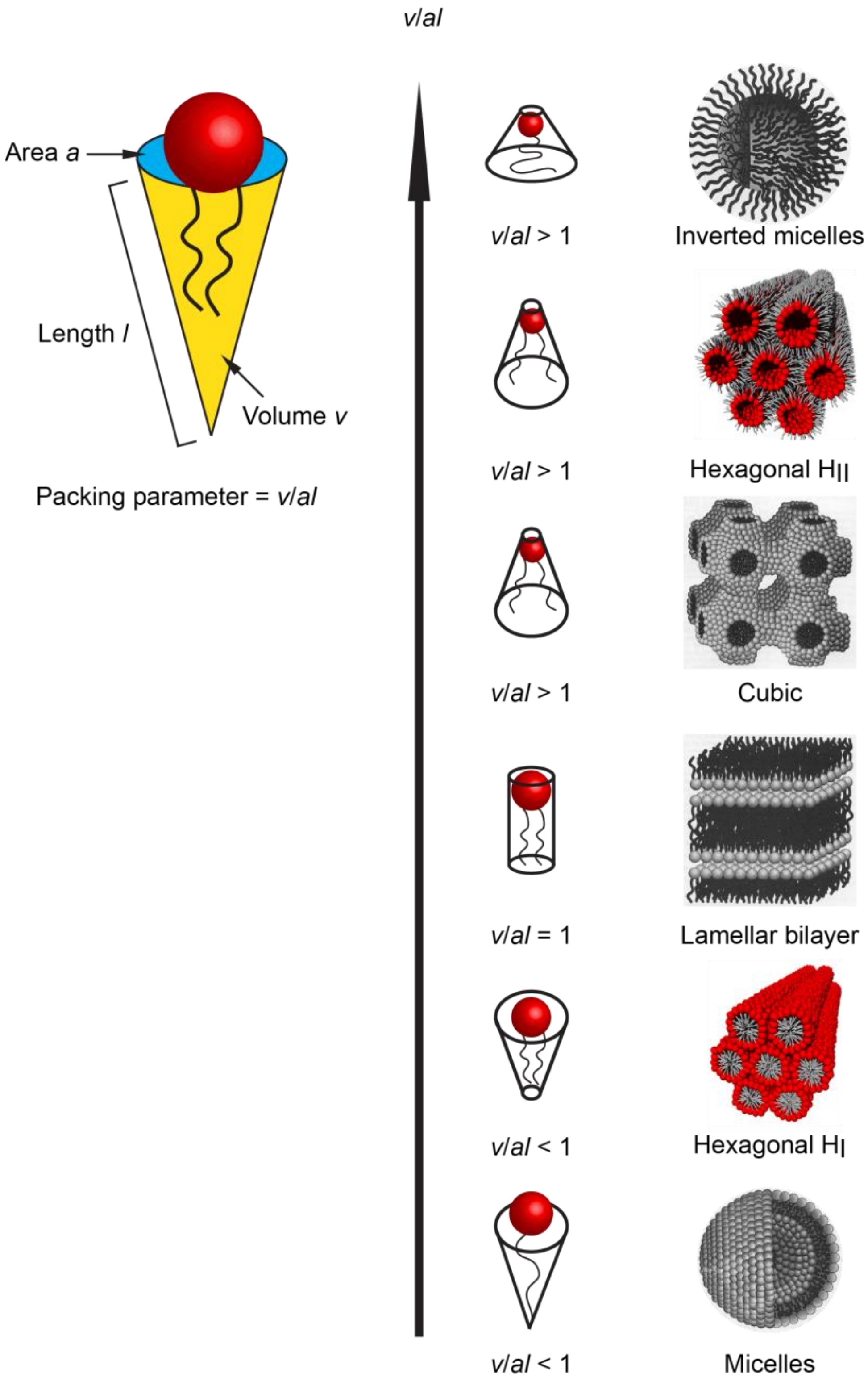

Figure 1.3 The different macromolecular assemblies of lipid

Lipids aggregate into different structures according to their packing parameter (*P*). The packing parameter is the cylindrical or conical volume of the fatty acid tail(s) (*v*) divided by the cross section area of the polar head group (*a*) and the length of the cylindrical or conical volume (*l*). 3D models adapted from Tresset (2009) and Holmberg (2003)

More importantly, membrane structures are constantly remodelled through different mechanisms, membrane fusion – merging of two membranes – is one of them. Membrane fusion is required in a wide range of cellular activities such as vesicle trafficking in exocytosis and endocytosis, fertilisation and synaptic transmission (De Matteis and Godi, 2004, Rizo and Rosenmund, 2008, Collas and Poccia, 2000). The mechanisms of membrane fusion will be covered in section 1.4. Recently, the implications of the specific physical properties of phospholipids on membrane fusion in biomembranes have been studied by several groups (Larijani *et al.*, 2014, Rafikova *et al.*, 2010). In this thesis, we investigated how membrane fusion is required for the formation of the nuclear envelope (NE), which is one of the most important cellular compartments in a eukaryotic cell.

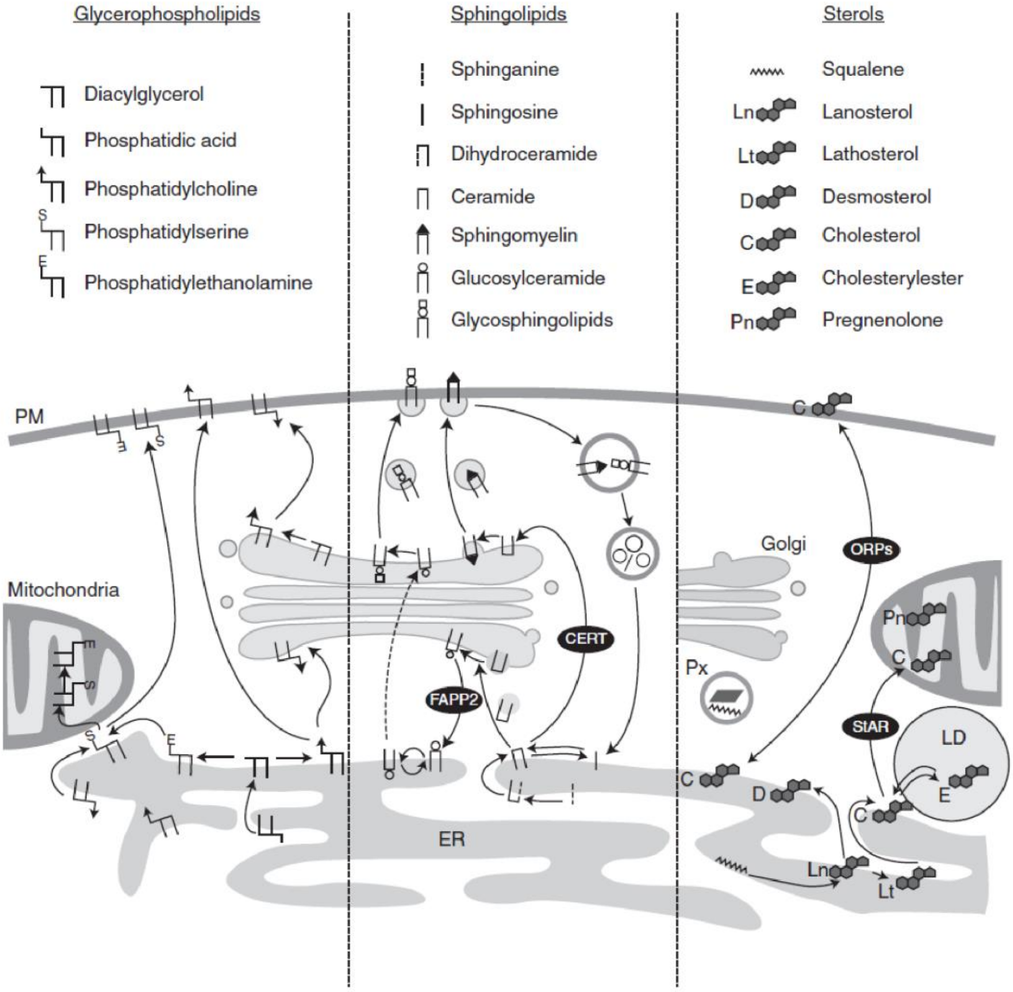

Figure 1.4 **Biosynthesis and trafficking of major membrane lipids**

Lipids can be classified into three major classes: the phospholipids (glycerophospholipids), sphingolipids and sterols. (Left) Phospholipids are synthesised in the ER and are transported through both vesicular and non-vesicular mechanisms. However, not much is known about the exact mechanisms. (Middle) Sphingolipids are initially synthesised in the ER, and are transported to the Golgi or other membranes. Some sphingolipids are recycled back to the ER for sphinoglipids and phospholipids synthesis. (Right) Sterols are mainly produced in the ER and then directly transported to the plasma membrane and mitochondria through protein carriers. Arrows indicate the direction of lipid transport and black ellipses indicate some key lipid carrier proteins. Adapted from Blom *et al.* (2011). © Cold Spring Harbor Laboratory Press.

1.2 The nuclear envelope – a multi-functional and dynamic subcompartment

The NE is a complex membrane compartment (Figure 1.5). It is a physical barrier composed of double bilayers that separate the genome from the cytoplasm. The outer nuclear membrane (ONM) and the inner nuclear membrane (INM) are joined at the nuclear pore complexes (NPCs) which control the transportation between cytoplasm and nucleoplasm. The ONM is continuous with the ER. Underneath, the INM is a network of filamentous protein called nuclear lamina which provides mechanical support to the NE and interacts with many NE proteins.

Irregularity of the NE is associated with various cancers including bladder (Borland *et al.*, 1993), breast (Seker *et al.*, 2002), papillary thyroid carcinoma (Fischer *et al.*, 2001), head and neck (Maiolino *et al.*, 2002) and many other examples reviewed in de Las Heras *et al.* (2013) and Zink *et al.* (2004). Abnormal NE phenotypes such as increased in malleability and lobulations have a prognostic significance. In addition, defects in NE proteins such as the lamins and nucleoporins (Nups) result in a group of diseases call laminopathies (Chi *et al.*, 2009, Burke and Stewart, 2002, Broers *et al.*, 2006, Hutchison, 2014). NE associated proteins are also involved in chromosome organisation thus in genome stability (Dellaire *et al.*, 2009). Recruitment of immunoglobulin heavy chain (*Igh*) loci to the INM results in its transcriptional repression, suggesting a role for INM and lamina proteins in gene regulation (Reddy *et al.*, 2008). In addition, the NE may participate in calcium signalling, reviewed in Mauger (2012).

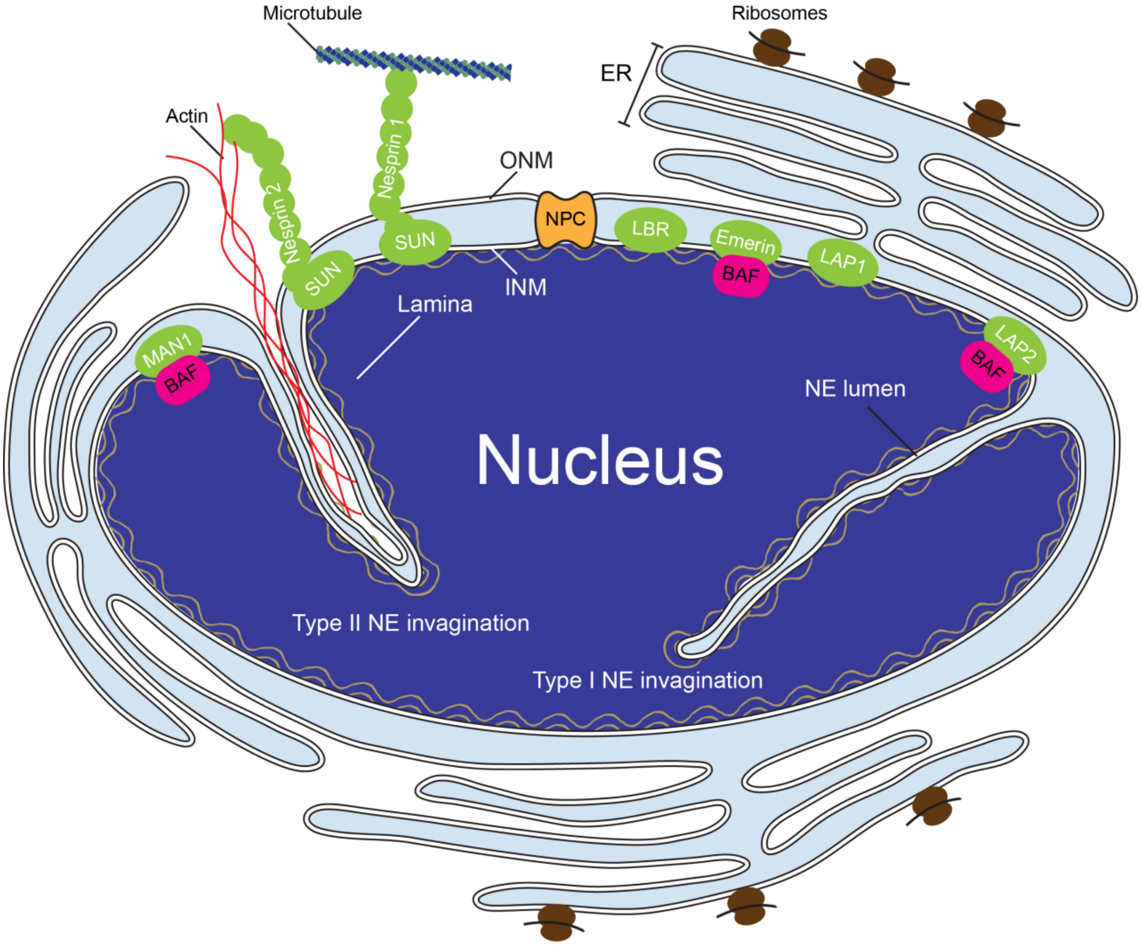

Figure 1.5 The nuclear envelope is a complex membrane compartment
Structure of the NE: The outer nuclear membrane (ONM) is continuous with the ER and is connected with the inner nuclear membrane (INM) at the nuclear pore complex (NPC). The ONM shares similar biochemical content as the ER whereas the INM contains a unique population of NE proteins. The nuclear lamina underneath the INM serves to maintain nuclear stability and interacts with a large family of NE proteins (green) and chromatin associated proteins (pink). Type I and type II NE invaginations are special structural arrangements of the NE, regulated by various mechanisms (Malhas *et al.*, 2011). Figure not in scale.

The NE is a dynamic compartment and its remodelling is highly regulated at different mitotic stages. During cell division, metazoans (higher eukaryotes) undergo "open" mitosis in which their NE breaks down and reassembles. In contrast, lower eukaryotes undergo "close" mitosis which does not require a NE breakdown (NEBD). Some cells undergo "semi-closed" mitosis wherein the NE is partially opened (syncytial cells in *Drosophila melanogaster* embryo) or NPCs are temporally disassembled for the access of mitotic spindles (fugus *Aspergillus nidulans*) prior to NE reassembly (De Souza *et al.*, 2004, Guttinger *et al.*, 2009). The details of different mitotic strategies of eukaryotes are shown in Figure 1.6.

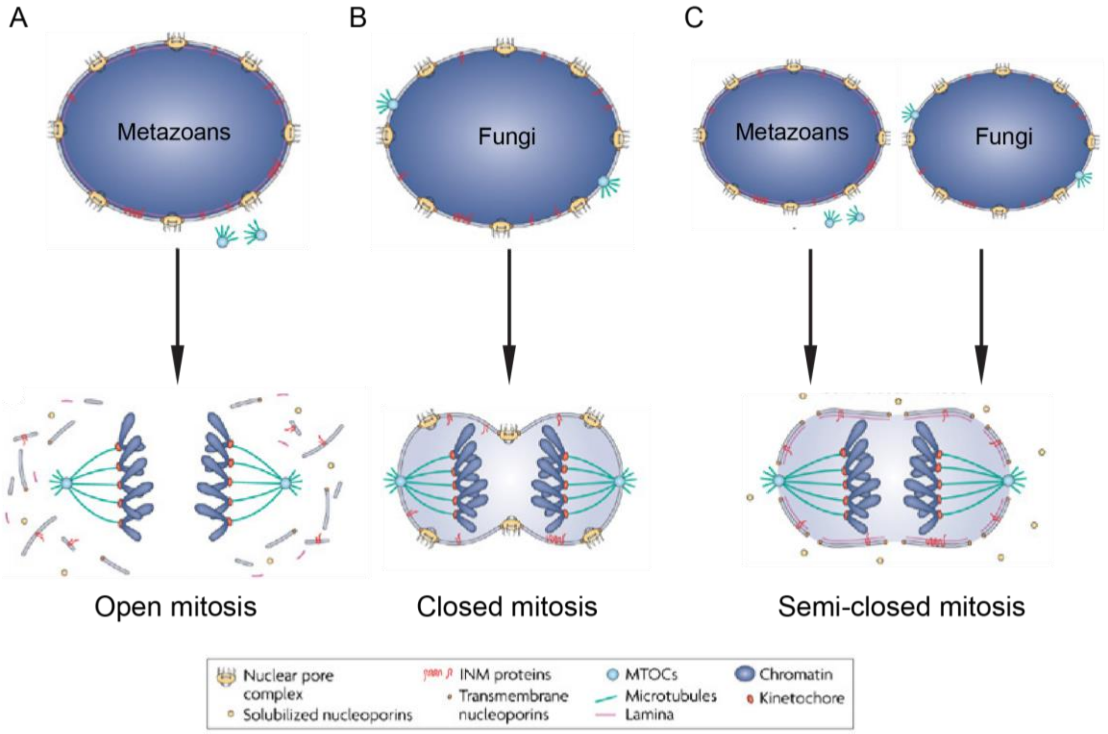

Figure 1.6 Three mitotic strategies used in eukaryotes

(A) Metazoans undergo open mitosis. The NE is disassembled completely and dissociated from the chromatin to allow the access of cytoplasmic spindles emanated from the microtubules-organising centre (MTOC). (B) In closed mitosis executed by lower eukaryotes, the NE remains intact. The MTOC is either inserted to the NE during mitosis or already existed in the NE. Nuclear spindles emanated from the MTOC then direct chromosome separation in a closed NE. (C) Early embryos of *Caenorhabditis elegans* (metazoans) and fungus *Aspergillus nidulans* (lower eukaryotes) undergo semi-closed mitosis. The NE either partially opens up near to centrosomes (*Caenorhabditis elegans*) or opens up through disassembly of NPC to allow the spindle microtubules bind to the chromosomes (*Aspergillus nidulans*). Adapted from Guttinger *et al.* (2009).

In our work, we have been interested in studying the NE reassembly of mammalian cells which undergo open mitosis. Figure 1.7 illustrates the completeness of the NE at different mitotic stages. Mammalian NE disassembles at prophase and this involves complicated molecular mechanisms including the stepwise disassembly of lamina, intervention of microtubules on the chromosomes (Georgatos *et al.*, 1997) and dynein-NE interaction (Gonczy, 2002). NE proteins are reabsorbed to the mitotic ER at this stage (Ellenberg, 2002). The NE reassembly starts at anaphase, and at this stage the mitotic ER has contact with the rim of separating chromosomes (Lu *et al.*, 2011). The NE is completed at late telophase marked by the two intact daughter nuclei. Finally at cytokinesis the cytoplasm is separated between two daughter cells.

The mechanism of NE reassembly is not fully understood although there are two independent models proposed in the field. The details of these two models will be described in the following section. Given the multiple functions and dynamics of the NE, the investigation of the architecture and molecular mechanism of NE reassembly is essential to understand its disease relevance.

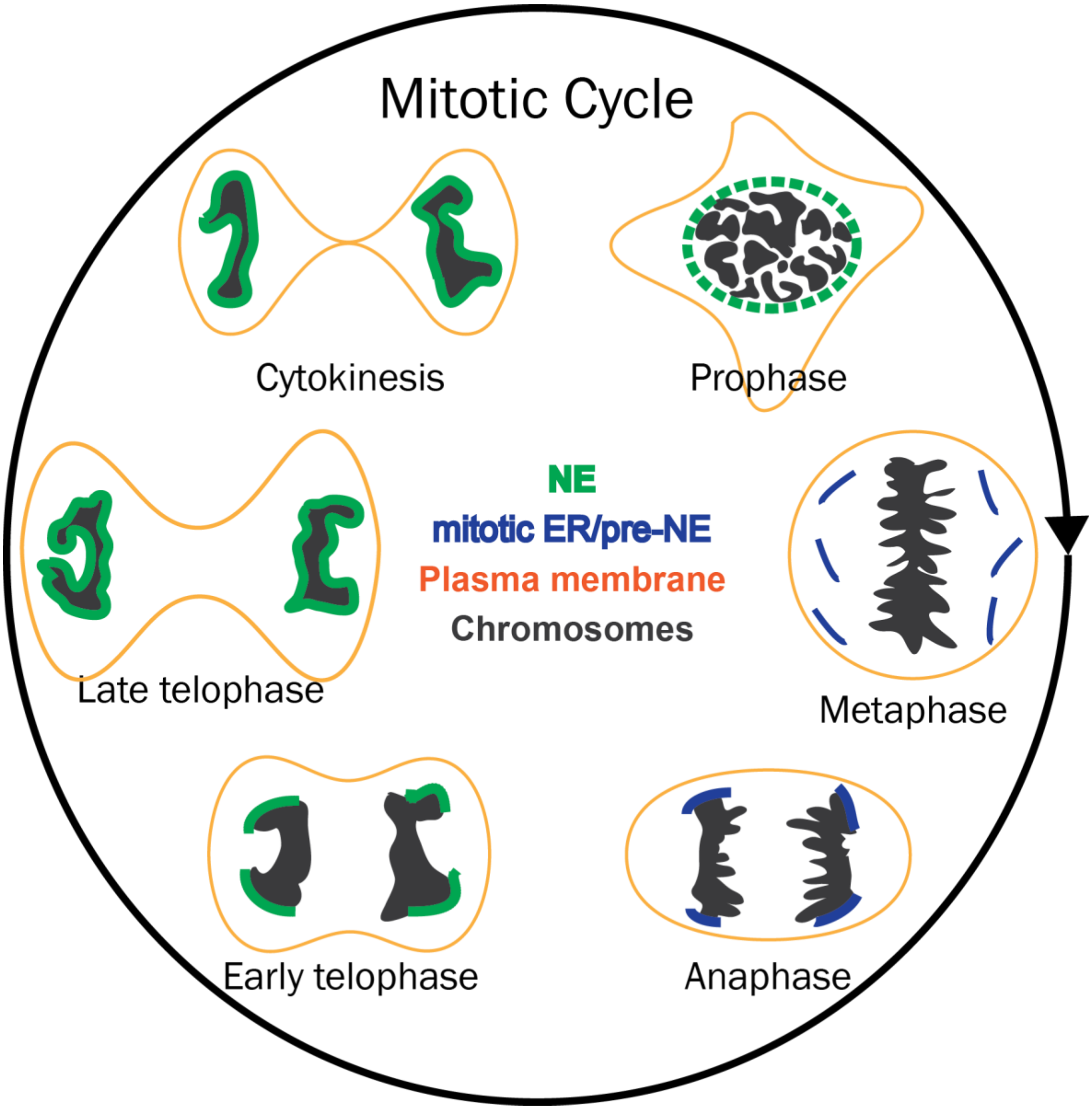

Figure 1.7 NE at different mitotic stages of mammalian cells

At prophase, chromosomes condense and the NE starts to disassemble. The disassembled NE and NE proteins retract to the mitotic ER. Chromatin alignment happens at metaphase and there is no NE at this stage. At anaphase, recent studies have indicated the contact of cisternal ER/pre-NE at the radial periphery of the separating chromosomes (see section 1.3.1). At telophase, the NE continues to reform around the decondensing chromosomes and the reassembly is completed at late telophase. At cytokinesis, the contractile ring composed of actin filaments and myosin cleaves the cytoplasm, resulting in two separated daughter cells.

1.3 Two models of nuclear envelope assembly

The outer bilayer of the NE is linked to the ER and can be seen as an ER subunit. NE reassembly during mitosis is closely associated with the mitotic ER. The two proposed NE assembly models are based on two apparently contradictory observations: the first model is based on confocal imaging of NE proteins that redistribute to the mitotic ER *in vivo* and the second model is based on assembly of membrane vesicles derived from fragmentation of the ER in cytoplasmic homogenates and/or related *in vivo* experiments. These two models have several features in common and therefore should not be seen as mutually exclusive, as summarised in Figure 1.8.

1.3.1 The ER envelopment model

The critical component of the ER envelopment model is the presence of NE proteins in NE precursors such that these NE precursors can be targeted to chromosomes. There are thousands of NE transmembrane proteins (NETs) in the ONM and INM (Korfali *et al.*, 2010, Wilkie *et al.*, 2011). The NETs are relevant to various diseases such as dystrophies and laminopathies (Broers *et al.*, 2006, Schirmer *et al.*, 2003), and some of them such as Lem2 are required for normal NE morphology (Ulbert *et al.*, 2006). In *Xenopus* cell-free assay, truncated recombinant LAP2β protein disrupts NE assembly (Gant *et al.*, 1999) and NEP-B78 may be required for targeting vesicles to the decondensing chromatin as antibody against NEP-B78 disrupts NE reassembly (Drummond *et al.*, 1999).

In mammalian cells, NETs are absorbed by the mitotic ER after NE breakdown. For instance, lamin B receptor (LBR) that binds to heterochromatin is present in the mitotic ER (Yang *et al.*, 1997a, Ellenberg *et al.*, 1997). This allows the ER to be targeted to chromosomes (Collas *et al.*, 1996, Ellenberg *et al.*, 1997). The ER envelopment model suggests that mitotic ER tubules bind to chromosomes and the flattening of these ER tubules against the chromosome surface gives rise to the new NE; membrane fusion is not the principle mechanism of NE reassembly in this model (Anderson and Hetzer, 2007).

In fact, the architecture of mitotic ER is a subject of debate. An exclusively tubular network of ER has been observed in mitotic cells and overexpression of reticulons (proteins that promote tubular ER) causes delay of NE formation (Anderson and Hetzer, 2008). However, there is no direct observation of tubule-to-cisternae ER organelle shaping at the chromosomes. On the other hand, recent studies have shown that the mitotic ER of various mammalian cell lines is composed primarily of extended cisternae using high resolution electron tomography (Lu *et al.*, 2009). The contact between chromatin and cisternal ER has been shown to initiate NE assembly at anaphase (Lu *et al.*, 2011). Cisternal ER has also been observed in *Caenorhabditis elegans* embryos. (Poteryaev *et al.*, 2005). Given the above results, the targeting of the mitotic ER to the chromosomes has an obvious role in NE assembly.

Nevertheless, for the mitotic ER to form a continuous membrane around the nucleus at least one gap must be sealed but *in vitro* data suggests that there are multiple gaps to be sealed during NE assembly (Wiese *et al.*, 1997). NPCs have been thought to seal these gaps (Antonin *et al.*, 2008, Burke, 2001), and depletion of nucleoporin POM121 inhibits NE assembly *in vitro*. However, depletion of POM121 does not prevent NE assembly *in vivo* (Antonin *et al.*, 2005). Moreover, the NE of echinoderm sperm does not have any nuclear pore (Longo and Anderson, 1969), meaning that NE assembly can be NPC-independent. In summary, the ER envelopment model suggests an assembly description but it lacks a definitive mechanism to explain how the necessary fusion occurs during completion of the NE.

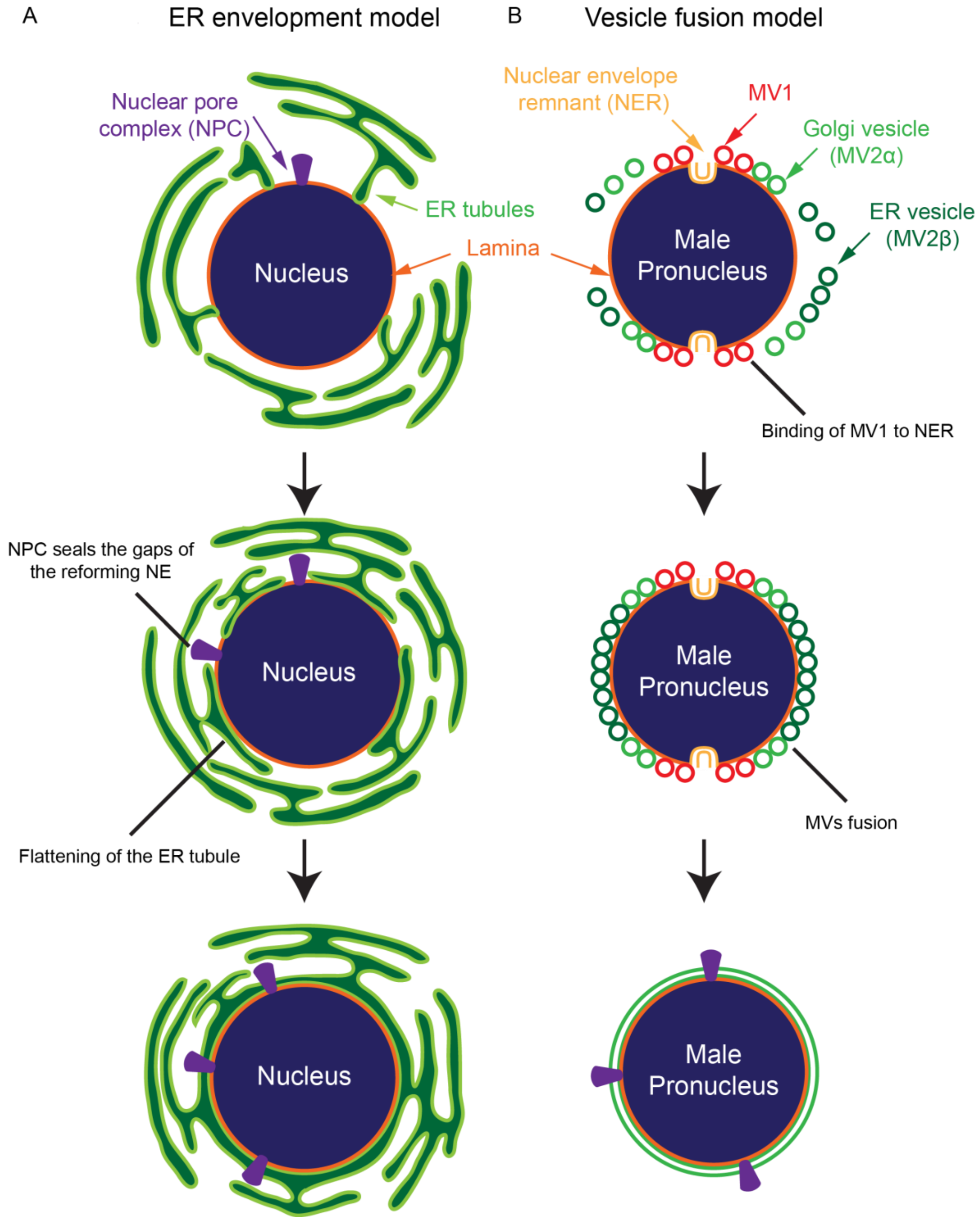

Figure 1.8 Two major models of NE assembly

(A) The ER envelopment model. The mitotic ER tubules are targeted to the chromosomes due to the presence of NE proteins that interact with the lamina/chromosomes, and flattening of the bound ER contribute to the NE. NPC is suggested to seal the gaps of ER envelopment. (B) The vesicle fusion model is based on the NE assembly assay of the echinoderm male pronucleus (MPN). MV1 vesicles bind to the nuclear envelope remnants (NER) and followed by binding of membrane vesicles originated from the ER (MV2β) and Golgi (MV2α). MV1 is enriched in poly-phosphoinositides and PLCγ. These machineries generate fusogenic lipids required for membrane fusion so that the vesicular NE precursors can undergo fusion in order to form a complete NE of the MPN.

1.3.2 The vesicle fusion model

The vesicle fusion model postulates that fusion of membrane vesicles (MVs) and ER membranes are required for forming a complete NE, and fusogenic lipids play an important role in this model. The model is supported by both *in vitro* and *in vivo* evidence. Cell-free assays based on male pronucleus (MPN) formation of *Xenopus* and echinoderms (sea urchins) have isolated vesicles essential for NE reassembly (Collas and Poccia, 1996, Drummond *et al.*, 1999). Moreover, early electron microscopy studies have visualised accumulation of MVs around the nucleus of fused pronuclei of echinoderms (Longo, 1972) and the presence of fusion intermediates in rabbit egg *in vivo* (Meyer and Longo, 1979).

Moreover, detailed biochemical information has been provided by NE assembly cell-free assay derived from MPN formation of echinoderms. *In vivo*, when a sperm nucleus enters the egg, its poreless NE is rapidly disassembled except that NERs remain at the tip and the base of the conical nucleus. The MPN formation is then followed by disassembly of the lamina, decondensation of the chromatin and reformation of the lamina and NE with NPC. The cell-free assay is highly similar to the *in vivo* process, in which demembranated sperm with NERs is supplied with membrane fractions separated from the fertilised egg homogenate to form a complete NE (Cameron and Poccia, 1994). Two populations of NE precursor termed MV1 and MV2, are essential for NE reassembly in the echinoderm cell-free assay in the presence of GTP (Collas and Poccia, 1996).

MV1s are non-ER, non-Golgi derived vesicles that bind to the nuclear poles (NE remnants) of the sperm. MV2 can be further sub-fractionated into MV2α and MV2β, which are enriched in Golgi and ER marker respectively. MV2α binds exclusively to the nuclear poles of the sperm and is required for the fusion of MV2β to MV1. MV2β is analogous to the mitotic ER in the ER envelopment model, as both of which are the major NE precursors and contain LBR (Poccia and Collas, 1997).

More importantly, MV1 has a distinctive lipid-protein profile (Figure 1.9). MV1 is enriched in poly-phosphoinositides and PLCγ (Byrne *et al.*, 2007, Larijani *et al.*, 2001). PLCγ is able to generate DAG and IP_3 from PtdIns(4,5)P_2 wherein localised production of DAG but not IP_3 is responsible for membrane fusion (Larijani *et al.*, 2001). Furthermore, a protein-free lipid composition which mimics MV1 can substitute MV1 for its binding and NE assembly function (Barona *et al.*, 2005). PLCγ has been found to associate with a tyrosine kinase SFK (Byrne *et al.*, 2009). Recently, the direct activation of PLCγ by SFK has been demonstrated using an amplified time-resolved FRET (Förster resonance energy transfer) (Byrne *et al.*, 2014). Such protein-lipid interactions provide a mechanistic explanation for the model.

Furthermore, PLCγ-enriched vesicles have been detected *in vivo* around the cortex of the egg, and the vesicles are distinguishable from the ER network. PLCγ-enriched vesicles come to the vicinity of the MPN at 2 min post-fertilisation during NE reassembly (Byrne *et al.*, 2007). PLCγ-enriched vesicles are also present in the regions of karyomeres (individual chromosome with a NE) fusion (Byrne *et al.*, 2014). This suggests that MV1 is a distinctive compartment *in vivo* and PLCγ-dependent fusion is required for NE formation. In summary, the vesicle fusion model emphasises on the localised production of DAG in the NE precursors. These precursors can be vesicles or other membrane structures with protein markers interacting with the chromosomes and lamina.

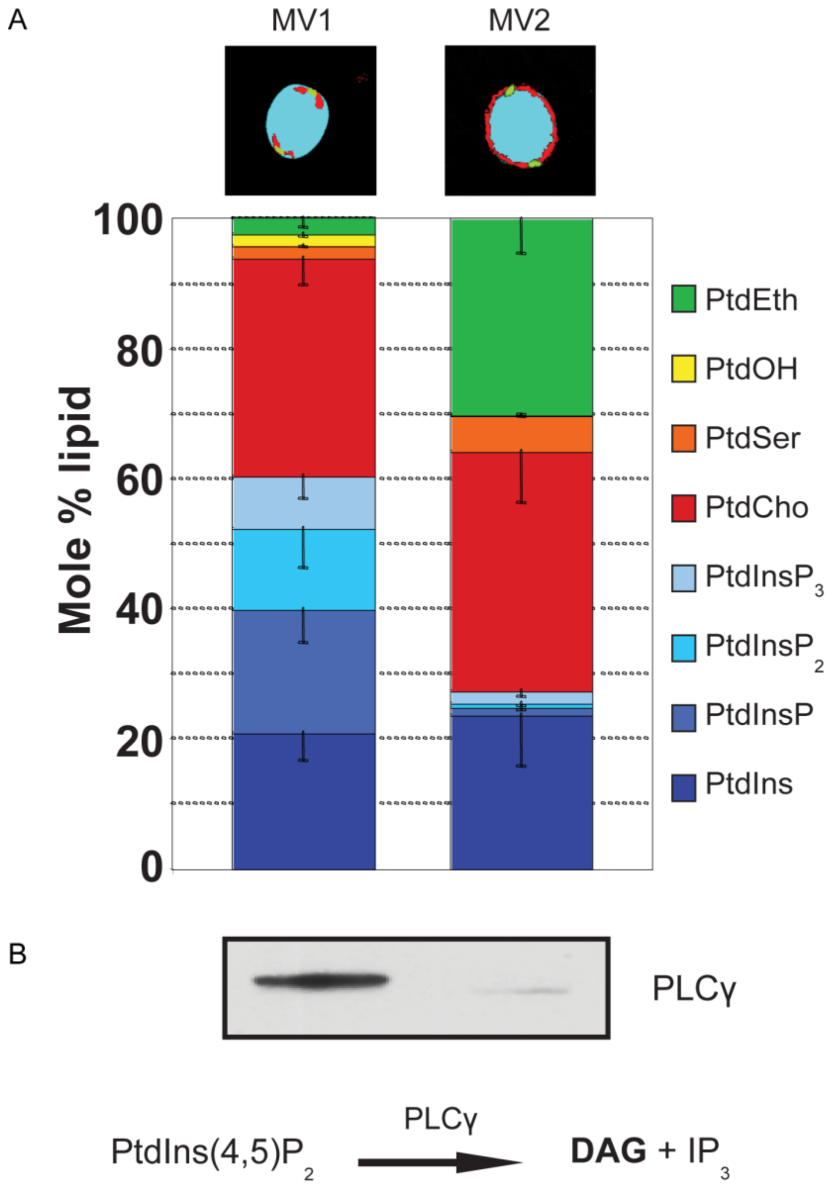

Figure 1.9 MV1 has distinctive lipid and protein profile compared to MV2

(A) Total membrane fraction (MV0) was separated by sucrose gradient into different fractions (MVs), and the binding property of MVs towards the decondensed nuclei was tested in the cell-free assay. Top images indicate the nuclear pole (yellow) and the localisation of binding MVs (red). MV1 binds to the nuclear pole and MV2 binds to the rest of the decondensed nuclei after the binding of MV1. LC-ESI-MS/MS was used to determine the phospholipid quantities of MV1 and MV2, that are expressed in mole percentage (n = 3 or 4). MV1 is highly enriched in poly-phosphoinositide species especially PtdInsP$_2$ (25 fold) and PtdInP$_3$ compared to MV2. (B) Equal volume of samples was separated by SDS-PAGE and PLCγ probed by Western blotting. Densitometry was used to calculate the proportion of PLCγ per MV fraction showing that MV1 has >100 fold PLCγ enrichment compared to MV2; densitometry protocol is described in Byrne *et al.* (2007). PLCγ can catalyse PtdInsP$_2$ into DAG (a fusogenic lipid) and IP$_3$. The presence of PLCγ and PtdInsP$_2$ on MV1 suggests a conceivable production of DAG and therefore fusogenicity. Adapted from Byrne *et al.* (2007).

1.3.3 The reconcilable model

There are several common features between the two models. First, the ER contributes to the majority of the NE in both models. Second, both models suggest the presence of NE transmembrane proteins (NETs) in the NE precursors so that the NE precursors can be targeted to the chromatin. For instance, LBR is detected at the mitotic ER in mammalian cells and also at the MVs in echinoderms cell-free assay.

The formation of the NE by ER coalescence should not be seen contradictory to vesicles binding and fusion. The ER vesicles in the cell-free assay are the result of homogenisation, although ER vesiculation has also been reported in mitosis (Jesch and Linstedt, 1998), as well as at the level of the NE and Golgi (Liu *et al.*, 2003). Hence, apart from tubular or cisternal mitotic ER, vesicular ER may also bind to chromosomes and contributes to NE reassembly. At the same time, non-ER vesicles which do not contain LBR have been isolated and are required for NE reassembly and membrane fusion. Together, mammalian NE reassembly may involve simultaneously ER envelopment and vesicle fusion (homotypic and heterotypic).

The vesicles fusion model provides a molecular mechanism on how fusion can occur and such a mechanism can be incorporated to the morphological description provided by the ER envelopment model.

1.4 Mechanism of membrane fusion

Membrane fusion is a complex process which involves participation of both lipids and proteins, but the contribution of lipids and proteins in membrane fusion is usually studied separately. Nevertheless, the underlying principle of fusion is changing the curvature of membranes. As mentioned earlier, the effective shape of non-lamellar lipids gives them a tendency to be curved and this is known as the spontaneous (or intrinsic) curvature.

The shape of membranes varies. In order to define a 3D membrane structure, the total curvature *(J)* and the Gaussian curvature *(K)* are used to represent sphere, tubule, saddle and other more complicated structures (Figure 1.10-A). To simplify this, the spontaneous curvature of a membrane is usually described by its principle curvature *(C)* in 2D. In this case, the ratio of the curvature radius (*R*) to the thickness of the membrane *(d)* is used to describe the degree of curvature (Figure 1.10-B). Moreover, according to whether the membrane bends towards the polar head groups or the fatty acid chains, membrane curvature can be positive, neutral or negative (Figure 1.10-C).

Membrane fusion is an unfavourable energetic event. First, the membranes are stabilised by strong hydrophobic forces. Second, electrostatic forces from the polar head groups repulse opposing membranes (Chernomordik and Kozlov, 2005). In general, there are three distinctive steps in membrane fusion: the adhesion of membrane, hemifusion and pore formation (Burger, 2000, Goni, 2014). There are two membrane fusion models which differ in the arrangement of hemifusion intermediates. However, recent findings tend to agree with the progression as revealed in Figure 1.11. The latest hemifusion model, also known as stalk-pore hypothesis, suggests a stepwise mechanism for fusion to happen. Two adhered membranes overcome the energetic barrier of hydration by protruding a “dimple”, which is a single point minimising the surface area of hydration. Membrane tension is built when the dimples contact each other, and this is energetically favourable for the formation of a hemifusion stalk. The proximal layers of the membranes are joined and expand outward to form a hemifusion diaphragm. The expansion continues and creates a fusion pore. Finally the fusion pore opens, resulting in the exchange of material from two originally separated membrane compartments.

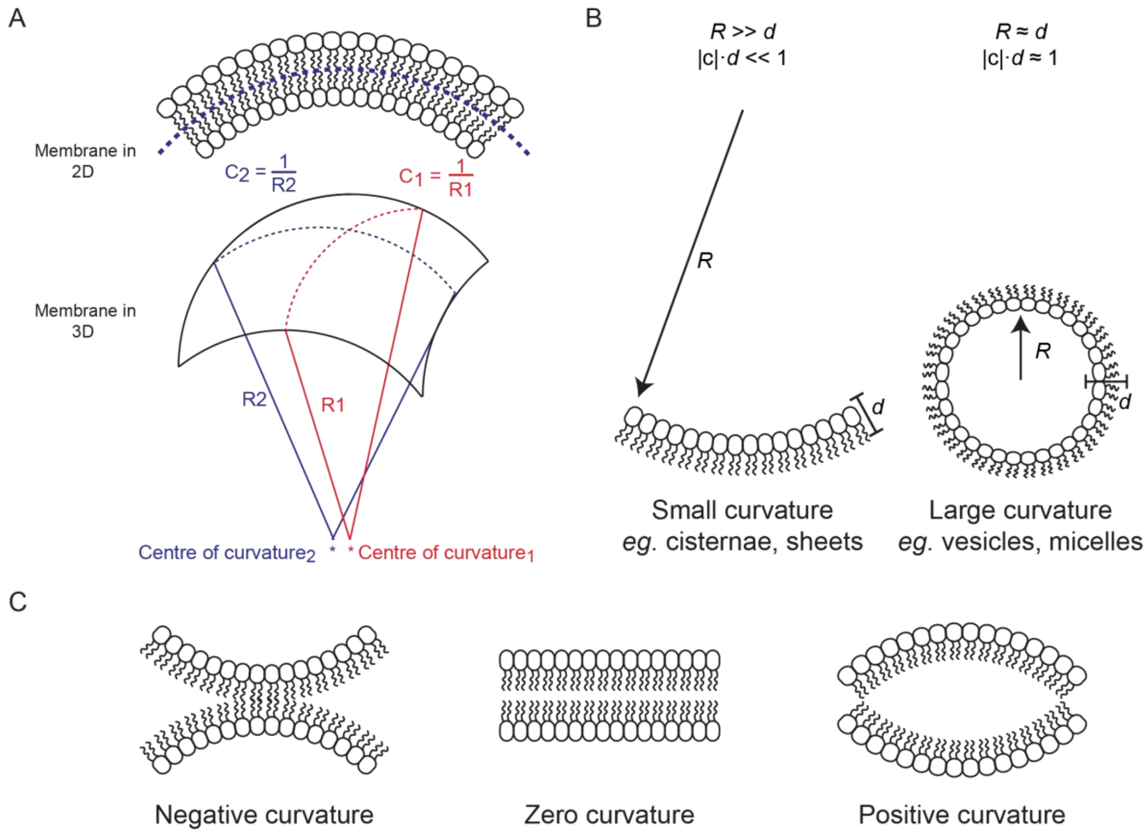

Figure 1.10 Geometric aspects of membrane curvature

(A) The geometry of 3D membrane structure can be described by the radii (R1 & R2) of two perpendicular arcs (red and blue dashed lines). The reciprocal of the radii is known as the principle curvatures (*C1* & *C2*) and the 3D structure can be mathematically represented with the total curvature ($J = C1 + C2$) and the Gaussian curvature ($K = C1 \times C2$), details are described in Shibata *et al.* (2009). (B) The geometry of membrane curvature is simplified by considering only the curvature of an arc in 2D. When the radius of curvature (*R*) is much larger than the thickness of a membrane (*d*), the curvature is considered as small. Membrane compartments such as the Golgi cisternae or the ER sheets have small curvatures. When the radius of curvature is almost the same as the thickness of a membrane ($R \approx d$), the curvature is considered as large. Vesicles and micelles have large membrane curvatures. (C) When a lipid monolayer bends towards the direction of polar head groups it is considered having negative curvature whereas when a lipid monolayer bends towards the direction of fatty acid chains it is considered having positive curvature. A perfectly flat lamellar membrane has zero curvature.

Extreme membrane curvature is necessary for the formation of hemifusion intermediates (Figure 1.11, red and green colours). However, it takes elevated energetic levels to generate a high degree of curvature (Shibata *et al.*, 2009). To overcome the energetic barrier of membrane fusion, interplay between lipids and proteins is required *in vivo*.

Membrane fusion has been observed in protein-free membranes. For instance, liposomes enriched in negatively curved phospholipids exhibit spontaneous fusion whereas incorporation of positively curved lipids in liposomes inhibits fusion (Chernomordik and Zimmerberg, 1995, Larijani and Dufourc, 2006). Therefore, the lipid composition of a membrane is critical for membrane fusion.

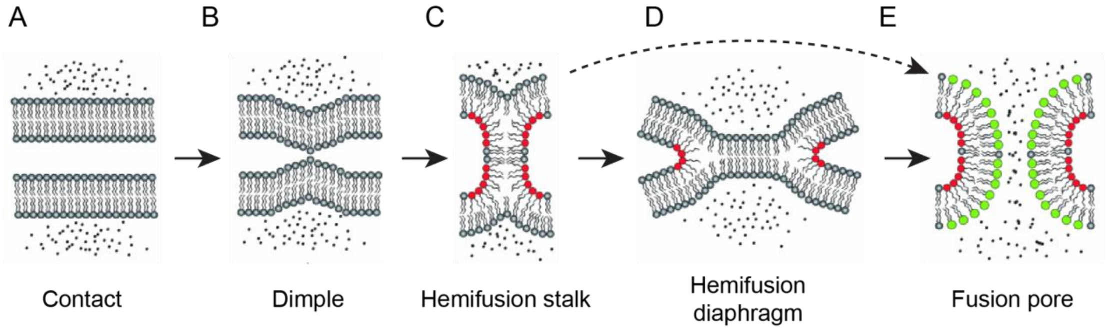

Figure 1.11 Progression of membrane fusion through the hemifusion stalk

Fusion can be dissected into multiple steps. (A) Two separate membranes approach each other and come into contact and there is a hydration barrier between the membranes. (B) Point-like protrusion, or dimple, overcomes the energetic barrier of hydration by diminishing the contacting surface area. (C) A hemifusion stalk is formed where the proximal leaflets are fused and distal leaflets remain unfused. (D) The hemifusion stalk expands and results in a hemifusion diaphragm. (E) Finally, the expanding hemifusion diaphragm becomes a fusion pore, resulting in a flow between two cellular compartments. Alternatively, the direct formation of fusion pore from hemifusion stalk has been proposed. However, theoretical calculations suggest that this is unlikely (Kozlovsky *et al.*, 2002). Red indicates the region of negative curvature and green indicates the region of positive curvature in the hemifusion intermediates. Figure adapted from Poccia and Larijani (2009).

Nevertheless, protein machineries are usually involved in generating membrane curvature. Proteins either stabilise curved membranes or mechanically force a membrane to attain a specific shape (Frolov *et al.*, 2011). Moreover, proteins can be targeted to membrane based on its lipid composition thus trigger a site-specific membrane fusion. Some proteins are able to facilitate fusion by making the transition from unfused membranes to hemifusion intermediates more thermodynamically favourable (Zimmerberg and Kozlov, 2006). The mechanisms of membrane fusion are case-specific co-operations between lipids and proteins. Below, the major mechanisms for protein and lipids to generate membrane curvature are described.

1.5 Generation of membrane curvature by proteins

There are several major mechanisms for proteins to generate membrane curvature that are illustrated in Figure 1.12. The most direct mechanism to alter membrane curvature is by mechanical force generated from the cytoskeleton. A typical example is the remodelling of membranes in cell motility where cytoskeletal proteins build up membrane tension affecting the local curvature (Raucher and Sheetz, 2000). Endocytic secretion also correlates with membrane tension manipulated by cytoskeleton (Dai *et al.*, 1997). Alternatively, tubules can be pulled out from membrane sheets such as the Golgi, by the binding of kinesin, a microtubule motor.

Protein scaffolding constrains the curvature of membranes through the rigidity of proteins. For instance, clathrin and its adaptor proteins maintain the spherical shape of vesicles (Fotin *et al.*, 2004). Similarly, proteins from the dynamin family can form oligomers to confine a membrane into tubular shape (Hinshaw and Schmid, 1995, Neumann and Schmid, 2013). The role of BAR (Bin-Amphiphysin-Rvs) domains in changing membrane curvature is relatively well studied in which its dimer binds better to highly curved membranes (Peter *et al.*, 2004). Recently, BAR domains have been shown to control the number and size of vesicles in chromaffin cells (Pinheiro *et al.*, 2014).

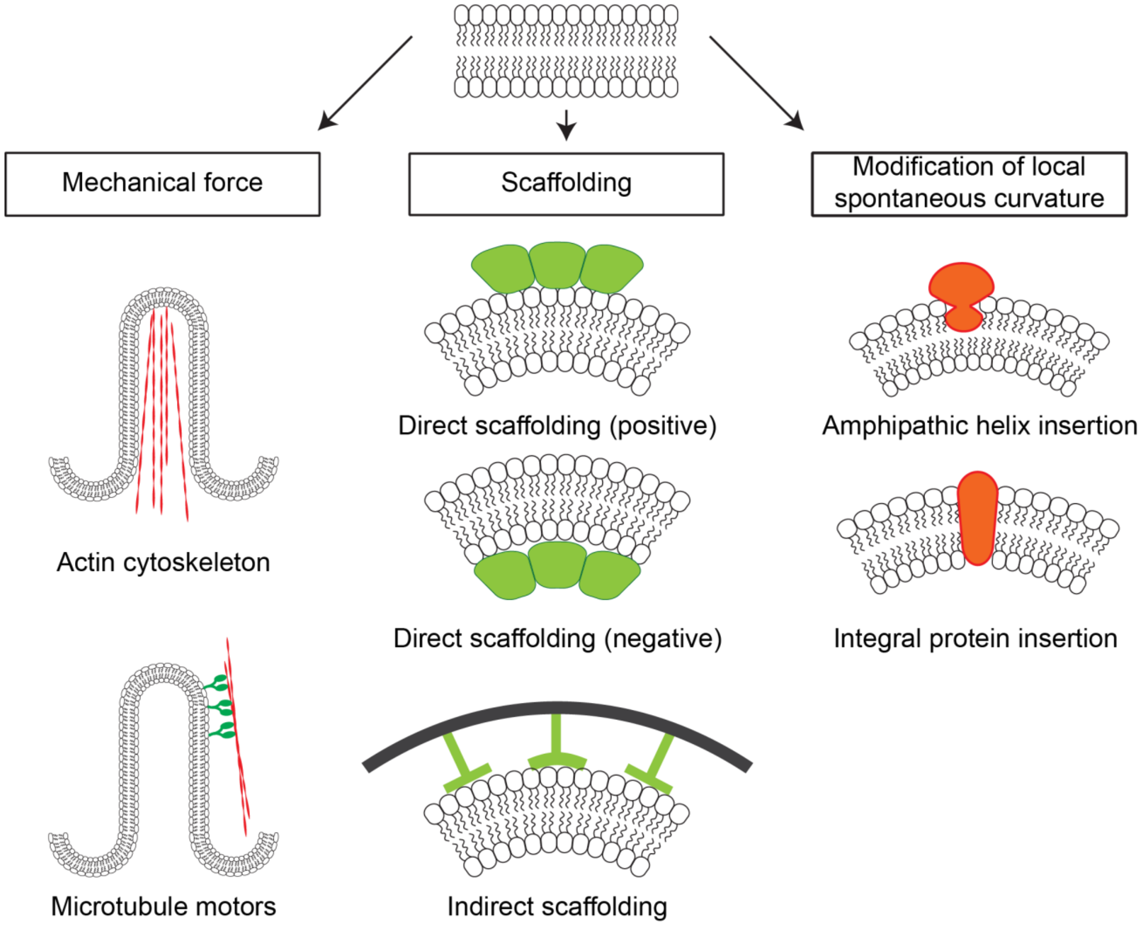

Figure 1.12 Mechanisms by which proteins generate membrane curvature

(A) Proteins exerting external mechanical forces can alter the curvature and shape of a membrane. (B) A membrane can adapt to the shape of rigid proteins through direct and indirect scaffolding. (C) Curvature can be generated by insertion of an amphipathic helix in one of the monolayers of the membrane or through wedging of an integral protein. Figure redrawn from McMahon and Gallop (2005).

In terms of membrane fusion, proteins from the SNARE family have been comprehensively studied. These proteins mediate fusion by their rigidity thus forcing two opposite membrane into proximity (Duman and Forte, 2003). SNAREs generate energy through protein-lipid and protein-protein interaction and recently SNAREs are seen by many investigators as a way to overcome fusion barriers at different occasions. For instance, SNAREs may couple at the hemifusion stalk for its elongation and widening. This accelerates the whole membrane fusion process (Risselada and Grubmuller, 2012). Moreover, inhibition of SNAREs by α-SNAP blocks NE membrane fusion in a *Xenopus* cell-free system, and this implies that NE fusion can be mediated by SNAREs (Baur *et al.*, 2007).

In addition, membrane curvature can be altered by the local spontaneous curvature mechanism, based on the insertion of amphipathic moieties of proteins into the bilayer. A shallow insertion of amphipathic helices increases the positive curvature on a monolayer and such asymmetry creates an overall area difference thus a change in curvature (Campelo *et al.*, 2008). For instance, epsin tubulates liposomes when its PtdIns(4,5)P_2-binding ENTH domain penetrates into the outer leaflet of the bilayer. As the ENTH pushes the head groups of lipid apart, it triggers the membrane deformation (Ford *et al.*, 2002). A protein superfamily known as reticulons makes use of both protein scaffolding and modification of local spontaneous curvature to maintain the tubular network of the ER (Voeltz *et al.*, 2006). Reticulons usually have hydrophobic domains that penetrate the cytoplasmic leaflet of the ER. These hydrophobic domains can form "wedge-like" hairpins to stabilise the ER tubules (Sackmann, 2014). Furthermore, integral membrane proteins such as acetylcholine receptor and ion channels protein which have a conical shape can displace lipids around them, creating a curvature that matches the shape of the receptors. The effect of integral proteins on membrane curvature is even stronger when they cluster (Mackinnon, 2004, Unwin, 2005).

1.6 Generation of membrane curvature by lipids

Many studies regarding membrane fusion and membrane curvature have emphasised the impact of proteins whereas lipids are usually considered to have a subordinate role. In fact, lipids play a central role in changing membrane curvature by their polymorphic nature. As mentioned earlier, lipid species can be classified into three major groups. The categorisation is based on the identity of the polar headgroups bound to the glycerol (specific to phospholipids) or ceramide (specific to sphingolipids) backbone. The branching, length and functional groups of the fatty acid chain, the size and charge of the head groups, and the effective shape of lipids define the physical and biological properties of a biomembrane. Figure 1.13 illustrates how various membrane properties can be influenced by lipid composition. This section mainly illustrates how spontaneous curvature (effective shape) of lipids generates membrane curvature.

Figure 1.14-A shows a curved membrane composed of lipids with positive, zero and negative spontaneous curvature and the corresponding lipid species that can be found in mammalian cells. Lipids alone can give rise to membrane curvature. However, a localised change of membrane composition is required for membrane fusion and this usually involves interplay between lipids and proteins. More importantly, the lipids have to be distributed asymmetrically between the membrane leaflets to generate curvature. The concept that spontaneous curvature of membrane is homeostatically regulated in live membranes is not new (Gruner, 1985). However, the detailed mechanism of asymmetric distribution in biomembranes is still being uncovered.

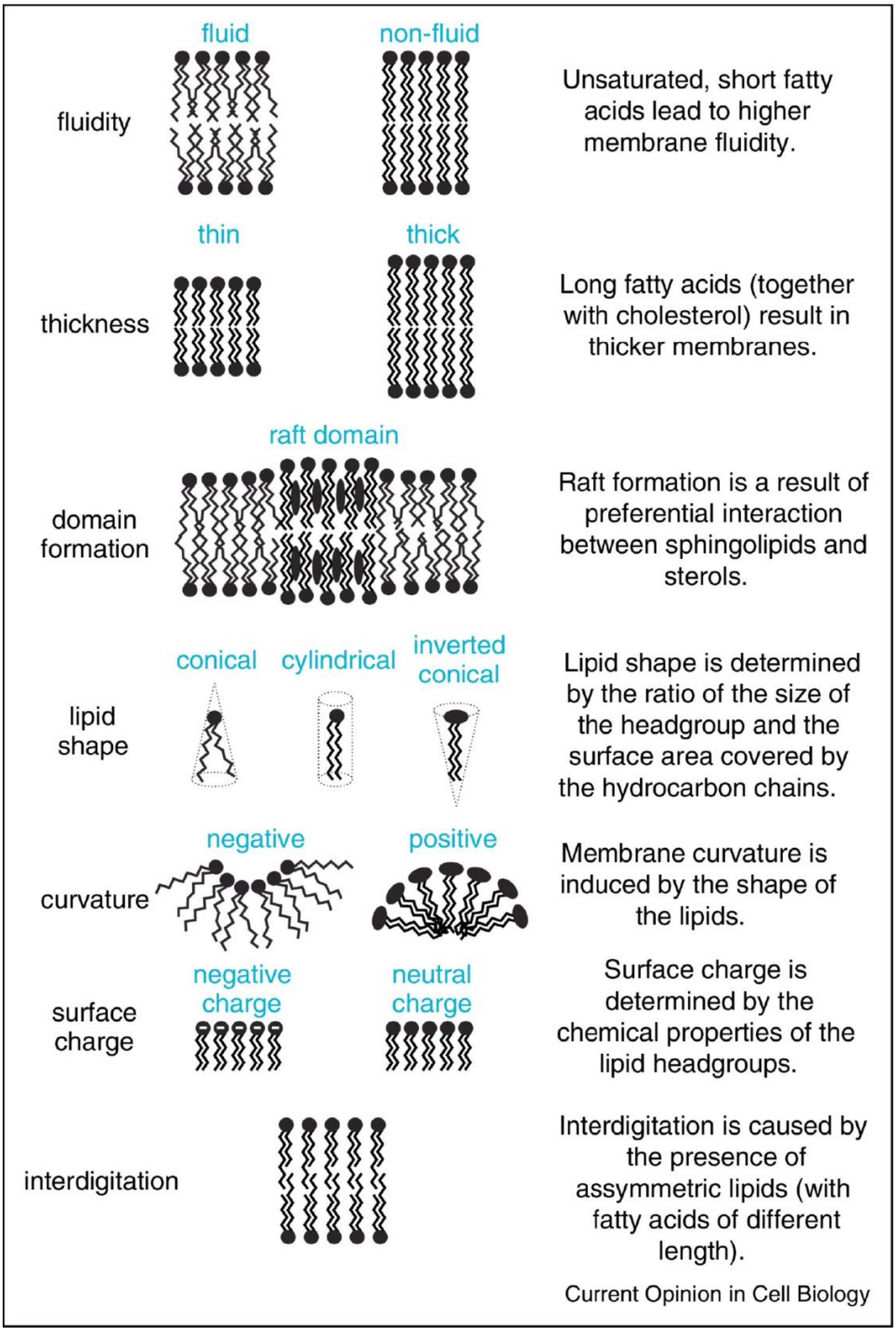

Figure 1.13 Polymorphic nature of lipids gives rise to various membrane properties

Inherent chemical and geometry characteristics of lipid are super diverse wherein the combination of different headgroups and fatty acid chain is the key principle to produce such polymorphism. Adapted from Klose *et al.* (2013).

There are two major approaches to achieve the asymmetric distribution of lipids. The first is transportation of lipids and the second is biochemical modification of lipids (Figure 1.14). Lipid carrier protein can actively transport lipids from one leaflet of the membrane to the other (Farge and Devaux, 1992). ATP-dependent translocase transport PtdSer and PtdEtn from the exoplasmic to the cytosolic leaflet of mammalian erythrocytes (Bevers *et al.*, 1999). Phospholipid flippases Drs2P flips PtdSer to the cytosolic leaflet of TGN and it is required for vesicles formation (Graham, 2004). Fatty acid chains and head group (effective shape) of lipids are prone to enzymatic activities. For instance, phospholipase A2 cleaves the fatty-acid chain of lipids at its sn-2 position and increases the spontaneous curvature of a lipid molecule; inhibition of phospholipase A2 activity blocks endocytic fusion (Mayorga *et al.*, 1993, Brown *et al.*, 2003). Similarly, phospholipase C cleaves the headgroup of lipids and is required for membrane fusion (Goni and Alonso, 2000, Larijani *et al.*, 2001).

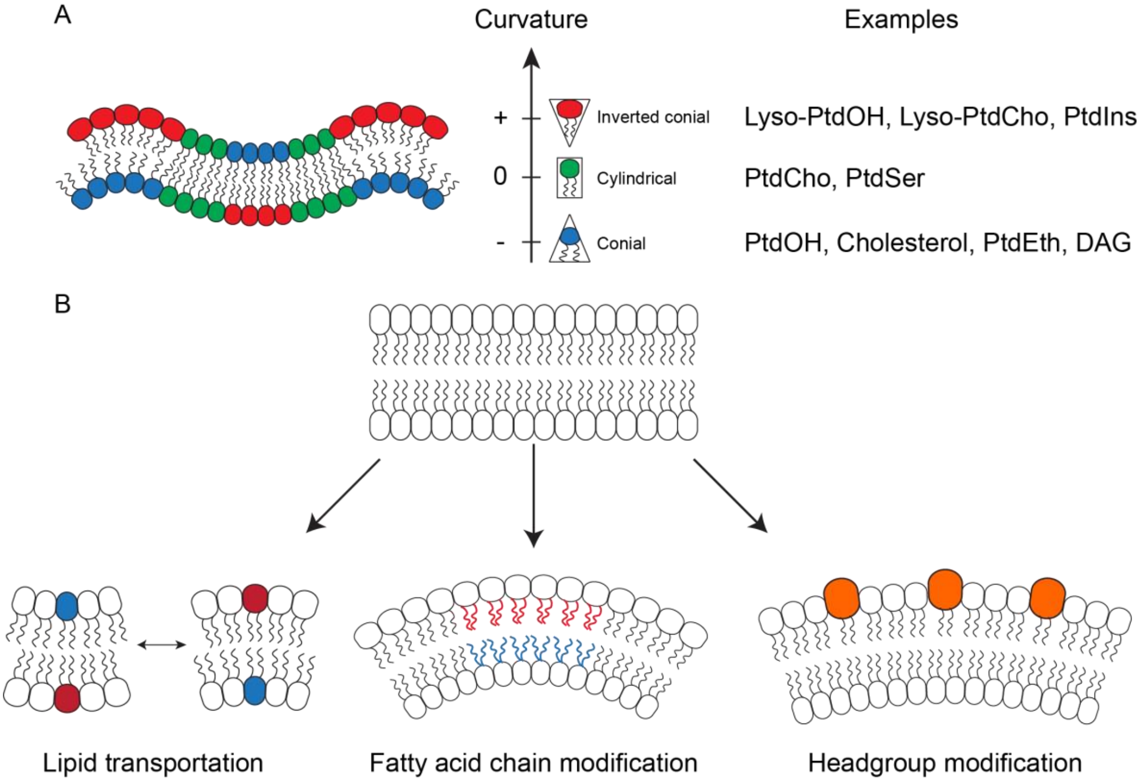

Figure 1.14 Asymmetric distribution of lipids generate membrane curvature

(A) To generate membrane curvature, lipids of different spontaneous curvatures (effective shapes) are asymmetrically distributed in the two leaflets of a membrane. In mammalian cells, there is a wide variety of lipids to fulfil such function. (B) Membrane curvature can also be generated by transportation of lipids and biochemical modification of their fatty acid chains and headgroup.

Studies of lipid-protein interplay are emerging, such that cholesterol has been shown affecting the conformation of a viral fusion protein and mediates membrane curvature (Ivankin *et al.*, 2012). Yet not much is known about the general fusion mechanisms in different organelles.

1.6.1 Role of phosphoinositides in membrane fusion

The role of phosphoinositides (PIs) and derivatives in membrane fusion is our major interest. PIs are special members in the phospholipid family due to their unique properties. The most abundant PI in mammalian cells is phosphatidylinositol (PtdIns), which makes up to 90% of the total PIs (Vanhaesebroeck *et al.*, 2001). The 3-, 4-, and 5-positions of the inositol ring of PtdIns can be phosphorylated to generate seven distinct molecules. All seven molecules exist in higher eukaryotes, and they either serve as precursors of second messengers (Berridge and Irvine, 1984) or directly regulate signalling pathways (Liscovitch *et al.*, 1994). The different phosphorylated forms of PtdIns are rapidly interconverted and are regulated by a massive network of kinases and phosphatases (Payrastre *et al.*, 2001). The signalling role of PIs has been extensively studied whereas their structural role in membrane fusion mechanism is not fully understood (Larijani *et al.*, 2014).

The role of PIs in membrane fusion can be viewed from several aspects. First, PIs have been shown to have compartmental specificity using confocal microscopy, such that PtdInsP(3,5)P_2 is localised in yeast vacuoles (Payrastre *et al.*, 2001) and PtdIns4P is localised in the Golgi (Weixel *et al.*, 2005). However, isolated membrane fractions usually contain multiple phosphorylated isoforms of PtdIns (Rawyler *et al.*, 1982, Byrne *et al.*, 2007), suggesting that the compartmental specificity is not solely depended on a single PI but the proportion of certain PIs in the membrane. The distinctive profile of PIs among different membranes appears to be the sign post for PI-modifying enzymes and associated small GTPases (Grosshans *et al.*, 2006), in which small GTPase like Rab participates in several key steps of membrane fusion (Zerial and McBride, 2001).

In addition, PIs have been identified in exocytotic and endocytotic processes acting as the regulators of fusion machineries, where membrane fusion is a central element of exocytosis and endocytosis. For instance, the deficiency in PtdIns(4,5)P_2-binding of exocyst Exo70 leads to blocking of exocytosis in mammalian cells and it indicates the importance of PtdIns(4,5)P_2 in docking and fusion of secretory vesicles (Liu *et al.*, 2007). Direct PtdIns(4,5)P_2 depletion in the plasma membrane prevents endocytosis of the transferrin receptor (Varnai *et al.*, 2006). Similarly, depletion of PtdIns3P and PtdIns(3,4,5)P_3, and inhibition of the interaction between these PIs and their effectors result in malfunction of exocytosis and endocytosis (Huynh *et al.*, 2003, Fili *et al.*, 2006, Vieira *et al.*, 2003).

As mentioned previously, lipids with negative spontaneous curvature are required for membrane fusion. PIs play a structural role in providing the membrane curvature necessary for membrane fusion (Zhendre *et al.*, 2011). Table 1.1 lists the spontaneous membrane curvature of some phospholipids and related derivatives. Among these lipids, DAG, a PtdIns(4,5)P_2 derivative, has the most extreme negative curvature. Inclusion of DAG in model membranes facilitates vesicles fusion (Villar *et al.*, 2001, Villar *et al.*, 2000). Also, DAG circumvents the requirement of GTP hydrolysis in echinoderm NE assembly assay, indicating its downstream role in NE assembly (Byrne *et al.*, 2005, Larijani *et al.*, 2001, Dumas *et al.*, 2010).

Moreover, model membranes mimicking MV1 fusogenic vesicles, enriched in polyunsaturated PtdIns, are shown to have high fluidity using solid-state NMR spectroscopy (Larijani and Dufourc, 2006). Such character induces molecular disorder in the membrane and promotes fusion (Zhendre *et al.*, 2011). Membrane fusion is associated with the enrichment of DAG effectors such as PLC. PLC is enriched at the sites that require membrane fusion, such as the region of phagocytosis (Botelho *et al.*, 2000) and contact point between female and male pronucleus (Byrne *et al.*, 2014). This indicates that localised accumulation of DAG *in vivo* is a universal condition for membrane fusion. Therefore, to understand the mechanism of NE assembly, particularly the role of fusogenic vesicles during this process, we needed to identify the membrane compartments that were enriched in DAG, its phospholipid precursors, and related modifying enzymes.

Table 1.1 Spontaneous membrane curvature of phospholipids and derivatives

Lipid	Net Charge	Spontaneous curvature, Å^{-1}	References
Lyso-PtdOH	-1	+ 0.05^{a,b}	(Kooijman *et al.*, 2005)
Lyso-PtdCho	0	+ 0.026^{a}	(Kooijman *et al.*, 2005)
PtdSer	-1	+ 0.069^{b}	(Fuller *et al.*, 2003)
PtdIns	-1	/	/
PtdCho	0	- 0.007^{a} to - 0.005^{b}	(Fuller *et al.*, 2003)
PtdOH	-1	- 0.022^{b}	(Kooijman *et al.*, 2005)
Cholesterol*	0	- 0.037^{a} to - 0.044^{b}	(Fuller *et al.*, 2003)
PtdEth	0	- 0.037^{a} to - 0.045^{b}	(Fuller *et al.*, 2003)
DAG	0	**- 0.090^{a}**	(Fuller *et al.*, 2003)

Values of spontaneous curvature are expressed as $1/R_{0p}$ and were calculated in the presence of 18:1/18:1-PtdEth in water (a) or pH 7 buffer (b); R_{0p} is the radius of the curvature. *Cholesterol is a sterol lipid. Table adapted from Jethwa (2014).

1.7 Membrane compartments involved in nuclear envelope assembly

Both the ER envelopment model and the vesicle fusion model suggest that mitotic ER is involved in NE assembly. The vesicle fusion model suggests that Golgi-originated vesicles (MV2α) and MV1 are additionally involved.

1.7.1 The endoplasmic reticulum

The morphological organisation of mitotic ER and the presence of NE proteins in mitotic ER in relation to NE assembly have been discussed above. The ER is a site for *de novo* phospholipid synthesis (Fagone and Jackowski, 2009). There are less than 10% PIs in the ER (van Meer and de Kroon, 2011) and the fate of these PIs during mitosis and how they may contribute to NE reassembly is unknown. The complexity of phospholipids organisation is of major importance. In mammalian cells, PIs are synthesised from CDP-DAG by phosphatidylinositol synthase (PIS), and PIS activity has been detected in the mobile vesicular fraction of ER (Kim *et al.*, 2011, Imai and Gershengorn, 1987) and at the leading edge of tubular ER (English and Voeltz, 2013). Early studies have shown the synthesis of PtdIns(4,5)P_2 in the ER and have suggested the possibility of two PtdIns(4,5)P_2 pools, a PLC-sensitive one and a PLC-insensitive one (Helms *et al.*, 1991). This may also imply a possibility to have two pools of DAG, serving different functions. In a recent study, depletion of DAG in unfertilised sea urchin eggs led to a tubule-to-sheet transition of the ER, and delays in karyomere fusion (Wang *et al.*, 2013). Interestingly, both signalling molecule 1,2-DAG and its non-signalling isomer 1,3-DAG prevented the morphological transition caused by DAG depletion, meaning that DAG is likely to have both signalling and structural role in organelle shaping and membrane fusion.

1.7.2 The Golgi apparatus

The mammalian Golgi is a compartment specialised in transportation of both proteins and lipids through vesiculation (Shorter and Warren, 2002). The fate of mitotic Golgi is a subject of debate. In some studies, mitotic Golgi has been reported to breakdown into small tubuloreticular fragments (Lucocq, 1992, Lucocq *et al.*, 1995) whereas others have revealed Golgi vesicles (Warren, 1993). Moreover, some groups have suggested that mitotic Golgi is dispersed into the ER (Zaal *et al.*, 1999, Thyberg and Moskalewski, 1992) but discrete vesicles of Golgi are also observed (Burke *et al.*, 1982, Colanzi *et al.*, 2000). There is a general agreement in the field that mitotic Golgi is organised into tubulovesicular clusters during telophase and reforms on the opposite sides of the nucleus (Seemann *et al.*, 2002, Wei and Seemann, 2009).

In yeast, Golgi-associated vesicles trafficking is required to maintain NE shape (Webster *et al.*, 2010) and mutation of epsilon-COP gene ANU2 which is involved in ER-to-Golgi transport can cause NE defect (Kimata *et al.*, 1999). There may be a conserved role for mammalian Golgi in regulating the NE morphology.

In terms of phospholipid profile, PtdIns4P is the predominant PI in the Golgi. PtdIns4P is a regulatory molecule but also an intermediate in the synthesis of several important PIs such as PtdIns(4,5)P_2. The presence of PtdIns(4,5)P_2 in the Golgi is suggested by the detection of PtdIns(4,5)P_2 metabolising enzymes, such as inositol(5)phosphatase and OCRL (De Matteis *et al.*, 2002). Although a direct hydrolysis of PtdIns(4,5)P_2 to DAG in the Golgi is unlikely, PtdIns(4,5)P_2 can activate PLD, which produces PtdOH required for DAG production (Cazzolli *et al.*, 2006).

In yeast, Golgi-DAG is produced by Pah1p from PtdOH (Karanasios *et al.*, 2010). In mammalian cells, sphingomyelin synthases regulate Golgi-DAG levels using PtdCho as substrate (Villani *et al.*, 2008). DAG is visualised at the curved tips of the Golgi stacks in mammalian cells (Peddie *et al.*, 2014). Accumulation of DAG in the cytoplasmic leaflet of TGN membranes promotes vesicle fission (Bard and Malhotra, 2006) but whether there is a population of Golgi vesicles enriched in DAG and involved in NE assembly still requires investigation.

1.8 Aim and objectives

MV1 fusogenic vesicles have been isolated from the echinoderm cell-free assay and its lipid-protein composition has been characterised. Moreover, localised DAG production is required for membrane fusion in both model membrane system and *in vitro* assays. Also, earlier studies from our group have revealed the involvement of phosphoinositides and their derivatives in mammalian NE assembly, especially their spatiotemporal distribution during mitosis (Hobday, 2012, Domart *et al.*, 2012). Nevertheless, the role of fusogenic vesicles and their biochemical composition in mammalian cells is unknown. We hypothesise that MV1-like vesicles are required for mammalian NE reassembly and we aim to understand their function in membrane fusion. A major objective of this thesis is to address the NE fusion mechanism in mammalian cells by asking several key questions:

1. Are there MV1-like vesicles/compartments required for mammalian NE assembly?
2. What is the composition of MV1-likes vesicles?
3. What is the role of DAG in mammalian NE assembly
4. What is the origin of the MV1-like vesicles?

Two approaches were used to study fusion mechanisms in mammalian NE assembly and the key steps are shown in Figure 1.15. The biochemical approach aimed at isolating MV1-like vesicles in order to reconstitute a fusion assay and to characterise isolated MV1-like vesicle by lipid mass spectrometry and proteomics. In parallel, a cell biology approach was used to identify and characterise MV1-like vesicles *in vivo* using high resolution imaging techniques. In addition, we modulated the DAG level in endomembranes and investigated its impact on NE assembly.

This thesis contains five Result Chapters and each chapter has its own brief introduction and discussion section. Chapter 3 describes the density gradient separation of MV1-like vesicles from other cellular compartments. Chapter 4 investigates the localisation of PtdIns(3,4,5)P$_3$ in mammalian cells and the performance of a PtdIns(3,4,5)P$_3$-specific probe conjugated to miniSOG, a novel tag allowing EM visualisation. In Chapter 5, we studied the role of DAG in mammalian NE assembly by modulating the DAG levels at the NE/ER using a dimerisation device. Chapter 6 identifies the presence of potential fusogenic vesicles and describes the photo-conversion optimisation of the miniSOG tag. In Chapter 7, we modulated the DAG levels at the Golgi and determined its impact on NE assembly using serial block face scanning electron microscopy (SBF SEM). The major discoveries of this thesis and future direction of the study are summarised in the overall Discussion section.

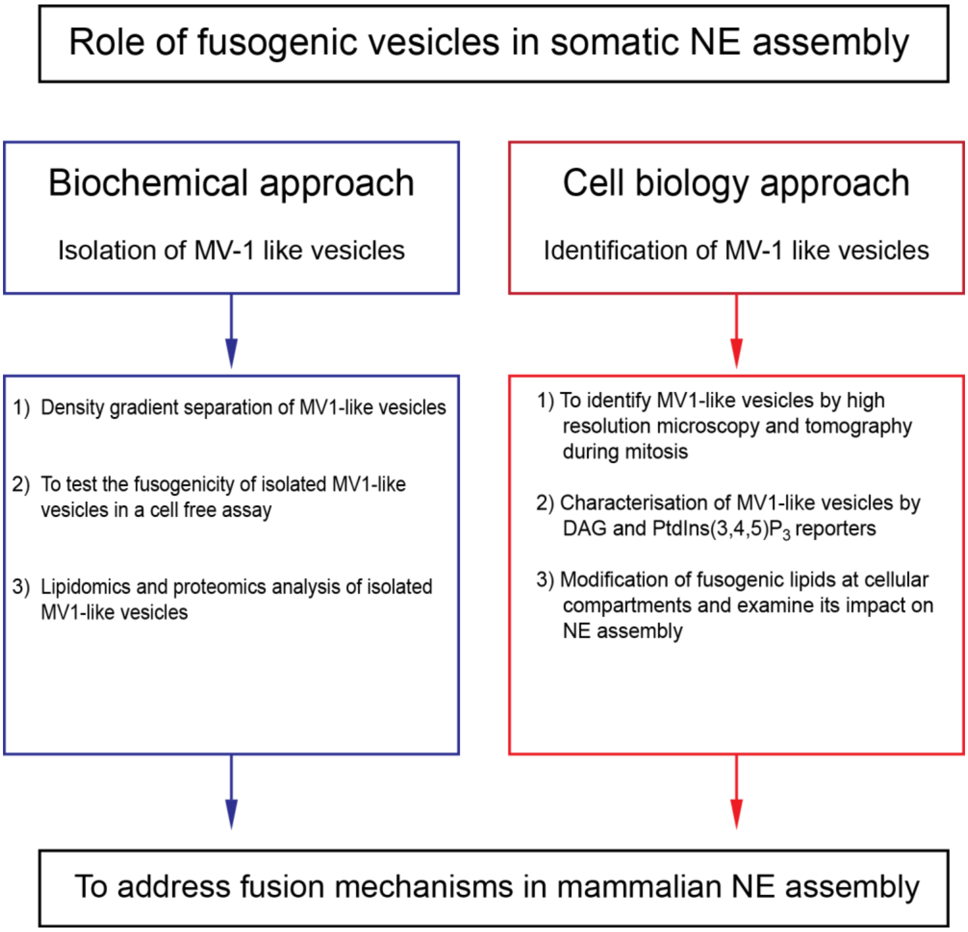

Figure 1.15 Parallel approaches to address fusion mechanisms in mammalian NE assembly

Chapter 2 Materials and Methods

2.1 Antibodies

Details of primary and secondary antibodies and their working dilutions for different applications are listed in Table 2.1 and Table 2.2.

2.2 Buffers and Reagents

I. *General biochemistry materials*

4X SDS loading buffer	0.01% (w/v) bromophenol blue, 20% (v/v) glycerol, 4% (w/v) SDS, 250 mM Tris base, pH 6.8; add 50 mM β-mercaptoethanol prior to use
20X MOPS running buffer	1 mM EDTA, 50 mM MOPS, 0.1% SDS, 50 mM Tris base, pH 7.7; dilute to 1X in ddH_2O prior to use
BSA blocking buffer	3% BSA (w/v) in PBS-T
Cell lysis buffer	0.5 mM EDTA, 150 mM NaCl, 10 mM Tris HCl, pH 7.5; add 1% (v/v) Triton X-100 and 1 protease inhibitor cocktail tablet (Complete, Mini, Roche) per 10 ml lysis buffer prior to use
Phosphate buffered saline (PBS)	2.7 mM KCl, 2 mM KH_2PO_4, 137 mM NaCl, 10 mM Na_2HPO_4, pH 7.4
Tris-buffered saline (TBS)	50 mM Tris-Cl, 150 mM NaCl, pH 7.4
PBS-T	0.2% (v/v) Tween-20 in PBS
10X immunoblot transfer buffer	1.9 M glycine, 250 mM Tris base; dilute in a ratio of 1:2:7 transfer buffer: methanol: ddH_2O prior to use
Versene EDTA	0.02% (w/v) EDTA, 0.3 mM KH_2PO_4, 0.0003% (w/v) phenol red, 27 mM NaCl, 1.62 mM Na_2HPO_4
Wash buffer	2% (w/v) low-fat milk powder in PBS-T

II. *Subcellular fractionation materials (MV1-separating gradient)*

Homogenisation buffer (HB)	250 mM sucrose, 10 mM Tris, 17 µg/ml benzamidine; add 1 mM AEBSF and 1 protease inhibitor cocktail tablet (Complete, Mini, Roche) per 10 ml buffer prior to use
Membrane wash buffer (MWB)	1:4 HB:PBS (v/v)

Known proteolytic activities targeted by Complete, Mini protease inhibitor tablets

Protease	Enzyme conc. (µg/ml)	pH	% inhibition immediately after addition
Pancreas-extract	20	7.8	84
Thermolysin (Metalloprotase)	0.5	7.8	10
Chyrmotrypsin	2	7.8	90
Trypsin	2	7.8	81
Papain	330	7.8	74

III. Subcellular fractionation materials (TGN-separating gradient)

TGN-separating gradient HB	250 mM sucrose, 10 mM HEPES-KOH, pH 7.2, 1m M EDTA, and 1 mM MgOAc; add 1 protease inhibitor cocktail tablet (Complete, Mini, Roche) per 10 ml buffer prior to use
TGN-MWB	1:4 TGN-HB:TBS (v/v)
TGN-separating gradient	0.3 M sucrose & 1.2 M sucrose, 10 mM HEPES-KOH pH 7.2

IV. Nuclei isolation materials

Nuclei Buffer A	0.5 mM DTT, 10 mM Hepes, 10 mM KCl, 1.5 mM $MgCl_2$, pH 7.9
Nuclei Buffer S1	10 mM $MgCl_2$, 0.25 M sucrose
Nuclei Buffer S2	0.5 mM $MgCl_2$, 0.35 M sucrose

V. Molecular Biology materials

6X loading buffer	0.25% bromophenol blue, 30% glycerol in water, 0.25% xylene cyanol FF
50X tris acetate EDTA (TAE)	1 M acetic acid, 50 mM EDTA, 2 M Tris
Lysogeny broth (LB)	0.5 g/l NaCl, 10 g/l tryptone, 5 g/l yeast extract
LB agar	1.5 % (w/v) in LB medium
SOC medium	20 mM glucose, 10 mM $MgCl_2$, 10 mM $MgSO_4$, 2.5 mM KCl, 10 mM NaCl, 2% tryptone, 0.5% yeast extract
Tris EDTA buffer (TE)	1 mM EDTA, 10 mM Tris base, pH 7.5

VI. Cell Biology materials

IF blocking buffer	3% (w/v) fatty acid free BSA, 0.05% saponin in PBS/TBS
Tris buffered saline (TBS)	150 mM NaCl, 10 mM Tris Base, pH 7.4
Trypsin/versene EDTA	0.05% (w/v) trypsin, 0.02% (w/v) EDTA, 0.3 mM KH_2PO_4, 0.0003% (w/v) phenol red, 27 mM NaCl, 1.62 mM Na_2HPO_4
HBSS solution (Gibco)	Components refer to catalog number 14025092

VII. Electron microscopy and photo-oxidation materials

Solution X	30 g Na_2HPO_4 in 1050 ml ddH_2O (0.2 M)
Solution Y	15 g $NaH_2PO_4{\cdot}2H_2O$ in 500 ml ddH_2O (0.2 M)
0.1 M phosphate buffer	202.5 ml solution X, 47.5 ml solution Y & 250 ml ddH_2O, pH 7.4
0.1 M cacodylate buffer	10.7 g sodium cacodylate in 500 ml ddH_2O, pH 7.4
DAB solution	2.5 mM diaminobenzidine in 0.1 M phosphate or cacodylate buffer
Blocking buffer	20 mM aminotriazole, 50 mM glycine, 10 mM KCN, pH 7.4

Table 2.1 **Details of primary antibodies used**

Antibody	Supplier	Cat#	Clone	Host	WB	IF
Na,K-ATPase α1 subunit	Novus Biologicals	NB300-146	464.6	Mouse	1:1000	
Calreticulin, pAb	Enzo life science	ADI-SPA-600	polyclonal	Rabbit	1:1000	
Anti-Calreticulin	Abcam	Ab2907	polyclonal	Rabbit		1:50
BiP (C50B12)	Cell Signaling	3177	C50B12	Rabbit	1:1000	
Anti-GFP	In-house		3E1	Mouse	1:2000	
Anti-Human Golgin-97	Molecular Probes	A-21270	CDF4	Mouse	1:1000	1:100
Anti-PLCγ-1	Millipore	05-163	Clonal blend B-2-5, B-6-4, B-20-3,D-7-3 E-9-4	Mouse	0.5 μg/ml	
Anti-PI3K p85	Abcam	Ab86741	M253	Mouse		1:100
PI3 Kinase p110α (C73F8)	Cell Signaling	4249	C73F8	Rabbit		1:500
PIK3CA	LSBio	LS-C105341	EP383Y	Rabbit		1:100
Anti-PI3 Kinase, p110β	Millipore	09-482	Polyclonal	Rabbit		1:100
Anti-Rab 5	Synaptic systems	108011	621.3	Mouse	1:1000	
Rab 7 (H-50)	Santa Cruz	Sc-10767	polyclonal	Rabbit	1:1000	
Ran	BD Transduction Laboratories	610340	TC4, Gsp1, ARA24	Mouse	1:5000	

Table 2.2 Details of secondary antibodies used

Antibody	Fluorophore	Supplier	Cat#	Host	IF
Anti-GST antibody	DyLight 650	Abcam	Ab117497	Goat	1:250
Anti-GST antibody	DyLight 488	Abcam	Ab117508	Goat	1:250
Anti-Mouse IgG (H+L)	AlexFluor 647	Molecular probes	A21236	Goat	1:500
Anti-Rabbit IgG (H+L)	AlexFluor 647	Molecular probes	A21244	Goat	1:500
Anti-Mouse IgG (H+L)	AlexFluor 546	Molecular probes	A-11030	Goat	1:500
Anti-Rabbit IgG (H+L)	AlexFluor 546	Molecular probes	A-11010	Goat	1:500
Anti-Mouse	Dylight 488	Jackson Lab	715-485-150	Donkey	1:250
Anti-Rabbit	Dylight 488	Jackson Lab	111-485-003	Donkey	1:250

2.3 Biochemistry – Subcellular fractionation and related experiments

2.3.1 Cell homogenate and postnuclear supernatant (PNS) preparation

To obtain sufficient cells for subcellular fractionation, cells were cultured in six 500 cm^2 cell culture dishes (Corning) with a seeding density of ~15 x 10^6; see section 2.5.1 for cell maintenance. When reached 90% confluency, cells were dissociated from the culture dishes by adding 15 ml Versene/EDTA solution and washed with PBS or TBS before any homogenisation. There were approximately 1.5 x 10^8 cells used in each batch of homogenate/PNS preparation.

2.3.2 Different homogenisation methods

MV1 homogenisation method

Cells were washed with 5 ml HB at 100x*g*, 4°C for 5 min and resuspended in 5 ml HB on ice for 5 min. Every 2.5 ml of the suspension was homogenised by passing through a 22G needles 10 times. The homogenate was centrifuged at 10,000x*g*, 4°C for 10 min to obtain the PNS.

Gruenberg & Howell homogenisation method

Cells were washed with 15 ml HB at 100x*g*, 4°C for 5 min and resuspended in 5 ml HB on ice for 5 min. Every 1 ml of the suspension was homogenised by a ball bearing cell cracker, with a ball size of 8.002 mm (9 μm clearance) for 6 times. The homogenate was centrifuged at 1,000x*g*, 4°C for 10 min to obtain the PNS, which was diluted 3 times in PBS and washed once before gradient separation.

MV1/Gruenberg & Howell combined homogenisation method

Cells were washed with 15 ml HB pelleted at 100x*g*, 4°C for 5 min and resuspended in 5 ml HB on ice for 5 min. Every 1 ml of the suspension was homogenised by a ball bearing cell cracker, with a ball size of 8.002 mm (9 μm clearance) for 6 times. The homogenate was centrifuged at 10,000x*g*, 4°C for 10 min to obtain the PNS.

PIS-organelle-separating gradient homogenisation method

Cells were washed with 15 ml HB and resuspended in 5 ml HB on ice for 5 min. Every 2.5 ml of the suspension was homogenised by passing through a 25G needles 15 times. The homogenate was centrifuged at 2,000x*g*, 4°C for 5 min to obtain the PNS.

TGN-separating gradient homogenisation method

Cells were washed with 30 ml TGN-HB and resuspended in 5 ml TGN-HB. Every 1 ml of the suspension were homogenised by passing through a 22G needles 7 times and the homogenate was centrifuged at 1,700x*g*, 4°C for 10 min to obtain the PNS. The PNS was washed once before gradient separation.

2.3.3 Biochemical gradient fractionation

The PNS/total membrane fraction was fractionated by different biochemical gradients:

Sucrose density gradient (MV1-separating gradient)

PNS collected from the MV1, Gruenberg & Howell, or the combined protocol were centrifuged at 150,000x*g*, 4°C for 2 h. The pellet (total membrane fraction) was gently resuspended in 0.5 ml MWB and loaded on a sucrose gradient. The sucrose gradient was prepared by mixing the 0.1 M and 2 M sucrose solution (5.5 ml each) in a two-chamber gradient mixer (Fisher scientific) with constant stirring at the outlet chamber. The 0.1-2 M sucrose gradient was layered into an ultracentrifuge tube using a Densi-flow fractionator. The loaded sucrose gradient was centrifuged at 150,000x*g*, 4°C for 20 h. Separated fractions were collected gently by a micropipette. The fractions were washed once by MWB, resuspended in 75 µl MWB and analysed by Western blotting.

OPTIPREP density gradient (PIS-organelle-separating gradient)

OPTIPREP gradient was prepared as described by (Kim *et al.*, 2011). The low and high concentration solutes were 10% and 25% OPTIPREP (Sigma) diluted with 0.25 M sucrose, 60 mM Tris/HCl and 6 mM EDTA respectively. The PNS-loaded gradient was centrifuged at 200,000x*g*, 4°C for 17 h in a SW40 rotor. Separated fractions were collected gently by a micropipette, washed once by MWB, resuspended in 75 µl MWB before Western blot analysis.

Velocity gradient (TGN-separating gradient)

The velocity gradient was prepared as described by (Celis, 1998), mixing 5.5 ml 0.3 M sucrose and 6 ml 1.2 M sucrose solutions using a tilted-tube-rotation gradient maker (Biocomp). The tilted rotations were: 1) 50° angle at 30 rpm for 10 min, 2) 80° angle at 12 rpm for 1 min. The PNS-loaded gradient was spun at ~111,000x*g*, 4°C in a SW40 rotor for an hour. The fractions were collected gently by a micropipette, washed once by MWB, resuspended in 75 µl MWB and analysed by Western blotting.

2.3.4 SDS polyacrylamide gel electrophoresis (SDS-PAGE)

Biochemical gradient-separated fractions or cell lysates (see 2.5.5) were analysed by SDS-PAGE. Samples were mixed with 4X SDS loading buffer in a 3:1 ratio and boiled at 95°C for 10 min to denature the proteins. Afterwards, samples were loaded into a 4-12% Bis-Tris gel (Invitrogen) alongside a protein ladder (PageRuler, Thermo Scientific). The electrophoresis was run at 125 V for 2 h until the dye front had reached the bottom of the gel. For proteins over 50 kDa MOPS running buffer was used whereas for proteins below 50 kDa MES running buffer was used. Protein of interest was detected by western blotting.

Alternatively, proteins on the gel were visualised by incubation with GelCode reagent (Thermo Scientific), a coomassie blue (G-250-based) staining reagent. Gels were fixed in 50% methanol/7% acetic acid (v/v) in deionised water for 15 min and washed with deionised water for another 15 min. Fixed gels were incubated with GelCode on a shaker for 1 h and destained with deionised water overnight before image acquisition by scanner (Epson).

2.3.5 Western blot analysis

After SDS-PAGE, proteins were transferred from the gel to an Immobilon-P PVDF membrane (Millipore). The methanol-equilibrated PVDF membrane was placed under the gel and was sandwiched by four transfer buffer-soaked 3-millimeter blotting papers on both sides. Proteins were transferred at 12 V for 2 h in a trans-blot semi-dry transfer apparatus (Biorad).

The membrane was blocked with 3% BSA (w/v) in PBST for 1 h at room temperature before primary antibody incubation. Primary antibody was diluted in the blocking buffer according to the manufacturer's protocol and incubated with the membrane at 4°C for 16 h or at room temperature for 2 h, depending on antibodies. The membrane was then washed 5 times with washing buffer. After this, the membrane was incubated with secondary antibody diluted in 5% (w/v) low-fat milk powder in PBST for 1 h at room temperature. The membrane was washed 5 times with washing buffer and rinsed briefly with PBS before image acquisition.

Equal volumes of ECL1 and ECL2 reagents (Amersham) were mixed, spread evenly on the membrane and incubated for 2 min to develop chemiluminescent signals with an emission of 428 nm. The signals were detected using an ImageQuant LAS 4000 system (GE Healthcare) and images were captured by the inbuilt CCD camera. The membranes were normally exposed for 1 to 5 min.

2.4 Molecular biology

2.4.1 DNA constructs

DNA constructs provided by external sources are listed below. Details of oligonucleotides used in this study are listed in Table 2.5 and Table 2.6.

Table 2.3 Constructs obtained from external laboratories or other investigators

Construct	Source	Laboratory
GST-GRP1^{PH}	Nick Leslie	University of Dundee
miniSOG	Roger Tsien	University of California San Diego
GCNT1	Sharon Tooze	London Research Institute
ST6GALNAC1	Sharon Tooze	London Research Institute
GRASP65^{GRASP}-GFP	Yanzhuang Wang	University of Michigan
GRASP65$^{GRASP.G2A}$-GFP	Yanzhuang Wang	University of Michigan

2.4.2 Oligonucleotides/primers

All primers were synthesised by Sigma-Aldrich custom oligos service and HPLC-purified, and were diluted in deionised water to 2.5 μM as working stocks. Design of primer followed the rules below:

PCR primer: Typical length ranged from 30-50 base pair (bp) with at least 20 bp complementary to the target sequence; the melting temperature (Tm) should be 55-65°C and the GC content (%GC) should be 45-65%. The 3' end of the primer should end with a guanine or a cytosine to enhance binding to the target sequence. The Tm difference between a pair of primers was minimised in most conditions, usually not over 3°C. The putative primers were analysed by oligo analysis tools so that they were designed to avoid self-complementarity and secondary structures. If secondary structures meant to exist, its T_m should be below the PCR annealing temperature.

Sequencing primer: Typical length should be smaller than 25 bp and the T_m ranged from 55-65°C.

Mutation primers: Rules of design followed the Stratagene Quickchange manual. The length was recommended to be within 25-45 bp to avoid formation of secondary structure. The T_m should be over 78°C and the %GC should be 40-60%, with at least one flanking guanine or cytosine at the 5' and 3' ends. The equation of the T_m for primer of substitution mutagenesis is

$$81.5 + 0.45(\%GC) - \frac{675}{N} - \%mistmatch,$$

where N is the number of base pairs.

Table 2.4 Details of PCR primers

Name	Sequence 5' to 3'	Length	T_m (°C)	%GC	Notes
PCR_Bam-C1aC1b-S	att gga tcc gcc acc ATG CAC AAG TTC ATG GCC ACC	36	73	56	Amplify C1aC1b with flanking Bam site
PCR_Bam-C1aC1b-AS	aat gga tcc CCA CAG TTG GGA GCC ACG TTG G	31	71	58	
PCR_Bam-GFP-S	ccg gga tcc gcc acc ATG GTG AGC AAG GGC GAG GAG C	37	78	64	Amplify GFP-C1aC1b for making tSOG-GFP-C1aC1b and GFP-C1-tSOG with flanking Bam sites
PCR_Bam-C1aC1b-AS	aat gga tcc ccA CAG TTG GGA GCC ACG TTG G	44	78	61	
PCR_Bam-C1aC1b-AS2	aat gga tcc tca ACA GTT GGG AGC CAC GTT GG	39	72	56	
PCR_BsrGI-GRP1PH-S	tgt aca agg gcg gaA TGG AAA GTA TCA AGA ATG AGC CG	36	65	42	Amplify GRP1^{PH}-SOG/tSOG with N-terminus BsrGI and C-terminus NotI
PCR_NotI-SOG-AS	gcg gcc gct taT CCA TCC AGC TGC ACT CCG	30	73	67	
PCR_BsrGI-SOG-S	tgt aca agg gcg gaA TGG AGA AGA GCT TCG TGA TCA CC	32	66	50	Amplify tSOG-GRP1PH with N-terminus BsrGI and C-terminus NotI
PCR_NotI-PH-AS	gcg gcc gct taT TTC TTA TTG GCA ATC CTC CTT TTC C	31	67	52	
PCR_BamHI-GCNT1-S	gga tcc gcc acc ATG CTG AGG ACG TTG CTG CGA AGG AG	38	75	63	Amplify GCNT1
PCR_BamHI-GCNT1-AS	gga tcc TCA GTG TTT TAA TGT CTC CAA AGC TTT GTG TCT CAA ATG C	46	68	41	
PCR_BamHI-ST6GALNAC1-S	gga tcc gcc acc ATG AGG TCC TGC CTG TGG AGA TGC AGG CAC CTG AGC C	49	80	65	Amplify ST6GLANAC1
PCR_BamHI-ST6GALNAC1-AS	gga tcc TCA GTT CTT GGC TTT GGC AGT TCC GGG ACC AGG ACG CTG G	46	77	61	
Age_ATG-2FKBP-S	atc acc ggt gcc acc atg GGA GTG CAG GTG GAA ACC ATC TCC	42	63	58	Amplify 2FKBP-GCNT1 with N-terminus Age site and C-terminus Bam site
GCNT1-STOP-BamHI-AS	gat gga tcc TCA GTG TTT TAA TGT CTC CAA AGC TTT GTG TC	41	62	38	
GCNT1-BamHI-AS	gat gga tcc GTG TTT TAA TGT CTC CAA AGC TTT GTG TC	38	59	38	
GCNT1-BamHI-AS-2	gga tcc cGT GTT TTA ATG TCT CCA AAG CTT TGT GTC TC	38	62	41	
ECoRI_ST6GALNAC1-S	gaa ttc gcc acc ATG AGG TCC TGC CTG TGG AGA TGC AGG CAC CTG AGC C	49	78	61	Amplify 2FKBP-ST6GALNAC1 with N-terminus ECoRI site and C-terminus Bam site
ST6GALNAC1-STOP-BamHI-AS	gat gga tcc TCA GTT CTT GGC TTT GGC AGT TCC	33	67	52	
ST6GALNAC1-BamHI-AS	gat gga tcc GTT CTT GGC TTT GGC AGT TCC	30	67	53	
ST6GALNAC1-BamHI-AS-2	gga tcc cGT TCT TGG CTT TGG CAG TTC CGG GAC C	34	73	62	
PCR_ECoRI-GRIP-S	gaa ttc gcc acc ATG GGG CTA GGG GCA AGC AGC GAG C	37	71	68	Amplify GRIP-GFP and GRP-GFP.G2A with N-terminus ECoRI site and C-terminus NotI site
PCR_ECoRI-GRIP.G2A-S	gaa ttc gcc acc ATG GCG CTA GGG GCA AGC AGC GAG C	37	71	68	
PCR_NotI-stop-GFP-AS	gcg gcc gct taC TTG TAC AGC TCG TCC ATG CCG AGA G	37	64	58	
BsrGI-2FKBP-S	tgt aca agg cca cca tgG GAG TGC AGG TGG AAA CC	35	72	57	Amplify 2FKBP with flanking BsrGI sites
2FKBP-BsrGI-AS	tgt aca tta CTC CAG CTT CAG CAG CTC CAC GTC GAA C	37	70	51	

Table 2.5 Details of sequencing primers

Name	Sequence 5' to 3'	Length	T_m (°C)	%GC	To sequence
FKBP end 5'	`ggc agc ggg cca agc tga cc`	20	67	75	FKBP
FKBP end 3'	`ggt cag ctt ggc ccg ctg cc`	20	67	75	
GRP1PH f	`cgc tgg ttc atc ctc aca gat aac tgc c`	28	65	54	GRP1PH
GRP1PH r	`cgt ctt gca ggc ctt gat gac ttg acc`	27	65	56	
M13 rev	`cag gaa aca gct atg ac`	17	47	47	Blunt TOPO plasmid
M13 for	`gta gcg tct gga gag act acg`	21	57	57	
pTriEX-UP	`ggt tat tgt gct gtc tca tca`	21	54	43	pTriEX plasmid
pTriEX-DOWN	`tcg atc tca gtg gta ttt gtg`	21	53	43	
Q69M-S	`gag ggc gat gcc acc`	15	56	73	GFP N-terminus
Seq_ST6GALNAC1-S	`ggt cct gcc tgt gga gat gca gg`	23	65	65	ST6GALNAC1
Seq_ST6GALNAC1_mid-S	`gca cca ccc ttt ggc ttc atg gag c`	25	66	60	
Seq_ST6GALNAC1_mid-AS	`gct cca tga agc caa agg gtg gtg c`	25	66	60	
Seq_ST6GALNAC1-AS	`gct ttg gca gtt ccg gga cc`	20	62	65	
Seq_GCNT1-S	`tga gga cgt tgc tgc gaa gga g`	22	63	59	GCNT1
Seq_GCNT1-mid-S	`gcc atc cca taa aga aga aag gtg g`	25	60	48	
Seq_GCNT1-mid-AS	`cca cct ttc ttc ttt atg gga tgg c`	25	60	48	
Seq_GCNT1-AS	`cca aag ctt tgt gtc tca aat gc`	23	57	43	
SOG f	`gga gct gac cga gta ttc cag aga gg`	26	63	58	miniSOG
SOG r	`cgc ttt ttg tgt agt tta tca gct gca cgg`	30	64	47	

Table 2.6 Details of mutation primers

Name	Sequence 5' to 3'	Length	T_m (°C)	%GC	Notes
Muta_C1b_(-Bam)-S	gtc aac atg ccc cac aag ttc gg**C** atc cac aac tac aag gtc ccc ac	47	75	55	To remove *Bam* site in the C1b domain for digestion
Muta_C1b_(-Bam)-AS	gtg ggg acc ttg tag ttg tgg at**G** ccg aac ttg tgg ggc atg ttg ac	47	75	55	
Muta_C1bW264G-S	cac tgt ggg tcc ctg ctc **GGG** ggc ctc ttg cgg cag ggc	39	81	74	To make non-DAG-binding C1 mutant
Muta_C1bW264G-AS	gcc ctg ccg caa gag gcc **CCC** gag cag gga ccc aca gtg	39	81	74	
Muta_PH-tSOG_(-Bam)-S	gga ttg cca ata aga aac ggg at**G** ca**G** cgg tcg cca cca tgg aga aga gc	50	86	56	To remove *Bam* site in the linker
Muta_PH-tSOG_(-Bam)-AS	gct ctt ctc cat ggt ggc gac cg**C** tg**C** atc ccg ttt ctt att ggc aat cc	50	86	56	
Muta_tSOG-PH_(-Bam)-S	cat cgg agt gca gct gga tgg a**GG** cgc cac cat gga aag tat caa g	46	86	57	
Muta_tSOG-PH_(-Bam)-AS	ctt gat act ttc cat ggt ggc g**CC** tcc atc cag ctg cac tcc gat g	46	86	57	
Muta_GCNT1_(Bam>ECoRI)-S	gtg ctg gaa ttc gcc ctt g**A**a t**T**c gcc acc atg ctg agg acg	42	84	57	To change the *Bam* site to *ECoRI* site for ligation
Muta_GCNT1_(Bam>ECoRI)-AS	cgt cct cag cat ggt ggc g**A**a t**T**c aag ggc gaa ttc cag cac	42	84	57	
Muta_GRP1^{PH}.K273A-S	gac cga gaa ggc tgg ctg ctg **GC**g ctg ggg ggt cgt gtg aag	42	93	69	To make non-PtdIns(3,4,5)P_3-binding mutant
Muta_GRP1^{PH}.K273A-AS	ctt cac acg acc ccc cag **CG**c cag cag cca gcc ttc tcg gtc	42	93	69	
Muta_GRP1^{PH}.R284A-S	gtc gtg tga aga cct gga aac gg**G** **C**ct ggt tca tcc tca cag ata ac	47	84	53	To make non-PtdIns(3,4,5)P_3-binding mutant
Muta_GRP1^{PH}.R284A-AS	gtt atc tgt gag gat gaa cca g**GC** ccg ttt cca ggt ctt cac acg ac	47	84	53	
Muta_ST6GALNAC1.E141G-S	gaa cac act gtc acc cag ag**G** gca aga tgc agg gat ggc ct	41	87	59	To remove mutation from the given construct
Muta_ST6GALNAC1.E141G-AS	agg cca tcc ctg cat ctt gc**C** ctc tgg gtg aca gtg tgt tc	41	87	59	
Muta_ST6GALNAC1(Bam>ECoRI)-S	tgc tgg aat tcg ccc ttg **A**at **T**cg cca cca tga ggt cct g	40	82	55	To remove mutation from the given construct
Muta_ST6GALNAC1(Bam>ECoRI)-AS	cag gac ctc atg gtg gcg **A**at **T**ca agg gcg aat tcc agc a	40	82	55	

2.4.3 Polymerase Chain reaction (PCR)

Typical reaction mix and thermal cycler programme for PCR is shown below. To make DNA more labile for heat denaturation, DMSO was added to a replicate of each reaction. All PCRs were performed in MJ Research PTC-225 Peltier Thermal cycler with the annealing temperature ranging from 45-65°C, depending on the T_m of the primers.

Table 2.7 Reaction mix for PCR

	Volume (μl)
Template DNA (200 ng/μl)	5
Sense primer (2.5 μM)	5
Anti-sence primer (2.5 μM)	5
dNTP mix (40 mM each)	1
Pfu buffer 10X	5
Pfu Turbo (2.5 U/ml) (Stratagene)	1
(DMSO)	2 if added
H_2O	to 50 μl

Table 2.8 Thermal cycler programme for PCR

Step	Programme	Temp. (°C)	Duration
1	DNA denaturation	95	2 min 30 s
2	DNA denaturation	95	50 s
3	Annealing	55	2 min
4	Extension	68	3 min (depending on the length of amplicon)
5		-	Go to step 2, x19 cycles
6	Complete	4	∞

2.4.4 Nucleotide sequencing

Reaction mix for sequencing and its thermal cycler programme is shown below. The Big Dye Terminator (BDT) reagent and sequence analysis service were provided by in-house facility.

Table 2.9 Reaction mix for sequencing

	Volume (μl)
DNA (200 ng/μl)	1
Sequencing primer (2.5 μM)	2
BDT (ABI Prism)	8
H_2O	to 20 μl

Table 2.10 Thermal cycler programme for sequencing

Step	Programme	Temp. (°C)	Duration
1	DNA denaturation	95	1 min
2	DNA denaturation	95	10 s
3	Annealing	45	1 min
4	Extension	60	4 min
5		-	Go to step 2, x24 cycles
6	Complete	4	∞

2.4.5 Site-direct mutagenesis

To introduce point mutations, site-directed mutagenesis was performed according to the Stratagene Quickchange manual. Mutation primers were designed as described above. Reaction mix of mutagenesis and its thermal cycler programme is shown below. The annealing temperature ranged from 45-60°C, depending on the T_m of the primers. Reactions were limited to 12 cycles to minimise mutations introduced by the polymerase.

Table 2.11 Reaction mix for mutagenesis

	Volume (µl)
DNA (10 ng/µl)	5
Mutation primer sense (2.5 µM)	5
Mutation primer anti-sense (2.5 µM)	5
dNTP mix (40 mM each)	1
Pfu buffer 10X	5
Pfu Turbo (2.5 U/ml) (Stratagene)	1
(DMSO)	2 if added
H_2O	to 50 µl

Table 2.12 Thermal cycler programme for mutagenesis

Step	Programme	Temp. (°C)	Duration
1	DNA denaturation	95	2 min
2	DNA denaturation	95	50 s
3	Annealing	55	1 min
4	Extension	68	8 min (depending on the length of plasmid)
5		-	Go to step 2, x12 cycles
6	Complete	4	∞

The completed mutagenesis reaction was incubated with 1 µl DpnI enzyme at 37°C for an hour. This ensures the original parental template (methylated) is digested and improves the bacterial transformation efficiency. The reaction was analysed by agarose gel electrophoresis, gel-extracted and purified before bacterial transformation (see below).

2.4.6 Restriction Digestion

To specifically select a DNA fragment (insert) and place it into alternative plasmids, DNA of interest was digested by restriction enzyme(s). If two restriction enzymes are used (double digestion), a compatible enzyme buffer for both enzymes is required to maximise their enzymatic activity. Typical reaction mix for digestion is shown below. Reactions were incubated at 37°C for 1 h; agarose gel electrophoresis was used to check the size of digested DNA.

Table 2.13 Reaction mix for restriction digestion

	Volume (µl)
DNA (1000 ng/µl)	5
Restriction enzyme(s)	1
10X Buffer	2
10X BSA	2
H_2O	to 20 µl

2.4.7 Agarose gel electrophoresis

Full-length plasmids or digestion products were analysed on a 0.8% (w/v) agarose gel made of 1X TAE buffer containing 0.5 µg/ml ethidium bromide. Reactions were mixed with 6X loading buffer in a 5:1 ratio and loaded into the wells of the agarose gel alongside a 1 kb DNA ladder (Invitrogen). Electrophoresis was run at 135 V in 0.5X TAE running buffer in a Mupid-One electrophoresis tank (Advance). DNA bands were visualised in a UV transilluminator with in-built camera (BioDoc-It imaging system, UVP).

Gel extraction and purification

The appropriate band was excised from the gel using a clean scalpel. The excised band was purified using a Qiagen QIAquick gel extraction kit according to the manufacturer's protocol.

2.4.8 Ligation

A ligation reaction contains two DNA fragments, the insert and vector 3 to 5 μg of each, were digested with the same restriction enzyme(s), gel-extracted and purified into water. To improve ligation efficiency, the vector was pre-incubated with 1 μl calf intestinal phosphatase (New England Biolabs) at 37°C for an hour to dephosphorylate its backbone before ligation. Reaction mix of ligation was ready for bacterial transformation after incubation at 16°C for 16 h.

Table 2.14 Reaction mix for DNA ligation

	Volume (μl)
Digested and dephosphorylated vector	1
Digested insert	1 or 6
T4 DNA Ligase (NEB)	1.5
10X Ligase buffer (NEB)	2
H_2O	to 20 μl

2.4.9 Subcloning

The gel-purified PCR product was inserted to the pCR-Blunt II Topo cloning vector (Invitrogen) according to the manufacturer's protocol. Four microliters of PCR product were mixed with 1 μl vector and 1 μl salt solution at room temperature for 5 min. The insert-including plasmids were transformed into chemically competent bacteria.

Bacterial transformation

Chemically competent *E. coli* strain DH5*α* Max Efficiency® (Invitrogen) and XL1-Blue (Stratagene) were used in routine cloning. Their genotypes are (F– Φ80lacZΔM15 Δ(lacZYA-argF) U169 recA1 endA1 hsdR17 (rK–, mK+) phoA supE44 λ– thi-1 gyrA96 relA1) and (recA1 endA1 gyrA96 thi-1 hsdR17 supE44 relA1 lac [F´ proAB lacI q Z Δ M15 Tn 10 (Tet r)]) respectively. In a transformation, 2 μl DNA were mixed with 50 μl competent bacteria in a 14-milliliter round bottom tube (BD Falcon) on ice for 10 min. The bacteria were heat-shocked in a 42°C water bath for 45 s and then incubated on ice for 2 min. The bacteria were supplemented with 300 μl SOC medium and incubated in a shaking incubator at 37°C, 200 rpm for an hour. The whole volume of bacteria was spread onto LB-agar plates containing the appropriate antibiotics (50 μg/ml kanamycin or 100 μg/ml ampicillin). The agar plates were inverted and incubated at 37°C overnight for colonies to develop.

Plasmid DNA extraction

Single bacterial colonies were picked with a sterile pipette tip, spotted onto a LB-agar plate (referred as the reference plate) and tipped into 7 ml LB medium containing the appropriate antibiotics (50 μg/ml kanamycin or 100 μg/ml ampicillin). The reference plate and the bacteria inoculated medium were incubated at 37°C for 16 h, with the medium incubated in a shaking incubator at 200 rpm. Bacteria were pelleted by centrifugation at 3,500xg, 4°C for 10 min. The bacteria pellet was submitted to in-house facility for small-scale DNA preparations (minipreps). Minipreps were done using a Qiagen liquid handling robot and Machery-Nagel plasmid purification kits.

Positive clones were either determined by restriction digestion or nucleotide sequencing (see above). The clones were then re-picked from the reference plate and cultured in 250 ml LB medium. The media were incubated in a shaking incubator as described above and the bacteria were harvested at 3,500x*g*, 4°C for 15 min. Large-scale DNA preparations (maxipreps) were done using the Qiagen Maxiprep Kit, purified plasmids were eluted in 500 μl TE buffer and stored at -20°C. The plasmid DNA concentration was measured and calculated with a NanoDrop spectrophotometer (Thermo Scientific) based on absorbance of the plasmid at 260 nm. Purified plasmids were sequenced afterwards.

2.5 Cell Biology

2.5.1 Mammalian cell lines and their maintenance

CHO and COS7 cell lines were obtained from Cancer Research UK Cell Services at Clare Hall. HeLa cell line was obtained from the American Type Culture Collection (ATCC), ATCC#: CCL-2.

Cells were cultured in DMEM/10% (v/v) FCS (CHO and HeLa) or DMEM/10% (v/v) DCS (COS7), supplemented with penicillin (100 U/ml) and streptomycin (100 μg/ml). Culture media and serum were obtained from Gibco (Invitrogen). Frozen cell aliquots were kept in FCS supplemented with 10% DMSO as a cryoprotectant and stored in liquid nitrogen. For recovery, frozen aliquots were thawed in a 37°C water bath and immediately transferred into growth medium. Cells were incubated at 37°C, 10% CO2 to 90% confluency and split at a ratio of 1:4 to 1:6 to the next passage. Cells between passage 10 and 25 were used.

2.5.2 Transfection

100,000 to 150,000 cells were seeded into a 35 mm glass-bottom dish, or MatTek dish, (MatTek Corporation, USA) or a single well of a 6-well plate followed by 1 day culturing before transfection. Chemical-based transfection was used (Lipofectamine LTX and Plus Reagent, Invitrogen). For each transfection reaction, 500 ng plasmid DNA was diluted in 200 μl OptiMEM medium; 4 μl Plus Reagent was added to the mixture, vortexed thoroughly and incubated at room temperature for 5 min. After that, 4 μl Lipofectamine LTX was added, the transfection mix was vortexed again and incubated for 15 min at room temperature. Complete medium was aspirated from the cells and replaced with 2 ml antibotic-free medium, and the 200 μl transfection mix was added on top. Transfected cells were incubated at 37°C, 10% CO_2 for 16 h. The medium was changed, replaced by 2 ml antibiotic-free medium and cells were let to recover for another 12-24 h before the experiments.

2.5.3 Treatments of cells

Depending on the context and purpose, cells underwent different treatments before confocal imaging (section 2.6).

EGF stimulation:	Cells were stimulated with 100 ng/ml human recombinant epidermal growth factor (Calbiochem) at 37°C for 2 min.
ER tracker labelling:	Cells were incubated with ER tracker diluted in HBSS at a final concentration of 1 μM for 10 min at 37°C, 10% CO_2.

Depending on the purpose, treated cells were either scraped into 200 μl lysis buffer for Western blotting (section 2.3.5), or fixed with 4% (w/v) PFA in PBS for 10 min before immunofluorescence preparation (section 2.5.6), or directly imaged live.

2.5.4 Rapalogue-induced enzyme recruitment

The rapamycin analogue AP21967 (Clontech Laboratories, Inc.), or rapalogue, was used as a dimeriser to recruit lipid-modifying enzymes to specific cellular organelles. Recruitment was done by adding antibiotic-free medium supplemented with rapalogue to live cells. The final concentration of rapalogue was 500 nM. Rapalogue-treated cells were examined every half hour until they reached the mitotic stage of interest.

2.5.5 Cell lysate preparation

After one PBS wash, cells were scraped into 200 μl lysis buffer and incubated on ice for 5 min. The mixture was centrifuged at 10,000x*g*, 4°C for 10 min, the insoluble fraction was discarded and the soluble fraction (cell lysate) was retained. Cell lysates were snap frozen in liquid nitrogen and stored at -20°C before further sample preparation.

2.5.6 Immunofluorescence

Cells were transfected, either treated or untreated, and fixed in 4% (w/v) PFA in PBS for 10 min. The cells were washed three times with 2 ml PBS and permeabilised with freshly prepared 0.5% saponin/3% fatty-acid free BSA (w/v) in PBS or TBS for 30 min wherein the fatty-acid free BSA was used to block the cells. Cells were washed once with PBS or TBS before primary antibody incubation.

Commercial primary antibodies were diluted in 0.5% saponin/3% BSA/PBS or TBS in a 1:50 to 1:100 ratio and recombinant proteins were diluted in the same solution (amount specified in result chapter). The primary antibody solution was added to the inner well of the MatTek dish. Unless specified in the manufacturer's protocol, cells were incubated with primary antibodies or recombinant proteins at room temperature for 1 h. After that, the primary antibody solution was aspirated and the cells were washed once with PBS or TBS. The cells were then incubated with secondary antibodies, diluted with the 0.5% saponin solution in 1:200 to 1:500 ratio, for an hour at room temperature. The secondary antibody solution was aspirated and the cells were washed once. The probed cells were kept in 2.5% (w/v) DABCO in PBS or TBS before imaging.

Alternatively, cells were mounted in ~10 µl ProLong Gold antifade reagent and carefully sealed by a coverslip. If necessary, cells were incubated with Hoechst 33342 at a final concentration of 1 µg/ml for 10 min at room temperature before mounting. In every incubation step, the cells were covered by foil to protect the samples from light.

2.5.7 Commentary on the use of a lipophilic dye during immunofluorescence

It is a common approach to label cells with lipophilic dye for membrane visualisation due to its simplicity, and it is a rapid way to determine changes of membrane morphology in live cells upon various treatments. $DiOC_6$ is a lipophilic dye usually used in live cells to reveal membrane structures like the NE, mitochondria network and ER (Koning *et al.*, 1993).

However, if antibody co-labelling is required, permeabilisation with detergent such as saponin can attenuate the fluorescent signal of $DiOC_6$ (Figure 2.1). Fixed cells pre-stained with $DiOC_6$ displayed a distinguishable fluorescence in the NE (yellow arrows) and mitochondria (magenta arrows) especially at the concentration of 2.5 and 5 µM (upper panels). When the cells pre-stained with $DiOC_6$ were permeabilised with 0.5% saponin, the fluorescence of DiOC6 was diminished. It was difficult to image the mitochondria and NE with the given intensity of the fluorescence (lower panels), especially in 0.5 and 2.5 µM $DiOC_6$-stained cells.

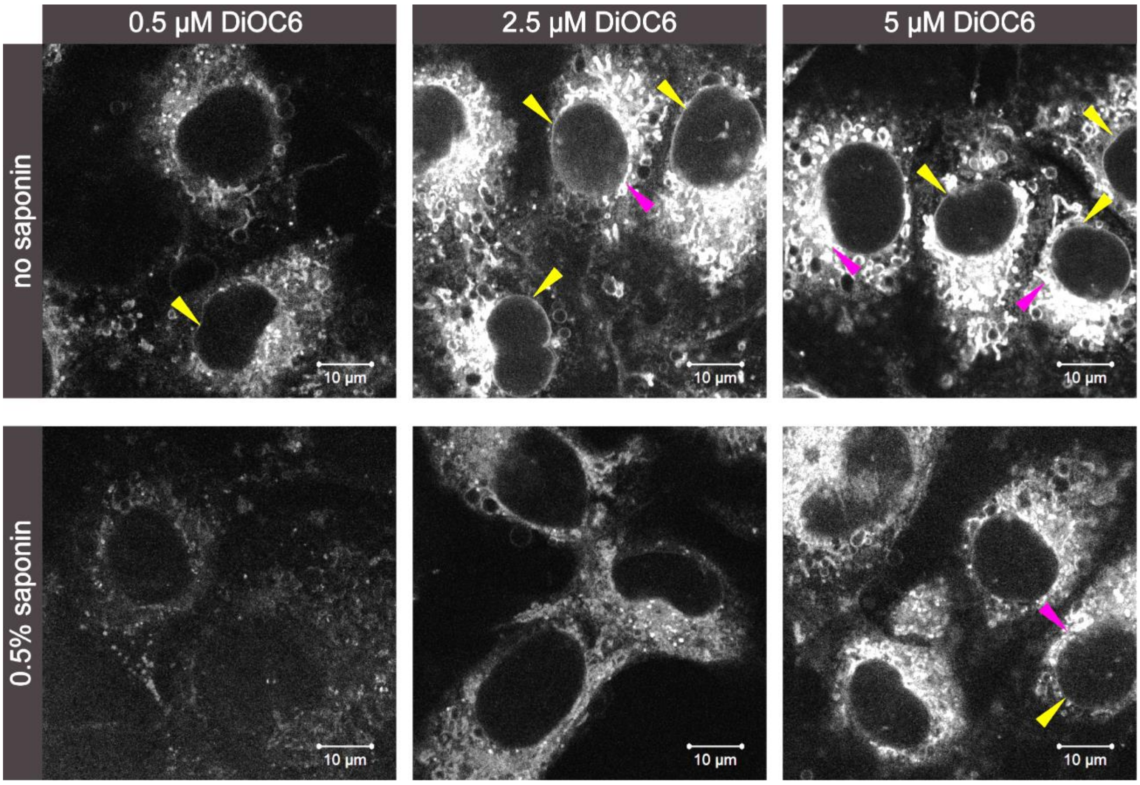

Figure 2.1 Saponin attenuates the fluorescence of the lipophilic dye $DiOC_6$

Live COS7 cells were incubated with different concentrations of $DiOC_6$ for 5 min and fixed with 4% PFA for 10 min. Cells were subsequently incubated with PBS buffer (upper panels) or permeabilised with 0.5% saponin/PBS for 30 min (lower panels) before confocal image acquisition. $DiOC_6$ stained the NE (yellow arrows) and mitochondria (magenta), and the staining increased with the concentration of $DiOC_6$. Permeabilised cells displayed a weakened fluorescent signal of $DiOC_6$ and it was more difficult to identify the NE and mitochondria. Cells stained with higher concentration of $DiOC_6$ preserved fluorescent signals better after permeabilisation. Scale bar, 10 µm.

Solution

To avoid losing the fluorescent signals of lipophilic dye such as $DiOC_6$, it is recommended to label the cells after permeabilisation.

2.6 Confocal microscopy

Confocal images were acquired on a Zeiss LSM Invert 710 microscope. A Zeiss Plane 25x objective lens (NA=0.8) and a Zeiss Plan-Appochromat 63x oil immersion objective lens (NA=1.4) were used. A CoolLED PE-1 source was used to replace the mercury illumination. During the visualisation of multiple fluorophores, emission filters were used to avoid cross excitation between channels. The filtersets were chosen as listed below.

Table 2.15 Filtersets of confocal microscope

Fluorophore	Laser wavelength	Emission filter
DyLight405, Hoechst33342	405 nm	420-480 nm band pass
DiOC6, DyLight488, GFP	488 nm	505-530 nm band pass
AlexFluor546, RFP,	543 nm	560-615 nm band pass
AlexFluor647, DyLight649	633 nm	650 nm long pass

For live cells imaging, complete medium was aspirated and replaced by phenol red-free medium before imaging. During image acquisition, cells were maintained at 37°C, 10% CO_2 in a heated environmental chamber of constant humidity. Laser power and acquisition parameters (z-stacks, size of pinhole and time series) were adjusted to minimise laser damage on cells.

Image processing

Confocal images were acquired using Zeiss LSM software ZEN. The .lsm files were analysed using image processing software Zen 2011 or Volocity 6.3. Images were exported in .tiff format.

2.7 Correlative light and electron microscopy (CLEM)

2.7.1 CLEM sample preparation

Cells were grown on gridded glass coverslips in MatTek dishes. Live cells were transfected, treated and followed to the required stage of mitosis using confocal microscopy. 1 volume of of 8% FA in 0.2 M PB was added to the cells in the confocal microscope to halt the cell cycle prior to imaging for brightfield and fluorescence signals. The cell of interest was located according to the grid number of its field. Secondary fixation was performed in 1.5% GA/2% FA in 0.1 M PB for 30–60 min. After fixation, coverslips were carefully removed from the MatTek dishes and washed several times in 0.1M PB. The cells were post-fixed in 1.5% potassium ferricyanide/1% osmium tetroxide for 1 h, before rinsing in PB, and incubating in 1% tannic acid in 0.05 M PB for 45 min to enhance membrane contrast. After a brief rinse in 1% sodium sulphate in 0.05 M PB, the coverslips were washed twice in distilled water, dehydrated through an ascending series of ethanol to 100% prior to infiltration with Epoxy resin and polymerisation at 60°C for 48 h. The coverslips were removed from the resin blocks by plunging briefly into liquid nitrogen. The cells of interest were identified by correlating the grid and cell pattern on the surface of the block with previously acquired confocal images. The area of interest was cut from the block and further trimmed by hand using a single edged razor blade to form a small trapezoid block face for serial ultrathin sectioning. Using a diamond knife, serial ultrathin sections of 70 nm thicknesses were cut through the entire extent of the cells of interest and collected on 1.5% formvar-coated single slot grids. The sections were counterstained with lead citrate to further enhance contrast prior to viewing in the electron microscope (FEI Tecnai G2 Spirit BioTWIN with Gatan Ultrascan CCD camera). EM grade FA and GA were used.

2.7.2 Segmentation of ultrastructure

Serial micrographs were stacked and aligned using Amira (Visage Imaging, Berlin).The pixels of NE, ER, centrioles and vesicles were manually traced based on their morphological features. The NE is a smooth double lipid bilayer and the nuclear pores appear to be a diaphragm-like structure on a cross section. The ER is either tubular or cisternal, and it can be distinguished from the NE by its attached ribosomes. The centrioles appear to be cylindrical when cut longitudinally whereas it appears to be a ring of 9 triplet microtubules on a transverse section. Vesicles are small spherical structures enclosed by a lipid bilayer, and they have circular cross sections on the micrograph.

2.8 Electron Tomography

For electron tomography, samples were prepared as detailed above but 200 nm-thick serial sections were collected through the entire extent of the cells of interest. Tomograms were acquired from the 200 nm sections at targeted regions in the reforming nuclear envelope – either at specific gaps, or where collections of vesicles were evident in close proximity to the reforming envelope. Images were collected at 1-degree intervals across a maximal tilt range of ±70 degrees, at a resolution of 2,048 x 2,048 pixels, with a per pixel resolution of 0.79 nm (FEI Tecnai G2 Spirit BioTWIN with Gatan Ultrascan CCD camera). Tomograms were processed with IMOD (an open-source, cross-platform image processing software) (Kremer *et al.*, 1996), using patch tracking for alignment, and simultaneous iterative reconstruction technique (SIRT) for volume reconstruction. The reconstructed volume was exported as a series of 2D tiff images, and the NE and adjacent membranous structures, including vesicles, were manually segmented and reconstructed using Amira (Visage Imaging, Berlin). Movies were created from the 2D tiff stacks using Quicktime Player 7 Pro, and compressed using Stomp (Shinywhitebox Ltd).

2.9 MiniSOG photo-oxidation

For miniSOG photo-oxidation experiment, the samples were fixed and stained differently. However, the dehydration, embedding, serial sectioning and imaging steps followed the conventional CLEM protocol as described above.

Cells were transfected with 250-500 ng miniSOG-conjugated construct for 16 h and let to recover in 2 ml antibiotic-free medium for 24 h. The medium was discarded and the cells were fixed with 2.5% GA (v/v) in 0.1 M cacodylate buffer (pH 7.4) on ice for 30 min. The cells were washed 5 times with cacodylate buffer and incubated in blocking buffer on ice for another 30 min. The blocking buffer was replaced with 2.5 mM DAB solution before photo-oxidation.

A Zeiss LSM Invert 510 confocal microscope was used as a photo-oxidation platform. Samples were loaded on a customised cooling chamber built by Christopher Applebee, engineer at Cell Biophysics Lab. The chamber has a cooling jacket in which cold water was circulated by a peristaltic pump (BioScience Tools) so that the samples were maintained at ~4°C. The lid of the chamber was connected to oxygen supply at a rate of 2.5 l/min to ensure samples were in an oxygenated environment. Figure of the setup is shown in Chapter 6.

Photo-oxidation was done by illuminating samples in the chamber with a 150 W mercury lamp through a FITC filterset. A photo-oxidised cell gives a dark brown colour that originated from the DAB reaction product. Typical exposure time of a photo-oxidation reaction was 30 min. After photo-oxidation, cells were washed 5 times with cacodylate buffer. The cells were re-fixed in 2% FA/1.5% GA (v/v) in cacodylate buffer on ice for 30 min and were washed once with cacodylate buffer. After that, cells were incubated with 0.2% (v/v) osmium tetroxide in cacodylate buffer on ice for 30 min, followed by three washes. The sample was kept in 1% FA/0.1M cacodylate buffer at 4°C before embedding.

2.10 Serial block-face scanning electron microscopy (SBF SEM)

Serial block-face scanning electron microscopy (SBF SEM) data was collected using a 3View2XP (Gatan, Pleasanton, CA) attached to a Sigma VP SEM (Zeiss, Cambridge). Cells were grown on gridded MatTek dishes and fixed as previously described at a specific stage of the cell cycle. In preparation for SBF SEM, the fixed cells were processed following the method of the National Centre for Microscopy and Imaging Research (Deerinck *et al.*, 2010), which impregnates the sample with high concentrations of heavy metals to introduce maximal contrast and conductivity when viewed in the SEM. The cell of interest was identified by correlation of grid reference with previously acquired confocal images; this area was trimmed to a small trapezoid, excised from the resin block, and attached to a SBF SEM specimen holder using conductive epoxy resin (Circuitworks CW2400). Prior to commencement of a SBF SEM imaging run, the sample was coated with a 2 nm layer of platinum to further enhance conductivity.

To relocate the cell of interest in the SEM, an overview was first acquired at 5 kV, sufficient to penetrate the platinum coating and generate an image of the underlying sample. Inverted backscattered electron images were then acquired through the entire extent of the cell of interest at a resolution of 8,192 x 8,192 pixels (horizontal frame width of 36.74 μm; pixel size of 4.5 nm) using a 2 μs dwell time and 50 nm slice thickness. The SEM was operated in variable pressure mode at 5 to 10 Pa, with high current mode active, at an indicated magnification of 7,000. The 20 μm aperture was used, at an accelerating voltage of 2 kV. Typically, between 300 and 400 slices were necessary for an entire cell, representing a total volume of approximately 400,000 μm^3.

As data was collected in variable pressure mode, only minor adjustments in image alignment were needed, particularly where the field of view was altered in order to track the cell of interest. Movies of each series were generated using Amira (Visage Imaging, Berlin), Quicktime Player 7 Pro, and Stomp (Shinywhitebox Ltd.).

2.11 Isolation of nuclei and its DAG composition analysis by lipid mass spectrometry

Nuclei were purified following the (Andersen *et al.*, 2005) protocol. ~1.5 x 10^8 HeLa cells were collected by adding Trypsin/versene EDTA solution to the culture dish. Collected cells were pelleted by centrifugation at 250xg, 4°C for 5 min and washed 3 times with ice cold PBS before resuspending into Nuclei Buffer A. 5 μl aliquot of the resuspension was examined under a benchtop light microscope. The cell suspension is ready for nitrogen gas cavitation when 90% of the cells are swollen.

Nitrogen gas cavitation was performed in a cell disruption bomb (Parr Instrument Company, USA). The cells were lysed at 200 psi and equilibrated on ice for 10 min before pressure release. The percentage of lysed cells was promptly checked using a benchtop light microscope. The lysate was washed in Nuclei Buffer A once, resuspended in Nuclei Buffer S1 (0.25 M sucrose content) and layered over Nuclei Buffer S2 (0.35 M sucrose content). The lysate were then centrifuged through the sucrose layers and resuspended in Nuclei Buffer S2. A small aliquot of pure nuclei (the final suspension) was reserved for confocal microscopy and the rest was submitted to phospholipids extraction and DAG analysis was performed on a LC/MS/MS system (Prominence HPLC, Shimadzu), as described in Jethwa (2014).

Chapter 3 Isolation of fusogenic vesicles from somatic mammalian cells

3.1 Introduction

One of the best ways to investigate and manipulate cellular mechanism is to develop a cell-free assay. The advantage of a cell-free assay relies on its simplicity so that investigators are able to identify key roles of biomolecules. However, to develop a cell-free assay is not a trivial task. Scientists have spent a long time constructing cell-free systems derived from *Xenopus* (Newport, 1987), *Drosophila* (Ulitzur and Gruenbaum, 1989) and sea urchins (Cameron and Poccia, 1994) in order to understand NE assembly.

In an *in vitro* NE assembly assay based on male pronucleus (MPN) formation in echinoderms, a membrane vesicle population known as MV1 has been isolated and demonstrated to be essential for forming a complete NE (Collas and Poccia, 1996). MV1 has been well characterised. It is enriched in PLCγ and its substrate PtdIns(4,5)P_2 and other phosphoinositides. The hydrolysis of PtdIns(4,5)P_2 to diacylglycerol (DAG) renders it a fusogenic compartment (Byrne *et al.*, 2007) (more details in introduction). Isolation of fusogenic MVs is well established in model organisms such as echinoderms and *Xenopus* whereas no comparable assay is available in somatic cells of higher organisms (see references above).

The cell-free assay derived from echinoderms has several advantages. Firstly, the sea urchins provide large amount of raw material for protein and lipid purification. Moreover, fertilised sea urchin eggs progress through their initial mitotic cycles with a high degree of synchrony allowing extraction of cellular components at various stages of the cell cycle. Despite the above facts, there is still a necessity to develop a cell-free assay based on mammalian cells, to provide a closer model to humans.

One major objective of this study is to isolate a fusogenic component analogous to MV1 or MV1-like vesicles in mammalian cells (see Chapter 6) so that the ultimate goal is to develop a mammalian NE assembly cell-free assay. Such an *in vitro* assay would provide information regarding the protein and lipid composition, fusogenic properties of MV1-like vesicles to other membrane compartments and also it would inform about its binding property to chromosomes, all of which will contribute to understanding the fusion mechanism during NE assembly.

Mammalian tissue culture cells provided the raw material in this study. Although tissue culture cells are relatively straight forward to obtain and maintain, they may be more difficult than tissues to fractionate due to differences in cytoskeleton organisation (Howell *et al.*, 1989). This chapter describes the optimisation of cell homogenisation and several gradient fractionation methods applied to isolate MV1-like vesicles from mammalian cells.

3.2 Isolation of MV1-like vesicles from interphase cell homogenate

The key concept in developing a cell-free assay depends on isolating the right cellular components. It would have been preferable to obtain cell homogenate from synchronised cells, since MV1-like vesicles may have an enhanced population and/or execute its fusogenic function at a specific mitotic stage. However, it had been demonstrated that several conventional cell synchronisation protocols only recover a scarce population of synchronised cells. For instance, the "shake off" protocol was shown to yield only 3% mitotic cells. Large amounts of isolated cellular components are required for lipid-protein characterisation thus any large-scale sacrifice of material is impractical. Alternatively, starvation was suggested to force cells to arrest at G0 phase so that cells may re-enter G1 phase in a more synchronous manner. However, it was shown that starvation did not result in any enrichment of the G1 phase cells (Hobday, 2012).

A common protocol used to synchronise cells is nocodazole treatment. Nocodazole is a drug that interferes with the polymerisation of microtubules and is often used in cell biology experiments to arrest cells at prometaphase (Amon, 2002). The synchronisation is even more efficient in a thymidine/nocodazole double block condition. It was reported that cells have depolymerised microtubules after release from nocodazole (Zieve *et al.*, 1980). Such an outcome is undesirable because biomolecules like PtdIns(4,5)P_2 and PLCγ, enriched in MV1 may mislocalise due to depolymerised microtubules. Furthermore, nocodazole was shown to inhibit NE assembly in a mammalian cell-free assay (Vaillant and Paulin-Levasseur, 2008). Therefore, considering the above drawbacks, an interphase cell homogenate was used as starting material to isolate MV1-like vesicles.

3.3 Optimisation of cell homogenisation

MV1 are characterised as low-density fractions enriched in PLCγ and free of Golgi and ER markers; MV1-like vesicles are expected to have similar characteristics. There are two critical steps to obtain subcellular fractions: 1) homogenisation of cells/tissues, 2) fractionation of homogenates. Initially we optimised the homogenisation step.

The MV1 isolation protocol was established for fertilised sea urchin eggs. The living environment of marine organisms is different from terrestrial organisms thus the homogenisation buffer (HB) used in this study was modified based on some related mammalian cell-free assays. A metaphase homogenate of CHO cells was shown to support NE assembly around mitotic chromosomes *in vitro* (Burke and Gerace, 1986) and a postnuclear supernatant (PNS) of CHO cell homogenate was used to reconstitute endocytic vesicle fusion in a cell-free assay (Gruenberg and Howell, 1989). Unless otherwise stated, the HB used in this study refers to the modified HB based on Gruenberg and Howell's work in 1989. Table 3.1 shows the composition of the original and modified HB. Multiple protease inhibitors were replaced by a protease inhibitor cocktail tablet and the serine protease inhibitor PMSF was replaced by a more stable substitute AEBSF.

Table 3.1 Recipe of homogenisation buffers

Chemicals	Gruenberg & Howell, 1989	This study
250 mM sucrose	✓	✓
10 mM Tris	✓	✓
1 mM iodoacetamide	✓	-
1 mg/ml antipain	✓	-
10 µg/ml aprotinin	✓	-
17 µg/ml benzamidine	✓	✓
1 µg/ml pepstatin	✓	-
1 tablet of EDTA-free Complete mini protease inhibitors	-	✓
1 mM PMSF	✓	-
1 mM AEBSF	-	✓

Optimisation of cell homogenisation was initially performed using CHO cells because it is the cell line used in the original study. HeLa cells were also used in homogenisation because a corresponding human genome database is available. This is useful for protein identification once MV1-like vesicles are isolated. Since MV1-like vesicles may be very low in quantity, approximately 1.5 x 10^8 cells were used in each homogenisation, corresponding to the number of cells used to isolate secretory granules or vesicles from the Golgi (Tooze, 2006).

The homogenisation steps in the MV1 isolation protocol (Byrne *et al.*, 2008) and Gruenberg and Howell's protocol were compared. The major differences between the two were the homogeniser and the centrifugation speed to produce PNS. Figure 3.1-A illustrates the key steps in these two homogenisations. In the former protocol cells were homogenised by passing through a 22G syringe needle whereas in the latter protocol cells were homogenised by a metal ball bearing; the centrifugation force to produce PNS were 10,000x*g* and 1,000x*g* respectively. The PNS was subsequently ultracentrifugated to produce the total membrane fraction, which was afterwards fractionated by MV1-separating gradients (Figure 3.1-B).

Figure 3.2 shows images of cell homogenates obtained using the two established protocols. Both protocols were able to produce membrane fragments (yellow arrows). Homogenised cells were indicated by reduced volume of the cytoplasm. However, some cells did not seem to be homogenised (red arrows). The ball bearing homogeniser visually generated more membrane fragments compared to a 22G syringe needle. This was indicated by enhanced observation of "clean nuclei" with the least nuclear membrane (white arrows). Fragmentation might be improved by increasing the number of passages through the homogeniser or reducing the volume of the solution that passes into the homogeniser, but over-homogenised cells may yield chromosome fragments that interact with and pull down MV1-like vesicle. The images of cell homogenates indicated the proportion of homogenised cells. To confirm the isolation of MV1-like vesicles, gradient separated-fractions were analysed by protein markers of various cellular organelles (see section below).

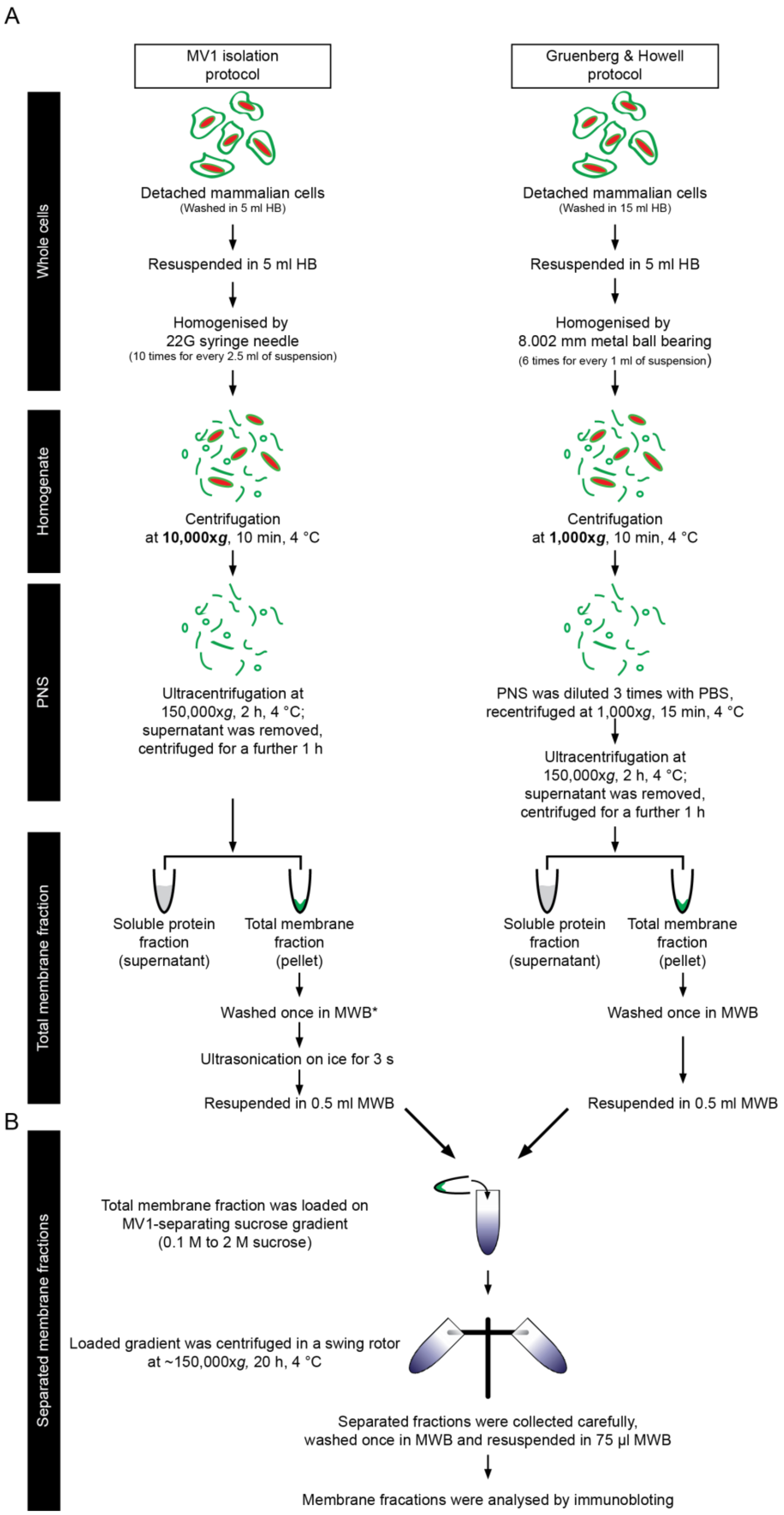

Figure 3.1 Fractionation flow chart of the MV1-separating gradient (different homogenisation protocols)

*Membrane wash buffer (MWB) = 1:4 HB:PBS

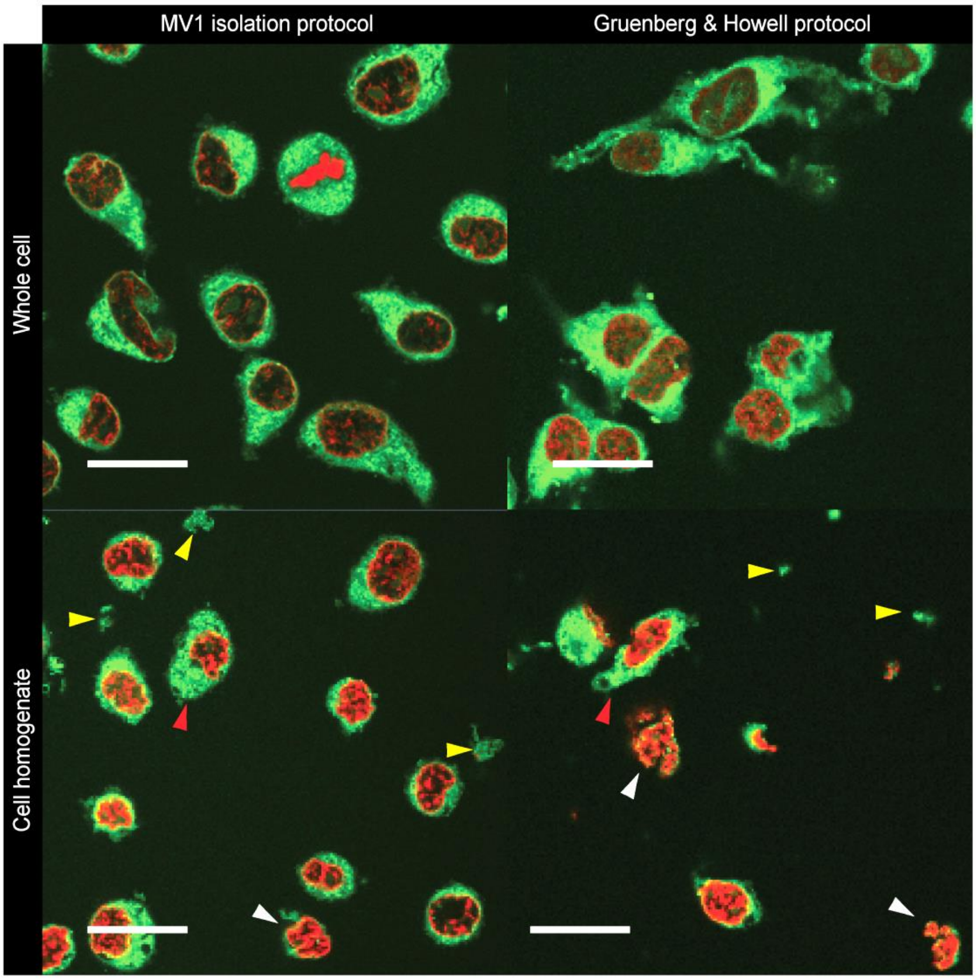

Figure 3.2 Cell homogenates obtained using two established protocols
HeLa cells were homogenised by a 22G syringe needle or a metal ball bearing. 200 µl of whole cells or homogenates were loaded and settled on a glass bottom cell culture dish. The cells or homogenates were stained with $DiOC_6$ (green channel) and Hoechst 33342 (red channel) and imaged by confocal microscopy. Red arrows indicate unhomogenised cells, yellow arrows indicate membrane fragments and white arrows indicate "clean nuclei" with the least nuclear membrane. Scale bar, 20 µm.

3.4 Isolation of MV1-like vesicles by density gradients

There are many devices to prepare a gradient but usually what matters most is the linearity of the gradient. By weighing the collected fractions, it was shown that the MV1-separating gradient and the Optiprep gradient were linear. The velocity gradient, however fitted into a sigmoid regression instead because the separation was not based on the cellular components reaching their density equilibrium (Figure 3.3). The regression lines allowed the fraction density to be determined. The range of density of the applied gradients is shown in Table 3.2.

Density gradients may only partially separate MV1-like vesicles from the rest of the cellular organelles because different cellular components may have a similar density. To determine the purity of separated membrane fractions, they were analysed for detection of a number of protein markers. As mentioned before, PLCγ being enriched in MV1 it is therefore a marker for potential fusogenic vesicles. The presence of Ran is an indicator of a functional NE, since this GTPase was detected in fully formed NE in a cell-free assay (Byrne *et al.*, 2005) and has been suggested to play a role in NE assembly (Hetzer *et al.*, 2002). Also, there was a two-fold enrichment of Ran in MV1 compared to MV2 (Byrne 2007, unpublished data). Protein markers of some membrane compartments were included to see if any of these cellular compartments were co-fractionated, details in Table 3.3.

Table 3.2 Range of density in the applied gradients

Fractionating gradient	Range of density (g/ml)
MV1-separating gradient	1.02 – 1.24
PtdIns synthesising-organelle-separating gradient (Optiprep gradient)	1.05 – 1.12
TGN-separating gradient (velocity gradient)	1.02 – 1.14

Table 3.3 Protein markers used for characterisation of separated fractions

Marker	Enriched in/specific to	Molecular Weight kDa
PLCγ	enriched in MV1	135
Ran	detected in functional NE	25
Calreticulin	ER marker	63
BiP	ER marker	78
Rab5	early endosome marker	24
Rab7	late endosome marker	23
Golgin-97	trans Golgi marker	97

	MV1-separating gradient	Optiprep gradient	Velocity gradient
R^2	0.9887	0.9556	0.9863

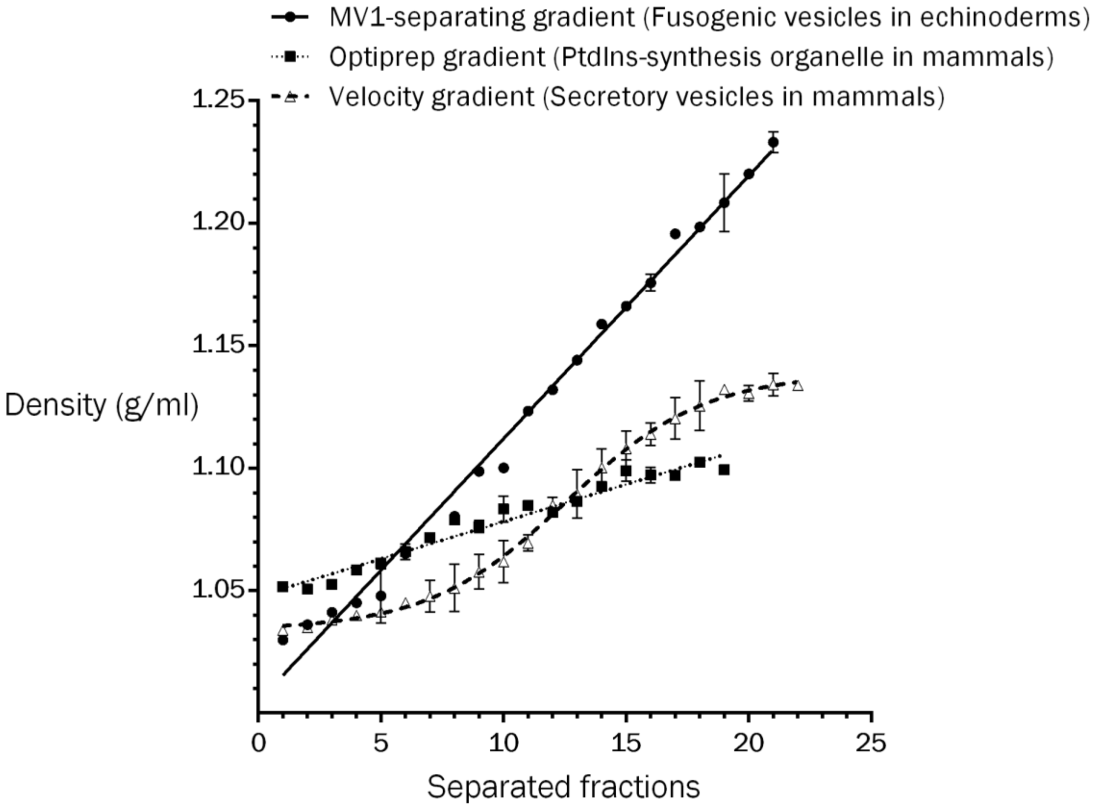

Figure 3.3 All gradients used in this study

Gradients were prepared according to their standard protocols. These gradients were chosen to separate different cellular components as indicated in the brackets. The gradients were aliquoted in 0.5 ml fractions from the low density end and weighed by an analytical balance.

3.4.1 CHO and HeLa cell homogenates separated by the MV1-separating gradient

It was predicted that MV1-like vesicles could be isolated by using well established protocols from previous studies. Strikingly, initial experiments indicated that modification of homogenisation was necessary. Figure 3.4 shows representative immunoblots of membrane fractions obtained using the two protocols described above. Using the MV1 isolation protocol, PLCγ, ER and Golgi markers were detected in few medium density fractions, but the signals of these markers were very weak. The ER marker was expected to distribute over a wide range of densities because the ER has rough and smooth subcompartments and comprises tubules and cisternae.

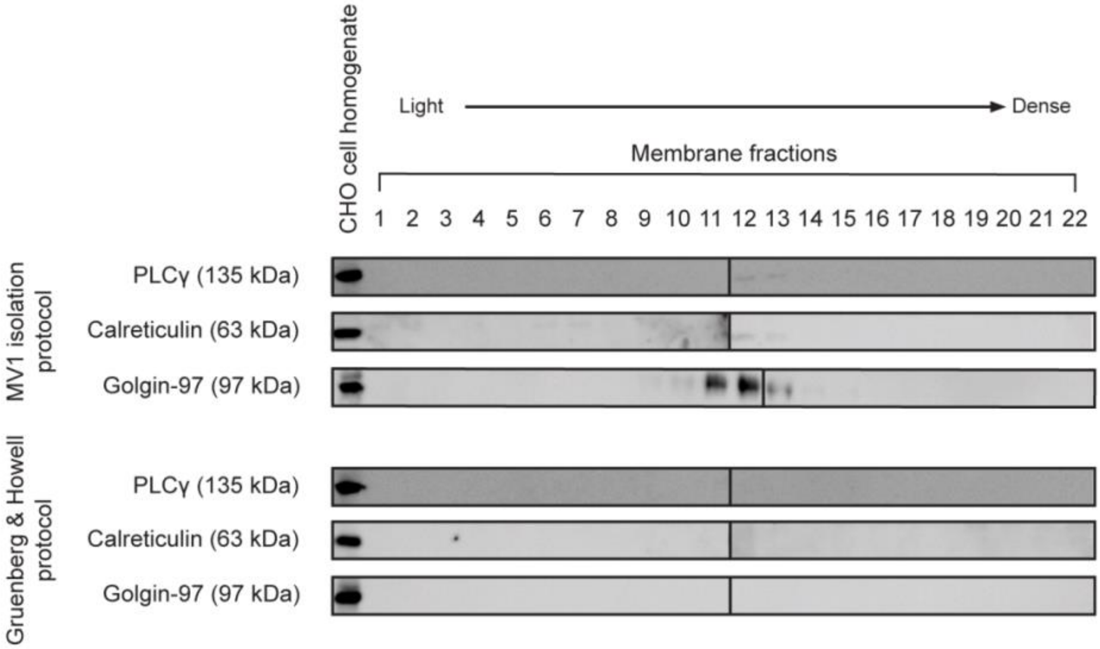

Figure 3.4 Separated membranes from CHO cell homogenates obtained using two established protocols

1.5 x 10^8 CHO cells were homogenised by the MV1 isolation or Gruenberg & Howell protocol (Figure 3.1-A). The PNS was fractioned into soluble proteins and total membrane fraction. The total membrane fraction was fractionated by the MV1-separating gradient into membrane fractions of different densities and analysed by immunoblotting. Sample loading in SDS-PAGE: CHO cell homogenate (5 μg); fractionated membranes (2% of the total membrane fraction). Individual immunoblots are indicated by a vertical black line. Immunoblots were exposed for 10 min and same exposure time was used for immunoblots using the same protein markers. Data are representative of 3 independent experiments.

In contrast, no signal for the markers were detected in the membranes prepared using the Gruenberg and Howell protocol. Possibly the PNS was diluted before ultracentrifugation and the total membrane fraction was not fully resuspended without ultrasonication (Figure 3.1-A). Therefore, recovery of the total membrane fraction was decreased. Hence, the two homogenisation protocols were combined and modified (Figure 3.5). Cells were homogenised by a metal ball bearing and centrifuged at 10,000x*g* to produce a PNS. The PNS was not diluted before ultracentrifugation and the total membrane fraction was ultrasonicated for a longer duration. An improvement of signal intensity was expected when using this combined protocol.

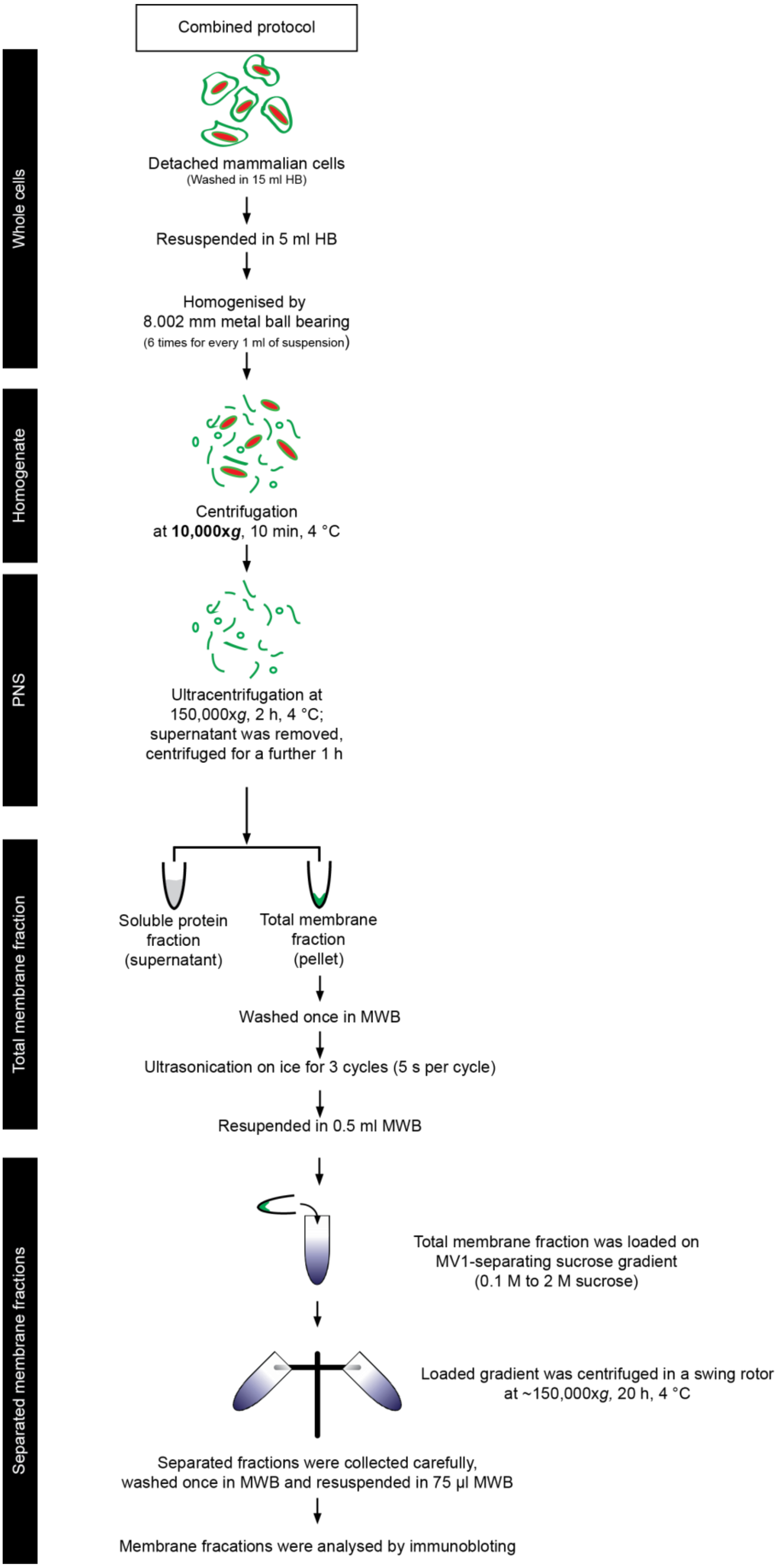

Figure 3.5 **Fractionation flow chart of the MV1-separating gradient (combined homogenisation protocol)**

*Membrane wash buffer (MWB) = 1:4 HB:PBS

Figure 3.6 shows representative immunoblots of membrane fractions obtained using the combined protocol. Stronger signals were detected from all selected markers. In general, endosomal markers Rab5 and Rab7 were detected in lower density fractions compared to the ER marker. Similar results were observed in another density gradient in which Rab11 (an endosomal marker) was separated from the ER and detected in lower density fractions (Woods *et al.*, 2002). Subcellular fractions of the Golgi were shown to have a lower density than those obtained from the ER in several density gradients (Balch *et al.*, 1984, Yang *et al.*, 1997b, Plonne *et al.*, 1999). However, in some membrane fractions, both BiP (ER) and Golgin-97 (Golgi) were detected.

In CHO cell membrane fractions, PLCγ and Ran were concentrated in fractions 8 to 11 (density 1.08 – 1.12 g/ml), with the endosomal markers following almost identical distributions (Figure 3.6-A). PLCγ and Ran are soluble proteins but only a very low signal was detected in the soluble protein fraction of CHO cells, most likely because the loaded fraction was not concentrated enough. A more concentrated soluble protein fraction was loaded in HeLa cell experiments.

In HeLa cell membrane fractions, the protein markers were slightly shifted to denser fractions (Figure 3.6-B). Another noticeable difference was that weak signals were also detected from each marker in the denser fractions. PLCγ and Ran were concentrated in fractions 10 to 14 (density 1.11 – 1.15 g/ml), along with the ER and Golgi markers. Again, the endosomal markers co-fractionated with almost all the PLCγ/Ran-positive fractions. Although CHO cell membranes resolved better than HeLa cell membranes, more PLCγ/Ran-positive and ER/Golgi-negative fractions were isolated from HeLa cells (Figure 3.6-B: fractions 5 – 7). Only one fraction showed the same property in CHO cell membranes (Figure 3.6-A: fraction 7). Interestingly, fraction 1 (density 1.02 g/ml) isolated from HeLa cells was only PLCγ/Ran-positive. However, this low density PLCγ/Ran-positive fraction was detected in 1 out of 3 experiments.

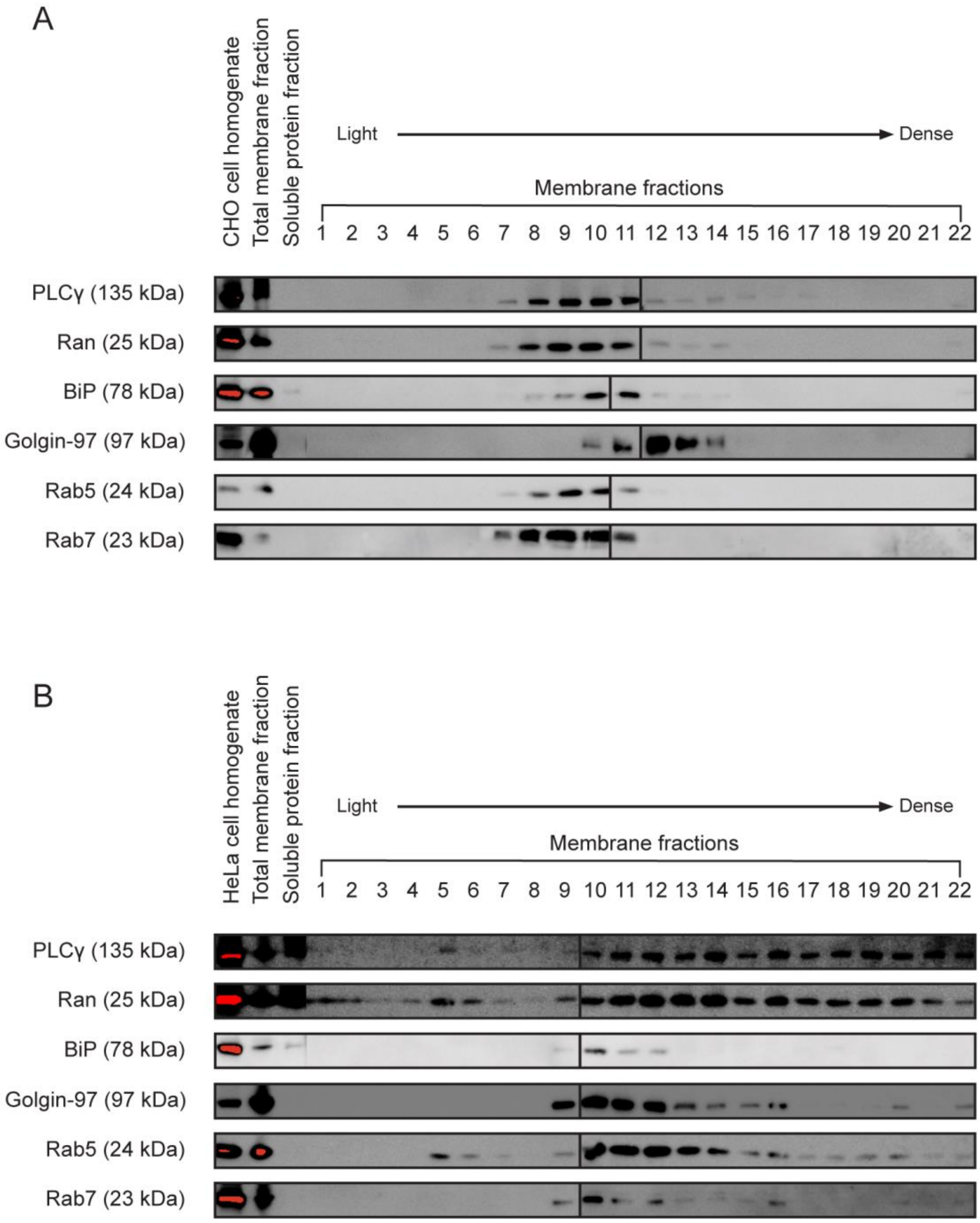

Figure 3.6 Separated membranes from A) CHO and B) HeLa cells obtained using the combined protocol

1.5 x 10^8 CHO/HeLa cells were homogenised using the combined protocol (Figure 3.5). The PNS was fractioned into soluble proteins and total membrane fraction. The total membrane fraction was fractionated by the MV1-separating gradient into membrane fractions of different densities and analysed by immunoblotting. Sample loading in SDS-PAGE: CHO/HeLa cell homogenate (5 µg); total membrane fraction (2.5% of PNS); soluble proteins (0.3% of PNS for CHO cell experiments and 1.5% of PNS for HeLa cell experiments); fractionated membranes (2% of the total membrane fraction). Individual immunoblots are indicated by a vertical black line. Immunoblots were exposed for 5 min and same exposure time was used for immunoblots using the same protein markers. Data are representative of 3 independent experiments.

3.4.2 CHO and HeLa cell homogenates separated by the PtdIns synthesising (PIS)-organelle-separating gradient (Optiprep gradient)

Given the limited separation of MV1-separating gradient, other density gradients were tried in parallel. Recently, membrane fractions enriched in phosphatidylinositol synthase activity were separated from the ER by an Optiprep based density gradient (Kim *et al.*, 2011). Optiprep (or iodixanol) is an iso-osmolar medium and is usually used as a sucrose alternative in subcellular fractionation. In this study, PIS signals were always associated with ER signals but their intensities were enhanced in low density fractions whereas ER signals were the strongest at high density fractions. More importantly, PIS activity was maximised at a single fraction.

PtdIns is phosphorylated to polyphosphoinositides such as PtdIns(4,5)P_2 and PtdIns(3,4,5)P_3 by various kinases and the PIS-organelle was shown to be very mobile and was frequently associated with other membranes (Kim *et al.*, 2011). Similar to the PIS-organelle, MV1-like vesicles may associate to other membranes where MV1-like vesicles are likely to have increased levels of phosphoinositides, the downstream products of PtdIns. Therefore, the PIS-organelle-separating gradient was tested to isolate MV1-like vesicles. Figure 3.7-A shows the workflow of this fractionation. A 25G syringe needle was used to homogenise cells in the PIS-organelle-separating protocol and Figure 3.8 shows an image of the cell homogenate, compared to the cell homogenate obtained by using a 22G syringe needle. Reduced volume of cytoplasm was observed in both homogenates. However, there were visually less membrane fragments or “clean nuclei” in the cell homogenate obtained using a 25G syringe needle.

Figure 3.9 reveals that PLCγ/Ran-positive fractions were co-fractionated with the ER (BiP), Golgi (Golgin-97) and endosomes (Rab5 and Rab7) in both CHO and HeLa cell membranes separated by the Optiprep gradient. Golgi signals were enriched in denser fractions relative to ER and endosomes signals. Using the same Optiprep gradient but another ER marker, Kim *et al.* (2011) had shown that fraction 16 to 21 are the ER fractions. However, we detected BiP, an ER marker, mainly in fraction 9 to 12. Ran was detected in all fractions with the first four fractions purely Ran-positive, this result was consistent in both CHO and HeLa cell membranes. The PLCγ/Ran-positive fractions, which were present in medium densities, could not be separated from the ER and the Golgi in this gradient.

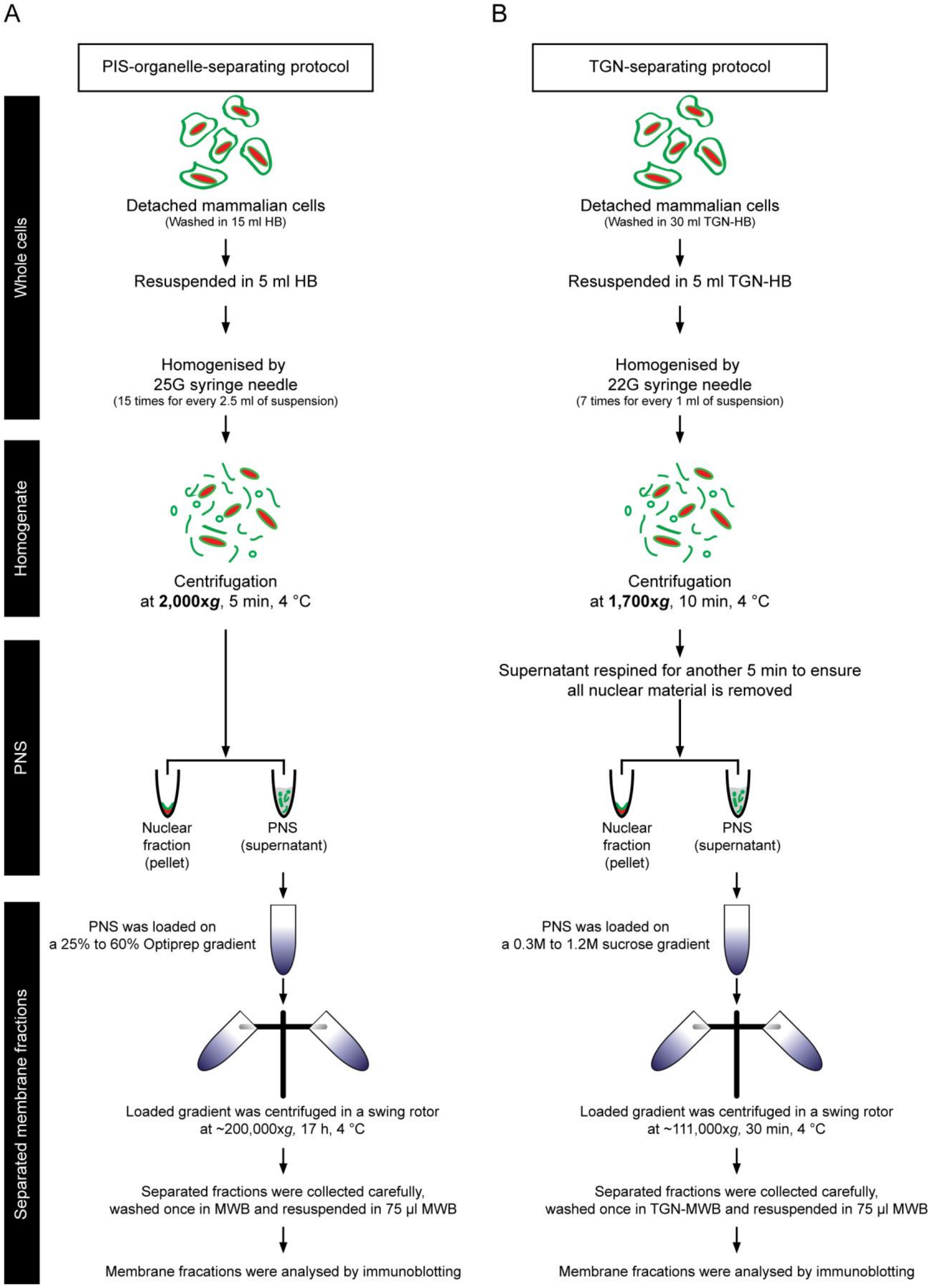

Figure 3.7 Fractionation flow chart of the PIS-organelle-separating gradient and TGN-separating gradient

Recipe of TGN-HB see Materials and Methods; TGN-membrane wash buffer (TGN-MWB) = 1:4 TGN-HB:TBS.

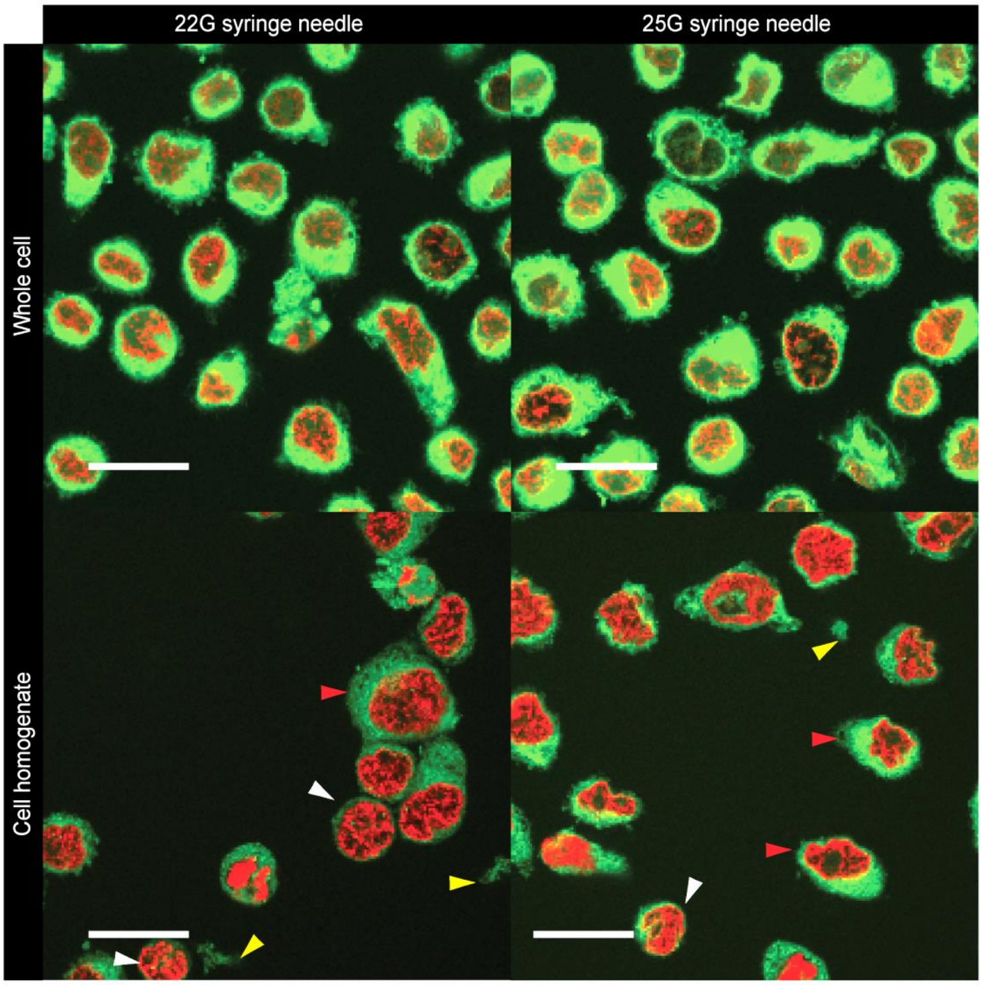

Figure 3.8 Cell homogenates obtained using 22G and 25G syringe needle

HeLa cells were homogenised by a 22G or 25G syringe needle. 200 µl of whole cells or homogenates were loaded and settled on a glass bottom cell culture dish. The cells or homogenates were stained with $DiOC_6$ (green channel) and Hoechst 33342 (red channel) and imaged with a confocal light microscope. Red arrows indicate unhomogenised cells, yellow arrows indicate membrane fragments and white arrows indicate "clean nuclei" with the least nuclear membrane. Scale bar, 20 µm.

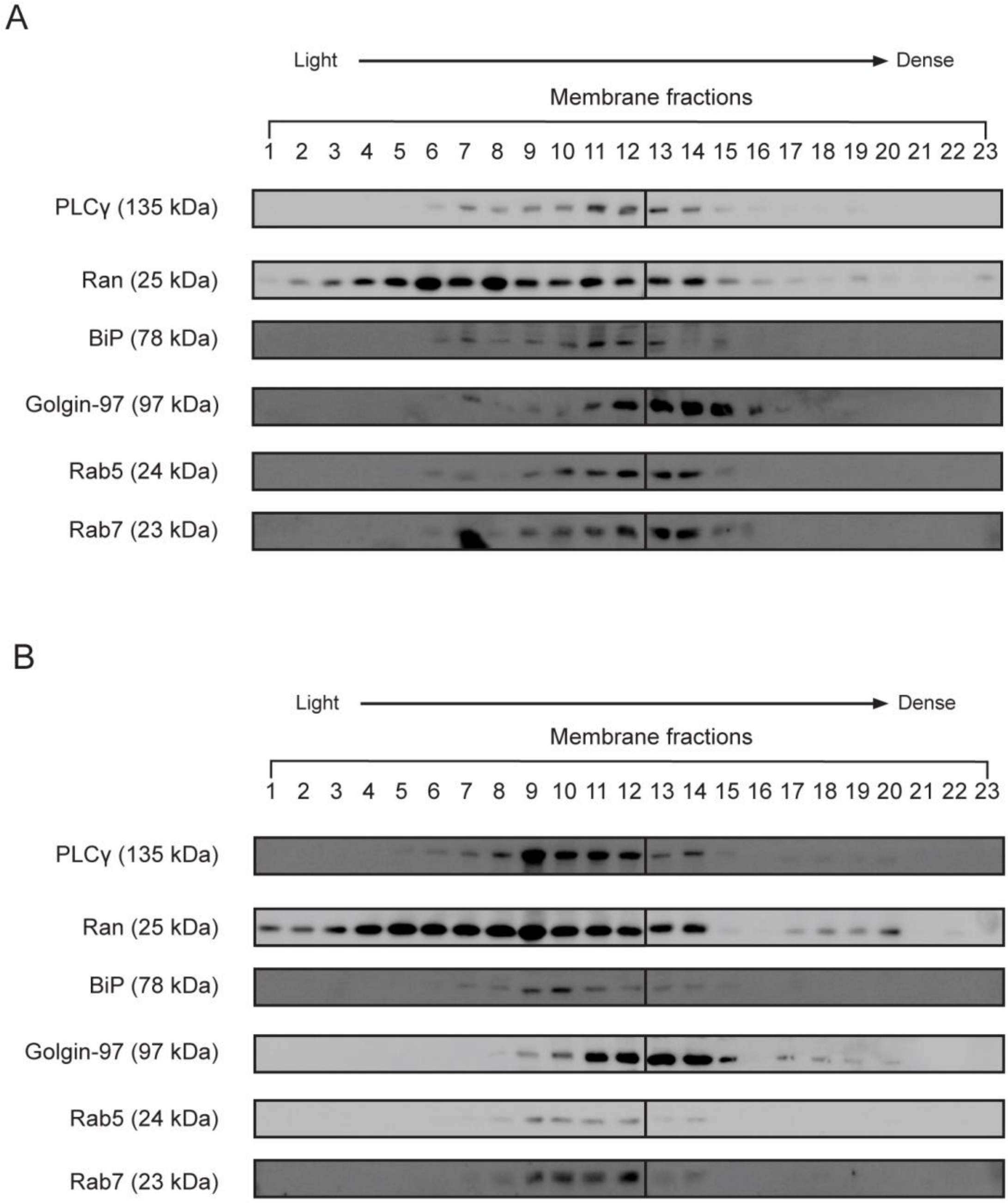

Figure 3.9 Separated membranes of A) CHO and B) HeLa cells fractionated by the PIS-organelle-separating gradient

1.5 x 10^8 CHO/HeLa cells were homogenised by a 25G syringe needle (Figure 3.7-A). The PNS was fractioned by the PIS-organelle-separating gradient into membrane fractions of different densities and analysed by immunoblotting. Sample loading in SDS-PAGE: fractionated membranes (1% of PNS). Individual immunoblots are indicated by a vertical black line. Immunoblots were exposed for 5 min and same exposure time was used for immunoblots using the same protein markers. Data are representative of 2 independent experiments.

3.4.3 HeLa cell homogenate separated by the TGN-separating gradient (velocity gradient)

Both the MV1-separating gradient and the Optiprep gradient provided limited separation of fractions analogous to MV1 from other organelles. Hence, a TGN-separating gradient was tested to separate MV1-like vesicles from the Golgi. Figure 3.7-B shows the flow chart of this fractionation procedure. This is an established sucrose-based gradient to separate cellular organelles based on size rather than density (Tooze, 2006). Larger components migrate faster than smaller ones thus this gradient is also known as velocity gradient. The velocity gradient was applied routinely to separate secretory granules/vesicles from the *trans*-Golgi. The separated fractions are affiliated to soluble proteins (fraction 1 – 3), immature secretory granules and constitutive secretory vesicles (fraction 4 – 11), mature secretory granules (fraction 12 – 19) and the *trans*-Golgi (fraction 20 onwards) (Figure 3.10, fraction affiliations).

HeLa cell homogenates were separated by the velocity gradient. Most of the markers were found in the soluble fractions (Figure 3.10). As expected, Golgin-97 was detected in the *trans*-Golgi fraction (Figure 3.10: fraction 24), indicating that the gradient functioned properly. An interesting remark here is that apart from the soluble fractions, fraction 5 was the only PLCγ-positive fraction. This fraction was only co-fractionated with Rab5. Its signal intensity was weak and only detected in one out of two experiments. Together, the above result demonstrated that a pure PLCγ or PLCγ/Ran-positive fraction is difficult to obtain and a successful isolation of such fractions may vary from batch to batch.

In summary, several biochemical gradients were applied to separate MV1-like vesicles. Although pure PLCγ/Ran-positive fractions were isolated in some gradients, the separations either lacked reproducibility or lacked resolution in these gradients. Also, fractionation from interphase cell homogenates was challenging, the input of cells used may not have been sufficient to reproduce a pure separation of MV1-like vesicles. Therefore, given the above limitations, a complementary cell biology approach was adopted.

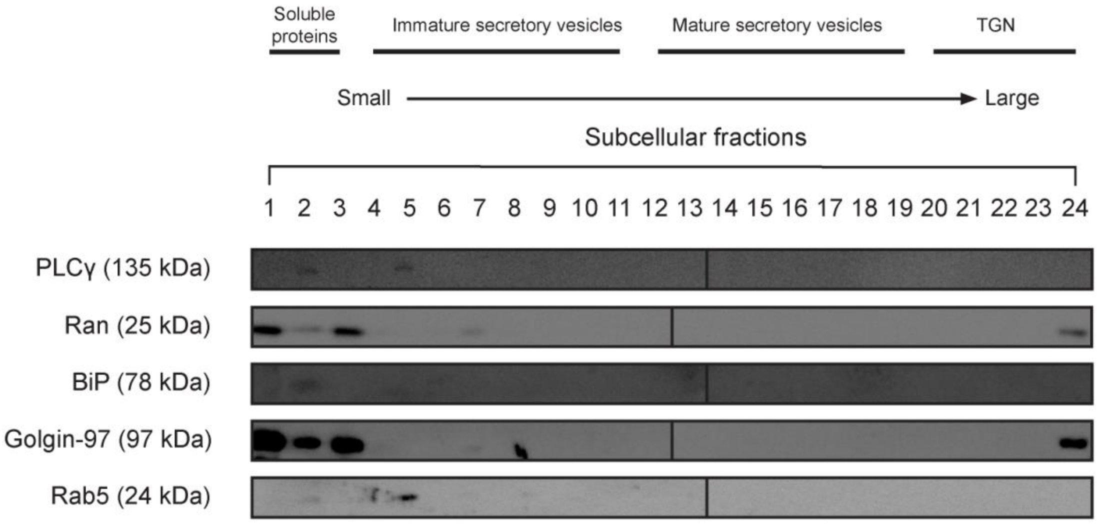

Figure 3.10 Subcellular fractions of HeLa cells fractionated by the TGN-separating gradient

1.5 x 10^8 HeLa cells were homogenised by a 22G syringe needle (Figure 3.7-B). The PNS was fractioned by the TGN-separating gradient into subcellular fractions of different sizes and analysed by immunoblotting. Sample loading in SDS-PAGE: separated fractions (1% of PNS). Individual immunoblots are indicated by a vertical black line. Immunoblots were exposed for 5 min and same exposure time was used for immunoblots using the same protein markers. Data are representative of 2 independent experiments.

3.5 Discussion

3.5.1 Performance of the different fractionating gradients

Subcellular fractionation is a laborious procedure with multiple steps. Imperfection is common in subcellular fractionation because most of the time enrichment of derived components rather than homogeneity is achieved. Several gradients were applied to isolate MV1-like vesicles on the basis of density or size of the organelles. At the moment PLCγ and Ran enrichments were considered the criteria for MV1-like vesicles because MV1 is enriched in both PLCγ and Ran (Byrne *et al.*, 2007) (also Byrne 2007, unpublished data). We aimed at isolating MV1-like vesicles in mammalian cells so that we could characterise their lipid and protein composition by lipid mass-spectrometry and proteomics analysis respectively, in order to provide further details about the potential proteins or lipids involved in somatic cell NE assembly.

Isolation of MV1 is well established and the typical density of MV1 is around 1.02 g/ml (Collas and Poccia, 1996). On an MV1-separating gradient, a PLCγ/Ran-positive fraction was isolated in the first fraction, corresponding to the density of MV1 (Figure 3.6-B: fraction 1). On a velocity gradient which separates cellular components by their size, the PLCγ signal was mainly found in low density fractions, within the range of 1.02 g/ml to 1.04 g/ml (Figure 3.10). Nevertheless, these fractions were isolated inconsistently thus further investigation was difficult. If MV1-like vesicles have an identical density to MV1, it would mean the population of MV1-like vesicles is extremely scarce and a fractionation method with higher recovery would be required.

It is also possible that MV1-like vesicles in mammalian somatic cells have a density different from sea urchin MV1. PLCγ/Ran-positive fractions were separated from the ER and the Golgi on an MV1-separating gradient, in a density between 1.06 g/ml and 1.08 g/ml (Figure 3.6: fractions 5 – 7). Again, the yield of these fractions was low. The Optiprep gradient could not separate any PLCγ/Ran-positive cellular components from other organelles, probably because the gradient has a narrower range of density. Also, cells were visually less homogenised when using a 25G syringe needle (Figure 3.8). The velocity gradient gave a clue regarding the size of MV1-like vesicle. Since the PLCγ-positive signal was detected in the immature secretory granules (ISGs) region of the gradient (Figure 3.10: fraction 5), it is expected that MV1-like vesicles would have comparable sizes. ISGs have a mean diameter of 80 nm measured by morphometric analysis and more precisely the ISGs fraction contains vesicles with diameters ranged from 40 nm to 140 nm (Tooze *et al.*, 1991). Thus, MV1-like vesicles may have similar diameters.

In all of the gradients used, PLCγ/Ran-positive signals were rarely separated from the early and late endosomes. It would mean that MV1-like vesicles have similar density and size as the endosomes. Alternatively, growth factor stimulation could cause accumulation of PLCγ in endosomes (Grimes *et al.*, 1996). Therefore, it is also possible that an endosomal population with recruited PLCγ was isolated and detected instead of MV1-like vesicles, or in those fractions a mixture of both could co-exist. To test this idea, the fractionation of serum-starved cells could be envisioned.

3.5.2 Possible improvements in isolating of MV1-like vesicles and alternatives

Density gradient separation is limited by the physical property of cellular compartments and the mixing of membranes after homogenisation. The purity of separated fractions depends on many factors such as the homogenisation conditions, the cell line and its culture conditions. MV1-like vesicles can be mitosis-specific components and in this case their abundance can be maximised by cell synchronisation. Although nocodazole was shown to inhibit NE assembly *in vitro* (Vaillant and Paulin-Levasseur, 2008), other synchronisation agents with an alternative mechanism of action may not have such drawback. For instance, hydroxyurea blocks cells at G1/S phase by inhibiting ribonucleotide reductase (Rosner *et al.*, 2013). Extended incubation with hydroxyurea followed by washing may improve the yield of mitotic cells. In parallel, maturating-promoting factor (MPF) that promotes mitosis could be added to the G1/S blocked cells to guarantee the cells enter mitosis simultaneously (Lohka *et al.*, 1988).

Although MV1 is isolated from the fertilised eggs of echinoderms without strict inhibition of protein phosphorylation/dephosphorlation, MV1-like vesicles may be subjected to these protein modifications. Hence, prevention of these may assure MV1-like vesicles to be in their native stage. Addition of kinase and phosphatase inhibitors may increase the chance to obtain MV1-like vesicles. Similarly, addition of redox inhibitors would serve the same purpose. Furthermore, MV1-like vesicles may have the ability to fuse with membrane components such as the exocytotic vesicles. Therefore, addition of membrane fusion inhibitors such as TAT-NSF (a polypeptide that inhibits the N-ethylmaleimide-sensitive fusion proteins) and other similar inhibitors may improve the isolation of MV1-like vesicles (Morrell *et al.*, 2005).

In terms of gradient analysis, a comprehensive proteomic analysis of MV1 would provide information regarding "better" markers so that more references could be available for isolation and characterisation of MV1 analogous components. Indeed, an ideal subcellular fractionation is usually coupled with immunoisolation. An affinity column would aid the isolation of PLC-enriched fractions. In humans, there are 15 PLC isozymes divided into six subgroups (Vines, 2012). Fusogenic vesicles may be enriched in PLC activity but we do not know which isozyme(s) corresponds to the NE fusion mechanism in somatic cells. Nevertheless, for PLCγ there are only two isoforms and those can be the initial candidates to be studied.

Subcellular fractionation involves tedious work. A complementary approach would be to verify the presence of fusogenic vesicles by morphological and compositional analysis *in vivo*. Morphological analysis can be combined with the use of immunochemistry or engineered molecular tags to identify the cellular structures with lipid-protein profile similar to MV1 or other vesicles involved in NE assembly.

3.5.3 The characteristics of mammalian fusogenic vesicles – another perspective

A non-ER, non-Golgi, low density fraction with PLCγ and Ran enrichment was the target of our isolation. From the results of the density gradient fractionations, however, PLCγ and Ran were mainly detected in medium density fractions (from 1.06 g/ml to 1.12 g/ml in the MV1-separating gradient, and from 1.06 g/ml to 1.08 g/ml in the Optriprep gradient). The intense PLCγ and Ran signals were always associated with the signals of ER, Golgi, early and late endosomes. Therefore, it is possible that PLCγ would be more evenly distributed in mammalian cells than in sea urchin eggs.

The above observation may actually reflect the true identity of fusogenic vesicles in mammalian cells. In MV1 isolation, a population of vesicles known as MV2 has a density from 1.04 g/ml to 1.08 g/ml (Collas and Poccia, 1996). MV2 can be further separated into MV2α or MV2β, in which MV2α is enriched in a Golgi enzyme and MV2β is enriched in an ER enzyme (Collas and Poccia, 1996). Moreover, MV2α exhibited a comparable binding profile as MV1 to the chromatin and is required for fusion of MV1 to MV2β to form the NE. Since the PLCγ enrichment in mammalian cells shared more similarities to MV2 vesicles, it is reasonable to infer that fusogenic vesicles in mammalian cells are enriched in PLCγ and Ran and have similar densities as MV2. These fusogenic vesicles may also contain protein markers enriched in MV2.

3.6 **Summary**

Several biochemical gradients were applied to isolate MV1-like vesicles from mammalian cells. Although some isolated fractions shared properties with MV1, they were only sporadically isolated and their yield was low. In parallel, enrichment of PLCγ was mainly found in medium density fractions, suggesting that fusogenic vesicles in somatic mammalian cells may have distinct features compared to MV1 and possibly share some properties with MV2. By gradient analysis only we were not able to conclude that our isolated fractions were MV1-like vesicles, therefore a complementary cell biology approach was adopted. The following chapter will describe the localisation of phosphoinositides enriched in MV1. By probing these lipids in mammalian cells, we expect to identify cellular compartments where fusogenic vesicles reside.

Chapter 4 Localisation of PtdIns(3,4,5)P_3 in mammalian cells

4.1 Introduction

Phosphoinositides are mostly trace molecules in cells. Nevertheless, phosphoinositides are biologically important because many of them function as secondary messengers in cell signalling pathways. For instance, PtdIns(3,4,5)P_3 is required for AKT activation (Alessi and Cohen, 1998) and PtdIns(4,5)P_2 is required for GTPase activity of the trafficking protein Arf (Randazzo and Kahn, 1994). Phosphoinositides are unique phospholipids because their inositol headgroup can be reversibly phosphorylated on three positions, such capacity results in a diverse population of signalling molecules recognised by various protein effectors. Moreover, phosphoinositide-modifying enzymes play a regulatory role in membrane fusion events. For instance, PI3 kinase activity is required for the fusion of the endosomes (De Camilli *et al.*, 1996, Li *et al.*, 1995).

The structural role of phosphoinositides in the membrane has usually been overlooked. The size difference between the fatty acid tails and the headgroup of phosphoinositides gives rise to the various spontaneous curvatures. The localisation of phospholipids in a membrane compartment and their asymmetric distribution across a membrane bilayer will determine local membrane curvature which in turn influences the organelle shape and related function (Larijani and Poccia, 2012, Larijani *et al.*, 2014). *In vitro* data suggests a role for phosphoinositides in NE assembly. The fusogenic vesicles that initiate NE assembly (MV1) are enriched in the phosphoinositides PtdIns(4,5)P_2 and PtdIns(3,4,5)P_3 (Byrne *et al.*, 2007). PtdIns(4,5)P_2 can be hydrolysed to DAG which is necessary for membrane fusion. The role of DAG in mammalian NE assembly will be discussed in Chapter 5. This chapter investigates the localisation of PtdIns(3,4,5)P_3 in mammalian cells.

While MV1 has been shown as a compartment in echinoderms (Byrne *et al.*, 2007, Byrne *et al.*, 2014), the existence of similar vesicular NE precursors in mammalian cells has yet to be demonstrated. We predict MV1-like vesicles exist and function as NE precursors in mammalian NE assembly. MV1-like vesicles will have a similar lipid-protein profile as MV1, and therefore will likewise be enriched in PtdIns(4,5)P_2 and PtdIns(3,4,5)P_3.

To investigate the presence of endomembrane-PtdIns(3,4,5)P_3 in mammalian cells, we used the PtdIns(3,4,5)P_3-binding PH domain of GRP1 (GRP1^{PH}). GRP1^{PH} was fused to miniSOG, a novel tag that allows EM visualisation, in order to identify PtdIns(3,4,5)P_3-enriched vesicles at high resolution.

4.2 Investigating phosphoinositides localisation by imaging

The localisation of phosphoinositides to subcellular compartments has typically been determined by lipid-binding domains fused to fluorescent proteins. Recently quantum dot-tagged lipid-binding domains have been used to visualise intracellular phosphoinositides (Irino *et al.*, 2012). Although such imaging approaches are not quantitative, and phosphoinositides detection is limited by the specificity of the tools available, it allows the validation of phosphoinositides localisation by co-labelling cells with organelle markers. As such this was the initial approach tested in this study.

4.2.1 The choice of PtdIns(3,4,5)P_3-binding domains

While phosphoinositide synthesis has been shown to occur specifically at the cytoplasmic leaflet of the ER and to a lesser extent at the Golgi (Fagone and Jackowski, 2009, Vidugiriene and Menon, 1993), the localisation of PtdIns(3,4,5)P_3 to endomembranes has been rarely reported. Table 4.1 lists the cellular localisation of several commonly used PtdIns(3,4,5)P_3 reporters. A recombinant probe was used by Lindsay *et al.* to detect PtdIns(3,4,5)P_3 whereas the rest of the studies used transient transfection to detect PtdIns(3,4,5)P_3. Apart from the GRP1^{PH} domain, all other PH domains merely localised at the plasma membrane (see Table 4.1).

The choice of lipid-binding domain, as a transfection probe, is very important. It is acknowledged that PH domains with a strong binding affinity can affect lipid turnover and therefore result in the sequestering of the target lipid in an exclusive compartment This is known as the "masking" effect (Balla *et al.*, 2000). When the binding affinity of a lipid probe is too strong, the target lipid cannot dissociate from the probe easily. The cell will sense a lack of lipids in the required compartment and may draw the target lipid from other compartments, resulting in an exclusive localisation of the probe. Table 4.2 shows the binding affinity of some commonly used PtdIns(3,4,5)P_3-binding

PH domains. Among them GRP1^{PH} has a relatively low binding affinity and this may explain why GRP1^{PH} can detect PtdIns(3,4,5)P_3 in endomembranes whereas other PH domains mainly localise at the plasma membrane. Moreover, endomembrane-PtdIns(3,4,5)P_3 was detected by Lindsay *et al.* (2006) at the EM level using a GST-GRP1^{PH} recombinant probe and immunogold labelling, although no corresponding light microscopy images were shown.

In addition to its reported endomembrane localisation, GRP1^{PH} has a high selectivity for PtdIns(3,4,5)P_3. GRP1^{PH} binds to PtdIns(3,4,5)P_3 with a 650-fold higher affinity relative to PtdIns(4,5)P_2 (Klarlund *et al.*, 2000). Therefore, even though it has a relatively low binding affinity compared to other PH domains it is still a useful tool to target PtdIns(3,4,5)P_3. We constructed several GRP1^{PH} probes to target endomembrane-PtdIns(3,4,5)P_3. These probes were fused with various tags necessary for different detection methods (Table 4.3).

Table 4.1 PH domains used for detecting PtdIns(3,4,5)P_3 in live or fixed cells

Domain	Localisation	References
AKT^{PH}	Plasma membrane	(Watton and Downward, 1999)
ARNO^{PH}	Plasma membrane	(Venkateswarlu *et al.*, 1998b)
BTK^{PH}	Plasma membrane	(Varnai *et al.*, 1999)
GRP1^{PH}	Plasma membrane, ER, NE, inner mitochondrial membrane	(Lindsay *et al.*, 2006, Venkateswarlu *et al.*, 1998a)
PDK1^{PH}	Plasma membrane	(Komander *et al.*, 2004)

Table 4.2 PtdIns(3,4,5)P_3-binding affinity of different PH domains

Domain	K_D (nM)	Relative affinity	References
AKT^{PH}	0.4 – 6.4	High	(Rong *et al.*, 2001)
ARNO^{PH}	70	Low	(Venkateswarlu *et al.*, 1998b)
BTK^{PH}	40 – 100	Low	(Saito *et al.*, 2001, Baraldi *et al.*, 1999)
GRP1^{PH}	50 – 140	Low	(Klarlund *et al.*, 2000, Corbin *et al.*, 2004)
PDK1^{PH}	0.2 – 4	High	(Komander *et al.*, 2004, Currie *et al.*, 1999, Ziemba *et al.*, 2013)

Table 4.3 GRP1^{PH} probes used in this study

Probe (N' – C')	GRP1^{PH} genotype	Detection method	Resolution
GFP-GRP1^{PH}	WT	Transfection	LM
GFP-GRP1^{PH}.K273A	Non-binding mutant	Transfection	LM
GST-GRP1^{PH}	WT	Recombinant probe	LM
GST-GFP-GRP1^{PH}-tSOG	WT	Transfection, recombinant probe	LM & EM
GST-GFP-GRP1^{PH}.K273A-tSOG	Non-binding mutant	Transfection, recombinant probe	LM & EM
GST-GFP-GRP1^{PH}.R284A-tSOG	Non-binding mutant	Transfection, recombinant probe	LM & EM
GST-GFP-GRP1^{PH}.K273A/R284A-tSOG	Non-binding mutant	Transfection, recombinant probe	LM & EM

tSOG = tandem miniSOG domains; LM = light microscopy; EM = electron microscopy

4.3 Detecting PtdIns(3,4,5)P_3 by transient transfection

As described above, transfection probes with a strong binding affinity may sequester target lipid in an exclusive compartment. Despite this limitation, endomembrane-PtdIns(3,4,5)P_3 has been visualised in PC12 and NIH3T3 cells using GRP1^{PH} transfection probes (Gray *et al.*, 1999, Venkateswarlu *et al.*, 1998a). Hence, we tested the usefulness of chimeric GRP1^{PH} in detecting PtdIns(3,4,5)P_3 in our cell lines.

GRP1^{PH} and its non-PtdIns(3,4,5)P_3-binding mutant were conjugated to GFP in order to detect endomembrane-PtdIns(3,4,5)P_3 (Figure 4.1-A). Figure 4.1-B indicates that the GFP-tagged GRP1^{PH} correctly expressed in mammalian cells without GFP cleavage. Figure 4.1-C shows the localisation of GFP-GRP1^{PH} in live HeLa and COS7 cells under basal conditions. GFP-GRP1^{PH} localised at the plasma membrane (white arrows) and also to endomembranes of high expressing cells (green arrows). On the other hand, GFP-GRP1^{PH}.K273A, a non-PtdIns(3,4,5)P_3-binding mutant, did not localise at the plasma membrane except in some very high expressing cells. An obvious nuclear localisation of GRP1^{PH} transfection probe was observed. This had been reported previously by Venkateswarlu *et al.* who had suggested that its nuclear localisation was due to free entry of the probe because of its small molecular size. However, such observation might also suggest some unknown nuclear protein-binding sites of GRP1^{PH}.

GFP-GRP1^{PH} has been shown translocated to the plasma membrane upon NGF and EGF stimulation in PC12 cells (Venkateswarlu *et al.*, 1998a). When stimulated with EGF, GFP-GRP1^{PH} displayed an explicit plasma membrane localisation (white arrows) in HeLa cells and also translocated to endomembranes (green arrows) that resemble the ER (Figure 4.2, upper panels). The translocation of GRP1^{PH} was time-dependent, being the strongest after 30 min of EGF treatment and weaker at earlier time-points. In contrast, the K273A mutant did not translocate to the plasma membrane and endomembranes except after 30 min of EGF treatment (Figure 4.2, lower panels). In summary, the GRP1^{PH} transfection probe is PtdIns(3,4,5)P_3-specific and able to target endomembrane-PtdIns(3,4,5)P_3 in both basal and stimulated mammalian cells.

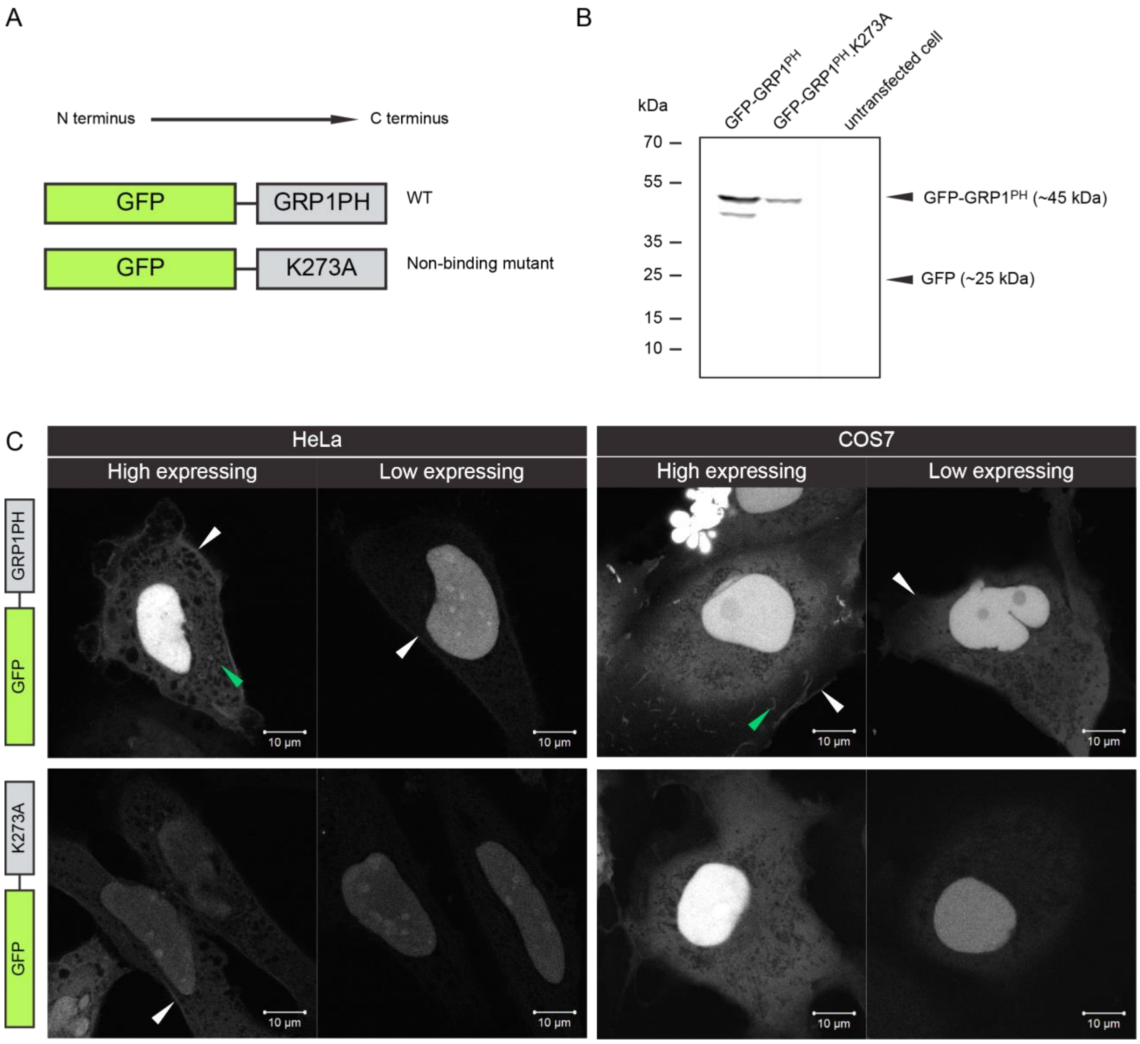

Figure 4.1 **GFP-GRP1^{PH} is localised to the plasma membrane and endomembranes of cells under basal conditions**

(A) Schematics of GRP1^{PH} constructs tagged with GFP; length of the domains is in scale with the number of base pairs. GRP1^{PH}.K273A is an established non-PtdIns(3,4,5)P$_3$-binding point mutation (Klarlund *et al.*, 2000). (B) HeLa cells were transfected with 250 ng WT or mutant GRP1^{PH} probe. Lysates of the transfected cells were subjected to Western blot analysis. The GRP1^{PH} probes were correctly expressed in the transfected cells, as indicated by the bands of the predicted size (45 kDa). There was no cleavage of GFP from the constructs, indicated by the absence of a corresponding band at 25 kDa. (C) Live confocal images of HeLa and COS7 cells transfected with 250 ng GFP-GRP1^{PH} or GRP1^{PH}.K273A for 16 h. Plasma membrane localisation (white arrows) of GFP-GRP1^{PH} was detected in both high and low expressing cells. GFP-GRP1^{PH} also displayed an ER-like localisation (green arrows) in high expressing cells. GRP1^{PH}.K273A did not localise at the plasma membrane except in some high expressing cells, of which an increased intracellular fluorescence was also observed. Nuclear fluorescence of GFP-GRP1^{PH} was observed in all transfected cells, with uncharacterised mechanism. Scale bar, 10 µm.

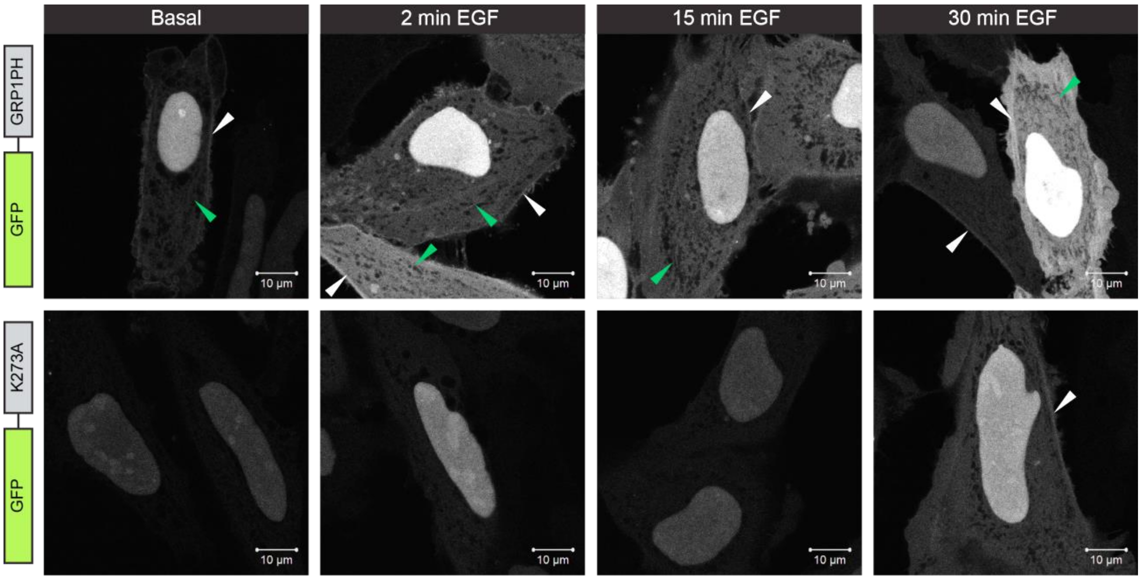

Figure 4.2 Translocation of GFP-GRP1^{PH} to the plasma membrane in response to EGF stimulation

HeLa cells were transfected with 250 ng GFP-GRP1^{PH} or GFP-GRP1^{PH}.K273A for 16 h and stimulated with 100 ng/ml EGF for 2, 15 and 30 mins. Stimulated cells were fixed with 4% PFA and imaged by confocal microscopy. WT and mutant GRP1^{PH} transfected cells responded differently to EGF stimulation. An explicit plasma membrane (white arrows) and endomembranes (green arrows) translocation were observed in GFP-GRP1^{PH} transfected cells in all time-courses, and stimulated cells showed the strongest cytoplasmic fluorescence after 30 min of EGF treatment. The translocation of GFP-GRP1^{PH}.K273A to the plasma membrane was not observed except after 30 min of EGF treatment, suggesting that the non-binding property of K273A mutation is not absolute *in vivo*. Scale bar, 10 µm.

4.4 Detecting PtdIns(3,4,5)P_3 with a recombinant probe

GRP1^{PH} transfection probe localised at the plasma membrane and endomembranes in the above experiments. However, we could not rule out the possibility that the expression of the probe may affect phospholipid dynamics through signalling pathways. Hence, the localisation of a transfection probe might not necessarily represent the genuine distribution of the targeted phosphoinositide. For instance, we had demonstrated that PtdIns(4,5)P_2 was sequestered at the plasma membrane when transfected with the high affinity probe PLCδ1^{PH} whereas endomembrane-PtdIns(4,5)P_2 could only be detected by a PLCδ1^{PH} recombinant probe (Hobday, 2012). Therefore, to determine the *in situ* PtdIns(3,4,5)P_3 localisation, we took a complementary approach and developed a GST-GRP1^{PH} recombinant probe.

For a recombinant probe to enter a fixed cell, detergent is required to permeabilise the plasma membrane. Depending on their physical properties such as the critical micelle concentration and charge, detergents may extract the lipids of interest from membranes or affect the performance of lipid-binding dyes (Chapter 2 commentary). Saponin is a mild detergent commonly used in phospholipid studies (Goldenthal *et al.*, 1985). It forms complexes with cholesterol thus creating pores in the plasma membrane, allowing the entry of macromolecules (Francis *et al.*, 2002). However, the impact of saponin on membrane ultrastructure is usually neglected.

Figure 4.3 illustrates the dose-dependent effect of saponin on the ultrastructure of endomembranes. In both 0.1% and 0.5% saponin-treated cells, the matrices of the mitochondria displayed a "hollow" phenotype, indicated by the lack of electron density in those regions (red arrows). The outer membranes of the mitochondria were deformed showing a ruffle phenotype (red brackets). The deformations were more severe in the 0.5% saponin-treated cell. Although mitochondria were disrupted by saponin, the NE and other endomembranes remained intact in saponin-treated cells compared to the control cell. Despite the use of detergent is an inevitable step in the application of recombinant probes, the recombinant GST-GRP1^{PH} should give us the most reliable information about PtdIns(3,4,5)P_3 localisation in endomembrane compartments.

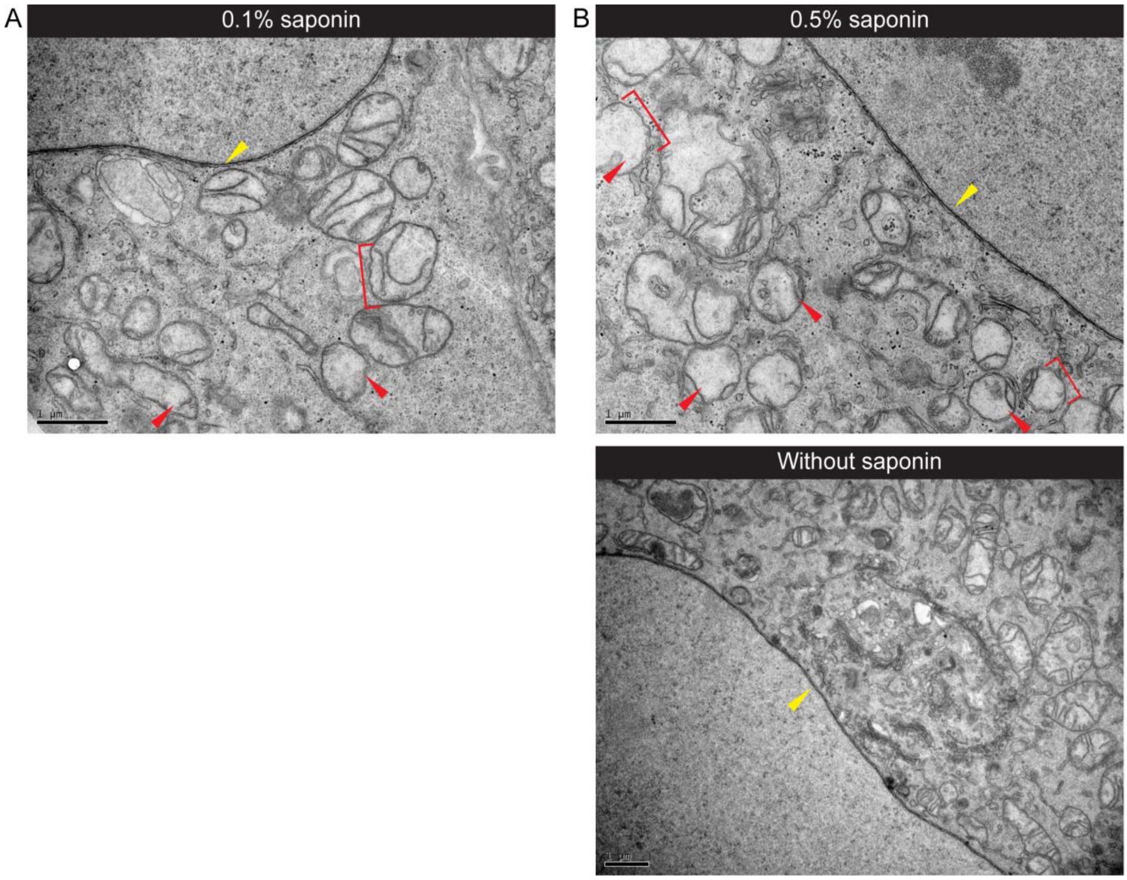

Figure 4.3 Saponin has a dose-dependent effect on membrane ultrastructure

HeLa cells were fixed with 4% PFA, permeabilised with 0.1% (A) or 0.5% (B) saponin, and prepared for electron microscopy. Cells were stained with 1% osmium tetraoxide, embedded in resin, serial sectioned and imaged by TEM. In both 0.1% and 0.5% saponin-treated cells, the matrix of some mitochondria was extracted and displayed a “hollow” phenotype (red arrows). Moreover, the outer membranes of some mitochondria were disrupted and ruffled in saponin-treated cells (red brackets) whereas in the control cell the outer membranes of mitochondria were smooth. The deformation of mitochondria was more severe in 0.5% saponin-treated cells than 0.1% saponin-treated cells. However, the NE (yellow arrows) and other endomembranes were intact in all saponin-treated cells compared to the control cell. Scale bar, 1 μm.

The GST-GRP1^{PH} recombinant probe was expressed and purified from bacteria using glutathione–sepharose beads (Figure 4.4-A). The PtdIns(3,4,5)P_3-binding specificity of purified GST-GRP1^{PH} was tested using a "lipid strip", a hydrophobic membrane that had been spotted with different lipids. Figure 4.4-B shows that GST-GRP1^{PH} only bound to PtdIns(3,4,5)P_3 on the strip. When GST-GRP1^{PH} was pre-incubated with Ins(1,3,4,5)P_4 (the soluble headgroup of PtdIns(3,4,5)P_3,) for an hour, the binding of GST-GRP1^{PH} to PtdIns(3,4,5)P_3 decreased. This indicates that our recombinant probe is PtdIns(3,4,5)P_3-specific.

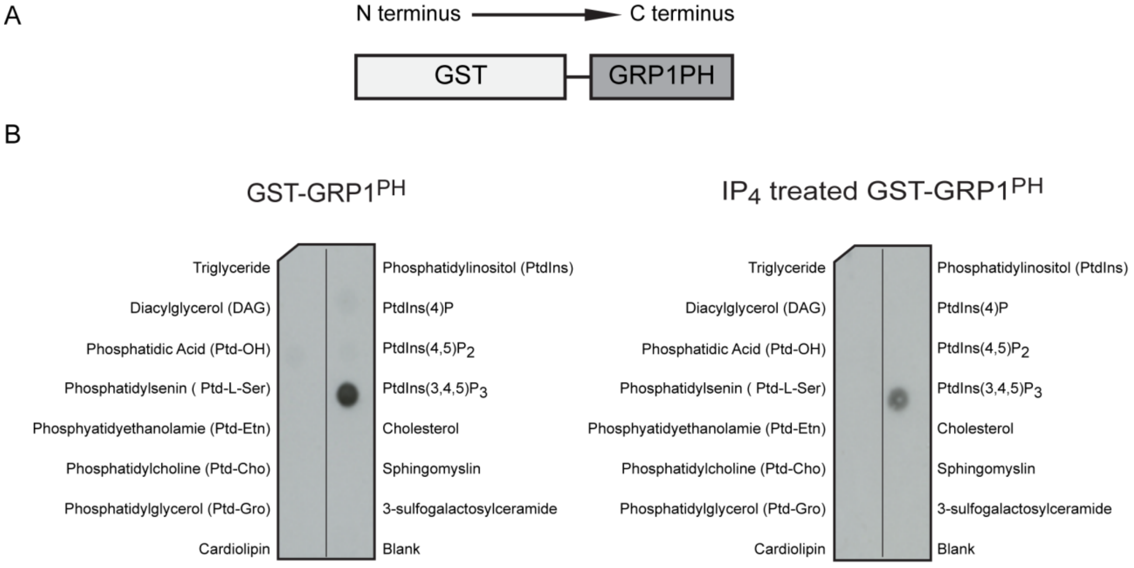

Figure 4.4 The GST-GRP1^{PH} recombinant probe is PtdIns(3,4,5)P_3-specific

(A) Schematic of the GST-GRP1^{PH} recombinant probe; length of the domains is in scale with the number of base pairs. GST-GRP1^{PH} was expressed and purified from *E. coli* DH5α, as described in Chapter 2. (B) The specificity of GST-GRP1^{PH} recombinant probe was analysed using a "lipid strip", a hydrophobic membrane spotted with different lipids. The lipid strip was blocked with 3% fatty acid-free BSA and incubated with either 0.5 µg/µl recombinant probe, or recombinant probe pre-incubated for 1 h with a 10x molar excess of Ins(1,3,4,5)P_4. This strip was subsequently incubated with an anti-GST antibody followed by a HRP-conjugated anti-mouse secondary antibody, treated with ECL and exposed to photographic film. GST-GRP1^{PH} binding to PtdIns(3,4,5)P_3 was diminished in the presence of Ins(1,3,4,5)P4. GST-GRP1^{PH} was obtained from Nick Leslie's group (University of Dundee) and the membrane strip experiment was performed by Marta Gutierrez (Unidad de Biofisica).

When applied to fixed and permeabilised cells, the recombinant GST-GRP1^{PH} localised at the plasma membrane and endomembranes; the major fluorescent signal was detected in the endomembranes and to a lesser extent in the plasma membrane (Figure 4.5). PtdIns(3,4,5)P$_3$ was detected in the perinuclear region that resembles the ER (green arrow) and Golgi (red arrow), consistent with the phosphoinositide synthesis in these compartments. Interestingly, there was also a clear NE localisation of GST-GRP1^{PH}, which had not been shown in any previous studies. When the cells were probed with GST-GRP1^{PH} pre-incubated with Ins(1,3,4,5)P$_4$, the organelles referred to above were not labelled. Instead a punctate fluorescent signals was observed.

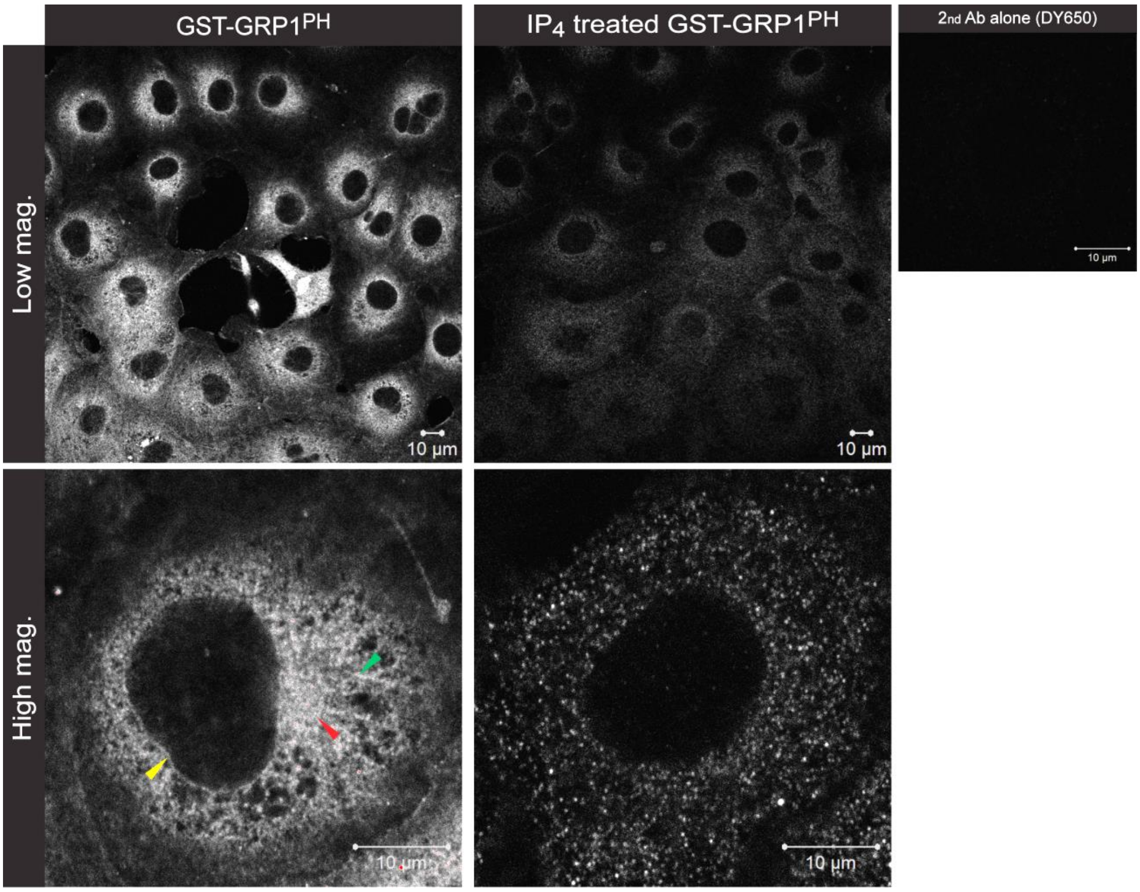

Figure 4.5 GST-GRP1^{PH} is localised to endomembranes that resemble the NE, ER and Golgi
COS7 cells were fixed with 4% PFA, permeabilised with 0.5% saponin and incubated with GST-GRP1^{PH} or GST-GRP1^{PH} pre-incubated with Ins(1,3,4,5)P$_4$ for 1 h at room temperature. The cells were subsequently incubated with a DY650-conjugated anti-GST antibody before confocal imaging. GST-GRP1^{PH} localised to endomembranes that resemble the NE (yellow arrow), ER network (green arrow) and Golgi (red arrow). The probe also localised at the plasma membrane to a lesser extent. Ins(1,3,4,5)P$_4$ pre-incubated GST-GRP1^{PH} displayed a diminished punctate fluorescent signal throughout the cell. Scale bar, 10 µm.

To confirm the localisation of GST-GRP1^{PH}, and therefore of PtdIns(3,4,5)P$_3$ to specific organelles, immunofluorescence experiments were performed on cells labelled with GST-GRP1^{PH}, in addition to markers of the ER and NE (Figure 4.6). The global Pearson's correlation coefficient (PCC) suggested that localisation of GST-GRP1^{PH} had a low positive correlation with the tested endomembrane markers. Although a perfect colocalisation between PtdIns(3,4,5)P$_3$ and the tested markers was not observed, the fact that GST-GRP1^{PH}, MAb414 and calreticulin had similar NE localisation suggested an association or presence of PtdIns(3,4,5)P$_3$ at the NE (Figure 4.6-A &B, yellow arrows). Due to time constraints, co-localisation experiments between GST-GRP1^{PH} and Golgi-specific markers were not performed.

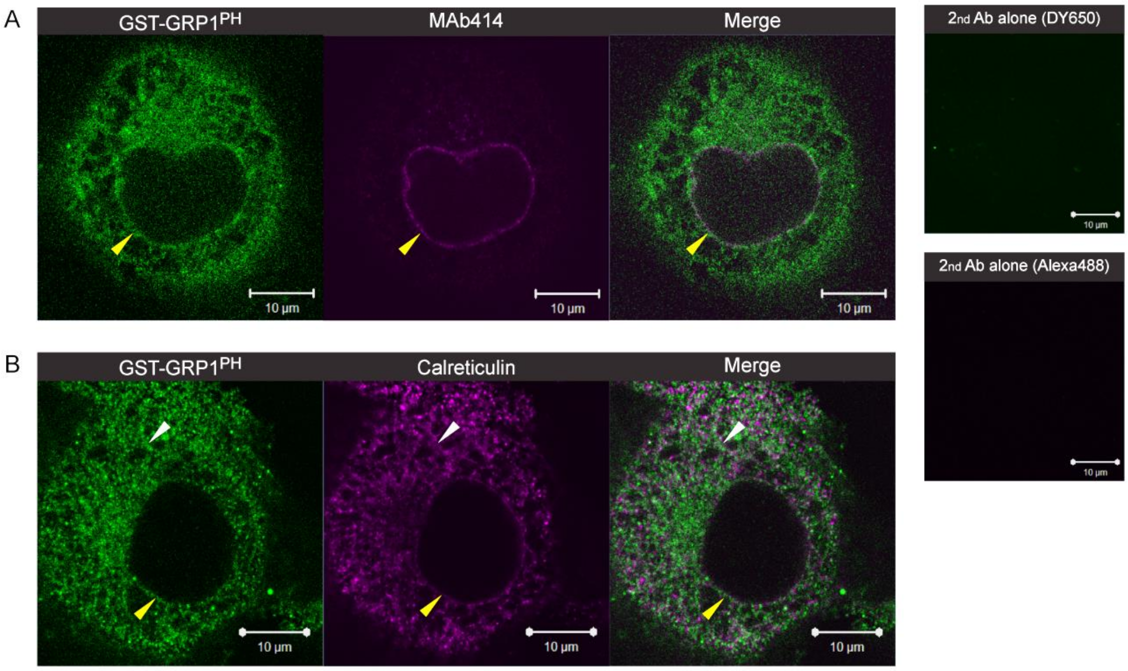

Figure 4.6 GST-GRP1^{PH} partially co-localises with ER and NE markers

COS7 cells were probed with GST-GRP1^{PH} (green) as described in Figure 4.5. In parallel, the cells were probed with either a marker for (A) the NE (MAb414) or (B) ER (calreticulin), imaged using an Alexa 488-conjugated secondary antibody (magenta). Both the localisation of MAb414 and GST-GRP1^{PH} displayed a circular fluorescence around the nucleus (yellow arrows). Similarly, localisation of GST-GRP1^{PH} resembled that of calreticulin at the NE (yellow arrows) but to a lesser extent at the ER network (white arrow). The degree of colocalisation between GST-GRP1^{PH} and the endomembrane markers was analysed by the image analysis software Volocity 6.3 (PerkinElmer). The global Pearson's correlation coefficient (PCC) of GST-GRP1^{PH} localisation relative to that of MAb414 and calreticulin are 0.38 ± 0.05 and 0.52 ± 0.03 respectively, averaged from n = 5 region of interest. Scale bar, 10 µm.

4.5 Identification of the PtdIns(3,4,5)P_3-generating enzyme in the endomembranes

Class I PI3 kinases are soluble proteins which exclusively produce PtdIns(3,4,5)P_3, upon cell stimulation. Class IA PI3 kinases (PI3KCA) are thought to function mainly at the plasma membrane but they have also been reported associated with the NE and with vesicles (Katso *et al.*, 2001, Rameh and Cantley, 1999). This observation is reminiscent of the localisation of PtdIns(3,4,5)P_3 targeted by GRP1^{PH}. Moreover, it has been shown that the plasma membrane translocation of GRP1^{PH} requires PI3 kinase activity, since the translocation is inhibited by LY294002 and by deletion of the p85 regulatory domain of PI3 kinases (Venkateswarlu *et al.*, 1998a). The presence of PI3KCA on endomembranes would strongly support the data above, demonstrating the presence of an endomembrane-PtdIns(3,4,5)P_3 pool. Therefore, we analysed the localisation of PI3KCA using immunofluorescence.

Figure 4.7-B – E shows the localisation of the regulatory p85α and catalytic p110α and p110β subunits of PI3KCA in basal HeLa and COS7 cells, detected by indirect immunofluorescence. p85α displayed a NE- (yellow arrows), Golgi- and ER- like localisation, plus a vesicular localisation throughout the cytoplasm of most cells. In some cells, a perceived absence of Golgi localisation (red arrows) was observed. Moreover, there was no observable plasma membrane localisation of p85 under basal conditions. The catalytic subunits, p110α and p110β displayed a Golgi-like localisation (green arrows) as well as a vesicular localisation throughout the cytoplasm.

The p85 subunit has been found associated with clathrin-coated vesicles upon NGF (nerve growth factor) stimulation (Howe *et al.*, 2001). In our experiments, both the p85 regulatory subunit and the two catalytic subunits displayed vesicular fluorescence in cells in addition to their endomembrane localisation under basal conditions. Whether these membrane-associated PI3KCA are active under these conditions will require further investigation. However, this indicates a potential production of PtdIns(3,4,5)P_3 in vesicles and/or endomembranes.

In the echinoderm NE assembly assay, fusogenic vesicles MV1 are enriched in PtdIns(3,4,5)P3. To verify the presence of similar PtdIns(3,4,5)P3-enriched vesicles in mammalian cells, a probe that allows high resolution imaging is required.

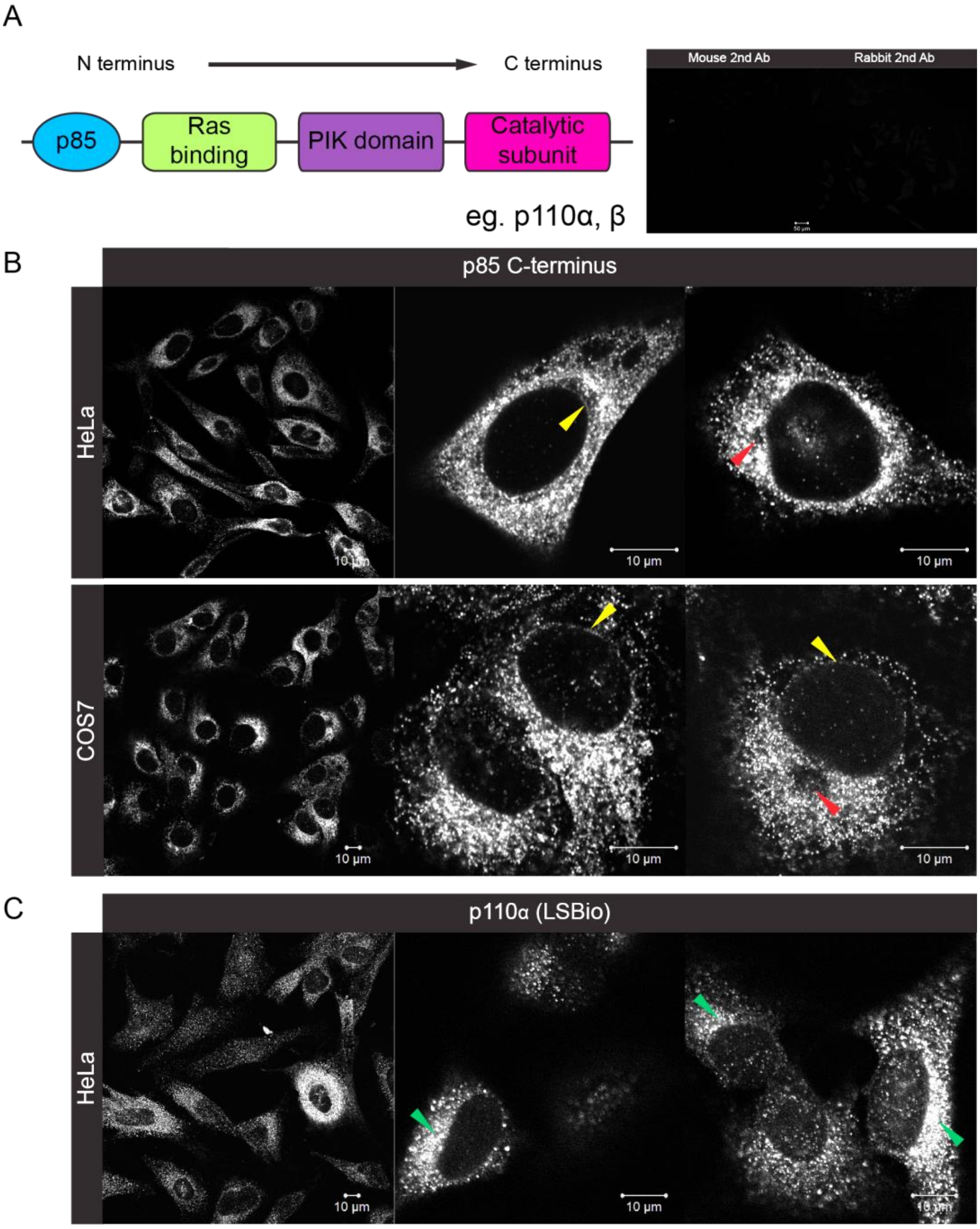

(Cont'd)

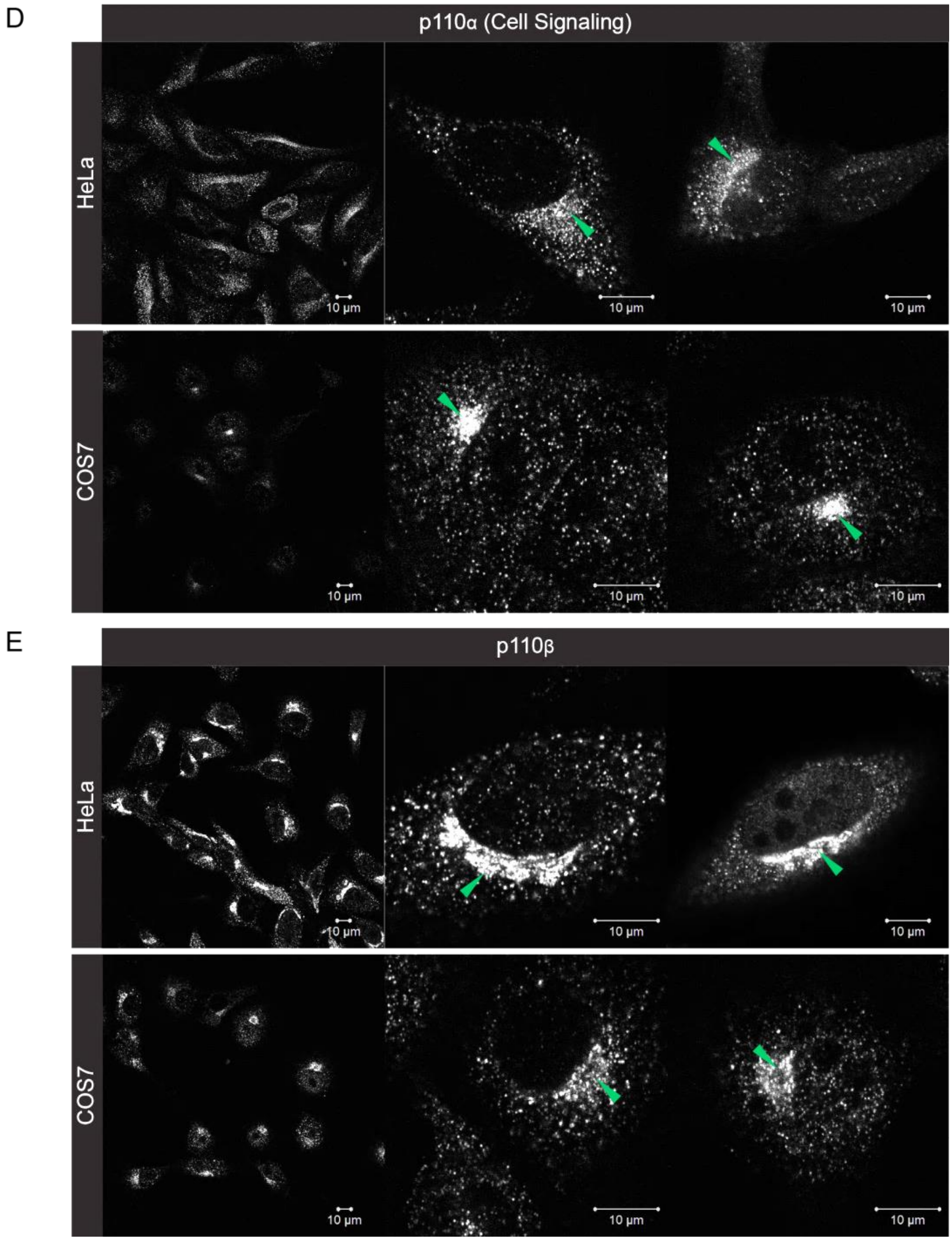

Figure 4.7 Class IA PI3 kinases is localised to endomembranes of mammalian cells

(A) Schematic representation of PI3KCA, which generates PtdIns(3,4,5)P$_3$. PI3KCA localisation was detected by indirect-immunofluorescence, using antibodies against different domains of the enzyme. Mammalian cells were fixed with PFA, permeabilised with 0.5% saponin, incubated with the specified primary antibody followed by a fluorescently conjugated secondary antibody before confocal image acquisition (for details see Chapter 2). (B) In both COS7 and HeLa cells, p85 was localised to endomembranes that resemble the NE (yellow arrows), ER and Golgi. Vesicular fluorescence was detected throughout the cytoplasm. In some cells, a perceived absence of Golgi localisation (red arrows) was also noticed. (C – D) p110α and (E) p110β localised to endomembranes that resemble the Golgi (green arrows) in both cell lines. Similar to the p85 regulatory domain, both p110α and 110β showed a vesicular fluorescence throughout the cytoplasm. Scale bar, 10 µm.

4.6 Development of a PtdIns(3,4,5)P_3-specific probe for high resolution imaging

The previous sections demonstrated that both PtdIns(3,4,5)P_3 and PI3 kinase subunits were localised to vesicle-like structures in the cell cytoplasm. Thus, it is possible that these vesicles may represent an equivalent to MV1 in mammalian cells. To confirm this, vesicles would need to be imaged at high resolution. In order to image PtdIns(3,4,5)P_3-containing, putative MV1-like vesicles at the EM level, GRP1^{PH} was fused to a novel tag called miniSOG. The mechanism of how miniSOG generates EM contrast and its optimisation will be discussed in Chapter 6.

Figure 4.8-A illustrates the miniSOG-GRP1^{PH} probe GFP-GRP1^{PH}-tSOG. Although miniSOG is a fluorescent tag, its fluorescent signal is weak and rapidly bleached. Thus, GFP was added to the constructs. A GST tag was also cloned at the N-terminus of the construct so that the probe could be compatible for recombinant protein production. Since recombinant protein purification is a laborious and time consuming process, transient transfection with GFP-GRP1^{PH}-tSOG was used initially to target endomembrane-PtdIns(3,4,5)P_3. Western blot analysis indicated no cleavage of GFP from the constructs (data not shown). MiniSOG might affect the localisation of the PtdIns(3,4,5)P_3-binding domain. Before using the miniSOG-tagged probe for high resolution imaging, its correct localisation was analysed by confocal microscopy.

Under basal conditions, GFP-GRP1^{PH}-tSOG revealed a distinctive endomembrane localisation compared to GFP-GRP1^{PH} in cells (Figure 4.8-B). Since the nuclear localisation was absent, we hypothesised that it was due to the increase in molecular size of the probe. The molecular size of miniSOG-GRP1^{PH} (98 kDa) surpasses the threshold (~45-60 kDa) for passive diffusion of small molecules through the NPC (Lyman *et al.*, 2002). The endomembrane localisation of GFP-GRP1^{PH}-tSOG resembled that of GFP-GRP1^{PH}; a slightly enhanced fluorescence was also noticed in the peri-Golgi region of the cells. Interestingly, GFP-GRP1^{PH}-tSOG showed a NE localisation which resembled that revealed by the GST-GRP1^{PH} recombinant probe.

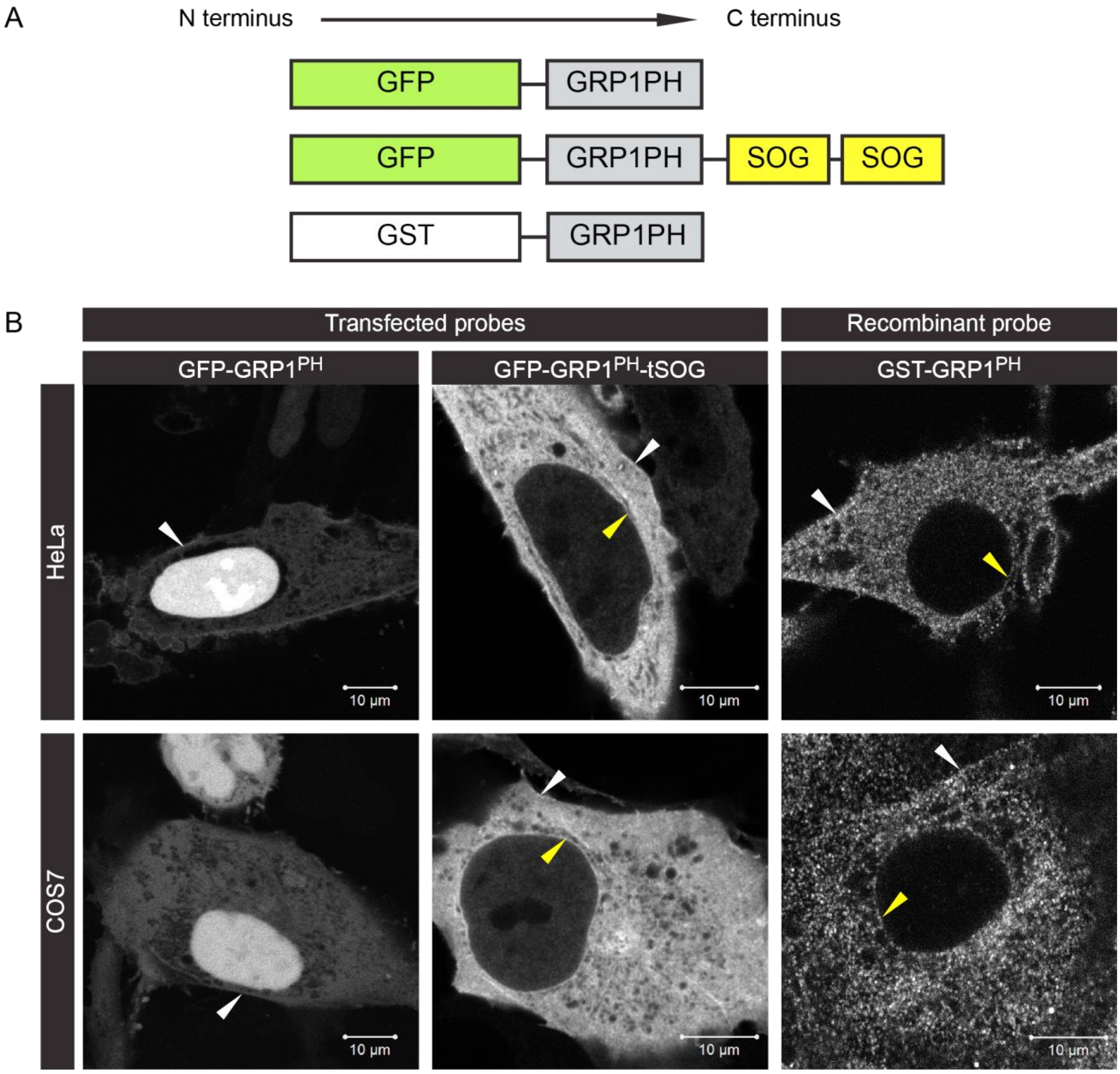

Figure 4.8 GFP-GRP1^{PH}-tSOG displays a distinctive localisation compared to GFP-GRP1^{PH}

(A) Schematics of GFP-GRP1^{PH}, GFP-GRP1^{PH}-tSOG transfected probes, and the GRP1^{PH} recombinant probe; length of the domains is in scale with the number of base pairs. GFP-GRP1^{PH}-tSOG also contains a GST proximal to the GFP (not shown). (B) PtdIns(3,4,5)P_3 in basal mammalian cells was labelled by transient transfection or recombinant protein probing. HeLa and COS7 cells were transfected with 500 ng GFP-GRP1^{PH} or GFP-GRP1^{PH}-tSOG for 16 h and imaged live. Alternatively, the cells were fixed with 4% PFA, permeabilised with 0.5% saponin and probed by GST-GRP1^{PH} as described in Figure 4.5. GFP-GRP1^{PH}-tSOG displayed both plasma membrane (white arrows) and endomembrane localisation. The plasma membrane localisation of GFP-GRP1^{PH}-tSOG resembled that of GFP-GRP1^{PH} and GST-GRP1^{PH}; the endomembrane localisation resembled that of GFP-GRP1^{PH}. In addition, GFP-GRP1^{PH}-tSOG localised at the NE (yellow arrows) like the GST-GRP1^{PH} recombinant probe. Scale bar, 10 µm.

To test whether the GFP-GRP1^{PH}-tSOG probe responded to growth factor stimulation (an indication of PtdIns(3,4,5)P_3-targeting), cells were stimulated with EGF. Upon EGF stimulation, translocation of GFP-GRP1^{PH}-tSOG to the plasma membrane and NE was observed (Figure 4.9). However, the increase in fluorescence at these compartments was not obvious. Further quantification will be required. In general, the NE (yellow arrows), ER (green arrows) and Golgi (red arrows) localisation of GFP-GRP1^{PH}-tSOG was more prominent in COS7 cells.

To confirm that GFP-GRP1^{PH}-tSOG co-localised with the organelles specified above, the cells were transfected with the GFP-GRP1^{PH}-tSOG probe, and subsequently labelled with specific markers for the NE, ER and Golgi (Figure 4.10). Calreiculin was used as a marker for the NE and ER. Both GFP-GRP1^{PH}-tSOG and calreticulin displayed a very similar NE localisation, a circle of fluorescence around the nucleus. GFP-GRP1^{PH}-tSOG also appeared in the proximity of the ER network labelled with calreticulin. The fluorescent signal of Golgi 97, a *trans*-Golgi marker, was detected in the *trans*- side of the Golgi-like localisation of GFP-GRP1^{PH}-tSOG. Together, these data suggested the presence of PtdIns(3,4,5)P_3 in the NE and *trans*-Golgi network.

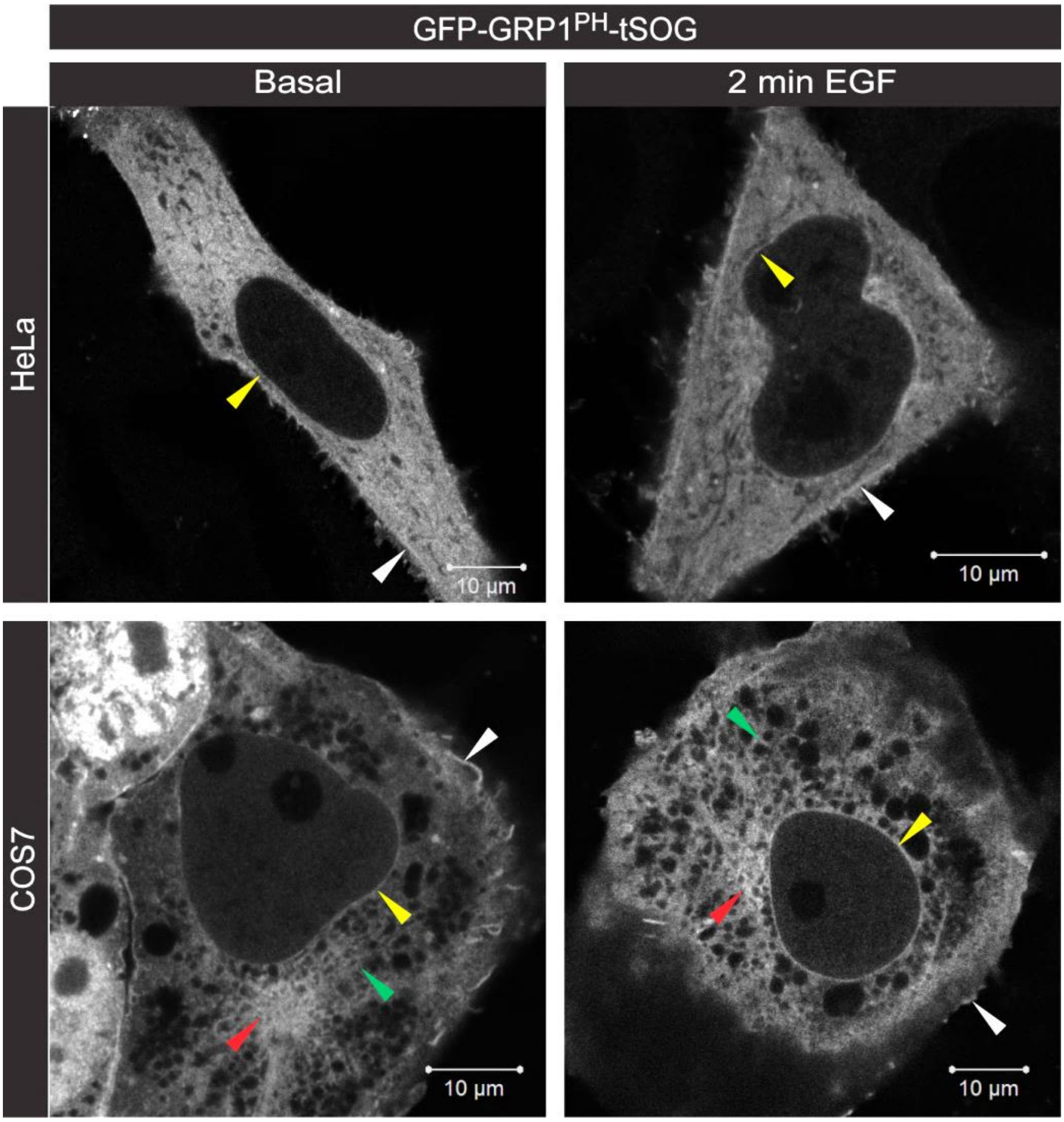

Figure 4.9 **GFP-GRP1^{PH}-tSOG translocates to the plasma membrane and endomembranes upon EGF stimulation**

HeLa and COS7 cells were transfected with GFP-GRP1^{PH}-tSOG for 16 h. The cells were either stimulated with EGF for 2 min or left without treatment prior to PFA fixation. The fixed cells were imaged by confocal microscopy. Under basal conditions, GFP-GRP1^{PH}-tSOG localised at the plasma membrane (white arrows) and endomembranes as shown in Figure 4.8. The endomembrane localisation resembled the NE (yellow arrows), ER (green arrows) and Golgi (red arrows) and was better visualised in COS7 cells. Upon EGF treatment, the plasma membrane and endomembrane localisation of GFP-GRP1^{PH}-tSOG appeared to have stronger signal but further quantification is required to confirm this. Scale bar, 10 µm.

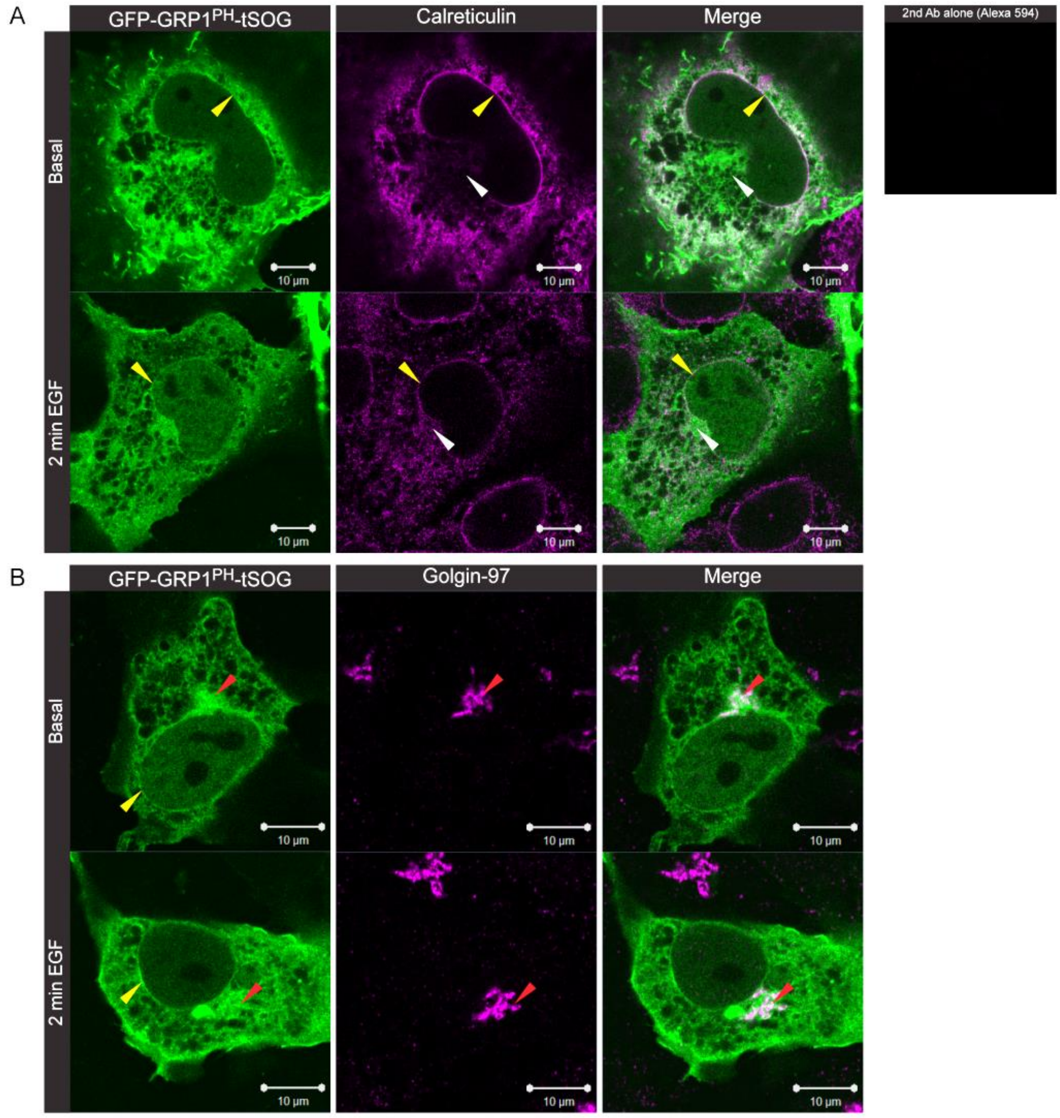

Figure 4.10 GFP-GRP1^{PH}-tSOG partially co-localises with specific organelle markers

COS7 cells were transfected with GFP-GRP1^{PH}-tSOG (green) for 16 h. The transfected cells were either stimulated with EGF for 2 min or untreated prior to PFA fixation. Fixed cells were permeabilised with 0.5% saponin for immunofluorescence. Permeabilised cells were incubated with primary antibodies against different organelles for 1 h followed by Alexa 594-conjugated secondary antibodies (magenta) for another hour before confocal image acquisition. (A) GFP-GRP1^{PH}-tSOG partially co-localisated with calereticulin at the visual level. In both basal and EGF stimulated cells, NE localisation of GFP-GRP1^{PH}-tSOG was similar to that of calreticulin (NE/ER marker), both of which displayed a circular fluorescence around the nucleus (yellow arrows). This indicates miniSOG-GRP1^{PH} targeted PtdIns(3,4,5)P_3 is present in the NE. However, the ER localisation of GFP-GRP1^{PH}-tSOG resembled that of calreticulin to a lesser extent. White arrows indicate the absence of calreticulin localisation to the Golgi of the cells. (B) Fluorescent signals of Golgin-97 (*trans*-Golgi marker) were detected within the Golgi-like localisation of GFP-GRP1^{PH}-tSOG in both basal and EGF simulated cells. This indicates the presence of PtdIns(3,4,5)P_3 in the *trans*-Golgi. Scale bar, 10 µm.

The specificity of miniSOG-GRP1^{PH} was tested in EGF stimulated cells. However, both GFP-GRP1^{PH}-tSOG and the non-PtdIns(3,4,5)P_3-binding K273A mutant (Figure 4.11-A) showed similar localisation at the plasma membrane and endomembranes (Figure 4.11-B). This observation was unexpected as in section 4.3 we demonstrated that the K273A mutant translocated to membranes only after 30 min of EGF stimulation. We suspected that the K273A mutation might not have abolished the PtdIns(3,4,5)P_3-binding completely, therefore we made the R284A mutant in the miniSOG-GRP1^{PH} probe known to almost completely abolish PtdIns(3,4,5)P_3-binding *in vitro* (Cronin *et al.*, 2004, Lumb and Sansom, 2012). A double mutant (K273A/R284A) was also constructed. Unfortunately, R284A and K273A/R284A mutants localised at the plasma membrane and endomembranes in both basal and stimulated cells, similar to the WT miniSOG-GRP1^{PH}, (Figure 4.11-C).

In summary, GFP-GRP1^{PH}-tSOG resembled GFP-GRP1^{PH} in terms of its plasma membrane and endomembrane localisation but it also localised at the NE like the GST-GRP1^{PH} recombinant probe. Further investigation of miniSOG-GRP1^{PH} is required in order to determine if the PtdIns(3,4,5)P_3 selectivity of the probes is disrupted during transient transfection.

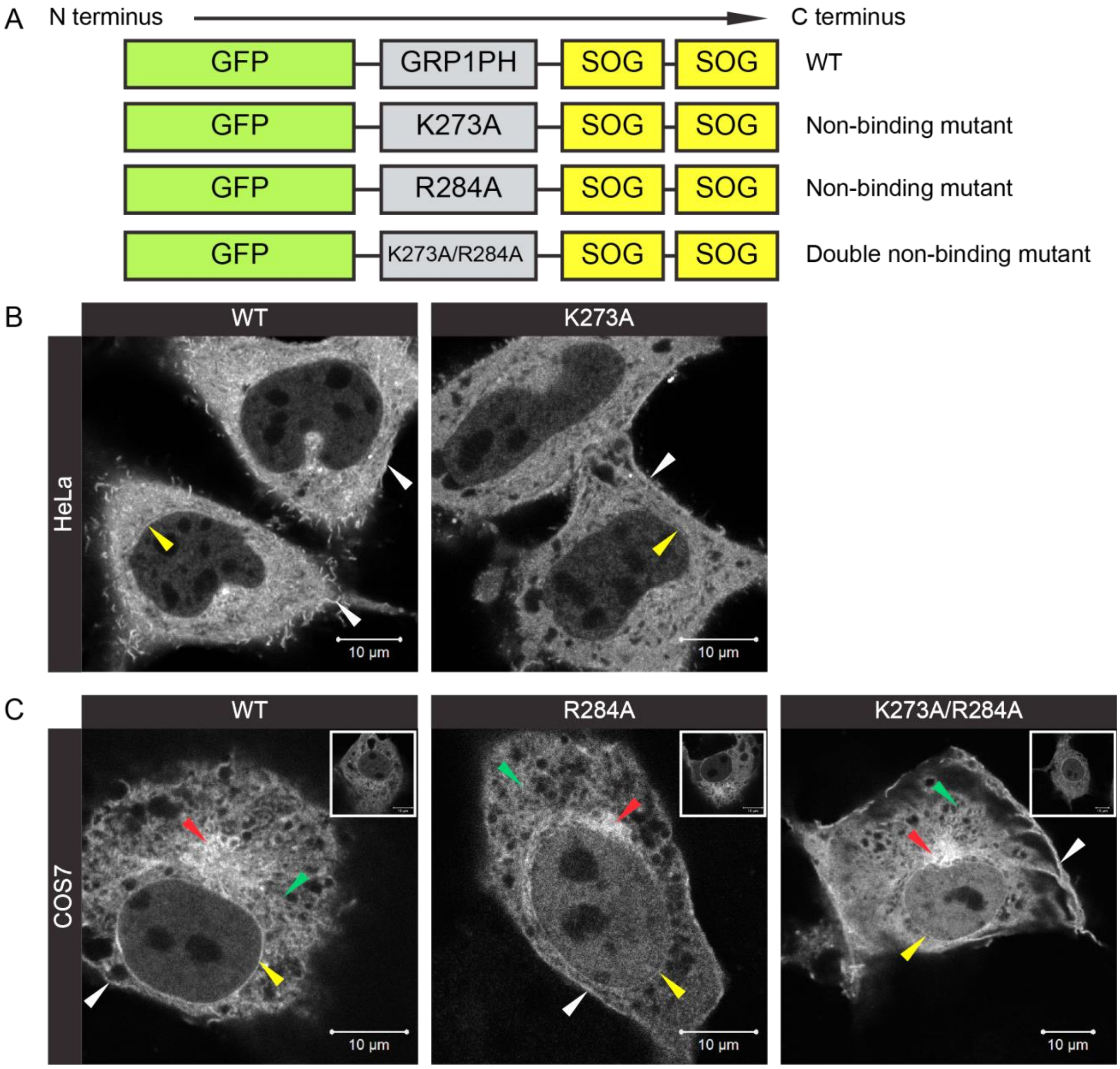

Figure 4.11 Non-PtdIns(3,4,5)P_3-binding miniSOG-GRP1^{PH} mutants localise similarly as the WT

(A) Schematic summary of miniSOG-GRP1^{PH} probes; length of the domains is in scale with the number of base pairs. Both GRP1^{PH}.K273A and GRP1^{PH}.R284A are non-PtdIns(3,4,5)P_3-binding mutants; GRP1^{PH}.K273A/R284A is a double non-binding mutant. The GST tag before the GFP in each probe is not shown in order to simplify the figure. (B) HeLa cells were transfected with WT or K273A miniSOG-GRP1^{PH} for 16 h. Transfected cells were stimulated with EGF for 2 min, fixed with 4% PFA and imaged by confocal microscopy. Both WT and K273A miniSOG-GRP1^{PH} localised at the plasma membrane (white arrows) and endomembranes. Yellow arrows indicate the NE localisation of the miniSOG-GRP1^{PH}. (C) Similarly, COS7 cells were transfected with WT and mutant miniSOG-GRP1^{PH} for 16 h, stimulated with EGF and fixed for confocal imaging. R284A and the double mutant localised in the plasma membrane (white arrows), NE (yellow arrows), ER (green arrows) and Golgi (red arrows) as did the WT miniSOG-GRP1^{PH}. Similar results were observed in basal COS7 cells (insets). Scale bar, 10 µm.

4.7 Discussion

4.7.1 Presence of PtdIns(3,4,5)P_3 in endomembranes

We hypothesised that MV1-like vesicles had a similar lipid profile as MV1, therefore enriched in PtdIns(4,5)P_2 and PtdIns(3,4,5)P_3. PtdIns(3,4,5)P_3 is a critical signalling molecule for various downstream targets (Wymann and Schneiter, 2008) and inhibition of PtdIns(3,4,5)P_3 production has been shown to prevent NE assembly *in vitro* (Larijani *et al.* (2001) and personal communication). Since MV1-like vesicles may be derived from endomembranes in mammals, we were particularly interested in demonstrating the presence of endomembrane-PtdIns(3,4,5)P_3. Endomembrane-PtdIns(3,4,5)P_3 is rarely reported because of the use of overexpressed reporters which affect the lipid dynamics after transfection. However, a reporter with lower binding affinity may solve this problem. Hence, $GRP1^{PH}$ was conjugated with various tags to detect PtdIns(3,4,5)P_3.

We tried to detect endomembrane-PtdIns(3,4,5)P_3 in mammalian cells by both transfection and recombinant probes. GFP-$GRP1^{PH}$ localised to endomembranes and at the plasma membrane of basal COS7 and HeLa cells (Figure 4.1). The K273A mutant of $GRP1^{PH}$ demonstrated that the localisation was specific to PtdIns(3,4,5)P_3 (Figure 4.2). $GRP1^{PH}$ has a relatively low binding affinity (high K_D) towards PtdIns(3,4,5)P_3 compared to other PtdIns(3,4,5)P_3 reporters such as $AKT1^{PH}$ and $PDK1^{PH}$. Therefore, this could mean that it has a relatively high dissociation constant (K_{off}), which results in faster exchange of molecules. The success in probing endomembrane-PtdIns(3,4,5)P_3 by $GRP1^{PH}$ suggested that this PH domain was able to bind PtdIns(3,4,5)P_3 but also had sufficient mobility not to be sequestered in an exclusive compartment, in contrast to other commonly used reporters.

PH domains from different proteins may localise differently. Human GFP-$GRP1^{PH}$ expressed homogenously in basal PC12 (rat) cells (Venkateswarlu *et al.*, 1998a) whereas murine $GRP1^{PH}$-GFP displayed distinctive endomembrane localisation in basal NIH3T3 (mouse) cells (Gray *et al.*, 1999). Interestingly, endomembrane-PtdIns(3,4,5)P_3 was detected by a murine $GFP1^{PH}$ in Lindsay *et al.* (2006) as well as in our study. Although the difference in expression of $GRP1^{PH}$ may be due to the choice of cell lines, investigators should also be aware of the potential differences in the binding affinity of orthologous proteins.

As mentioned before, the major drawback in delivering lipid-binding domains by transient transfection is the alteration of the lipid dynamics (Poccia and Larijani, 2009). Cells may compensate for the perceived depletion of PH domain-targeted lipids and synthesise additional lipids that affect the visualisation. To determine the *in situ* PtdIns(3,4,5)P_3 localisation, immunodetection is a better approach because it monitors a less disturbed lipid distribution. A monoclonal antibody was used to visualise PtdIns(3,4,5)P_3 in mammalian cells, but endomembrane-PtdIns(3,4,5)P_3 was not detected in basal cells (Chen *et al.*, 2002). Since GRP1^{PH} has a 650-fold selectivity for PtdIns(3,4,5)P_3 relative to PtdIns(4,5)P_2 (Klarlund *et al.*, 2000) whereas the anti-PtdIns(3,4,5)P_3 antibody has only a 100-fold selectivity for PtdIns(3,4,5)P_3 relative to other phosphoinositides, the recombinant GRP1^{PH} was eventually a better probe to use.

Cells need to be permeabilised to allow recombinant probes in; recombinant probes can also enter the cells by microinjection. However, microinjection in somatic cells is not a straight forward process. Therefore, we initially applied GST-GRP1^{PH} in permeabilised cells and determined the presence of PtdIns(3,4,5)P_3 in endomembranes. Despite the deformation of mitochondria caused by saponin the major endomembranes (the NE, ER and Golgi) were normal after permeabilisation (Figure 4.3).

GST-GRP1^{PH} localised to endomembranes which resemble the ER, NE and Golgi (Figure 4.5). This recombinant probe was shown to be PtdIns(3,4,5)P_3-specific as indicated by the lipid strip experiment, and the competition assay with the PtdIns(3,4,5)P_3 soluble headgroup Ins(1,3,4,5)P_4 (Figure 4.4 & Figure 4.5). GST-GRP1^{PH} partially co-localised with the two tested organelle markers (Figure 4.6). A perfect co-localisation between GST-GRP1^{PH} and MAb414 was not expected since MAb414 targets the nuclear pore complex and is known for its discontinuous localisation at the NE (Davis and Blobel, 1986). However, GST-GRP1^{PH} and MAb414 displayed a highly similar fluorescence around the nucleus, suggesting that they are very close and likely to co-exist in the same compartment.

Similarly, both GST-GRP1^{PH} and calreticulin localised at the NE, indicated by their similar localisation pattern. The partial overlapping between GST-GRP1^{PH} and calreticulin in the ER network may be due to the presence of PtdIns(3,4,5)P_3-microdomain in the ER. To further verify the localisation of GST-GRP1^{PH} in the ER, an ER membrane marker such as calnexin could be used.

This is the first study to localise PtdIns(3,4,5)P_3 in the NE. The NE is a subdomain of the ER thus PtdIns(3,4,5)P_3 localisation in the NE may be a result of these two interconnected compartments. Furthermore, plasma membrane localisation is not the major readout revealed by the recombinant probe, this is contrary to most of the findings in the literature suggesting that PtdIns(3,4,5)P_3 is mainly localised to the plasma membrane.

The presence of PtdIns(3,4,5)P_3 in endomembranes is also indirectly supported by immunodetection of PI3KCA subunits. The p85 regulatory domain was localised to endomembranes that resemble the NE, ER and Golgi and the class I catalytic domains (p110α, p110β) displayed a Golgi-like localisation. All of the tested domains showed a vesicular fluorescence throughout the cytoplasm. The presence of PI3KCA subunits and their substrate PtdIns(4,5)P_2 (Hobday, 2012) at the endomembranes suggests the potential production of PtdIns(3,4,5)P_3 in these compartments. Although the activity of the PI3KCA subunits is unknown, their vesicular distribution suggests the possibility of PtdIns(3,4,5)P_3-enriched vesicles in the cytoplasm.

In some cells, the p85 regulatory subunit displayed an absence of Golgi localisation, in contrast to the Golgi localisation of p110α subunit. Segregation of p85 and p110α was observed in L6 skeletal muscle cells and was suggested to be PtdIns(3,4,5)P_3-dependent (Patel *et al.*, 2003); GRP1^{PH} and p110α were detected within the insulin-induced actin mesh structure, in which they potentially resided on vesicles entrapped by the actin mesh. To ascertain whether the localisation of PI3KCA subunits detected by antibodies is specific and responsible for PtdIns(3,4,5)P_3 production, the experiments could be repeated in GFP-GRP1^{PH} transfected cell or stable cell lines, targeted by p85 and p110α/β siRNA. Or alternatively, cells targeted by p85 and p110α/β siRNA could be probed by recombinant GRP1^{PH} in parallel. A loss of GFP1^{PH}, and thus PtdIns(3,4,5)P_3

and/or PI3KCA signals is expected when p85 or p110α/β are depleted. Similarly, PI3 kinase inhibitor studies can determine the specificity of the above PI3KCA antibodies.

Furthermore, using an intramolecular FRET (Förster resonance energy transfer) lipid sensor (Sato *et al.*, 2003), investigators demonstrated that PtdIns(3,4,5)P_3 observed in endomembranes was produced *in situ* and the production was activated by receptor endocytosis. This evidence and our results support the presence of endomembrane-PtdIns(3,4,5)P_3 and PtdIns(3,4,5)P_3-enriched vesicles in mammalian cells.

4.7.2 GRP1^{PH}-miniSOG probes require further optimisation

The typical resolution of light microscopy is about 200 nm (Moravec, 1999) thus confocal microscopy does not have the resolution to visualise small membrane vesicles with a diameter less than 200 nm. Therefore GRP1^{PH} was fused to the miniSOG CLEM tag in order to visualise PtdIns(3,4,5)P_3-enriched vesicles at EM resolution. GFP-GRP1^{PH}-tSOG and GFP-GRP1^{PH} localised similarly at the plasma membrane and endomembranes (Figure 4.9). The increase in fluorescent signal of GFP-GRP1^{PH}-tSOG in these compartments was likely due to the fluorescence of the SOG domains.

Unlike GFP-GRP1^{PH}, GFP-GRP1^{PH}-tSOG localised at the NE (Figure 4.9 & Figure 4.10), as indicated by a partial co-localisation with the NE/ER marker. The NE localisation might be because of a higher PtdIns(3,4,5)P_3 dissociation constant (K_{off}) of GFP-GRP1^{PH}-tSOG compared to GFP-GRP1^{PH} so that the miniSOG probe is more mobile to bind to the NE. To test this, the difference of binding affinity between GFP-GRP1^{PH}-tSOG and GFP-GRP1^{PH} could be determined by fluorescence loss in photobleaching (FLIP) *in vivo*.

Moreover, the specificity of the miniSOG-GRP1^{PH} requires further investigation since the K273A, R284A and double K273A/R284A mutants localised very similarly compared to the WT construct in both basal and stimulated cells (Figure 4.11). All GRP1^{PH} mutants lost their PtdIns(3,4,5)P_3 binding ability *in vitro* (Guillou *et al.*, 2007, Knight *et al.*, 2010). However, the mutant probe may have different binding affinity or non-specific binding *in vivo.* The binding affinity of WT GRP1^{PH} has been shown to increase 12-fold by the inclusion of PtdSer into model membranes (Corbin *et al.*, 2004). Based on the same principle, the binding affinity of mutant GRP1^{PH} may be increased to a level comparable to the WT GRP1^{PH} *in vivo*. The similarity of localisation between WT and mutant miniSOG-GRP1^{PH} may be also due to the effect of miniSOG tags. MiniSOG showed oligomerisation at concentration above ~20 μM (Martell *et al.*, 2012). The local concentration of miniSOG-GRP1^{PH} at the membrane may be high enough for minSOG to form dimers, allowing the GRP1^{PH} mutants to localise similarly to the WT GRP1^{PH}. WT GRP1^{PH} should have a strong binding to the membranes compared to the GRP1^{PH} mutants. Therefore, after FLIP at the membranes, a less fluent diffusional movement would be expected for WT GRP1^{PH}. In contrast, mutant miniSOG-GRP1^{PH} should diffuse more fluently.

The specificity of miniSOG-GRP1^{PH} can be also tested by preparing the corresponding recombinant probes and applying them on membrane lipid strip or permeabilised cells. In addition, the specificity of miniSOG-GRP1^{PH} can be tested by addition of LY294002, a PI3 kinase inhibitor; loss of membrane localisation would be expected if the miniSOG-GRP1^{PH} probe is PtdIns(3,4,5)P_3-specific.

4.7.3 The ideal method to detect phosphoinositides

Both transient transfection and recombinant probe imaging approaches have advantages and drawbacks. Transient transfection is advantageous due to its simplicity. However, expression of PH domains will disturb the phosphoinositide dynamics and their readout may diverge from the genuine lipid localisation (Poccia and Larijani, 2009). Although recombinant PH domains are preferable tools to detect the *in situ* localisation of target lipids, the inevitable permeabilisation step causes deformation of membrane ultrastructure and limits the application of some general lipid-binding dyes. Considering the above, an ideal approach to target phosphoinositides would be microinjection of the correct concentration of recombinant PH domains. In this way, membrane ultrastructure of the cells would be preserved and injected recombinant probe fused to fluorescent protein could reveal the *in situ* localisation of lipids of interest with minimal effect on its dynamics. Alternatively, stable cell line with knock-in acute inducible lipid reporter could be a feasible tool to detect phospholipids. This system would allow the expression of the lipid reporter to be titred more accurately than conventional transfection.

4.8 Summary

Using transfection and recombinant GRP1^{PH} probes, PtdIns(3,4,5)P$_3$ was detected at the NE, ER, Golgi and at the plasma membrane. In addition, localisation of PI3KCA subunits suggested a potential PtdIns(3,4,5)P$_3$ production in endomembranes and also its presence in PtdIns(3,4,5)P$_3$-enriched vesicles. To visualise these vesicles at EM resolution, GRP1^{PH} was fused to the CLEM tag miniSOG. Although the miniSOG-GRP1^{PH} was able to target endomembrane-PtdIns(3,4,5)P$_3$, its specificity against PtdIns(3,4,5)P$_3$ will require further investigation before its application at the EM level.

Chapter 5 The role of DAG in mammalian NE assembly

5.1 Introduction

Many studies have emphasised the role of proteins rather than lipids in changes in membrane curvature, organelle shaping and membrane fusion, reviewed in Zimmerberg and Kozlov (2006) and Graham and Kozlov (2010). Such emphasis is due to lack of *in vivo* data regarding the role of lipids in membrane morphology. In fact, membrane morphology is very sensitive to changes in lipid composition. Several model membrane studies have shown that the change of lipid composition results in different structures. For instance, enrichment of certain lipids within a membrane converts the membrane from lamellar phase to non-lamellar phase. (Chen and Cheng, 1990, Epand *et al.*, 1992, Han and Gross, 1992).

The role of DAG in membrane fusion was suggested decades ago (Das and Rand, 1984). Using fluorescence anisotropy, investigators demonstrated that DAG facilitates fusion in model membranes (Basanez *et al.*, 1996, Allan *et al.*, 1978). In the vesicle fusion model, localised DAG production is essential for the polarised fusion of MV1 to MV2, generating a complete NE (Dumas *et al.*, 2010, Barona *et al.*, 2005). Moreover, solid-state NMR analysis of the membrane composition of fusogenic vesicles (MV1) showed that the presence of DAG and phosphoinositides destabilises membranes and promotes fusion (Zhendre *et al.*, 2011). However, the role of DAG in altering membrane morphology was not demonstrated in mammalian cells.

Our goal was to locally deplete DAG in the NE and determine its impact on mammalian NE assembly. A DAG reporter was constructed to monitor the presence of DAG in mammalian cells during mitosis. A chemical inducible device was used to target a DAG metabolising enzyme to the NE, and the morphology of cells lacking DAG at the ER and NE was examined by correlative light and electron microscopy (CLEM).

5.2 Localisation of DAG in mammalian cells

The C1 domains of PKC are established DAG reporters (Hurley and Grobler, 1997, Oancea *et al.*, 1998) and the localisation of various PKC C1 domains in mammalian cells has been investigated extensively (Hobday, 2012). GFP-PKCεC1aC1b (hereafter referred to as GFP-C1aC1b) transfected probe was used to detect DAG in mammalian cells. PKCεC1aC1b was used because it has the highest affinity for DAG compared to other C1 domains from various PKC isoforms (Hobday, 2012).

Figure 5.1-A shows the localisation of GFP-C1aC1b in interphase cells. In both HeLa and COS-7 cells, strong signals were detected at the NE (yellow arrow), ER (green arrows) and Golgi (white arrows). Live cells transfected with GFP-C1aC1b or labelled with NDB-DAG SUVs had identical NE, ER and Golgi localisation Figure 5.1-B). GFP-C1aC1b was co-localised to the ER network labelled with calreticulin antibodies (Figure 5.1, insets) whereas the non-DAG-binding mutant GFP-C1aC1b.W264G only displayed a minor fluorescence at the Golgi. This shows that our reporter is DAG specific (Figure 5.1-C).

Having established the specificity of GFP-C1aC1b interphase cells, we next examined the DAG localisation in mitotic cells. GFP-C1aC1b probed DAG in the reforming NE and ER of HeLa and COS-7 cells at telophase (Figure 5.1-E & F). The localisation of DAG in the reforming NE and ER was supported by the consistent distribution of DiOC$_6$ (general membrane marker), ER tracker and GFP-POM121 (nuclear pore marker) (Figure 5.1-G – I). In addition, the presence of DAG was stronger and more observable in the reforming NE as the cells progressed from early to late telophase. Having demonstrated DAG was present in the NE of both interphase and mitotic cells, the next step was to target DAG metabolism specifically at the NE in order to show that DAG has a functional role in NE reassembly.

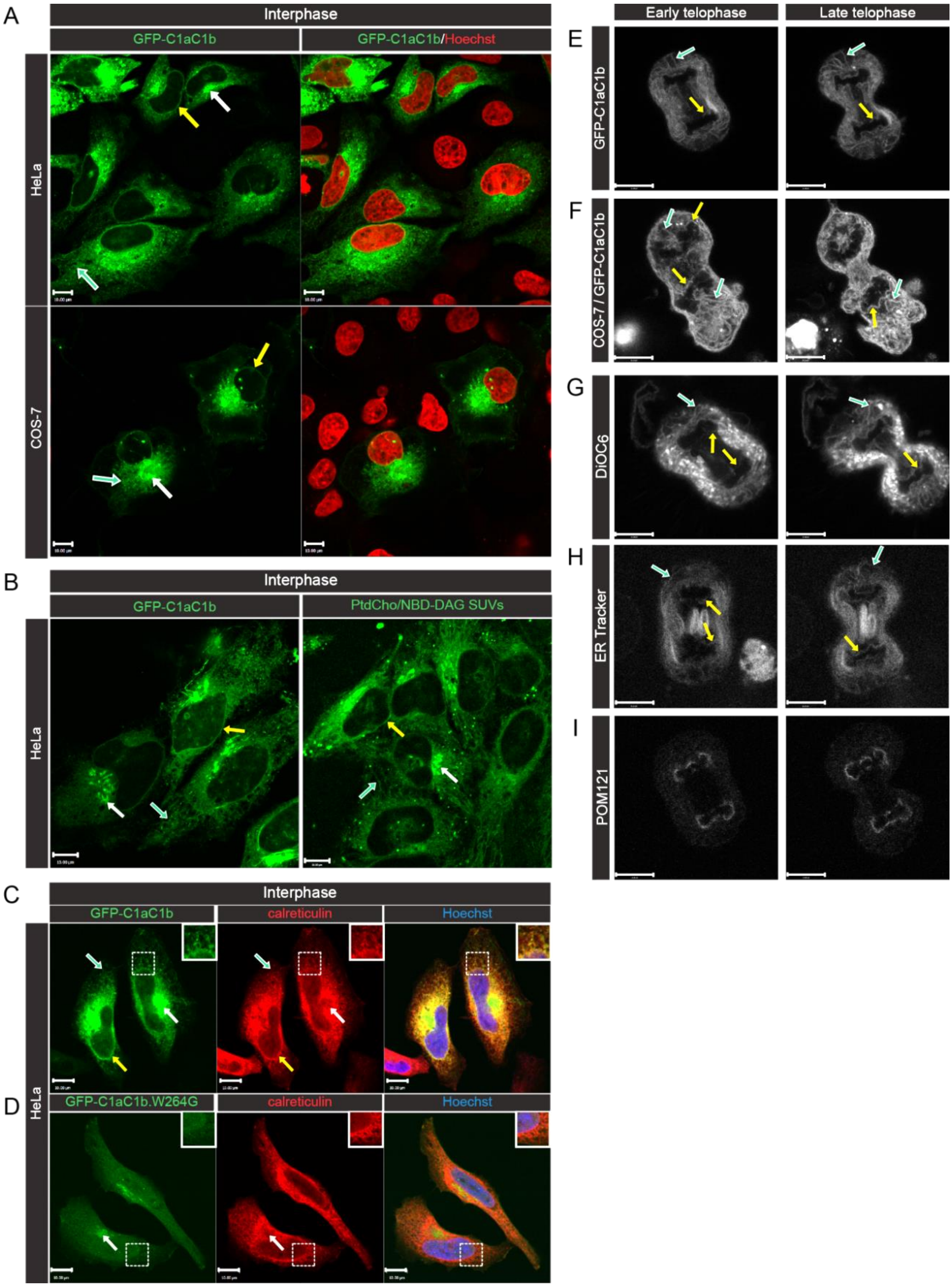
A
Interphase
GFP-C1aC1b
GFP-C1aC1b/Hoechst
HeLa
COS-7
B
Interphase
GFP-C1aC1b
PtdCho/NBD-DAG SUVs
HeLa
C
Interphase
GFP-C1aC1b
calreticulin
Hoechst
D
GFP-C1aC1b.W264G
calreticulin
Hoechst
HeLa
Early telophase
Late telophase
E
GFP-C1aC1b
F
COS-7 / GFP-C1aC1b
G
DiOC6
H
ER Tracker
I
POM121

(Cont'd)

Figure 5.1 DAG is localised to the NE, ER and Golgi in mammalian cells

(A) HeLa and COS-7 cells were transfected with GFP-C1aC1b, fixed, stained with Hoechst 33342 and imaged by confocal microscopy. (B) HeLa cells were transfected with GFP-C1aC1b (left) or labelled by addition of PtdCho/NBD-DAG (60:40 mole%) SUVs (right) before live confocal imaging. (C) GFP-C1aC1b co-localised with the indirect immunofluorescence of calreticulin (ER marker) at the ER (insets of the upper panels); chromosomes were stained with Hoechst 33342. In contrast, DAG localisation were absent from the NE and ER (insets of the lower panels) and reduced at the Golgi when the cells were transfected with GFP-C1aC1b.W264G (non-DAG-binding mutant). In interphase cells (A–C), DAG localised at the NE (yellow arrows), ER (green arrows) and Golgi (white arrows). HeLa (E) and COS-7 (F) cells were transfected with GFP-C1aC1b and followed though mitosis by live confocal microscopy. Localisation of GFP-C1aC1b followed similar distribution as DiOC_6 (G), ER tracker (H) and GFP-POM121 (I). Yellow arrows and green arrows in (E–I) indicate the NE and ER reassembly respectively. Scale bar, 10 µm. Confocal imaging experiments were performed by Marie-Charlotte Domart (Cell Biophysics and EM unit, London Research Institute).

5.3 Determining the role of DAG in mammalian NE assembly

5.3.1 DAG species in the NE

Early studies using two-dimensional thin-layer chromatography and gas chromatography revealed that there are only traces of DAG in the mammalian NE (Kleinig, 1970, Keenan *et al.*, 1972). However, little is known about the DAG species and their structural details such as the length and saturation of their fatty acid chains. The chain length and saturation of lipid define its elasticity thus affecting the membrane property and protein aggregation on the membrane (Lee, 2004, Rawicz *et al.*, 2000). Hence, an accurate quantification of DAG species will provide insight to understand their biological function in NE assembly and conduct follow-up functional or structural studies.

We isolated mammalian nuclei and analysed their DAG composition by lipid mass-spectrometry. ER and NE-enriched mammalian nuclei were isolated using nitrogen cavitation. Figure 5.2-A shows the morphology of isolated nuclei. After cavitation, the isolated nuclei retained only the NE and ER, and the proportion of clean nuclei with minimal ER attachment ranged from 42 to 64% (white arrows). Lipid mass-spectrometry analysis indicated that the ER and NE are enriched in unsaturated species of DAG (Figure 5.2-B) thus we targeted the unsaturated DAG species with a chemically-induced dimerisation device.

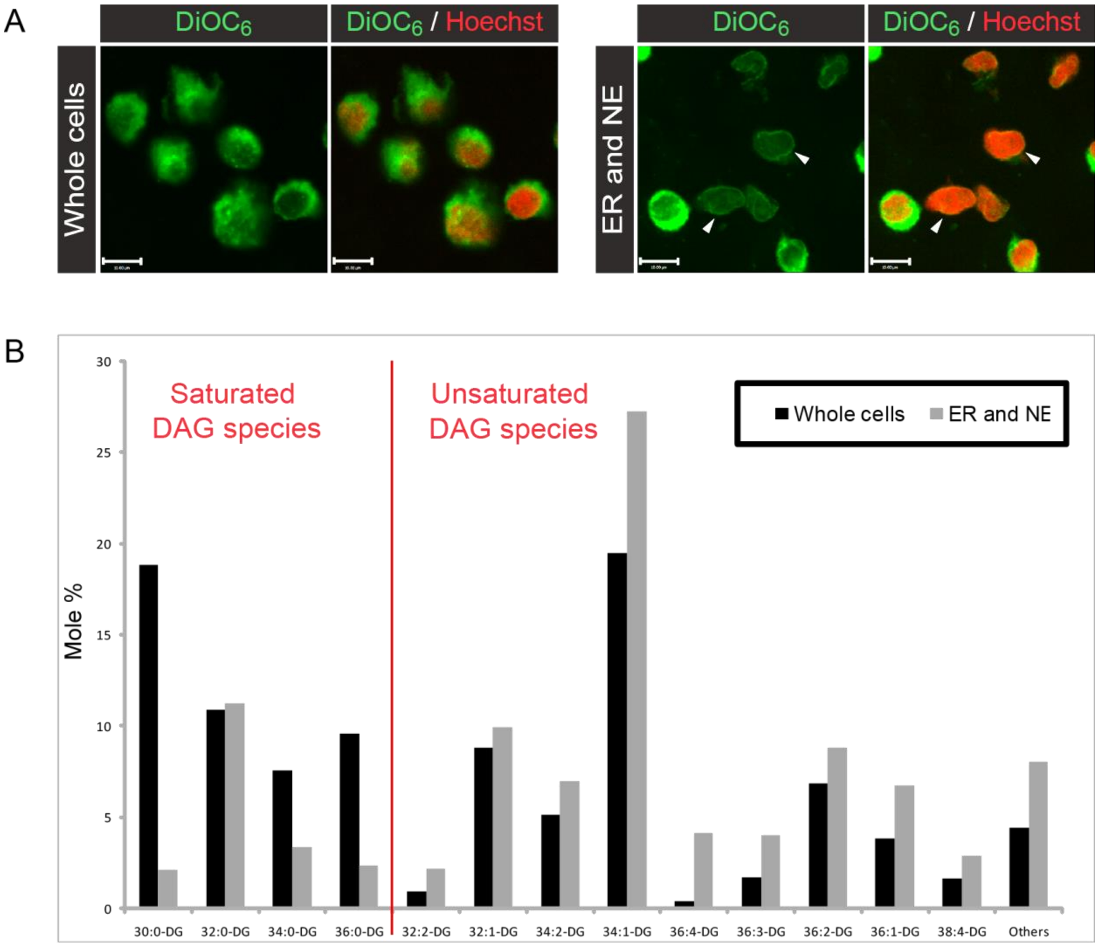

Figure 5.2 Enrichment of polyunsaturated DAG in purified mammalian ER/NE

(A) Nuclei were purified from HeLa cells. Nitrogen cavitation was performed in a pressure chamber at 200 psi (for details see Chapter 2). Whole cells and isolated nuclei were labelled with $DiOC_6$ (green) and Hoechst 33342 (red). White arrows indicate pure nuclei with minimal ER attachment. Scale bars, 10 μm. (B) Lipids were extracted from whole cells or isolated nuclei obtained in (A) and subjected to lipid mass-spectrometry analysis. The data was divided into saturated and unsaturated DAG species. Black bars, whole cell; grey bars, isolated nuclei. Quantitative analysis of DAG was a collaborative study with Michael Wakelam (Babraham Institute, Cambridge). Adapted from Domart *et al.* (2012).

5.3.2 Rapalogue dimerisation device

We developed a rapalogue-induced dimerisation device to modulate DAG. In contrast to chemical or peptide inhibitors that globally target DAG, the dimerisation tool executes a localised intervention in cellular process upon addition of a dimeriser (Fili *et al.*, 2006). In other words, we can modulate DAG in a spatial-temporal-specific manner. Figure 5.3-A explains the principle of the rapalogue dimerisation tool. Upon addition of rapalogue (the inducer), RFP and FKBP (rapalogue-binding domains) will be brought together by forming a heterodimer. This allows delivery of protein effector to a specific compartment.

To target the NE, the NE-targeting domain of lamin B receptor (LBR) was fused to FKBP. The NE-targeting and rapalogue-binding construct is referred to as GFP-2FKBP-LBRΔTM2-8. It displayed similar NE and ER localisation compared to GFP-LBR and endogenous LBR (Figure 5.4). FRB-conjugated lipid-modifying enzymes can form heterodimer with GFP-2FKBP-LBRΔTM2-8 in the presence of rapalogue, resulting in the recruitment of these enzymes at the NE and ER (Peel *et al.*, 2013).

The lipid-modifying enzymes were conjugated with FRB. There are two approaches to deplete DAG in the NE: 1) direct modification of DAG 2) restriction of the upstream precursor of DAG, PtdIns(4,5)P_2 (Figure 5.3-B). DGKεK was selected as the enzyme to phosphorylate DAG to PtdOH because this protein domain targets unsaturated DAG species (Pettitt and Wakelam, 1999), which are the major DAG species in the NE and ER according to our mass-spectrometry analysis (see section above). Alternatively, SKIP was used to dephosphorylate PtdIns(4,5)P_2 to PtdIns(4)P in order to deplete the DAG precursor (Schmid *et al.*, 2004).

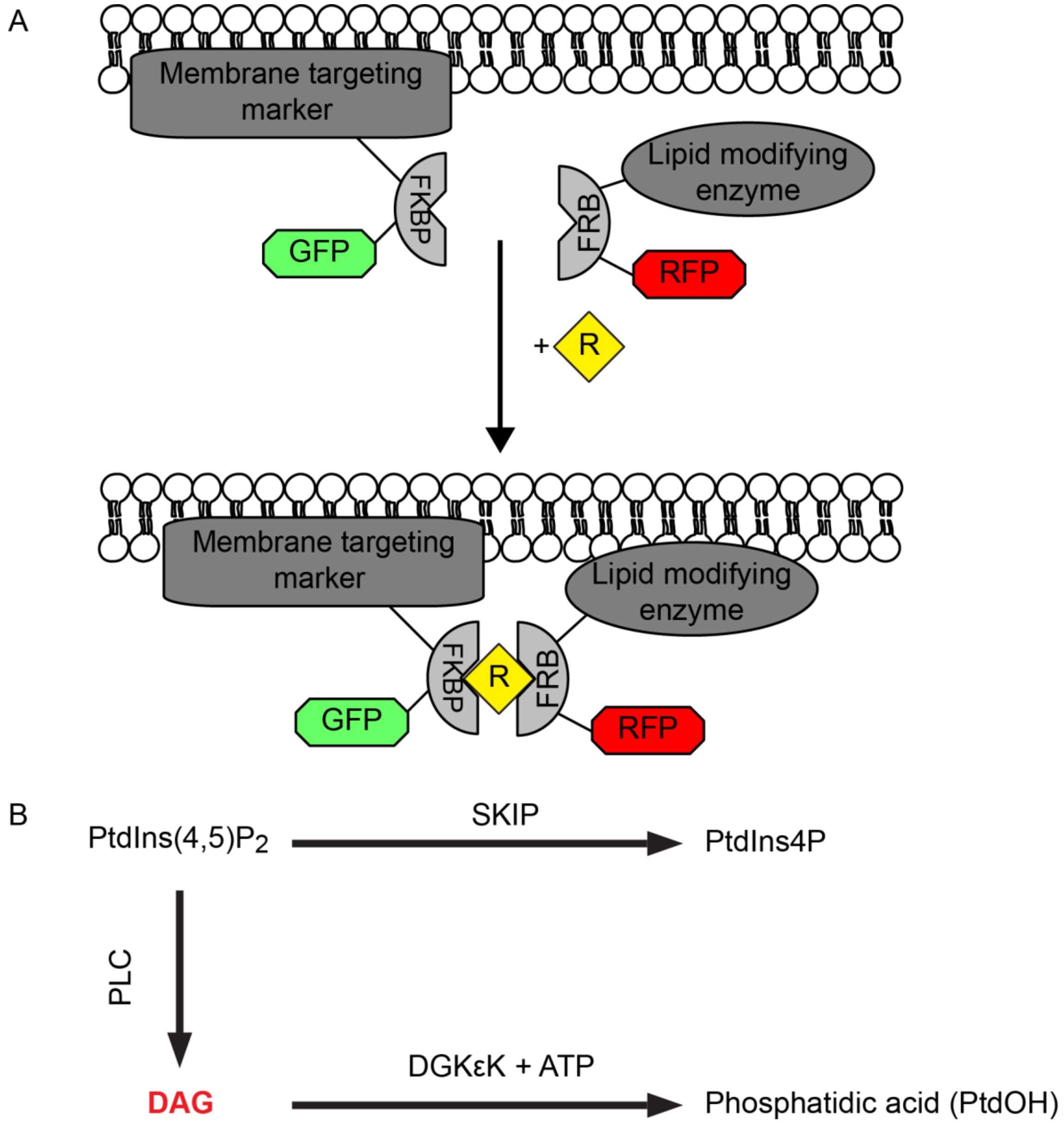

Figure 5.3 Principle of the rapalogue dimersiation device and the pathways to target DAG

(A) Acute intervention of lipid target. A membrane-targeting marker and a lipid-modifying enzyme are fused to the FKBP (FK506-binding protein) and FRB (FKBP12-rapamycin associated protein 1) domain respectively. FKBP and FRB are immunophilins that able to bind to the same immunosuppressants ligand rapamycin in order to form a heterodimer. In our dimerisation device, a rapamycin analog (hereafter referred to as rapalogue) functions as the heterodimeriser (yellow) to recruit the lipid-modifying enzyme to the targeted membrane through an immunophilins-heterodimeriser interaction. GFP and RFP are the fluorescent reporters of the membrane-targeting marker and lipid-modifying enzyme, respectively. (B) DAG can be depleted by phosphorylation to PtdOH using DGKεK or by converting its upstream precursor PtdIns(4,5)P_2 to PtdIns4P through SKIP.

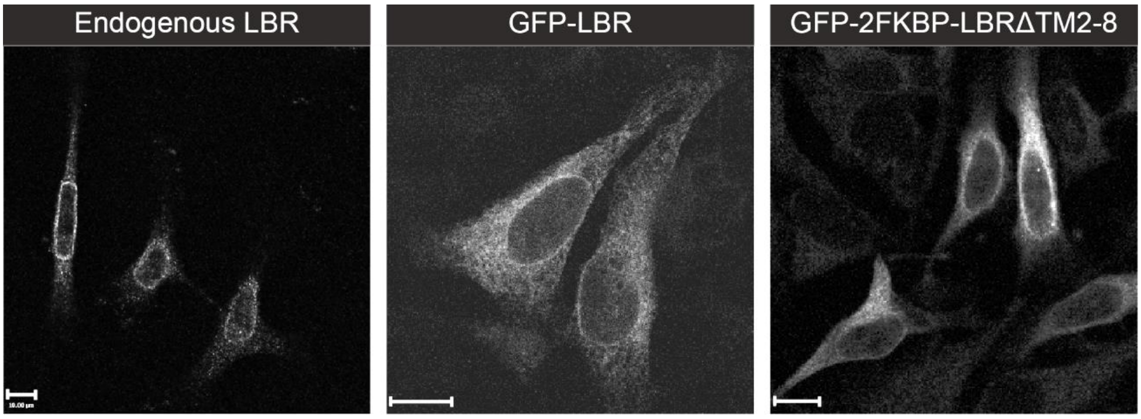

Figure 5.4 GFP-2FKBP-LBRΔTM2-8 correctly localises to the NE and ER

Left panel: Localisation of endogenous LBR in HeLa cells, detected by indirect immunofluorescence. Middle panel: HeLa cells transfected with GFP-LBR. Right panel: HeLa cells transfected with the rapalogue-binding GFP-2FKBP-LBRΔTM2-8 construct. All probes above displayed similar NE and ER localisation. Scale bar, 10 µm. Adapted from Domart *et al.* (2012).

5.3.3 Acute modification of DAG in the mammalian NE

GFP-2FKBP-LBRΔTM2-8 (LBR) successfully recruited the lipid-modifying enzymes (DGKεK and SKIP) to the NE upon treatment with rapalogue (Figure 5.5-B & Figure 5.6-B). In addition to being the targeting portion of the rapalogue dimerisation device, LBR was used as a tool to monitor the reassembly of the NE. Previous studies have shown that during mitosis, LBR localisation is redistributed to the ER and subsequently recruited back to the NE (Haraguchi *et al.*, 2000, Smith and Blobel, 1993). Hence, we expected to see a LBR localisation in the reforming NE of unperturbed cells.

Upon addition of rapalogue, DGKεK was predicted to recruit to the NE and phosphorylate DAG to PtdOH. This resulted in a fragmented NE in both HeLa and COS-7 cells, as determined by the LBR distribution (Figure 5.5-C–D). In contrast, when the cells were transfected with a non-catalytic DGKεK (Figure 5.5-G) or untransfected with DGKεK (Figure 5.5-F), a LBR localisation, indicative of a complete NE, was detected in telophase cells. The DGKεK.D434N mutant also demonstrated that the fragmentation phenotype is due to catalytic effect of DGKεK. The NE of the cells co-expressing LBR and DGKεK was intact in the absence of rapalogue (Figure 5.5-E).

DGKεK phosphorylated DAG at the NE/ER to PtdOH, and PtdOH is also a biomolecule with a negative membrane curvature (see Introduction). To ensure the disruption of NE was not due to the accumulation of PtdOH but rather the depletion of DAG, we removed the DAG precursor PtdIns(4,5)P_2 by recruiting SKIP to the NE. When the cells co-expressing LBR and SKIP were treated with rapalogue, the NE was fragmented (Figure 5.6-C). However, in the absence of rapalogue (Figure 5.6-D), or when a catalytically inactive SKIP was used (Figure 5.6-E), or both (Figure 5.6-F), cells underwent normal NE reassembly. In general, there were some cytoplasmic fluorescent patches in the LBR transfected cells and the fluorescence of these patches was possibly enriched when lipid modifying enzymes were recruited to the NE/ER in the presence of rapalogue.

While the above experiments allowed us to monitor NE reassembly, they did not allow us to visualise the expected changes in DAG. To directly observe the modulation of DAG, cells were triple transfected with a "dark" version of GFP-LBR, SKIP and GFP-C1aC1b. A minimal detection of DAG was expected under this condition. When treated with rapalogue, there was no detection of DAG around the chromosomes. However, vesicular fluorescence and some intense fluorescent patches of GFP-C1aC1b were detected in the cytoplasm, indicating DAG could be detected in these cells (Figure 5.7-A). In the absence of rapalogue, DAG was localised to the reforming NE (yellow arrow) and ER (green arrow) (Figure 5.7-B). Since C1aC1b will compete with DGKεK for DAG, we could not monitor the DAG localisation when DGKεK was used as the lipid-modifying enzyme.

In summary, DAG depletion in the NE by both direct and indirect approaches led to impaired NE assembly and possibly some impacts on other endomembranes. However, we lack ultrastructural information regarding the completeness of the NE and the identity of the cytoplasmic fluorescence at the light microscopy level. Therefore correlative light and electron microscopy was utilised to answer these questions.

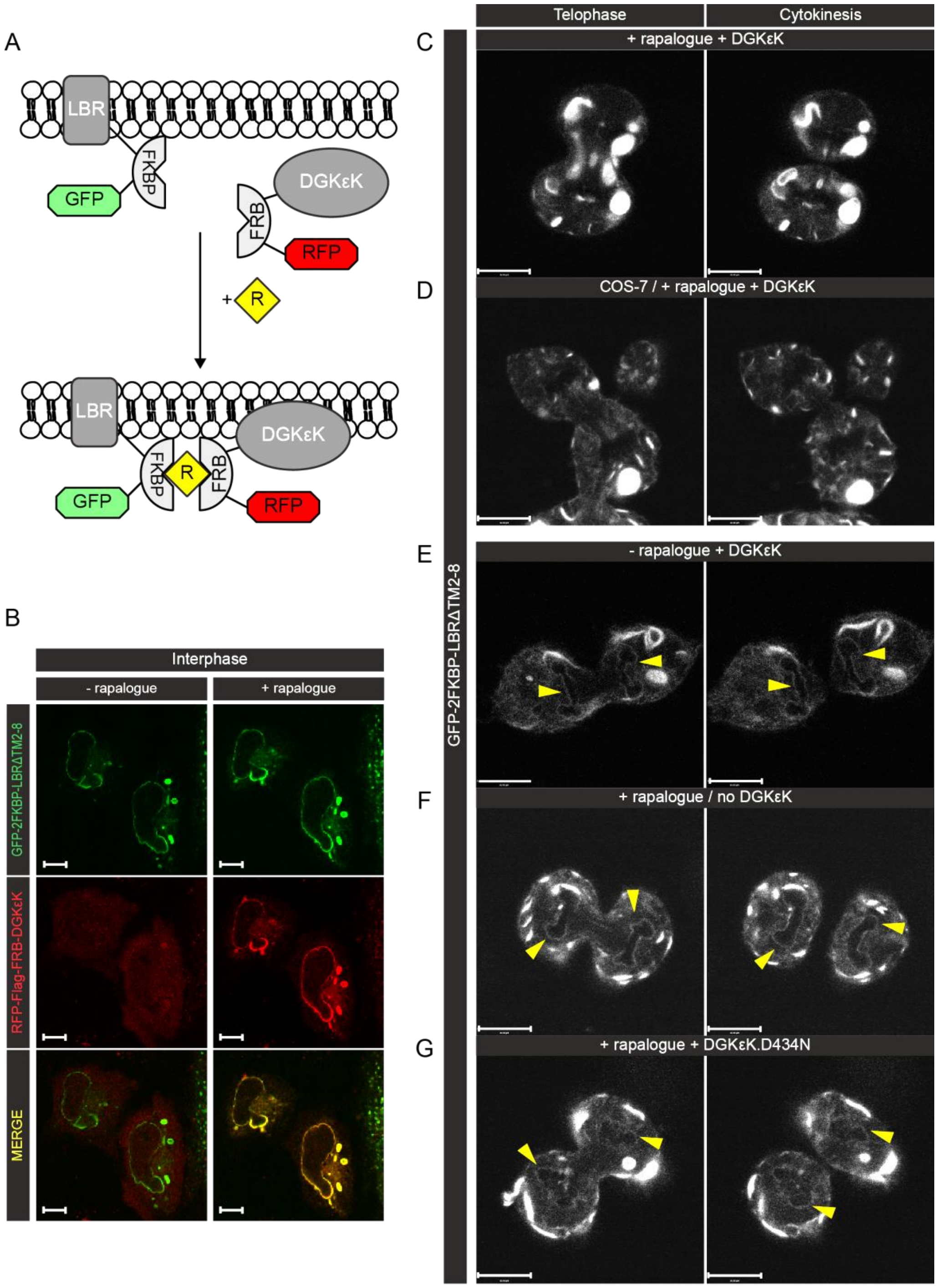

Figure 5.5 Acute depletion of DAG to PtdOH results in incomplete NE

(A) Diagram of rapalogue dimerisation device. Upon addition of rapalogue, RFP-Flag-FRB-DGKεK (DGKεK) will be recruited to GFP-2FKBP-LBRΔTM2-8 (LBR), and DAG will be phosphorylated to PtdOH. (B) Confocal images of live interphase cells double transfected with LBR (green) and DGKεK (red). 45 min after addition of 500 nM rapalogue, DGKεK was recruited to the NE and ER. HeLa (C) and COS-7 (D) cells co-expressing LBR and DGKεK underwent impaired NE reassembly when treated by rapalogue. HeLa cells in the absence of rapalogue (E) or expressing LBR alone (F) underwent normal NE reassembly. When DGKεK was replaced by its non-catalytic mutant (D434N) the NE reassembly was normal (G). Yellow arrows indicate LBR localisation in the reforming NE. Images representative of n = 10 experiments. Scale bar, 10 μm. Adapted from Domart *et al.* (2012).

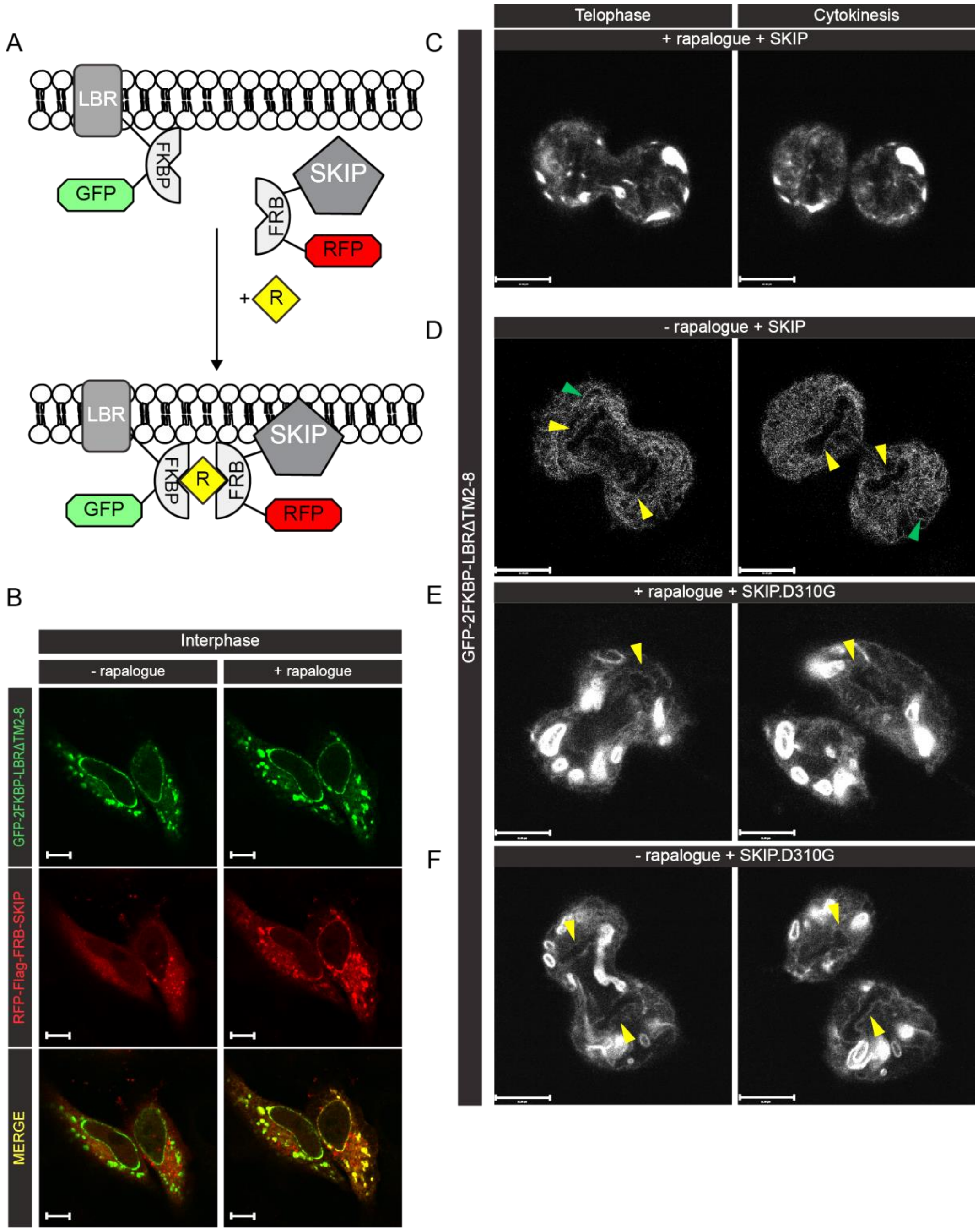

Figure 5.6 Acute depletion of PtdIns(4,5)P_2 results in an incomplete NE

(A) Diagram of rapalogue dimerisation device. Upon addition of rapalogue, RFP-Flag-FRB-SKIP (SKIP) is recruited to GFP-2FKBP-LBRΔTM2-8 (LBR), and PtdIns(4,5)P_2 is dephosphorylated into PtdIns4P. (B) Confocal images of live interphase cells double transfected with LBR (green) and SKIP (red). 45 min after addition of 500 nM rapalogue, SKIP was recruited to the NE and ER. (C) HeLa cells co-expressing LBR and SKIP underwent impaired NE reassembly when treated by rapalogue. HeLa cells in the absence of rapalogue (D) or expressing a non-catalytic SKIP (E), or both conditions (F) underwent normal NE reassembly (yellow arrows). Images representative of n = 3 experiments. Scale bar, 10 µm. Adapted from Domart *et al.* (2012).

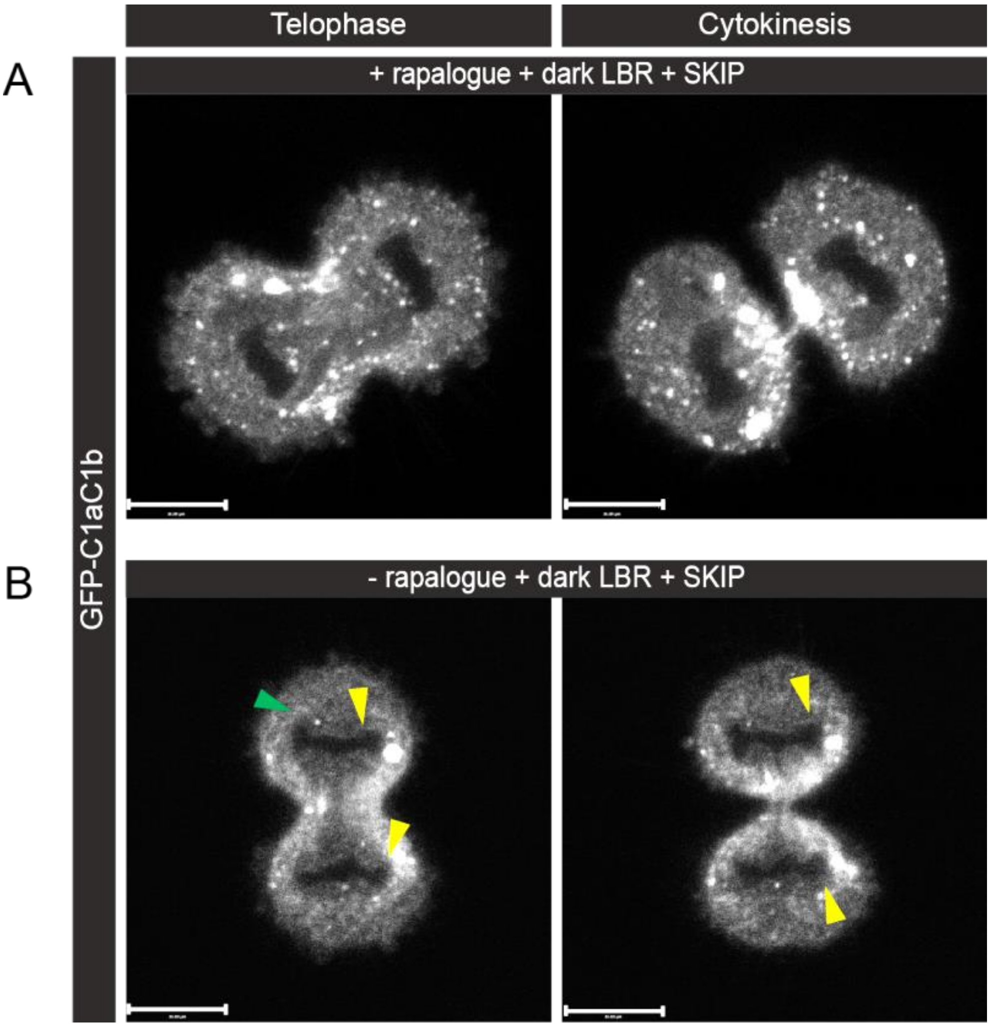

Figure 5.7 DAG is not accumulated in the NE when its precursor was removed

HeLa cells were triple transfected with a dark LBR, RFP-Flag-FRB-SKIP and GFP-C1aC1b. (A) When treated with rapalogue, the NE was not formed. (B) In the absence of rapalogue, DAG localisation was detected in the reforming NE (yellow arrows) and ER (green arrows). Scale bar, 10 μm. Adapted from Domart *et al.* (2012)

5.4 Correlative light and electron microscopy (CLEM) analysis of DAG-depleted mammalian NE and ER

Since light microscopy does not have the resolution to determine the presence of gaps in the reforming NE, CLEM was used to reveal the ultrastructure of fragmented NE and to assess DAG depleted phenotype of the ER. Figure 5.8 illustrates the work flow of CLEM. Live HeLa cells were imaged using confocal microscopy, fixed at the mitotic stage of interest, and embedded for TEM. The embedded cells were serial sectioned, imaged in order, aligned and manually segmented for 3D model reconstruction. Segmentation is a laborious and skill-demanding process because precision and experience are required to manually trace the morphology features of the NE and ER. Serial sectioning generated ~80 to 140 ultrathin sections (70 nm) through a cell of interest and for each cell it took at least four weeks to generate a 3D model from the initial confocal imaging. Therefore, CLEM experiments were performed once per condition. It took two months to manually segment the four cells described below.

Control cells (without modulation of DAG) labelled with $DiOC_6$ were fixed at anaphase (Figure 5.9-A) or telophase (Figure 5.9-B). At anaphase, the NE was incomplete with gaps of ~4 to 5 μm whereas at telophase the NE was almost complete with gaps of ~50 nm (Figure 5.9-A & B, purple arrows). Segmentations (Figure 5.9-A & B) and 3D models (Video 5.1) reveal a mainly tubular ER at early anaphase and a combination of ER sheets and tubules at telophase.

Figure 5.9-C & D reveal a fragmented NE with large gaps (purple arrows) in DAG depleted cells (modulated by DGKεK) fixed at early telophase and cytokinesis respectively. The gaps in the rapalogue treated telophase cell were about 5 μm in diameter and resembled the gaps in the control anaphase cell. In the rapalogue treated cytokinesis cell, large gaps (> 5 μm) were found in the NE facing the mitotic pole and the NE failed to form on the side facing the mid-body. The location of the gaps in DAG depleted cells was consistent with the lack of LBR localisation shown in the corresponding confocal images. The fragmented NE phenotype was more severe in the DGKεK high-expressing cell (cytokinesis) than in the low-expressing cell (telophase). Moreover, depletion of DAG resulted in a multi-lamellar phenotype of the ER (Figure 5.9-D, inset green arrows and Video 5.1). The multi-lamellar ER appeared to have some contact with the fragmented NE by a few tubules (Figure 5.9-D, inset yellow arrow) and such an aberrant phenotype corresponded to the intense cytoplasmic fluorescence of LBR shown in the confocal images (also see section above). Together these data demonstrate that depletion of DAG leads to failure of NE reassembly and abnormal phenotype of the ER.

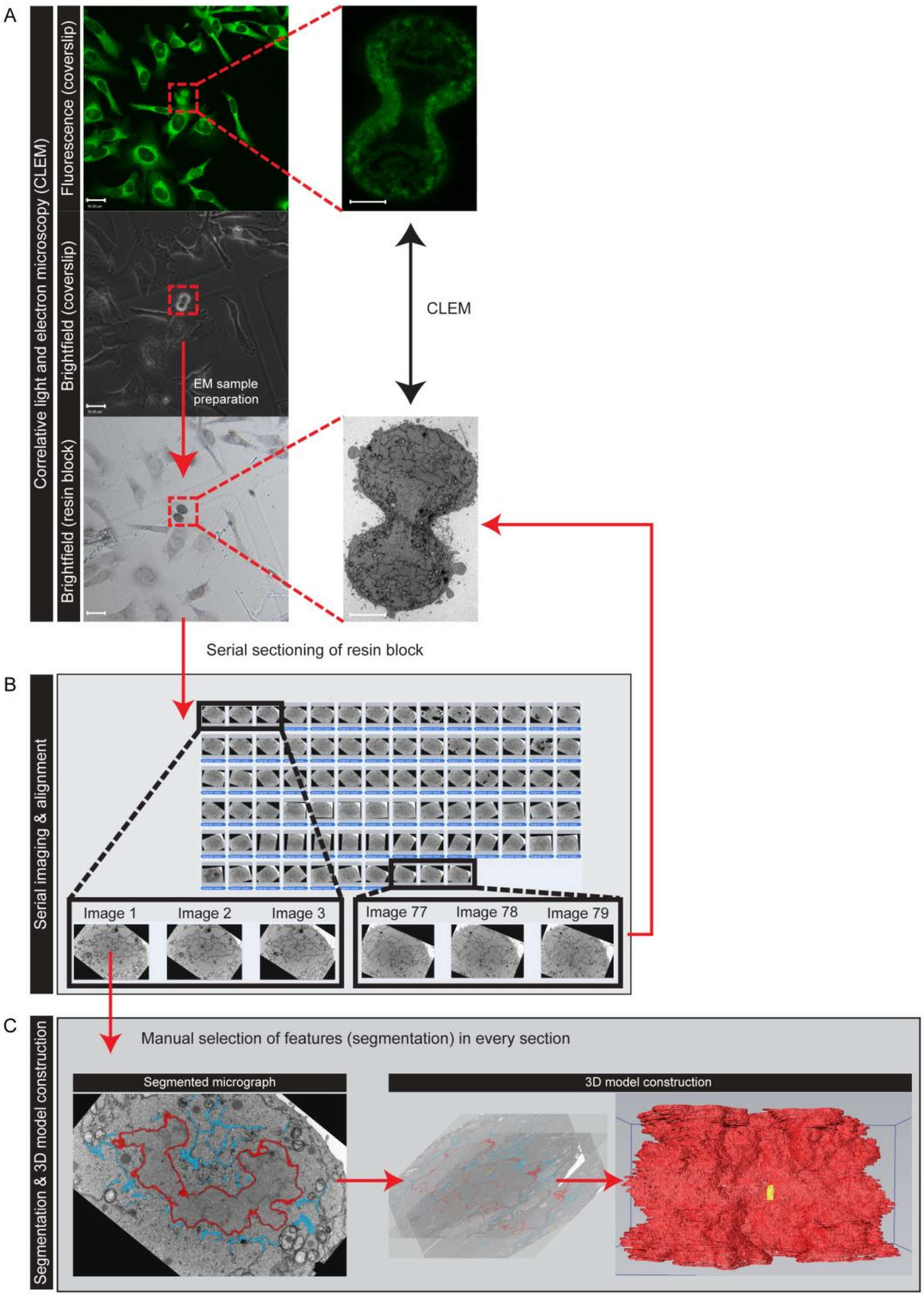

Figure 5.8 Correlative light and electron microscopy work flow

(A) Cells were cultured on gridded glass coverslips and transfected with the rapalogue dimerisation device. The cell of interest was identified and fixed at the required mitotic stage. The corresponding position was mapped on the grid using bright-field microscopy. Fixed cells were stained, dehydrated and embedded in resin. Scale bars, 10 µm. (B) Resin-embedded cells were relocated with respect to the imprinted grid and underwent serial sectioning. Approximately 80 to 140 sections with a thickness of 70 nm were collected through a single cell. The sections were imaged in order and the images acquired were aligned using Amira software. (C) The NE and ER were manually traced based on their morphological features (segmentation), and the segmentation was used to construct a 3D model. NE (red), ER (blue), centriole (yellow). 3D model in the figure represents the NE of a telophase cell.

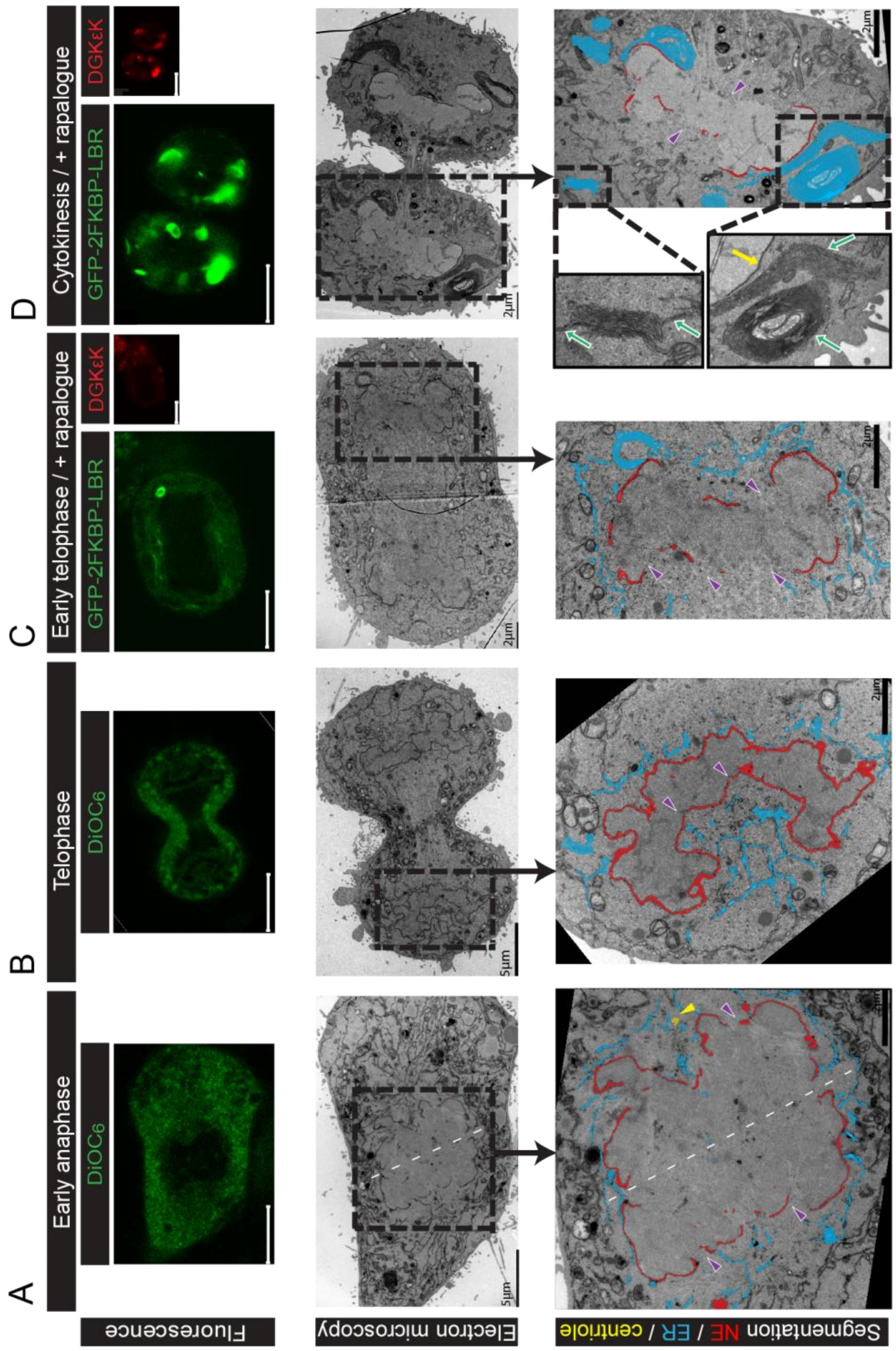
A
Early anaphase
DiOC6
B
Telophase
DiOC6
C
Early telophase / + rapalogue
GFP-2FKBP-LBR
DGKεK
D
Cytokinesis / + rapalogue
GFP-2FKBP-LBR
DGKεK
Fluorescence
Electron microscopy
Segmentation NE / ER / centriole
5µm
5µm
2µm
2µm
2µm
2µm
2µm

(Cont'd)

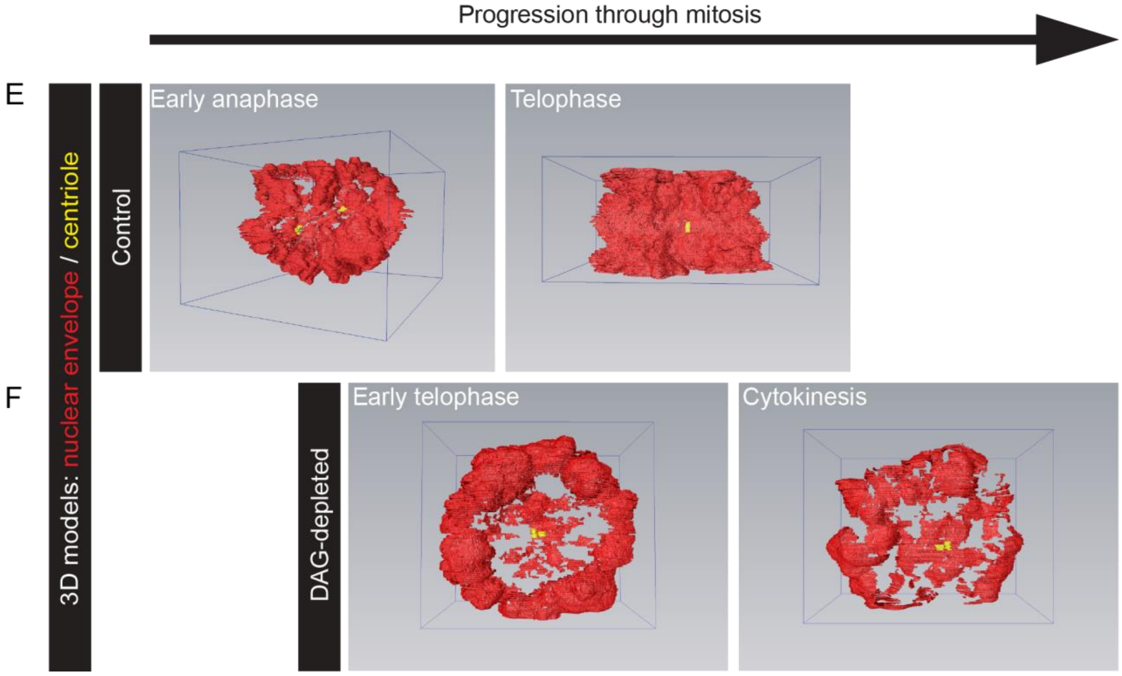

Figure 5.9 Large gaps were observed in the reforming NE of DAG-depleted cells

HeLa cells labelled with DiOC6 were followed through mitosis by confocal microscopy and fixed at early anaphase (A) and telophase (B). The cells were prepared for EM imaging and the NE (red), ER (blue) and centriole (yellow arrow) were manually segmented based on their morphological features. The dashed white line in the anaphase cells indicates the dividing cell's symmetry axis. Purple arrows indicate gaps in the reforming NE. Cells co-expressing GFP-2FKBP-LBRΔTM2-8 and RFP-Flag-FRB-DGKεK were treated with rapalogue, followed through mitosis, and fixed at early telophase (C) and cytokinesis (D). These DAG depleted cells were analysed by CLEM and segmented as described above. Large gaps (~ 5 µm) were observed at the reforming NE in both early telophase and cytokinesis cells (purple arrows). DAG depleted ER consisted multi-lamellar sheets (inset green arrows) and the multi-lamellar ER had a minimal contact with the reforming NE (inset yellow arrow). Scale bar: fluorescence 10 µm; EM: as shown in the electron micrograph. Segmentations from serial sections were constructed into 3D models of controls (E) and DAG-depleted (F) cells for a better visual comparison. Confocal imaging experiments were performed by Marie-Charlotte Domart (Cell Biophysics and EM unit, London Research Institute) (Domart *et al.*, 2012).

Video 5.1 3D models of control and DAG-depleted cells

Segmentations of NE (red), ER (blue) and centriole (yellow) from serial sections were constructed into 3D models. NE in DAG depleted cells were highly fragmented. Control anaphase (top left); control telophase (top right); DAG depleted telophase (bottom left); DAG depleted cytokinesis (bottom right). The models were rotated 360 ° at a speed of 12 frames per second.

5.5 Exogenous DAG addition rescues fragmented NE

The depletion of DAG showed an impact on the NE and ER during mitosis, and we speculated that the fragmented NE can be rescued by addition of exogenous DAG. Ideally, it would be preferable to monitor the DAG level in a rapalogue-treated, LBR/DGKεK co-expressing cell during the rescue. However, the DAG level cannot be efficiently probed with the C1aC1b domain, because it completes with DGKεK for the same substrate. Nevertheless, we can supply the cells with small unilamellar vesicles (SUVs < 50 nm diameter) containing known amounts of DAG.

SUVs composed of BIODIPY-PtdCho and unsaturated 18:0/24:4 1,2-DAG (80:20 mole%) were added to untransfected mammalian cells (Figure 5.10-A). Every cell was incorporated with SUVs 1 min post addition, indicated by the intracellular fluorescent of BIODIPY-PtdCho. 1,2-DAG-containing SUVs were added to rapalogue-treated, LBR/DGKεK co-expressing cells at metaphase and followed till telophase and cytokinesis. Localisation of LBR was detected in the reforming NE at both telophase and cytokinesis (Figure 5.10-B). Electron micrographs revealed that the reformed NE was virtually complete (Figure 5.10-C), and nuclear pores were found in the NE (yellow arrow). 3D models illustrate the fragmented NE of a rapalogue-treated cell and the NE recovery of a rapalogue-treated cell after addition of 1,2-DAG-containing SUVs (Figure 5.11). The ER retained its multi-lamellar phenotype after addition of the 1,2-DAG-containing SUVs (Figure 5.10-C, green arrows). Furthermore, the daughter cells of rapalogue-treated, LBR/DGKεK co-expressing cell did not go through a second mitotic division and died, but the daughter cells under the same condition which were rescued with 1,2-DAG-containing SUVs survived and underwent subsequent mitotic division (Video 5.2).

1,2-DAG is a second messenger for C1 domain-containing proteins and it is possible that the rescued phenotype was due to the activator of these proteins. To verify this, the rescue experiment was repeated using SUVs containing 1,3-DAG, which does not bind C1 domains (Sanchez-Pinera *et al.*, 1999). Figure 5.12 shows the structural formulae of 1,2-DAG and 1,3-DAG. SUVs containing 18:1/18:1 1,3 DAG were added to rapalogue-treated, LBR/DGKεK co-expressing cells at metaphase. Incorporation of the SUVs is indicated by white arrows (Figure 5.13-A). A fragmented NE was rescued by SUVs composed of PtdCho and unsaturated 1,3-DAG (80:20 mole%). The rescued NE was close to completion and nuclear pores were detected on the reformed NE (Figure 5.13-B & C). When a rapalogue-treated cell was rescued by 60:40 mole% PtdCho/1,3-DAG SUVs, a complete NE with nuclear pores was formed. Compared to the cell rescued by SUVs containing 20 mole% 1,3-DAG, the cell rescued by SUVs containing 40 mole% 1,3-DAG appeared to have less multi-lamellar ER sheets. Moreover, the fluorescence of 1,3-DAG-containing SUVs localised to the rescued NE (Figure 5.14).

Table 5.1 summarise the quantification of NE phenotype under different experimental conditions. In 11 single cell experiments, DAG-containing SUVs were able to rescue fragmented NE, with a reproducibility of 100% for 1,2-DAG-containing SUVs and almost 90% for 1,3-DAG-containing SUVs. Together, the novel findings in this chapter indicate both a signalling and structural role of DAG in NE assembly.

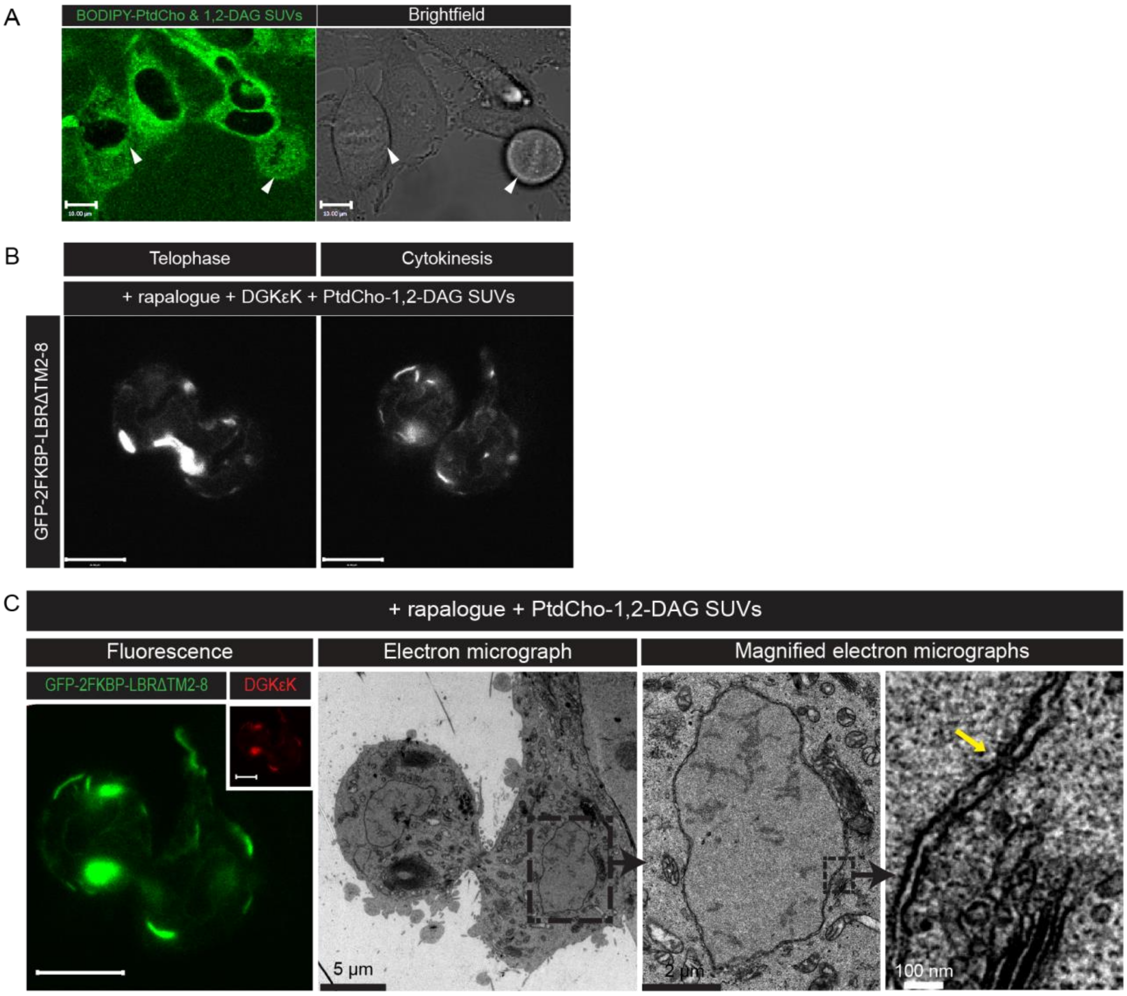

Figure 5.10 1,2-DAG rescues fragmented NE caused by DAG depletion

(A) Confocal image of metaphase HeLa cells 1 min post-addition of SUVs containing 18:0/20:4 1,2-DAG. The SUVs are made up of BODIPY-PtdCho and unsaturated 18:0/20:4 1,2-DAG (80:20 mole% respectively). Incorporation of SUVs was marked by the intracellular fluorescence of BODIPY (white arrows). (B) NE localisation of LBR during mitosis in rapalogue-treated, LBR and DGKεK co-expressing HeLa cells after addition of 1,2-DAG SUVs, imaged by confocal microscopy (C) Ultrastructure of DAG-depleted, 1,2-DAG SUVs rescued cell fixed at cytokinesis, imaged by CLEM. LBR (green), DGKεK (red). Yellow arrow indicates a nuclear pore in the complete NE. Scale bar, confocal: 10 μm, EM: as indicated on the images. Images representative of n = 11 experiments. Rescue experiment performed by Marie-Charlotte Domart (Cell Biophysics and EM unit, London Research Institute).

Video 5.2 1,2-DAG rescues fragmented NE caused by DAG depletion

CLEM images of aligned serial ultrathin sections of LBR/DGKεK co-expressing cell, treated with rapalogue and rescued with SUVs composed of Egg-PtdCho and 18:0/20:4 1,2 DAG (80:20 mole%). The rescued NE resembled that of a control interphase cell. The video is played at a speed of 1 frame per second.

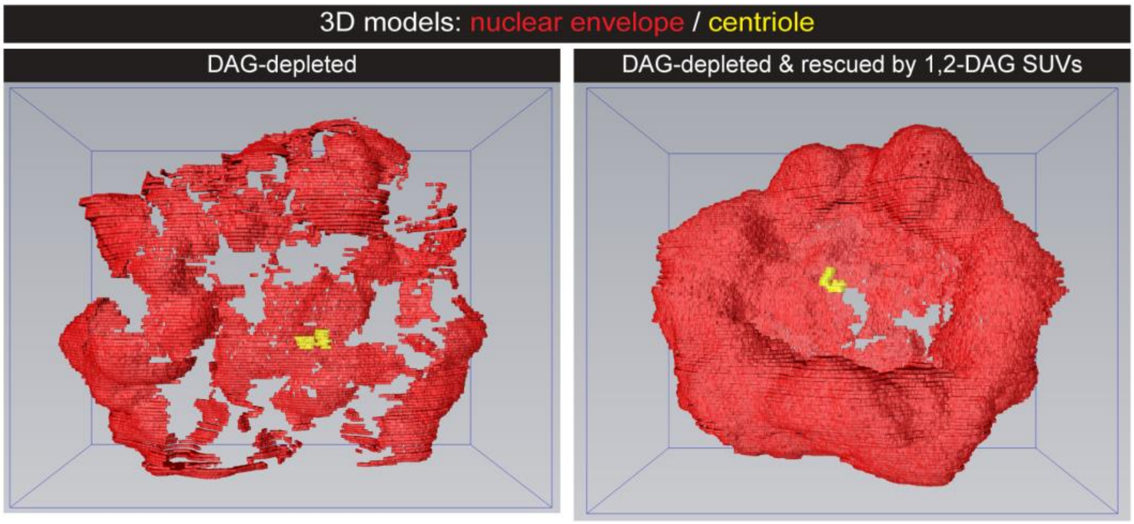

Figure 5.11 3D models of DAG-depleted and DAG-containing SUVs-rescued cells

Comparison of 3D models constructed from serial sections of a DAG-depleted cell (left) and a DAG-depleted but 1,2-DAG-containing SUV-rescued cell (right). The NE of the DAG-depleted cell was fragmented. In contrast, the NE of the 1,2-DAG-containing SUV-rescued cell was close to completion. NE (red), centriole (yellow).

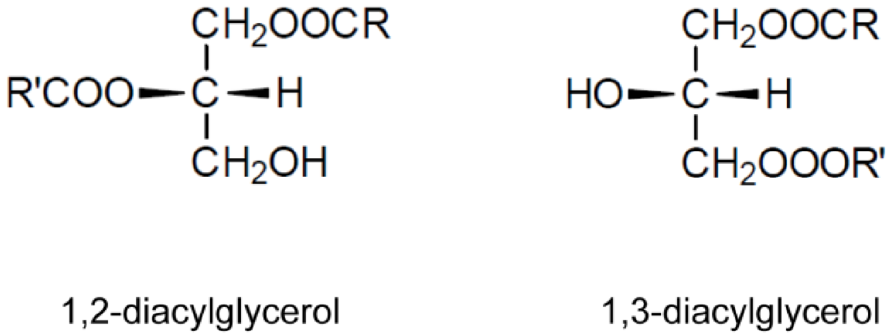

Figure 5.12 Structural formula of DAG isomers

The fatty acid chains attach to the sn-1 and sn-2 carbon position in 1,2-DAG whereas the fatty acid chains attach to the sn-1 and sn-3 carbon position in 1,3-DAG.

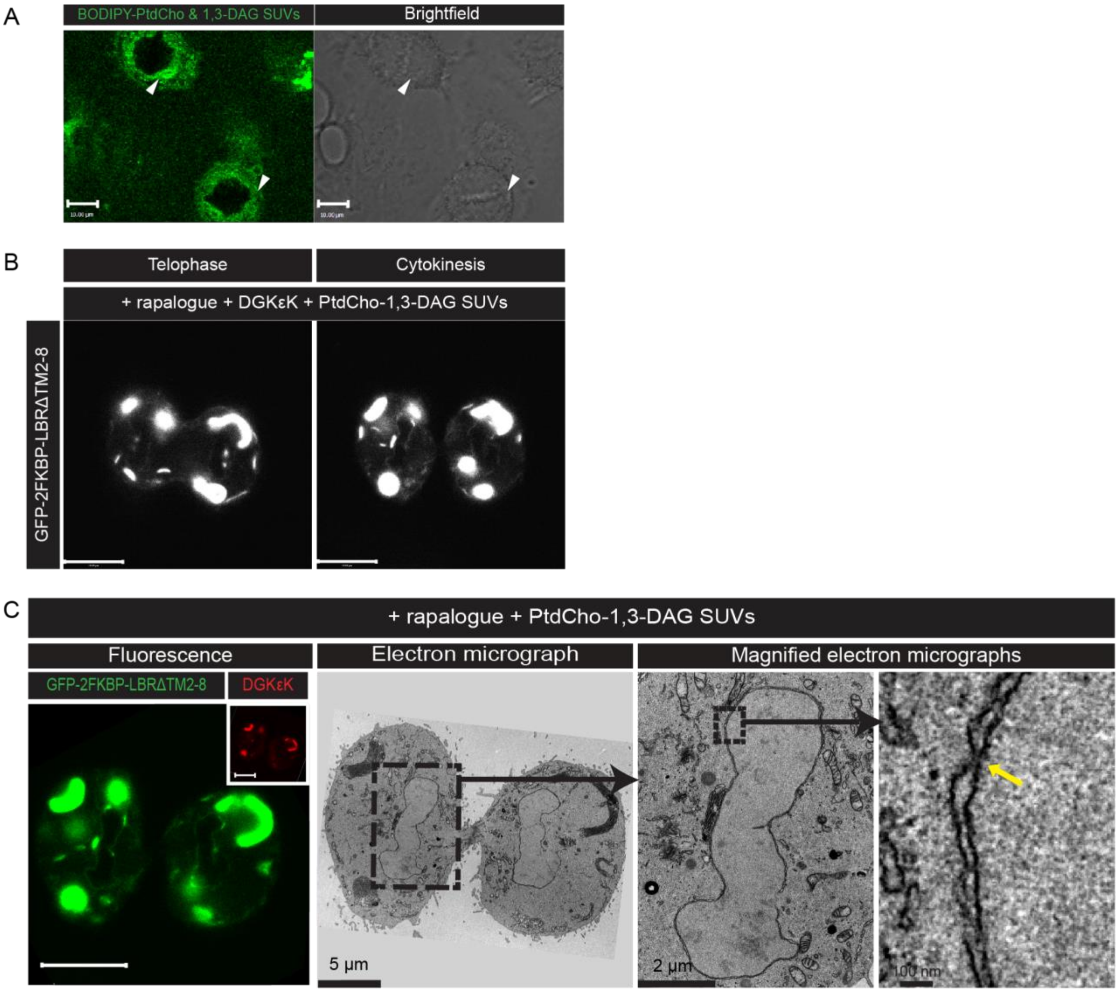

Figure 5.13 1,3-DAG rescues fragmented NE caused by DAG depletion

(A) Confocal image of metaphase HeLa cells 1 min post-addition of SUVs which consisted of BODIPY-PtdCho and unsaturated 18:1/18:1 1,3-DAG (80:20 mole%). Incorporation of SUVs was marked by the intracellular fluorescence of BODIPY (white arrows). (B) NE localisation of LBR during mitosis in rapalogue-treated, LBR and DGKεK co-expressing HeLa cells after addition of 1,3-DAG-containing SUVs, imaged by confocal microscopy (C) Ultrastructure of DAG-depleted, 1,3-DAG-containing SUVs-rescued cell fixed at cytokinesis, imaged by CLEM. LBR (green), DGKεK (red). The yellow arrow indicates a nuclear pore in the almost complete NE. Scale bar, confocal: 10 µm, EM: as indicated on the images. Images representative of n = 11 experiments. Rescue experiment done by Marie-Charlotte Domart (Cell Biophysics and EM unit, London Research Institute).

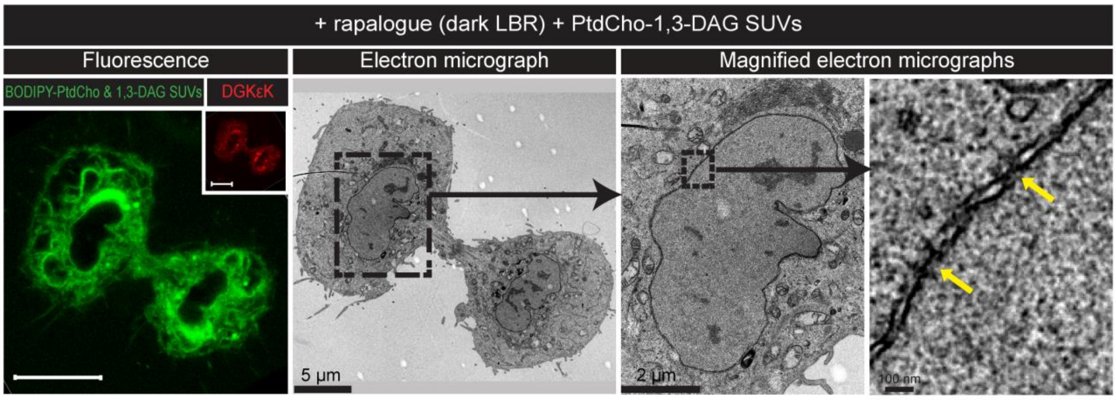

Figure 5.14 SUVs with higher proportion of 1,3-DAG completely rescue fragmented NE
A HeLa cell co-expressing dark LBR/DGKεK (red) was treated with rapalogue and rescued by SUVs (green) composed of PtdCho and 1,3-DAG (60:40 mole%). EM images show a complete NE with nuclear pores (yellow arrows) after rescue. Incorporation of 1,3-DAG-containing SUVs localised to the rescued NE. Scale bar, confocal: 10 μm; EM: as indicated on the images. Rescue experiment done by Marie-Charlotte Domart (Cell Biophysics and EM unit, London Research Institute).

Table 5.1 Quantification of NE phenotype of HeLa cells co-expressing LBR and DGKεK under different conditions

Condition	# independent single cell experiments	# cells co-expressing LBR-DGKεK	# (%)cells with complete NE	# (%) cells with fragmented NE
LBR/ DGKεK WT + rapalogue	10	25	6 (24%)	19 (76%)
LBR/ DGKεK.D434N + rapalogue	6	19	18 (94.7%)	1 (5.3%)
LBR/ DGKεK WT + rapalogue + 1,2-DAG-containing SUVs (Rescue experiment)	3	5	5 (100%)	0 (0%)
LBR/ DGKεK WT + rapalogue + 1,3-DAG containing SUVs (Rescue experiment)	8	53	47 (88.7%)	6 (11.3%)

Table adapted from Domart *et al.* (2012)

5.6 Discussion

5.6.1 The requirement of DAG at the reforming NE

In order for membrane compartments to have the required topology the membranes must exhibit curvature of the required relative amount. There are considerable studies suggesting the role of proteins in altering membrane curvature and organelle shaping (Voeltz *et al.*, 2006, Shibata *et al.*, 2009, Kozlov *et al.*, 2014). On the other hand, an asymmetric distribution of lipids or enrichment of lipid molecules in one of the lipid bilayer leaflets contributes to membrane curvature (Farsad and De Camilli, 2003, Farge and Devaux, 1992). To achieve a highly curved lipid bilayer, lipid with a conical shape such as DAG is required. DAG has a reduced head-to-tail ratio (negative spontaneous curvature) thus it facilitates the bending of membrane towards the head group. Localised DAG production is essential for NE formation in a cell-free assay (Dumas *et al.*, 2010, Barona *et al.*, 2005) and the fusogenic property of DAG has been demonstrated (Zhendre *et al.*, 2011, Barona *et al.*, 2005). Although the involvement of lipids have been understated in organelle shaping (Shibata *et al.*, 2009), we have shown by modulating specific lipid species required for generating membrane curvature, such as DAG, that they have an essential role in organelle shaping as well as membrane fusion.

The DAG reporter GFP-C1aC1b showed that DAG is present in the reforming NE during telophase in both HeLa and COS-7 cells and lipid mass-spectrometry confirmed the presence of unsaturated DAG species in the NE and ER. When DAG in the NE/ER was depleted using the rapalogue dimerisation tool, the NE was fragmented, and DAG was not detected in the NE. In addition, we demonstrated that the fragmented NE was due to a direct depletion of DAG rather than accumulation of PtdOH, by limiting the DAG precursor PtdIns(4,5)P_2 through SKIP. Similar result has also been shown in echinoderm cells (Byrne *et al.*, 2005, Domart *et al.*, 2012). A catalytically inactive lipid-modifying enzyme supported this argument as well. Furthermore, the severity of an aberrant NE phenotype corresponded to the expression level of DGKεK. The above findings suggest that DAG is essential for NE assembly.

CLEM analysis revealed large gaps in the reforming NE in the DAG-depleted cells. Our 3D model shows that the NE of a DAG-depleted early telophase cell resembled the NE of a control anaphase cell. Progression of mitosis did not allow the DAG-depleted cells to recover from its disrupted phenotype, indicated by the cell death in DAG-depleted cells. DAG had a role in ER shaping, as the source of the intense fluorescence was identified as multi-lamellar ER sheet by CLEM. Such phenotype might be due to the loss of negative membrane curvature provided by DAG, in which the ER was not able to form tubular structures without DAG.

Compared to protein knock-down or inhibitor treatment, our rapalogue dimerisation tool acutely modified membrane lipid components only at the NE and ER. Single cell experiments were performed and we achieved 76 to 95 % reproducibility (Table 5.1). In parallel to the DAG modulation in mammalian cells, similar findings were observed in unfertilised or fertilised egg membranes (Wang *et al.*, 2013). Microinjection of DGK and Synaptojanin 1 (a 5-phosphatase using PtdIns(4,5)P_2 as substrate) to sea urchin eggs resulted in an alteration of ER morphology and impaired NE assembly. Together, DAG depletion in mammalian cells and echinoderms by two different techniques concurred that DAG has a conserved role in NE assembly and ER structure modification.

5.6.2 DAG has a structural role in NE assembly

In mammals, the fragmented NE caused by DAG depletion was rescued by delivery of exogenous 1,2-DAG through SUVs. Incorporation of SUVs into the cells was rapid, indicated by the intracellular fluorescence of BODIPY-PtdCho 1 minute post addition. Rescued cells were able to form a complete NE with nuclear pores, and this indicates that the rescued NE is structurally and functionally complete. However, the ER of rescued cells retained the multi-lamellar phenotype. Such observation may be due to the fact the ER has a differential sensitivity to DAG depletion compared to the NE as well as the ER being a highly complex membrane compartment to reassemble.

Similarly, depletion of DAG in echinoderm embryos and oocytes affected nuclear membrane fusion as well as ER morphology but was rescued by the localised addition of DAG-containing SUV (Domart *et al.*, 2012). In both mammalian and echinoderm rescue experiments, there might be a possibility that the restored phenotype of the NE and ER was a result of PtdCho addition. However, DAG-containing SUVs prevented abnormal ER morphology caused by DAG-depletion whereas SUVs composed of 100% PtdCho could not (Wang *et al.*, 2013). Furthermore, SUVs containing PtdEtOH (phosphatidylethanolamine), a lipid estimated at half the degree of negative curvature as DAG, had intermediate rescuing abilities compared to DAG-containing SUVs (Wang *et al.*, 2013, Larijani *et al.*, 2014). Such observations suggest PtdCho has no effect in rescuing DAG-depletion.

The non-C1-binding DAG isomer 1,3-DAG was able to rescue a fragmented NE in DAG-depleted cells. This non-signalling DAG isoform confirmed that DAG has a structural role in addition to a signalling role in NE assembly. Moreover, an increased dose of 1,3-DAG improved the rescue. Similarly, when introducing 1,3-DAG to DAG-depleted eggs, normal NE and ER phenotypes were observed (Wang *et al.*, 2013). The dual role of DAG has been suggested by several groups (Wickner and Schekman, 2008, Allan *et al.*, 1978, Larijani and Poccia, 2009, Larijani *et al.*, 2014) but we are the first group to demonstrate its structural role in the regulation of NE structure in mammals.

DAG depletion alters the ability of membranes to form highly curved structures or undergo fusion. We propose that NE assembly or organelle shaping depends on both lipid and protein-dependent mechanisms. It was suggested that bent membranes may generate hydrophobic voids in its curved region, and to maintain an energetically favourable structure lipids with extreme spontaneous curvature are required to fill those voids (Kozlovsky and Kozlov, 2002). Since DAG exhibits an extreme spontaneous curvature and a rapid transbilayer movement (Bai and Pagano, 1997), it may serve as a good candidate to re-equilibrate across the bilayer in such a highly curved structure.

5.7 Summary

Using a rapalogue dimerisation device, we depleted DAG in the NE and ER of mammalian cells and this led to fragmentation of the reforming NE and affected the ER morphology, wherein these abnormalities were rescued by exogenous DAG. By using different DAG isomers, we demonstrated that in addition to its signalling role DAG also has a structural role in NE reassembly and organelle morphology. The structural role of DAG in NE assembly and ER shaping is conserved through the deuterostome superphylum, supported by related studies in echinoderms. In conclusion, this is the first study to demonstrate the dual roles of DAG in altering membrane curvature.

Chapter 6 Characterisation of fusogenic vesicles in mammalian cells

6.1 Introduction

Vesicles are small spherical organelles that consist of soluble cellular content enclosed by a lipid bilayer. Depending on their function, vesicles may have distinctive protein and/or lipid profiles. They are commonly involved in a variety of cellular activities such as exocytosis, endocytosis, intracellular transportation, and intercellular communication.

Many cellular compartments produce vesicles (Sundaramoorthy *et al.*, 2010, Christianson *et al.*, 2014, Scott *et al.*, 2014). Fusion events between vesicles and other membrane structures are widely reported and investigated (Woodbury and Hall, 1988, Brunger, 2001, Rizo and Rosenmund, 2008), and the production and fusion of vesicles plays an important role in maintenance of a functional cell.

Fusogenic vesicles that are involved in or essential for NE assembly were isolated from cell-free systems of different model organisms (Chapter 3). Recently, it has been reported that the nuclear localisation sequence (NLS) of nucleoplasmin recruits NE precursor MVs via importin α/β interaction in *Xenopus* egg extracts (Lu *et al.*, 2012). Vesicles may participate in different stages of NE assembly. In an echinoderm cell-free assay, MV1 initiates NE assembly by binding to chromatin (Collas and Poccia, 1996). Lu *et al.* (2012) suggested that vesicles derived from *Xenopus* egg extracts are involved in NE assembly at a later stage. However, the participation of vesicles in mammalian NE assembly has not been demonstrated *in vivo*.

Because of the following difficulties, there is no study pertaining to the role of vesicles in NE assembly done in live cells. First, it is impossible to distinguish subpopulations of vesicles by their morphology. Second, to identify fusogenic vesicles, protein and lipid markers are required. There are many lipid-binding domains with various affinities for the same lipid and this may lead to different observations of the lipid localisation (Chapter 4). Each lipid-binding domain needs to be chosen carefully for use as a lipid probe. Lastly, conventional light microscopy does not have enough resolution to identify vesicles even when they can theoretically be characterised by protein and lipid markers. Therefore, to identify MV1-like vesicles, a marker compatible with high resolution microscopy is required.

This chapter describes our investigation of the presence of vesicles which may be involved in mammalian NE assembly by electron tomography, and the quantitative analysis of putative MV1-like vesicles. We also tested a novel engineered tag that allows correlation of light microscopy with electron microscopy, in order to characterise fusogenic vesicles.

6.2 Quantification of vesicular structure in the vicinity of NE gaps

The role of DAG in NE assembly was demonstrated in Chapter 5 but the involvement of MV1-like vesicles in mammalian NE assembly remains unknown. We postulated that MV1-like vesicles are required to seal the gaps in a reforming NE by membrane fusion, and that these vesicles are likely to be present in the vicinity of NE gaps at late mitotic stages.

The ultrastructure of mitotic cells thus was examined by serial section TEM. Figure 6.1-A shows a HeLa cell fixed at telophase. The cell was resinated and cut into serial sections for micrographs acquisition. Serial micrographs were aligned and the cellular structures such as the NE, ER and centriole were manually selected on the micrographs based on their morphological features (segmentation). Figure 6.1-B shows the unmodified and segmented electron micrographs of the telophase cell. The ER and NE were selected based on their enhanced electron density on the micrograph and were distinguished by the presence of ribosomes and NPC on the membranes respectively. The centriole was selected based on its characteristic feature, a pair of perpendicular cylindrical structures, and the presence of 9 pairs of microtubule triplet in its cross section. In parallel, the NE gaps and putative vesicles were also segmented. Any opening in the reforming NE that was greater than 75 nm (the average lateral length of a NPC in the telophase cell) was segmented as a NE gap; a straight line was drawn from one edge of the NE gap to the other. A circular brush was used to select vesicles on the micrographs; any structure with a circular cross section and approximately equal diameter in *xy*- and *z*-direction was selected as a vesicle.

The segmentations were reconstructed into a 3D model which indicates how the vesicles were orientated relative to the reforming NE (Figure 6.1-C). Approximately 14,000 vesicles were selected throughout the cytoplasm of the cell. Some of which were very close to the NE gaps (Figure 6.1-B, white arrow) but some were further away. There was no obvious distribution pattern of these vesicles. Nevertheless, it is conceivable that among all marked vesicular structures, a subpopulation is MV1-like vesicles responsible for sealing the NE gaps. Vesicles involved in fusion events are more likely to be targeted to the gaps of the reforming NE. Hence, we focused on quantifying vesicles that were closer to the NE gaps, rather than those further away.

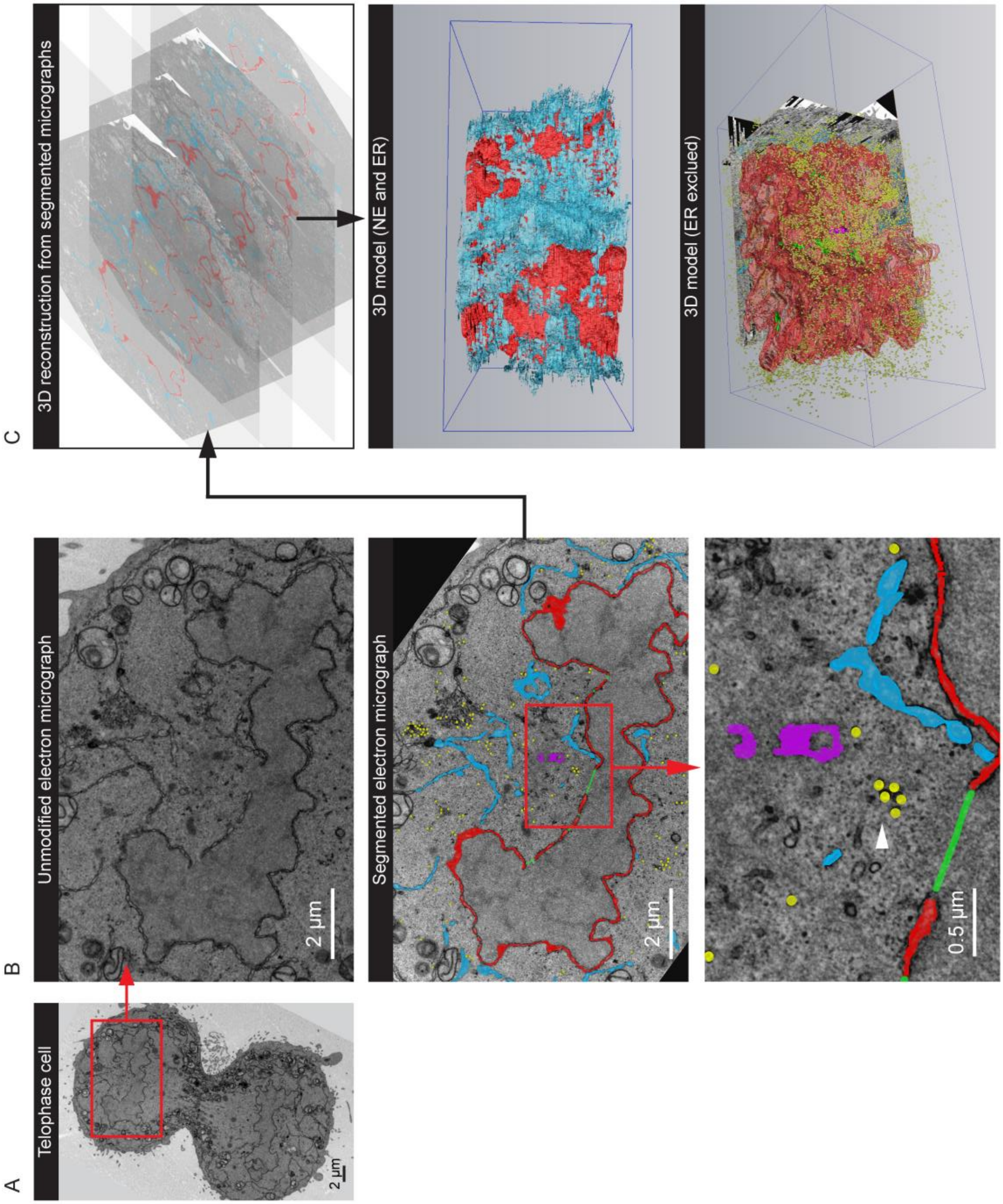
A
Telophase cell
2 µm
B
Unmodified electron micrograph
2 µm
Segmented electron micrograph
2 µm
0.5 µm
C
3D reconstruction from segmented micrographs
3D model (NE and ER)
3D model (ER exclued)

(Cont'd)

Figure 6.1 Numerous vesicles were found in the cytoplasm during mitosis

(A) Low magnification electron micrograph of a section taken through a HeLa cell fixed at telophase and preserved in resin. The cell was cut into serial 70 nm-thick-sections and imaged using a TEM. (B) The serial sections were aligned and manually segmented. Top panel depicts an unmodified electron micrograph. Middle panel depicts the segmented electron micrographs, of which the cellular organelles were segmented in different colours: NE (red), ER (cyan), centriole (purple); the NE gaps and vesicles were shown in green and yellow respectively. Bottom panel shows a segmented electron micrograph at high magnification in which the white arrow indicates a population of vesicles in the vicinity of a NE gap. (C) Segmentation of cellular organelles, NE gaps and vesicles were reconstructed into 3D models. The middle panel shows a 3D model of the reforming NE and ER. The bottom panel shows a 3D model of the NE, centriole, NE gaps and vesicles.

A systematic quantification helps to understand the spatial distribution of the vesicles. We compared the distribution pattern of the vesicles at the NE gaps versus the regions without gap. In addition, we compared the pattern among NE gaps of different sizes. The sizes of a NE gap were classified according to their total area. Figure 6.2 illustrates the method to calculate the total area of a NE gap. The length of the gap per section was measured and was multiplied by the depth of the micrograph (70 nm) to obtain the area per section. The area of the NE gap per section was summed to obtain the total area. In the telophase cell, the length of the NE gaps ranged from 76 nm to 977 nm and there were 22 small, 46 medium and 8 large NE gaps. The sizes and quantities of the NE gaps are summarised in Table 6.1. Small, medium and large NE gaps differed in their area by an order of magnitude accordingly.

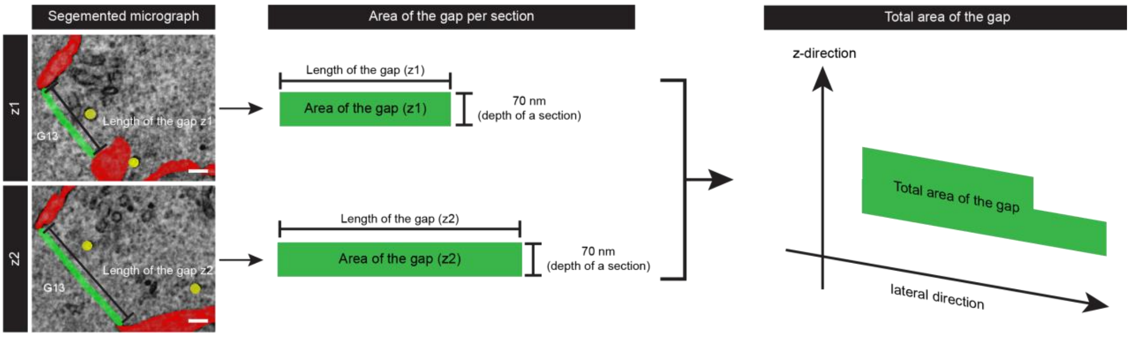

Figure 6.2 The size of a NE gap is defined by its area

To calculate the area of a NE gap, the length of the gap per section was measured and multiplied by 70 nm, which is the depth of the micrograph. The area of the NE gap per section was summed up to obtain the total area.

Table 6.1 The number and size of NE gaps in a telophase cell

Size	# of gaps	Min. area (nm^2)	Max. area (nm^2)	Mean area (nm^2)
Small gaps	22	5800	9900	7600 ± 300
Medium gaps	46	11000	82000	27000 ± 2700
Large gaps	8	100000	350000	220000 ± 32000

All values rounded to two significant digits.

Figure 6.3 depicts the method to determine the distribution pattern of the vesicles in the vicinity of the NE gaps and regions without gap. The vicinity referred to a circular sampling field with a radius of 1 μm; the radius was set at 1 μm so that the sampling field did not exceed the cell. The centre of the sampling field for a NE gap was one of its end points. The centre of the sampling field for a region without gap was a point chosen randomly by algorithm on the segmented NE, wherein the sampling field of a region without gap must not overlap with that of a NE gap. The number of vesicles in the sampling field and the distance of these vesicles from the centre of the sampling field were measured. The sampling field was divided into inner (radius = 0.5 μm) and outer (0.5 μm < radius < 1 μm) sections and the density of vesicles within these sections were calculated and summarised in Table 6.2.

The highest number of vesicles was found in the vicinity of the large NE gaps. There were 6.5-fold and 8.5-fold more vesicles in the vicinity of the large NE gaps compared to that of the small gaps and regions without gaps respectively (Table 6.2). Moreover, the mean number of vesicles in the vicinity of the NE gaps decreased as the size of gap decreased. Similarly, the vesicle density (#/μm^2) in the vicinity of the large NE gaps was the highest. In general, the vesicle density in the whole sampling field was approximately the same as the outer sampling field in all the NE gaps and regions without gap. For large and medium NE gaps, their inner sampling fields had higher vesicle density compared to the outer sampling fields. However, an opposite trend was observed in the small NE gaps and regions without gap.

Figure 6.4 shows the vesicle density (#/μm^2) in the inner and outer sampling fields of NE gaps and regions without gap. The vesicle density at the large NE gaps was significantly higher than that in the NE gaps of other sizes and regions without gap, in both inner and outer sampling fields. The vesicle density in the inner sampling field of the large NE gaps was 10 times higher than that of the small NE gaps and regions without gap. Such observation suggests a correlation between number of vesicles and the size of the NE gaps.

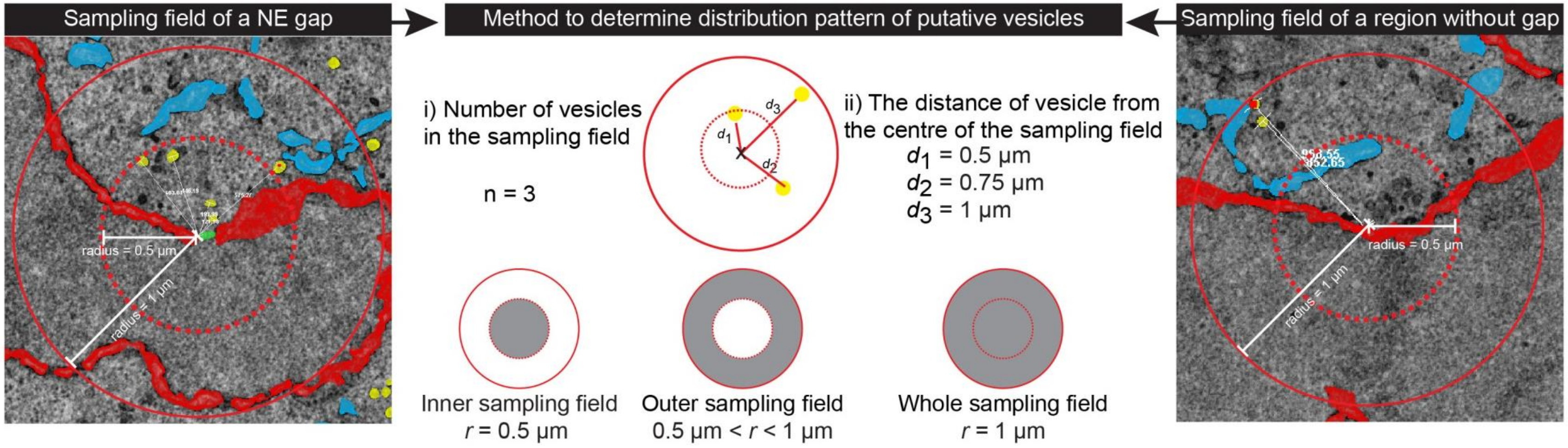

Figure 6.3 Method to determine the distribution pattern of vesicles in the vicinity of NE gaps and regions without gap

The vicinity of NE gaps and regions without gap was defined by a circular sampling field with a radius of 1 µm (circle of solid red line). The centre of the sampling fields for NE gaps was one of the end points of the gap; the centre of the sampling fields for regions without gap was a random point on the segmented NE. The sampling fields were further divided into inner (r = 0.5 µm, circle of dashed red line) and outer (0.5 µm < r < 1 µm) sampling fields, as indicated by the grey area shown in the middle panel. The number of vesicles and the distance of vesicles from the centre were measured in order to calculate the vesicle density (#/µm^2) in the sampling field.

Table 6.2 Vesicle density in the vicinity of NE gaps and regions without gap

	# of gaps / regions without gap	Mean # vesicles [whole sampling field]	Vesicle density (#/μm^2) [whole sampling field]	Vesicle density (#/μm^2) [inner sampling field]*	Vesicle density (#/μm^2) [outer sampling field]^
Regions without gap	10	3.80 ± 1.10	1.210 ± 0.35	0.762 ± 0.21	1.358 ± 0.45
Small gaps	22	2.91 ± 0.46	0.926 ± 0.15	0.752 ± 0.18	0.984 ± 0.16
Medium gaps	46	9.09 ± 1.24	2.893 ± 0.39	3.435 ± 0.77	2.715 ± 0.37
Large gaps	8	25.00 ± 6.34	7.966 ± 2.24	9.872 ± 2.81	7.330 ± 1.91

*inner sampling field ($r = 0.5$ μm); ^ outer sampling field (0.5 μm $< r < 1$ μm)

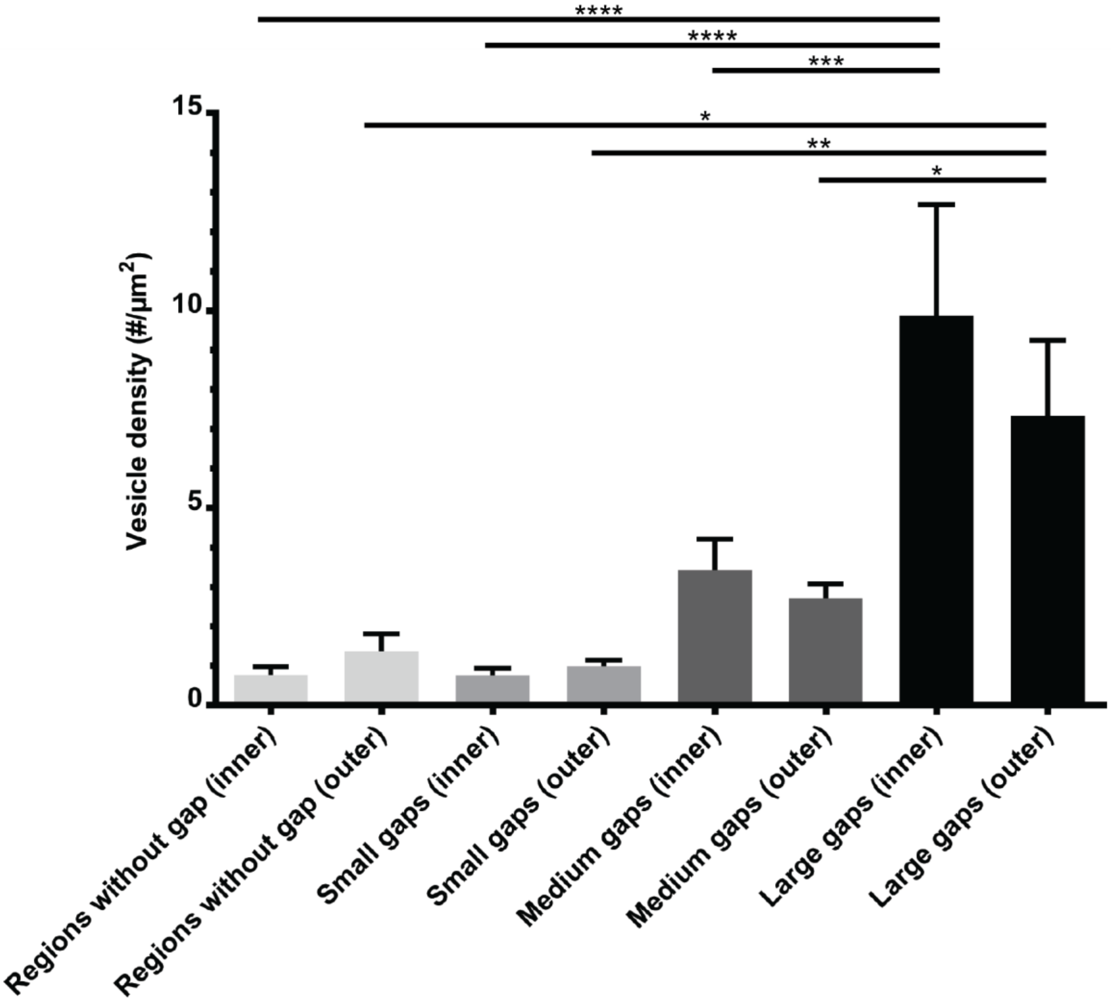

Figure 6.4 The vesicle density in the vicinity of large NE gaps is significantly higher than that in other regions

The vesicle density in the inner and outer sampling field of NE gaps of various size and regions without gap was plotted into a bar chart. The data was analysed by one way-ANOVA. The vesicle density in the inner sampling field of large NE gaps was significantly higher than that of small, medium NE gaps and regions without gap. Asterisk scale: * $P \leq 0.05$, ** $P \leq 0.01$, *** $P \leq 0.001$, **** $P \leq 0.0001$.

The physical characteristics of the vesicles may provide useful information to target MV1-like vesicle, therefore the diameter of the vesicles in the inner sampling field of all NE gaps was measured. For each vesicle, its diameters in *x*- and *y*- direction were measured and averaged as its true diameter. The diameters of all measured vesicle were plotted into a histogram with an interval of 5 nm (Figure 6.5). The diameter of the vesicles ranged from 40 to 80 nm, and the average diameter was 57 nm. Among the 164 measured vesicles, the average diameter was approximately 55 nm. The actual binding of these vesicles to the NE was not detected so that it is difficult to conclude that they are involved in fusion events. Thus, the identity of these vesicular structures will need further validation.

# vesicles in the vicinity of the NE gaps	Min. diameter (nm)	Max. diameter (nm)	Mean diameter (nm)
164	39.60	79.92	56.86 ± 0.49

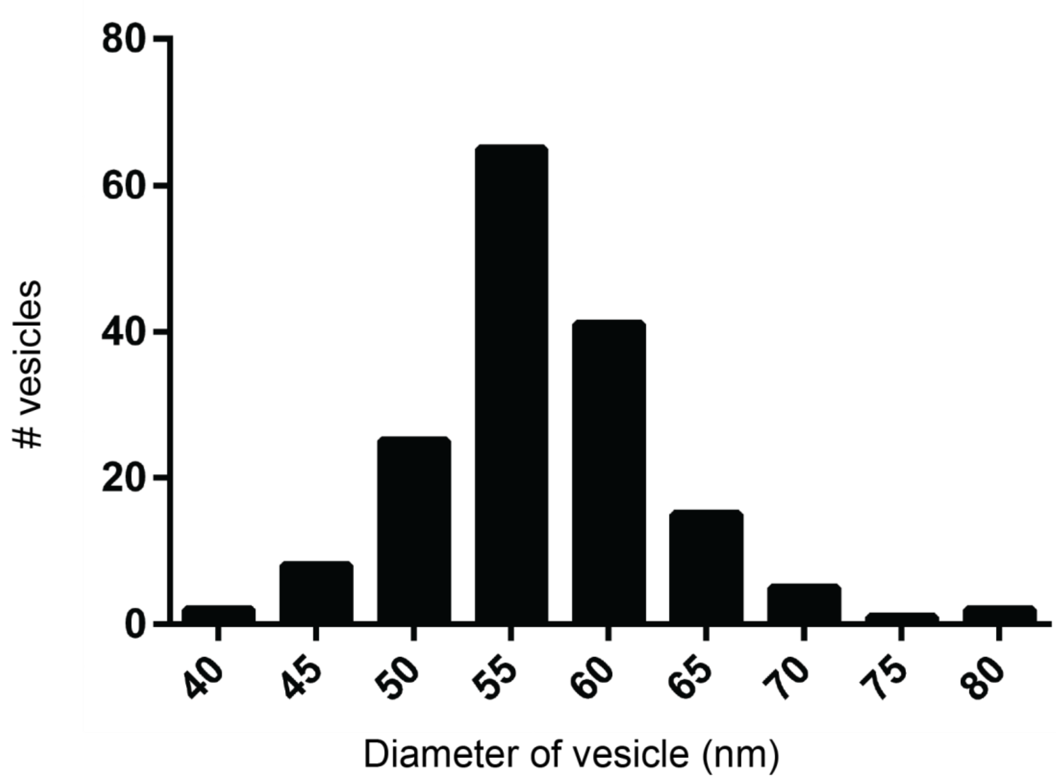

Figure 6.5 Most vesicles have a diameter of about 55 nm

The diameter of all vesicles in the inner sampling field of the NE gaps was measured. The diameter of a vesicle was averaged from its *x*- and *y*- diameter, and plotted into a histogram with a 5 nm interval. Among the 164 vesicles, their diameter ranged from 40 to 80 nm and most of the vesicles (n = 65) affiliated to the 55 nm-group.

6.3 Presence of vesicles in the vicinity of the reforming NE

Electron tomography (ET) was also used to identify vesicles in telophase cells. This technique is usually used to acquire high resolution volume data (Baumeister et al., 1999). Figure 6.6 illustrates the principle of ET. One major advantage of ET is that it has a virtual *z*-resolution several orders of magnitude higher than the *z*-resolution of serial section TEM. Virtual *z*-resolution of ET can reach 2.4 Å at the best performance (Scott et al., 2012) whereas the resolution of conventional TEM varies with different factors but is usually within the range of 20 to 40 Å (Milne et al., 2013). In serial section TEM, imperfect alignment of ultrathin sections could lead to inaccurate reconstruction of the 3D architecture of cellular structure but this could be avoided using ET since a relatively thick section was cut for tomogram construction. Moreover, the cross section of vesicles and tubular structures is very similar, both of which appear to be a circle and may have similar lateral diameter, and this could lead to misidentification of cellular structures. With better virtual *z*-resolution, ET was used to distinguish vesicles from various membrane components encompassing cisternae, tubules and saddle.

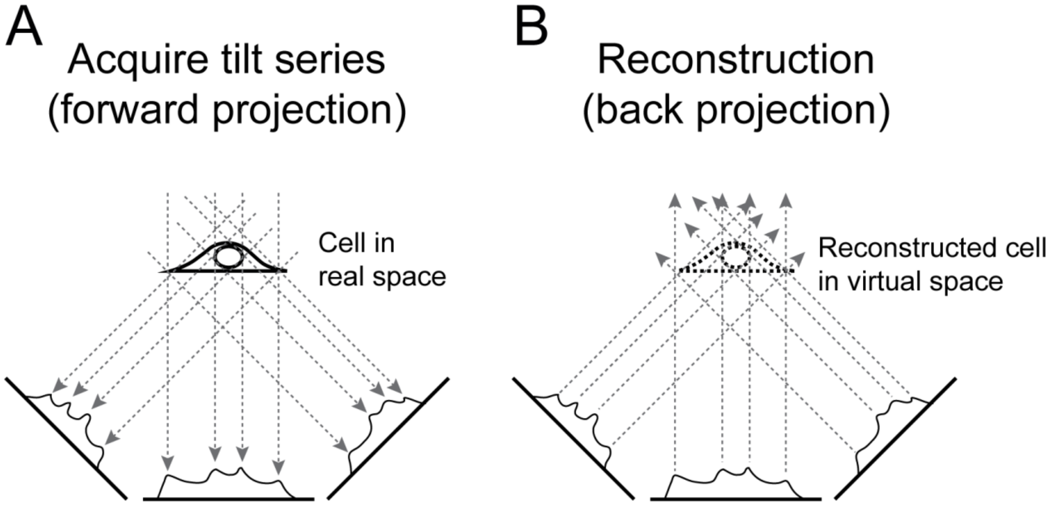

Figure 6.6 Principle of electron tomography

(A) A section through a cell is imaged at different angles (±70° tilt range), resulting in a series of 1D projection images, from which the intensity peaks are derived. Broken arrows pointing towards the intensity peaks indicate selected projection rays from high contrast features of the section. The pattern of the intensity peaks changes depending on the angle at which the section is imaged. B) The 1D projection images are projected back into the virtual space of a tomogram, where the projected rays are indicated by broken arrows pointing towards the virtual space. The section of the cell is reconstructed computationally into a 3D volume, indicated by the cell shown in broken lines. Adapted from Matt Russell (EM unit, London Research Institute).

Figure 6.7 and Figure 6.8 are two independent electron tomography analyses showing the regions of gaps identified from early telophase cells. Serial sections were cut through the cells and a 200 nm-thick mid-section from each cell was cut for tomogram construction. At low magnification, the NE appeared complete but discontinuities of the reforming NE (yellow arrows) can be seen at higher magnification (Figure 6.7-A & Figure 6.8-A).

Figure 6.7-B and Figure 6.8-B display the snapshots of the virtual *z*-sections from the tomograms. Top panels reveal the unmodified snapshots and bottom panels are the segmented snapshots. The NE (red) and its proximal vesicular structures (yellow) were segmented based on their enhanced electron density; the nucleus and the cytoplasm can be distinguished by their texture. A spherical object, such as a vesicle, will not extend more than its diameter in any direction (*x*-, *y*-, *z*-) in a space. A 55 nm vesicle can only be visualised within a small cubical volume (55 x 55 x 55 nm) when the visual field is progressing through any axes. In contrast, a tubular structure with the same diameter can be visualised throughout the 200 nm section when the visual field is progressing along its longitudinal axis. The membrane structures in close proximity to the NE gap were only observed within a small cubical virtual space (white arrows). Therefore, it is valid to conclude that these membrane structures were vesicles and not tubules. Multiple vesicles were found in close proximity to the NE gap of the early telophase cells.

The segmented tomograms were constructed into 3D models. Figure 6.7-C & Figure 6.8-C are snapshots of the 3D models at different angels, indicating the location of the vesicles relative to the reforming NE. Video 6.1 and Video 6.2 are videos showing the *z*-direction progression of the tomograms and the full rotation of the reconstructed 3D models. In conclusion, electron tomography confirmed the presence of vesicles in the vicinity of NE gaps during NE assembly. However, without a phosphoinositide/DAG reporter, the identities of these vesicles are still unknown. Therefore, the vesicles were probed by phosphoinositide or DAG-binding domain conjugated to a novel tag that allows visualisation of ultrastructure at EM resolution.

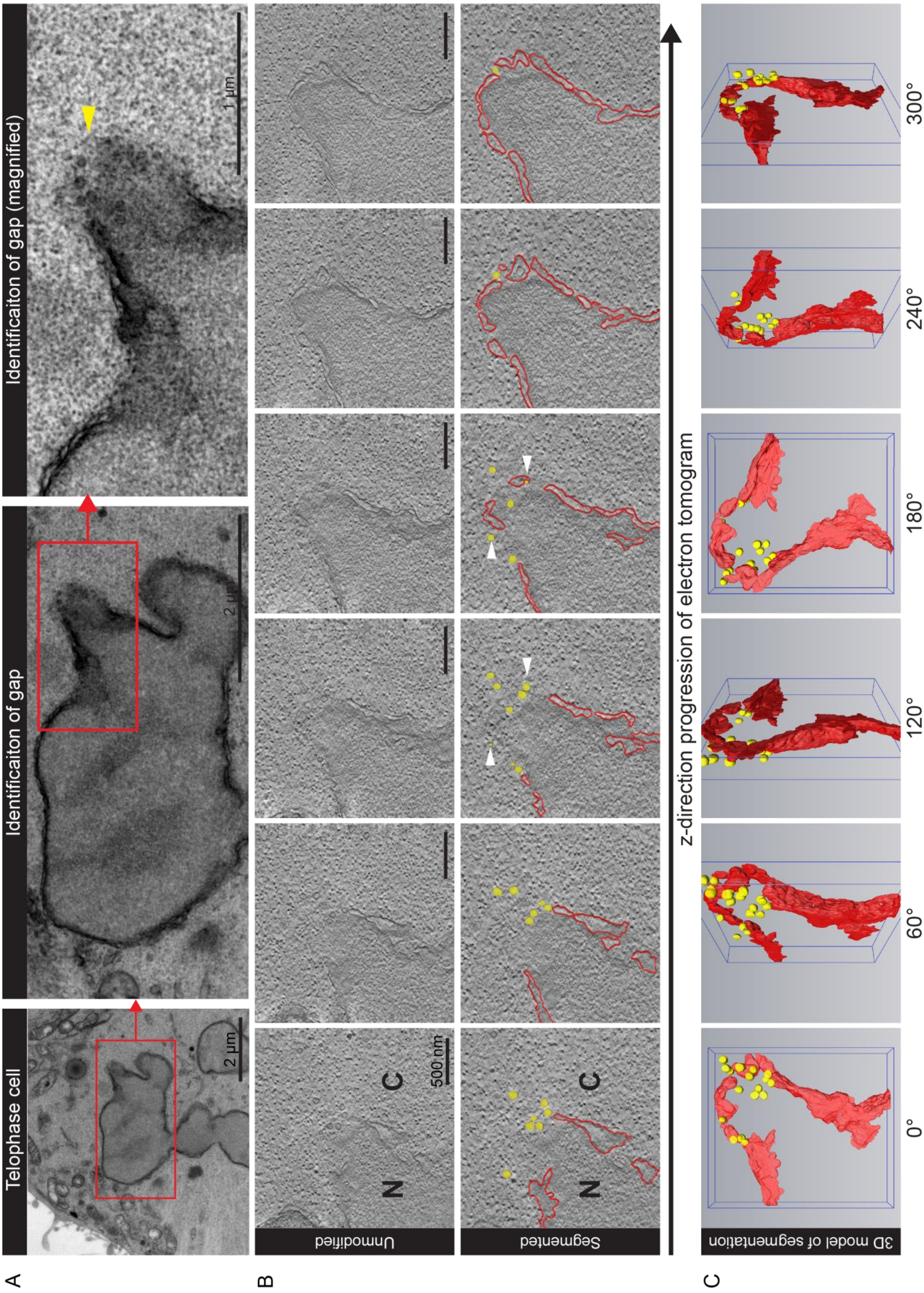
A
Telophase cell
2 µm
Identificaiton of gap
2 µm
Identificaiton of gap (magnified)
1 µm
B
Unmodified
Segmented
C
N
500 nm
z-direction progression of electron tomogram
C
3D model of segmentation
0°
60°
120°
180°
240°
300°

(Cont'd)

Figure 6.7 Multiple vesicles are observed at the gap of a reforming NE #1

(A) Electron micrographs from a 200 nm-thick section taken through a HeLa cell fixed at early telophase. A gap was identified (yellow arrow), and the section was analysed by ET to produce an electron tomogram and a corresponding video (Video 6.1-A). The tilt range of the tomogram is from -68 to +60 degrees, with final pixel size of 0.79 nm in *xy*. The final tomogram was ~163 nm in thickness after trimming the top and bottom. (B) Snapshots of the unmodified electron tomogram (upper panels) and the corresponding segmented version (lower panels). The reforming NE was segmented in red, with vesicles shown in yellow. White arrows indicate virtual space occupied by the vesicles along the *z*-axis. N: nucleus, C: cytoplasm. (C) 3D model snapshots of the reforming NE and proximal vesicles at different angles. Scale bar, as indicated in the figure.

Video 6.1 Multiple vesicles are observed at the gap of a reforming NE #1

Electron tomogram and segmentations described in Figure 6.7 were made into videos. Video 6.1-A shows the *z*-progression of the unmodified tomogram. Emergence and disappearance of the vesicles were observed from 0:04 to 0:08 s as the visual field progressed. Video 6.1-B displays the 3D model of the segmented gap region at full rotation. Videos are played at a speed of 10 frames per second.

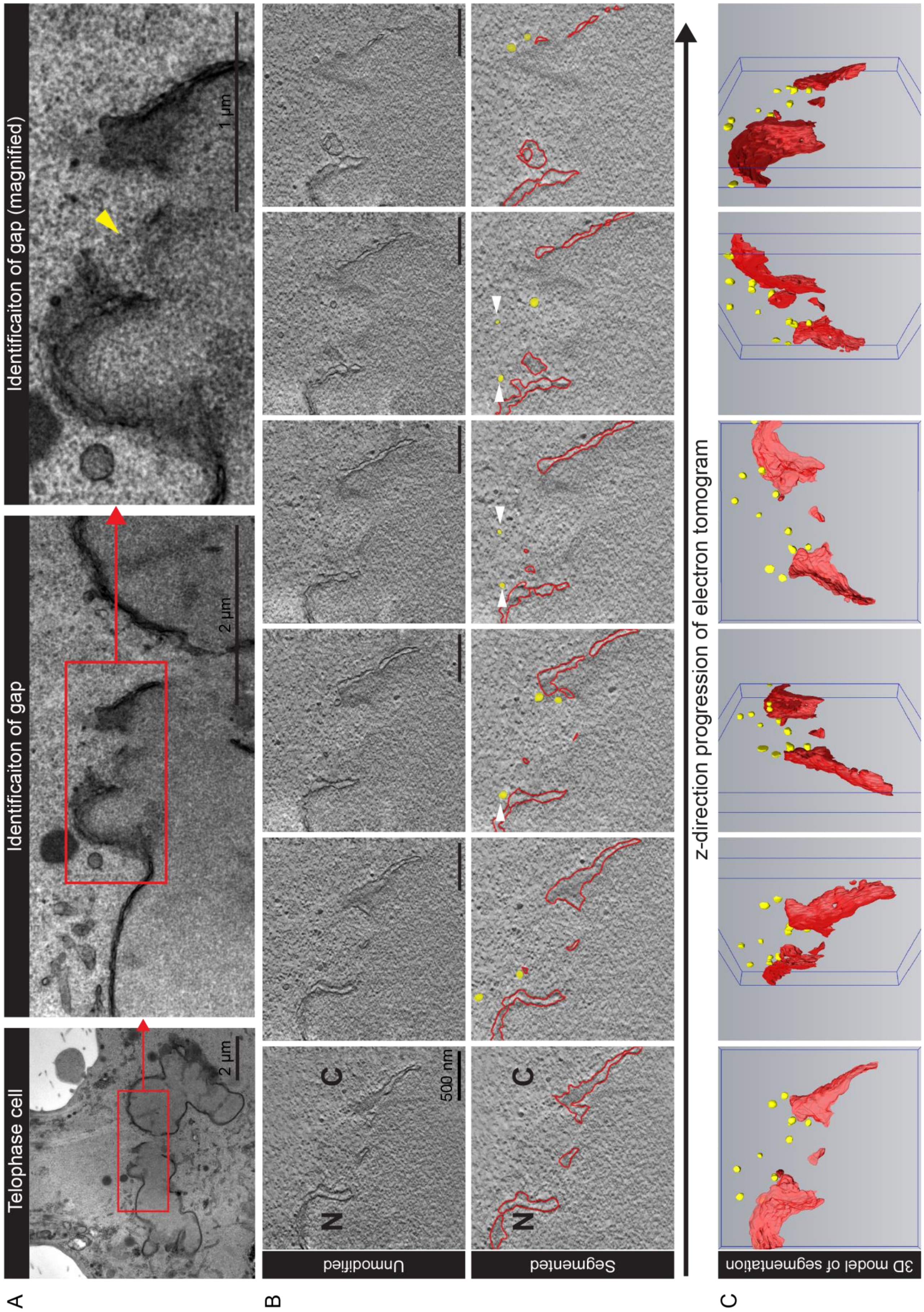
A
Telophase cell
2 µm
Identificaiton of gap
2 µm
Identificaiton of gap (magnified)
1 µm
B
Unmodified
Segmented
N
C
500 nm
z-direction progression of electron tomogram
C
3D model of segmentation
0°
60°
120°
180°
240°
300°

(Cont'd)

Figure 6.8 Multiple vesicles are observed at the gap of a reforming NE #2

Electron micrographs from a 200 nm-thick section taken through the same HeLa cell (different region) fixed at early telophase. Figure description is identical to Figure 6.7.

Video 6.2 Multiple vesicles are observed at the gap of a reforming NE #2

Electron tomogram and segmentations of region #2 were made into videos. Video 6.2-A shows the *z*-progression of the unmodified tomogram. Emergence and disappearance of the vesicles were observed throughout the visual field progression. Video 6.2-B displays the 3D model of the segmented gap region #2 at full rotation. Videos are played at a speed of 10 frames per second.

6.4 MiniSOG – a novel tool to characterise fusogenic vesicles at EM resolution

Fluorescent protein-fused lipid-binding domains allow visualisation of fusogenic lipids using light microscopy (Chapters 4 and 5). However, as the presumed fusogenic vesicles are very small (55 nm in diameter), they fall below the resolution limit of light microscopy. Therefore, a tool is required to correlate the functional localisation of phospholipids or DAG using light microscopy with its structural context using EM. Several techniques have been developed to specifically target cellular components in EM such as immuno-labelling (Roussel and Nussbaum, 1982), quantum dots made of electron dense molecules (Roussel and Nussbaum, 1982) and engineered probes which are photo-convertible to produce EM detectable signals (Giepmans, 2008). Most of these methods are not trivial and require a long time to optimise.

Immuno-labelling is a technique commonly used to probe a specific protein or lipid in cellular compartments. For instance, recombinant PH domains combined with anti-GST immunogold had been used to detect PtdIns(3,4)P_2 (Watt *et al.*, 2004) and PtdIns(3,4,5)P_3 (Lindsay *et al.*, 2006). Typical immuno-labels are secondary antibodies conjugated to gold or other heavy metals, or to other molecules which generate electron density from DAB/HRP reactions. However, immuno-labelling has several limitations. First, immuno-labelling is restricted by the availability of suitable antibodies. High affinity and high specificity interaction between immuno-label and antigen is not always guaranteed. Moreover, during EM sample preparation chemical fixation may destroy or mask the antigen (D'Amico *et al.*, 2009) and heavy metal staining may destroy reactivity of immuno-labels (Wright and Rine, 1989). Although pre- or post-embedding immuno-labelling could maximise the performance of immuno-labels, it requires thorough understanding of the structures of interest (De Paul *et al.*, 2012). Lastly, most immuno-labels are large molecules. For them to enter a cell, permeabilisation by detergent is required. Detergents would extract the lipid(s) of interest or damage the native cellular structures (Chapter 4). Hence, an alternative tool is required.

MiniSOG is a genetically engineered tag derived from a flavoprotein domain which produces singlet oxygen molecules upon photo-excitation, and can be expressed as a fusion protein (Shu *et al.*, 2011). The mechanism of photosensitised production of singlet oxygen and generation of EM contrast by miniSOG is shown in Figure 6.9.

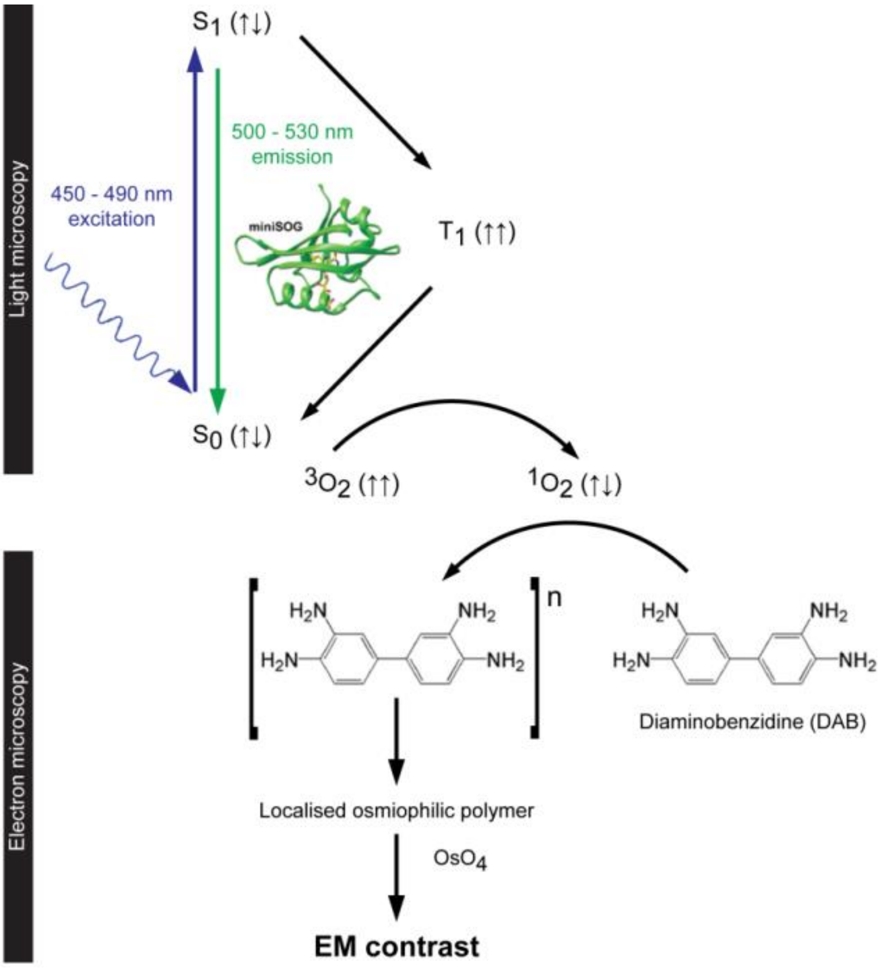

Figure 6.9 Photosensitised production of singlet oxygen by miniSOG to enhance EM contrast
MiniSOG at ground state (S_0) can be illuminated by a 450 – 490 nm light source to reach the excited singlet stage (S_1). Energy released from S_1 to S_0 generates fluorescence emission at 500 – 530 nm. Energy can be transferred from S_1 to a less excited stage T_1 (triplet stage with 2 unpaired electrons). When energy is released passing from T_1 to S_0, ground stage oxygen ($^3O_2$) is excited to singlet oxygen ($^1O_2$) simultaneously. DAB will react with the singlet oxygen and precipitate as localised polymers, which can be stained with osmium tetroxide (OsO_4) to generate EM contrast. ↑↓, paired electrons. ↑↑, unpaired electrons. Imaged adapted from Shu *et al.* (2011).

We developed several miniSOG fusion proteins as probes to target DAG and PtdIns(3,4,5)P_3 in subcellular compartments. Three miniSOG constructs were offered by the Tsien's group: the first contains a single miniSOG domain at the C terminus, the second contains tandem miniSOG domains at the N terminus, and the third contains tandem miniSOG domains at the C terminus. Herein the single and tandem miniSOG are referred as SOG and tSOG respectively. The localisation of miniSOG-fused GRP1^{PH} domain (PtdIns(3,4,5)P_3 marker) was covered in Chapter 4. This chapter will focus on the localisation of the miniSOG-fused DAG probe. A summary diagram of these constructs is shown in Figure 6.10-A.

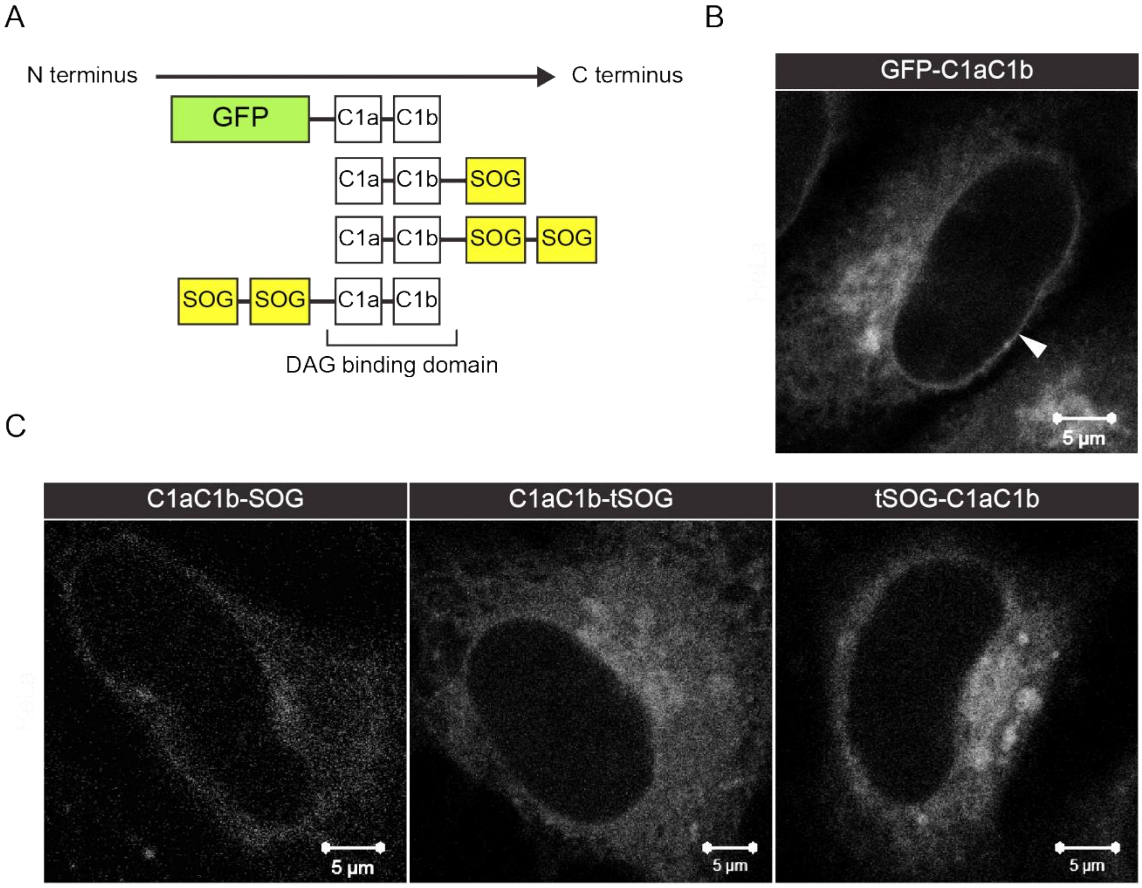

Figure 6.10 Fluorescence of miniSOG fusion proteins is weak

(A) Schematics of PKCε^{C1aC1b} domain fused to different tags; length of the domains is in scale with the number of base pairs. Localisation of (B) the established DAG probe GFP-C1aC1b and (C) different miniSOG-fused C1aC1b domains in HeLa cells. Cells were transiently transfected with 500 ng DNA construct for 16 h and imaged live by confocal microscopy. NE (white arrow), ER and Golgi localisation were detected in cells transfected with GFP-C1aC1b. The NE and ER localisation were almost absent in the cells transfected with different miniSOG conjugated probes, only a minor fluorescence was retained in the peri-Golgi region of the cells transfected with the tSOG-conjugated probes. Scale bar, 5 µm.

6.5 Localisation of miniSOG fusion proteins

The GFP-C1aC1b construct is an established DAG reporter and it localises to the NE, ER and Golgi (Domart *et al.*, 2012). However, the fluorescence of miniSOG-fused C1aC1b photobleached rapidly, resulting in weak fluorescent signals (Figure 6.10-B). Thus, it was difficult to determine the DAG localisation using these probes. Although tSOG-fused C1aC1b domains had slightly improved fluorescence and photobleached less rapidly, stable fluorescent signals are required to trace localised production of DAG during mitosis. Martell *et al.* (2012) added a second fluorescent protein to miniSOG-fused domains in order to improve its fluorescent signals. Similarly, we added GFP to the miniSOG-fused C1aC1b constructs (Figure 6.11-A).

Figure 6.11-B & C depict the localisation of C1aC1b tagged with both GFP and miniSOG. GFP-C1aC1b and GFP-C1aC1b-SOG expressed similarly in both HeLa and COS-7 cells, with a clear localisation to the NE (white arrows), ER (green arrows) and Golgi (yellow arrows). Localisation of GFP-C1aC1b-tSOG was comparable to that of GFP-C1aC1b but intense DAG patches, an over-expressed phenotype of C1aC1b, were also observed (red arrow). tSOG-GFP-C1aC1b displayed a punctate localisation to the ER but did not localise to the NE. These results suggest that localisation of miniSOG fusion protein can be affected by the orientation of miniSOG in the construct. Furthermore, a non-DAG-binding C1aC1b was also tagged with miniSOG. Figure 6.12 shows that GFP-C1aC1b.W264G-SOG localised homogenously in the cytoplasm and nucleus of the cells but not to any membranes compared to the WT construct. This non-DAG-binding construct served as the negative control in the photo-oxidation experiments.

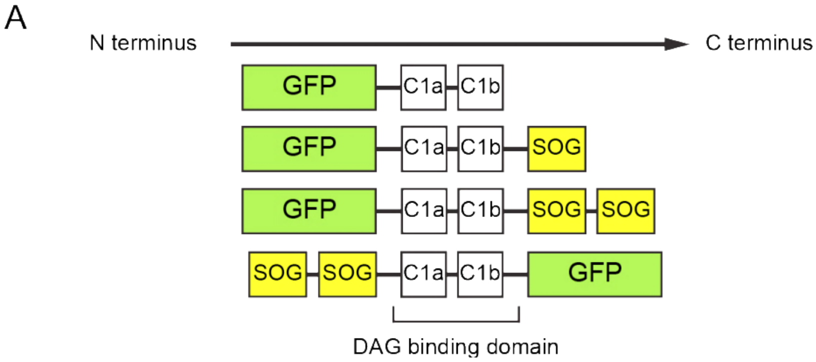

(Cont'd)

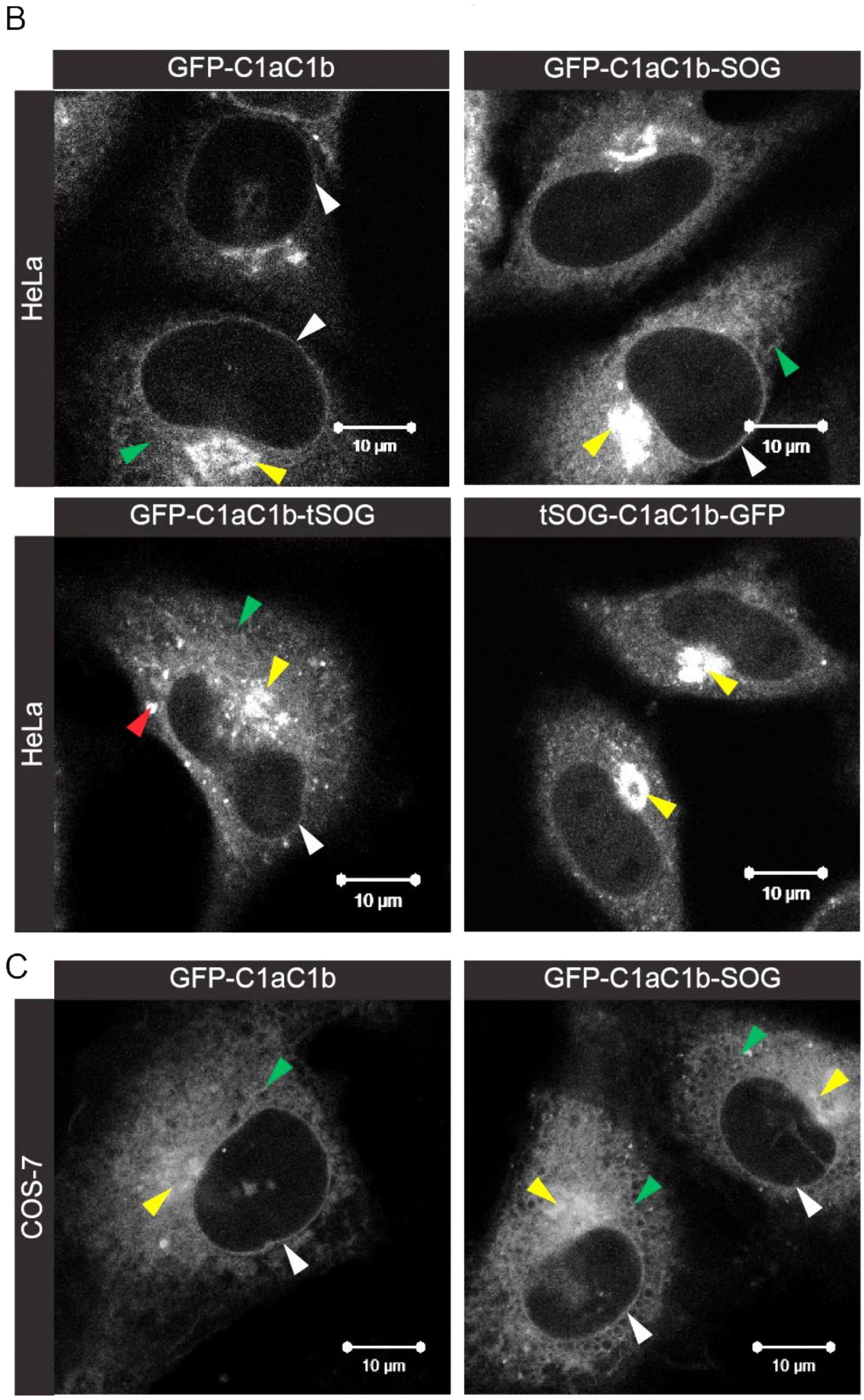

Figure 6.11 GFP tag improves fluorescence of miniSOG fusion proteins

(A) Schematics of PKCε^{C1aC1b} domain fused to both GFP and miniSOG tags; length of the domains is in scale with the number of base pairs. Localisation of these DAG probes in (B) HeLa and (C) COS-7 cells. The cells were transiently transfected with 250 ng DNA construct for 16 h. Identical NE (white arrows), ER (green arrows) and Golgi (yellow arrows) localisation were observed in GFP-C1aC1b and GFP-C1aC1b-SOG transfected cells. The red arrow indicates a patch of intense DAG localisation in a GFP-C1aC1b-tSOG transfected cell. Confocal light microscopy images were acquired in live cells. Scale bar, 10 µm.

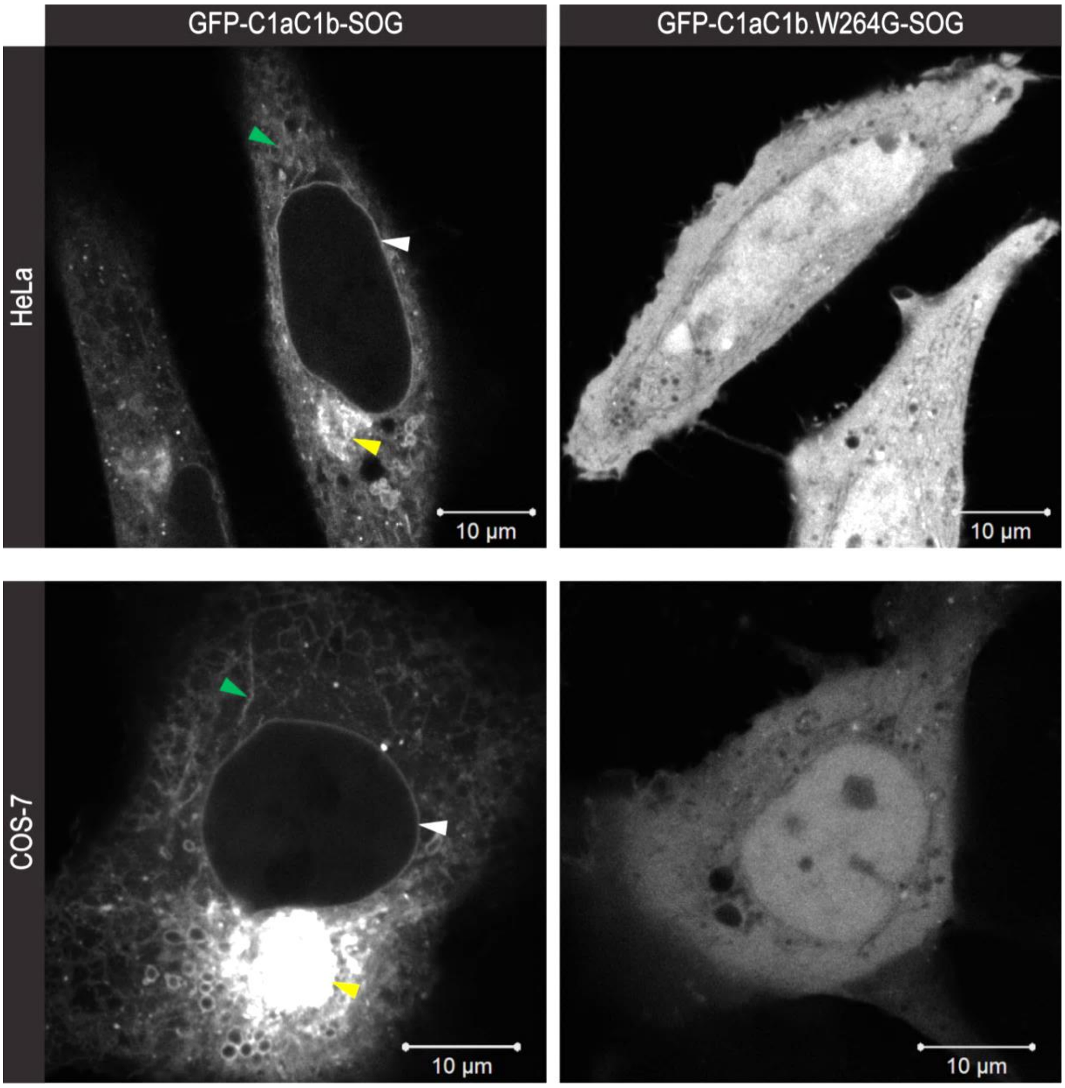

Figure 6.12 Mutant DAG probe shows no localisation to the NE, ER and Golgi
HeLa and COS-7 cells were transiently transfected with 250 ng DNA construct for 16 h. In HeLa and COS-7 cells transfected with GFP-C1aC1b-SOG, DAG localised at the NE (white arrows), ER (green arrows) and Golgi (yellow arrow). When transfected with the non-DAG-binding mutant GFP-C1aC1b.W264G-SOG, DAG localisation was absent from the NE, ER and Golgi in both HeLa and COS-7 cells. Confocal images were acquired in live cells. Scale bar, 10 μm.

6.6 Optimisation of miniSOG photo-oxidation and EM sample preparation

GFP-C1aC1b-SOG and GFP-C1aC1b expressed similarly (Figure 6.11-B & C) therefore GFP-C1aC1b-SOG was used as the probe in the photo-oxidation experiments. Photosensitised production of singlet oxygen requires a highly oxygenated environment for a good yield (Ruiz-Gonzalez *et al.*, 2013). To prevent the heating of samples caused by high energy wavelengths of light, a cooling system is also necessary. Figure 6.13 shows the customised photo-oxidation setup used in the following experiments (constructed by Christopher Applebee, Cell Biophysics Laboratory, London Research Institute and Biophysics Institute Bilbao). Samples were constantly oxygenated in a Petri dish chamber and cooled by a steel water jacket during photo-oxidation.

Table 6.3 lists the optimised procedure for photo-oxidation and EM sample preparations. Briefly, miniSOG fusion protein-transfected cells were fixed, photo-oxidised and embedded in resin for serial sectioning before acquisition of EM images. Many steps in the procedure required optimisation, including fixative concentration, photo-oxidation duration, and the concentration and combination of heavy metal staining reagents. Given the long protocol, optimisation of photo-oxidation and EM sample preparation was performed in interphase cells instead of mitotic cells. During photo-oxidation, the singlet oxygen generated by miniSOG reacts with DAB to produce a brown precipitate. Figure 6.14 shows that the cells transfected with miniSOG fusion protein can be distinguished from untransfected cells by their colour after 20 min photo-oxidation.

In the untransfected cells, EM contrast in the membrane compartments was due to osmium tetroxide staining; in the transfected cells, EM contrast of DAG enriched membranes was due to both osmium tetroxide staining and the miniSOG reaction products. Enhanced EM contrast was observed in the peri-nuclear regions of GFP-C1aC1b-SOG transfected cells, and within these regions some vesicles showed a slightly higher electron density (yellow arrows). Although the photo-oxidation reaction had worked, the structures of interest were not clearly distinguished from the rest of the cellular components with any degree of confidence.

In the initial experiments, photo-oxidised cells were stained with 1% osmium tetroxide and then stained *en bloc* with 2% uranyl acetate before serial sectioning. Both osmium tetroxide and uranyl acetate are heavy metal staining reagents that bind to proteins and lipids to allow EM visualisation. Osmium tetroxide is also a tertiary fixative for biological samples. We suspected that when the samples were stained by 1% osmium tetroxide, the background EM contrast might be too strong thus masked the EM contrast provided by the miniSOG reaction products. Therefore, a reduced background contrast might increase the chance to identify miniSOG reaction products from other cellular components.

We refined the protocol by decreasing the concentration of osmium tetroxide to 0.2% in the primary staining step. In addition, in preference to *en bloc* staining, samples were incubated with 2% uranyl acetate after serial sectioning as this offered more control over the level of uranyl acetate staining (Table 6.3, steps 14 & 24).

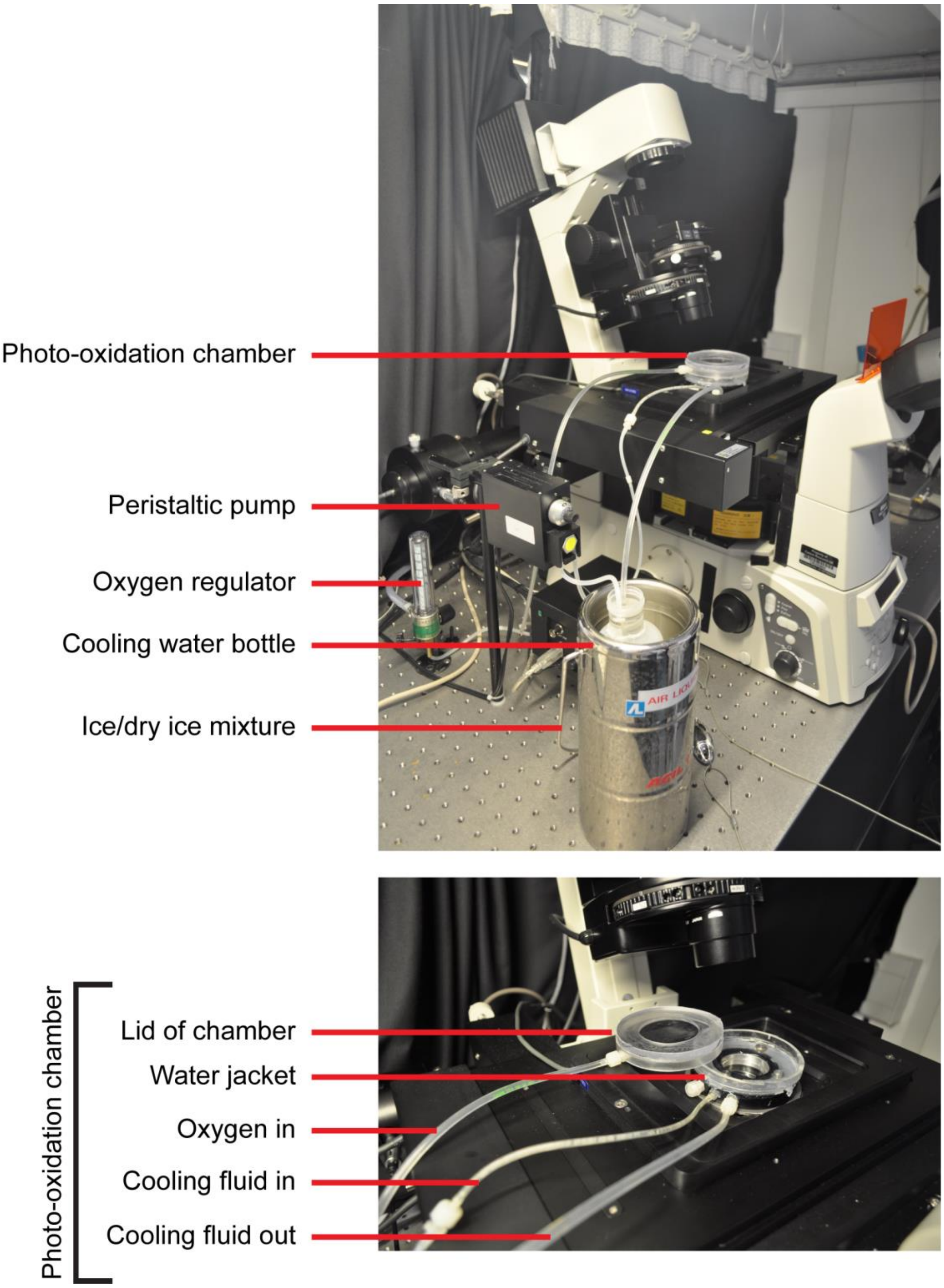

Figure 6.13 Photo-oxidation setup for miniSOG probes

Top: The customised setup for photo-oxidation comprised two major components. 1) An oxygen source controlled by a regulator and connected to the lid of the photo-oxidation chamber. 2) A cooling system to prevent the sample from overheating. **Bottom:** A close up of the photo-oxidation chamber. The chamber holds a 35 mm Petri dish; the dish is surrounded by a metal water jacket. Cooling water is circulated in the water jacket by the peristaltic pump. Setup was constructed by Christopher Applebee (Cell Biophysics Laboratory, London Research Institute and Biophysics Institute Bilbao).

Table 6.3 Photo-oxidation and EM sample preparation protocol for miniSOG fusion protein

	Step	Details
Photo-oxidation	1	Fix samples with 2.5% glutaraldehyde/2.5mM CaCl2 in 0.1M cacodylate buffer (pH 7.4) at RT for 5 min
	2	Incubate samples on ice for 30 min
	3	Wash samples x 5 with 0.1M cacodylate buffer
	4	Incubate samples in blocking buffer on ice for 30 min
	5	Wash samples x 1 with blocking buffer
	6	Prepare DAB solution
	7	Supply oxygen to oxidation chamber at 2.5 L/min and chill water jacket to 4 °C
	8	Replace blocking buffer with DAB solution
	9	Acquire image of the samples prior to photo-oxidation
	10	Photo-oxidise samples with mercury lamp or laser for 30 min
	11	Wash samples x 5 with 0.1M cacodylate buffer on ice immediately
EM sample preparation	12	Re-fix samples with 2% PFA/1.5% glutaraldehyde in 0.1M cacodylate buffer on ice for 30 min
	13	Wash samples x 1 with 0.1M cacodylate buffer
	14	Stain samples in 0.2% osmium tetroxide/0.1 M cacodylate buffer on ice for 30 min
	15	Wash samples x 3 with 0.1M cacodylate buffer
	16	Preserve samples in 1%PFA/0.1M cacodylate buffer at 4 °C before embedding
	17	Wash samples x 3 with 0.1M cacodylate buffer
	18	Dehydrate samples stepwise in ethanol (30%, 50%, 70%, 80%, 90%, 100% x 2); 5 min per step
	19	Dehydrate samples in prophylene oxide for 10 min
	20	Infiltrate samples with propylene oxide/epoxy resin mixture (50/50) for 1 h
	21	Infiltrate samples with 100% resin x 2; 2 h per infiltration
	22	Replace old resin with fresh 100% resin; incubate samples at 60 °C for 48 h to polymerise resin
	23	Locate the photo-oxidised cells in the polymerised resin and perform serial sectioning of the samples
	24	Incubate cut sections with 2% aqueous uranyl acetate at RT for 20 min before acquisition of EM images

RT = room temperature; blocking buffer: 50 mM glycine, 10 mM KCN, 20mM aminotriazole, pH 7.4

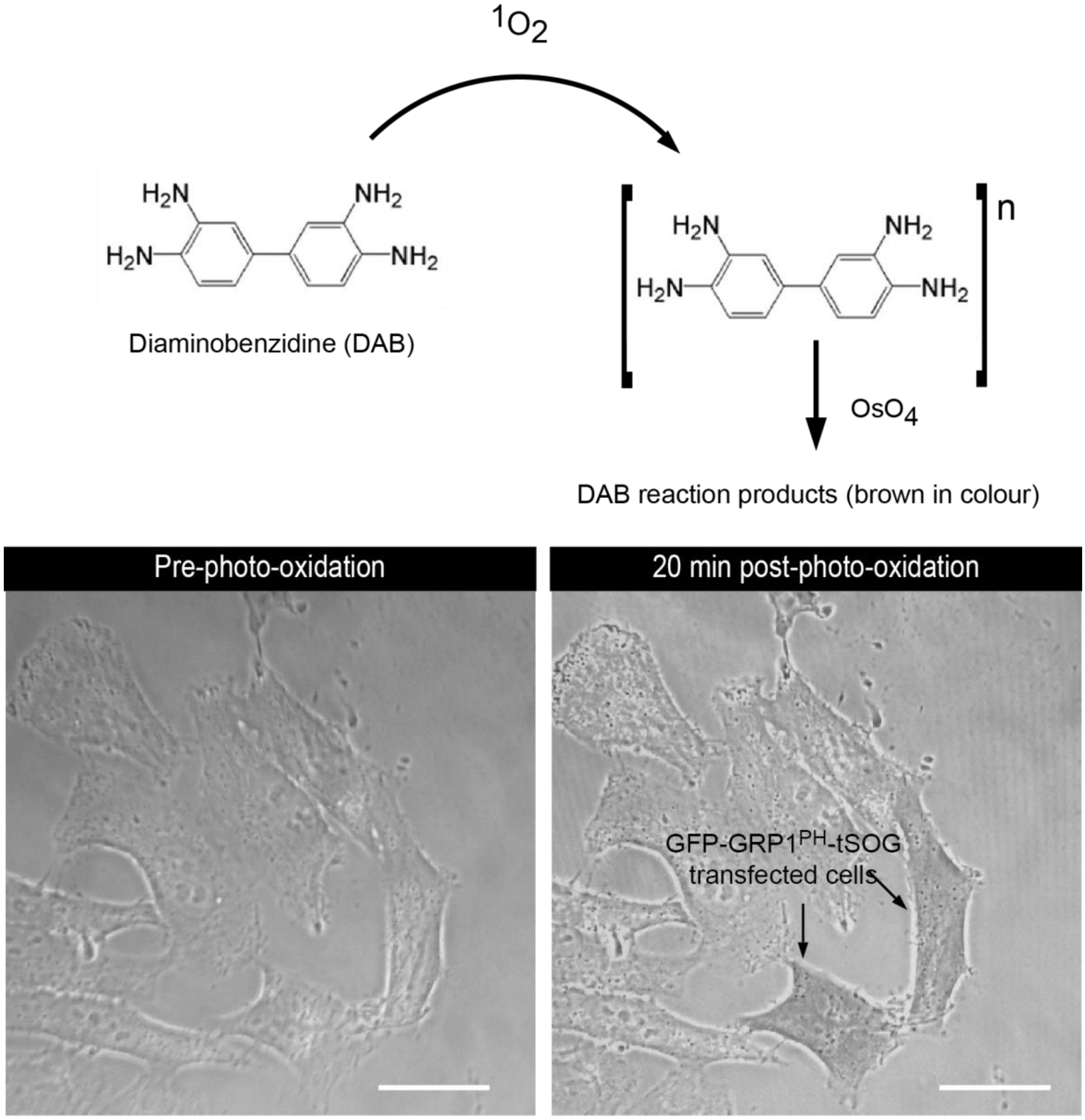

Figure 6.14 Photo-oxidation indicated by brownish colour of DAB reaction product

HeLa cells were transiently transfected with GFP-GRP1^{PH}-tSOG and fixed in 2.5% glutaraldehyde. Cells were excited at 488 nm for 20 min, at 4 °C in an oxygenated environment. Bright field images were taken before and after photo-oxidation. Scale bar, 20 µm.

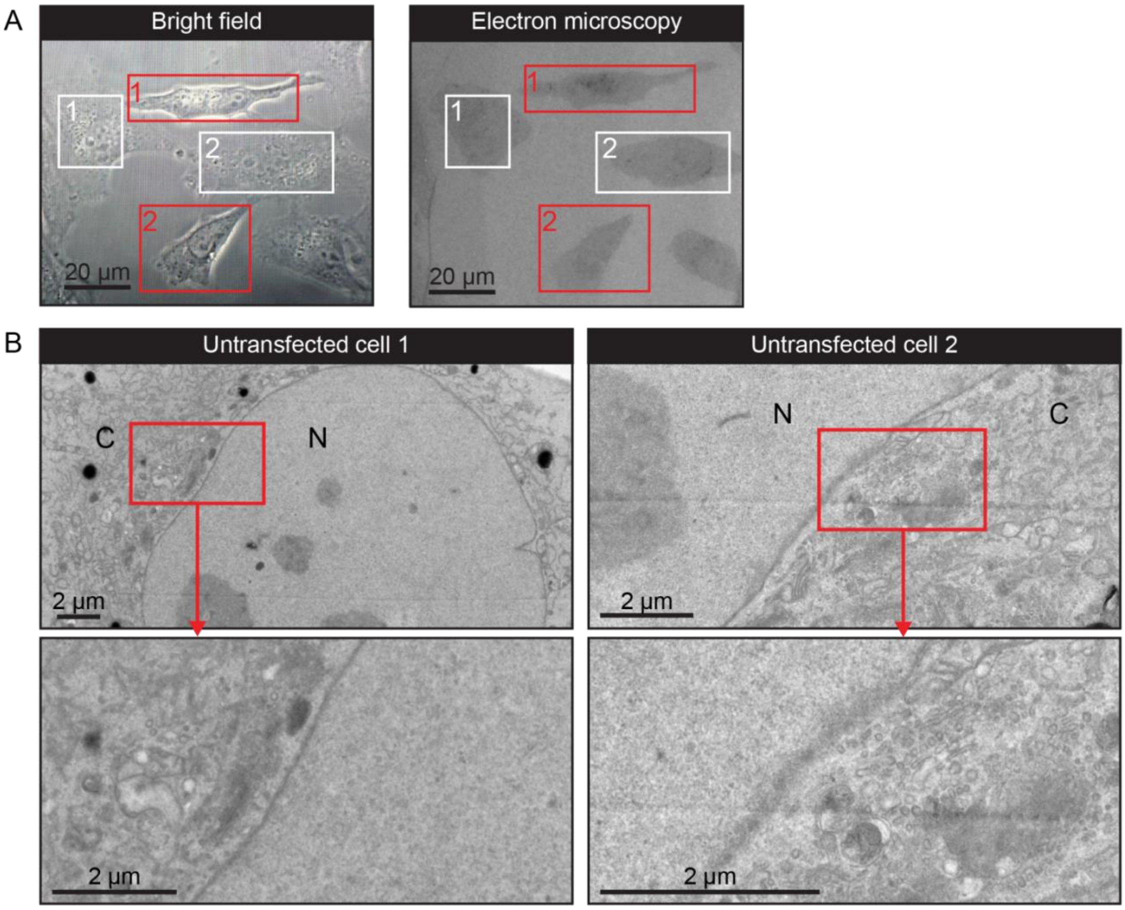
A
Bright field
Electron microscopy
1
2
1
2
20 µm
20 µm
B
Untransfected cell 1
Untransfected cell 2
C
N
N
C
2 µm
2 µm
2 µm
2 µm

(Cont'd)

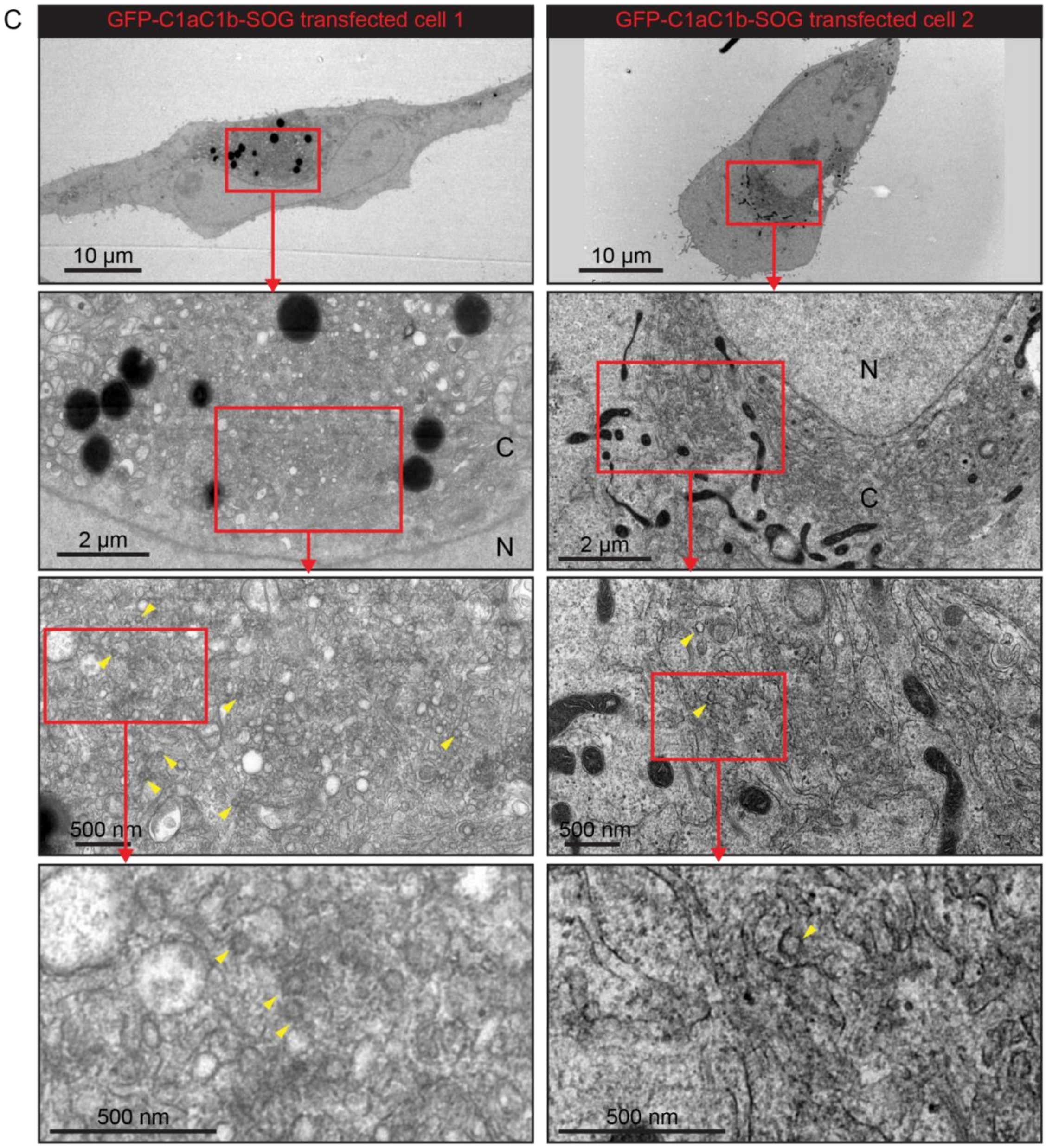

Figure 6.15 MiniSOG reaction products cannot be distinguished when sample was processed with 1% osmium tetroxide

(A) Identification of photo-oxidised cells in bright field and electron microscopy. HeLa cells were transfected with 250 ng GFP-C1aC1b-SOG for 16 h. After 30 min of photo-oxidation, the transfected cells showed brownish colour (red box) whereas the untransfected cells appeared relatively transparent (white box) in the bright field. (B & C) Electron micrographs revealed ultrastructure of photo-oxidised cells, both GFP-C1aC1b-SOG transfected and untransfected. In untransfected cells, the NE, ER and other membranes were stained by osmium tetroxide and were distinguished by their morphological features. In transfected cells, enhanced EM contrast, corresponding to the DAB precipitate observed in bright field, was detected in the peri-nuclear region. Within the peri-nuclear region, some vesicles had slightly higher electron density (yellow arrows) than the surrounding structures. N: nucleus; C: cytoplasm. Scale bar, as indicated in the figure.

Figure 6.16 shows electron micrographs of a HeLa cell transfected with GFP-C1aC1b-SOG, and photo-oxidised following the optimised protocol (Table 6.3). Decreased concentration of osmium reduced the background contrast in the micrographs and this allowed us to pick out the miniSOG reaction product at the vesicles. Compared to the result from the initial experiments, numerous vesicles with distinguishable EM contrast (Figure 6.16, yellow arrows) were found in the peri-nuclear region, some of which were 100 nm away from the NE (Figure 6.16, panel 2 & 4). Most of these vesicles have a larger diameter (65 – 70 nm) compared to those identified by serial section TEM; such observation was expected as these vesicles were surrounded by miniSOG reaction product (Figure 6.17). This findings suggest that DAG enriched vesicles are present in interphase cells, although the involvement of these vesicles in fusion events require further verification. We expected DAG localisation to the NE, ER and Golgi. However, we could not clearly identify miniSOG reaction product associated with these compartments.

Overall, the photo-oxidation protocol requires further optimisation since miniSOG reaction products was absent from the NE, ER and Golgi. Due to time constraints, the vesicles in vicinity of the gaps of the reforming NE were not characterised. However, this will be the next goal to achieve.

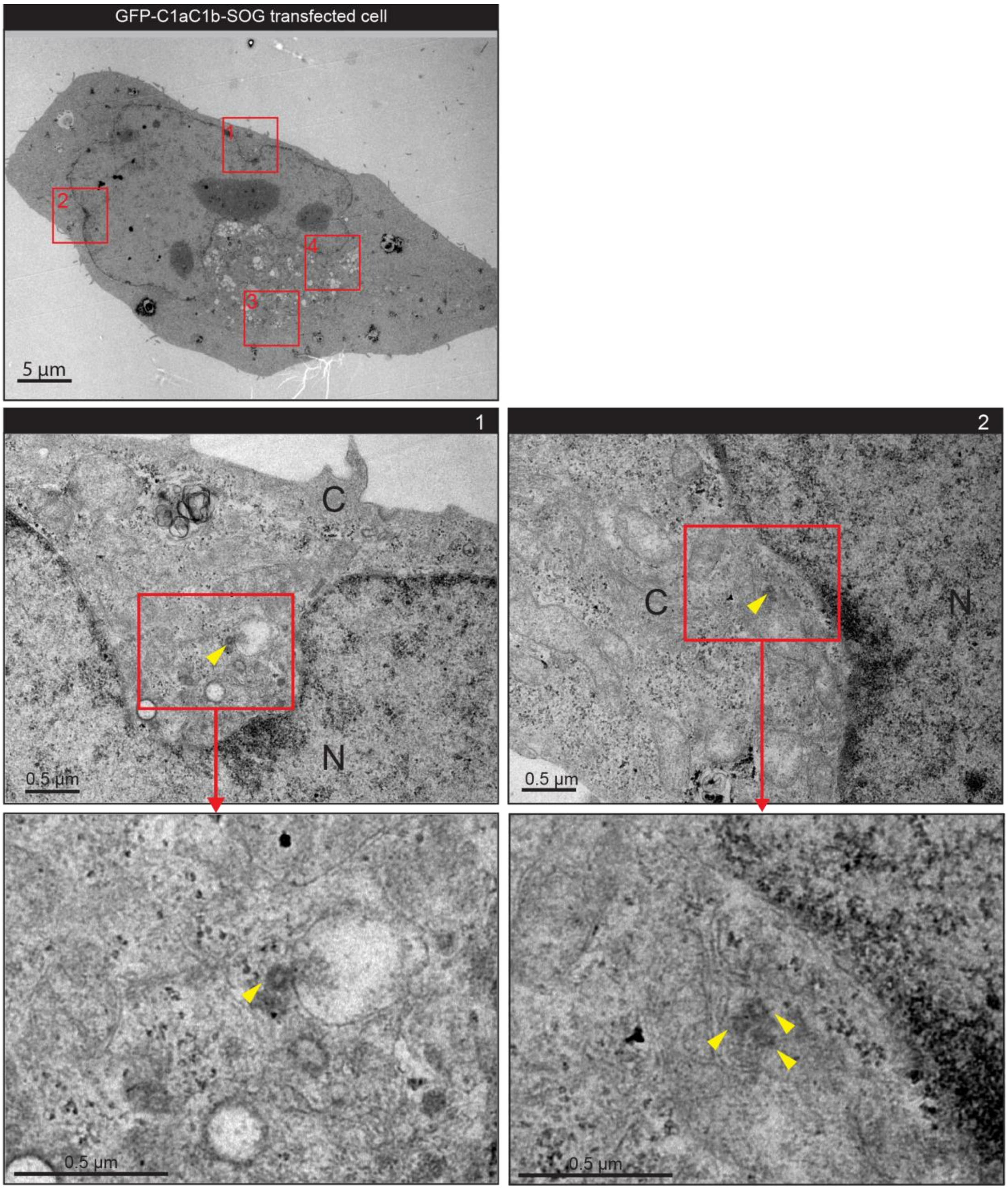
GFP-C1aC1b-SOG transfected cell
1
2
3
4
5 µm
1
C
N
0.5 µm
2
C
N
0.5 µm
0.5 µm
0.5 µm

(Cont'd)

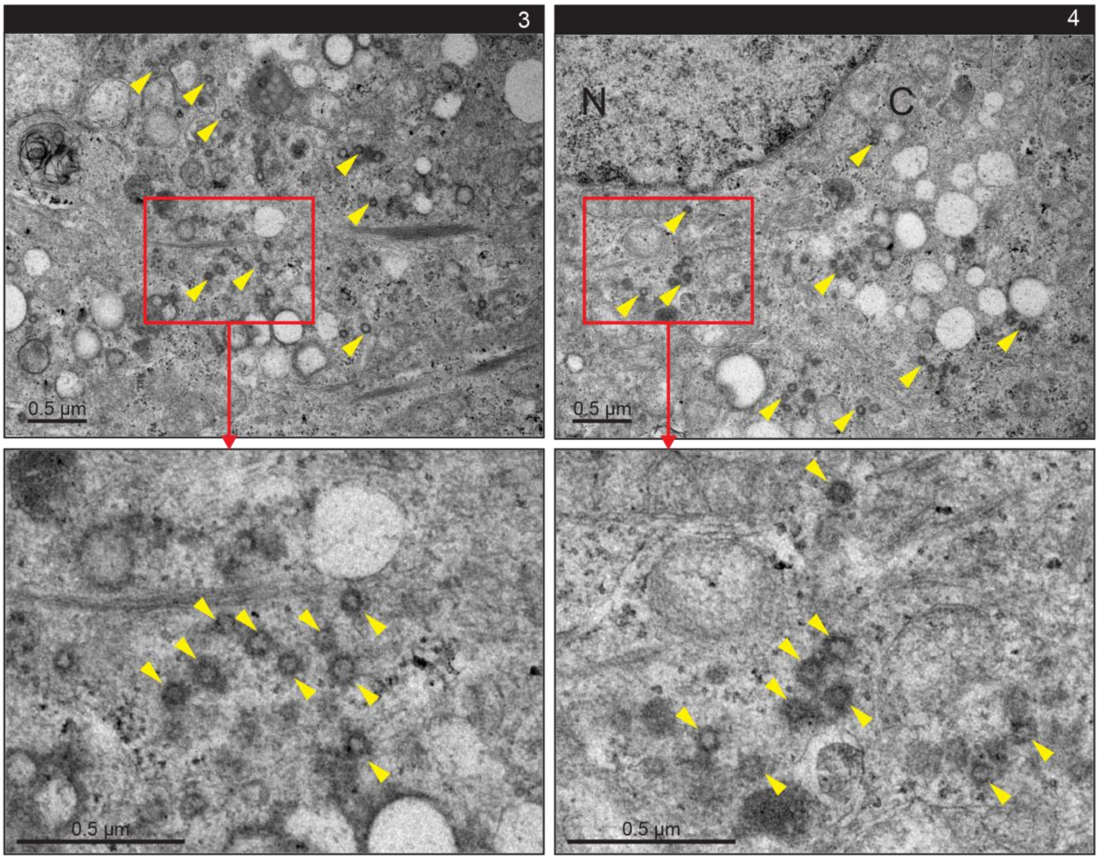

Figure 6.16 DAG-enriched vesicles are identified at reduced background contrast
Electron micrographs of an interphase HeLa cell transfected with 250 ng GFP-C1aC1b-SOG for 16 h. The cell was photo-oxidised for 30 min. Red boxes corresponding to the magnified area of the cells in the numbered panels. Samples were stained by 0.2% osmium tetroxide and incubated with 2% uranyl acetate after serial sectioning. In the magnified fields of view, numerous vesicles had enhanced electron density (yellow arrows) and were distinguished from the background EM contrast, some of which are very close to the NE. The electron density in the NE was punctate, and it was difficult to distinguish if miniSOG reaction products were associated with the NE. N: nucleus; C: cytoplasm. Scale bar, as indicated in the figure.

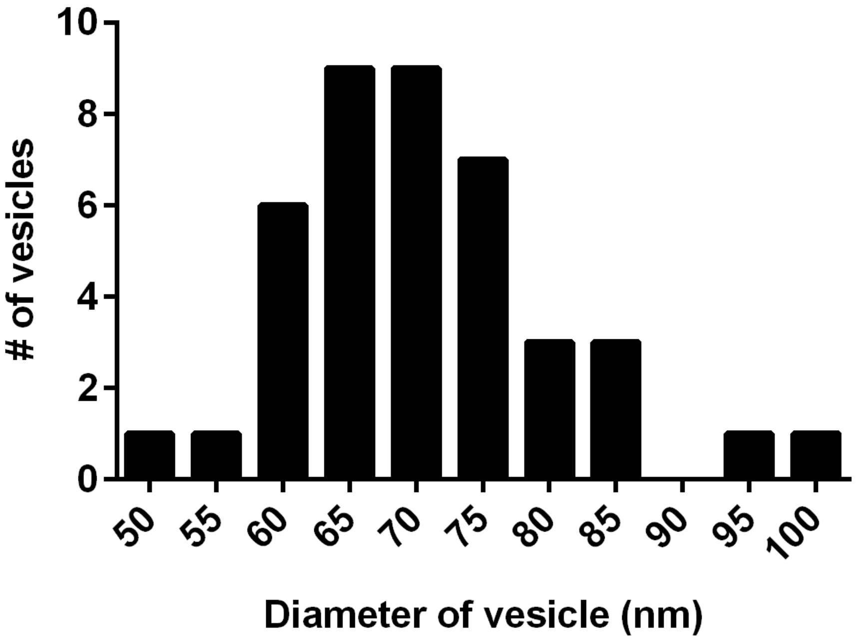

Figure 6.17 Quantification of miniSOG-labelled vesicles of an interphase cell

The number and diameter of miniSOG-labelled vesicles in the proximity of the NE (within a radius of 1 µm) were measured as described in Figure 6.5 and plotted into a histogram. The average diameter of these vesicles was 71 nm and most of the vesicles (n = 18) affiliated to the 65 and 70 nm-groups.

6.7 Discussion

6.7.1 The presence of fusogenic vesicles during NE assembly

Vesicles that promote NE assembly were isolated from several non-mammalian cell-free assays decades ago (Ulitzur and Gruenbaum, 1989, Zhang and Zhai, 1995, Byrne *et al.*, 2007). However, vesicles obtained in cell-free assays may be the result of homogenisation rather than the cellular components retaining their native structures. Although MV1 was shown to be a cellular compartment (Byrne *et al.*, 2014, Byrne *et al.*, 2007), similar fusogenic vesicles have not been identified in mammalian cells.

Using electron tomography, we obtained high resolution volume information of the reforming NE and multiple vesicles were found in close proximity to NE gaps. Further investigation is necessary to demonstrate that these vesicles are involved in NE assembly, but preliminary quantification revealed that more vesicles were found in the vicinity of NE gaps compared to regions without gap. These findings suggest that vesicles are required at the NE gaps and these vesicles may be involved in membrane fusion.

To determine the distribution pattern of vesicles, their distance from the centre of the sampling field was measured (Figure 6.3). However, the measured distance is not necessarily the closest distance between the vesicles and the gap because a NE gap is three dimensional. Our quantification did not measure the 3D distance between the vesicles and the NE gaps as it requires complicated algorithms to achieve this task. Nevertheless, the simplified quantification was able to unveil the distribution pattern of putative fusogenic vesicles in two dimensions.

The ER envelopment model suggests that reassembly of NE during mitosis relies on the binding and flattening of ER tubules around the nucleus to complete the NE, without any requirement for membrane vesicles or fusion (Anderson and Hetzer, 2007). Conversely, our findings verified the presence of vesicles in close proximity to the reforming NE and these vesicles might play a significant role in completing a reforming NE. This is the first study to examine the role of vesicles in NE reassembly of mammalian cells. The next step is to determine the lipid and protein composition, and therefore the fusogenic property of these vesicles.

6.7.2 Characterisation of fusogenic vesicles

MiniSOG is a very small molecule (12 kDa), and as such is less likely to affect the innate protein structure of lipid binding domains. It was also reported that incorporation of miniSOG does not perturb cellular functions such as calcium uptake (Martell *et al.*, 2012). However, our results showed that the localisation of DAG reporter was influenced by the orientation of the GFP and miniSOG tags relative to the DAG-binding domain. Hence, it is recommended to verify the localisation of a miniSOG- and GFP-fused protein using an established reporter. The GFP-C1aC1b-SOG reporter is DAG-specific as indicated by its non-DAG-binding mutant.

Photo-oxidation was performed across the field of view rather than targeted to a specific organelle of the cell therefore both miniSOG fusion protein-transfected and untransfected cells were excited by the same amount of energy. MiniSOG fusion protein-transfected cells were successfully photo-oxidised after 20 to 30 minutes. When processing samples with 1% osmium tetroxide, all subcellular structures were highly contrasted such that miniSOG reaction product could not be easily distinguished from non-targeted cellular components. Processing samples with 0.2% osmium tetroxide reduced electron contrast sufficiently to allow visual separation of miniSOG reaction product from surrounding structures.

Surprisingly, we were not able to identify similar miniSOG reaction product associated with the NE, ER and Golgi. Recently, imaging mass spectrometry has verified the specific binding of osmium tetroxide to different lipids (Belazi et al., 2009). It is possible that differences in the lipid composition of membranes may lead to differential staining patterns. Fusogenic vesicles are likely to have specialised lipid composition when compared to other major membranes, and this may explain why we were unable to identify miniSOG reaction product associated with the NE, ER and Golgi. To visualise DAG at the NE, ER and Golgi, improved signal of DAB reaction product would be required. DAB staining can be intensified by addition of nickel or cobalt ions during sample preparation and this has been reported and widely applied (Adams, 1981, Deitch *et al.*, 1990). Therefore, related optimisation could help us to detect all DAG-enriched membranes.

DAG-enriched vesicles were found in the peri-nuclear region of an interphase cell. This suggests that fusogenic vesicles are required by the cell throughout the cell cycle, in addition to sealing the gaps of the NE during mitosis. The next step in our studies will be to characterise the vesicles associated with NE gaps during mitosis using the miniSOG fusion protein. In addition to miniSOG, similar tools such as APEX (Martell *et al.*, 2012) and the biarsenical-tetracysteine system (Giepmans, 2008) are tags that provide EM contrast. Each of these tools has its own advantages and drawbacks. However, they could be used as alternative tools to target MV1-like vesicles.

6.8 **Summary**

In this chapter we verified the presence of vesicles in the vicinity of NE gaps. Quantitative analysis showed that the vesicle density was the highest in the vicinity of the large NE gaps and this suggest a potential role of vesicles in NE assembly. A novel tag called miniSOG was developed and tested in order to specifically characterise MV1-like vesicles. Although this tool requires further optimisation, preliminary results indicated that there were many DAG-enriched vesicles in the interphase cells and that these DAG-enriched vesicles might be the MV1-like vesicles required for fusion events. Other genetically engineered CLEM probes are also available to specifically target cellular components. However, the optimisation process will depend on the structures of interest and the biological question to be answered.

Chapter 7 Acute modification of DAG at the Golgi and its impact on nuclear envelope assembly

7.1 Introduction

By depleting DAG in the NE/ER, we demonstrated localised production of DAG is necessary for NE reassembly. A similar result to that was shown during NE assembly of the male pronucleus in echinoderm cell-free assays (Byrne *et al.*, 2007). In addition to the ER, the Golgi is another DAG-containing compartment.

DAG can be detected at the Golgi by using the GFP-C1aC1b probe (see Chapter 5). Also, the production of DAG at the Golgi is indirectly supported by the Golgi localisation of ceramide transfer protein (CERT), involved in the transfer of ceramide from the ER to the Golgi; sphingomyelin synthase (SMS) uses the transferred ceramide as substrate and simultaneously converts PtdCho to DAG (Perry and Ridgway, 2005). Golgi-DAG has been shown to recruit protein kinase D (PKD) leading to the formation of transport carriers to be delivered to the plasma membrane (Baron and Malhotra, 2002, Maeda *et al.*, 2001). Accumulation of DAG in the cytoplasmic leaflet of TGN membranes introduces negative curvature in its bilayer and promotes TGN vesiculation (Bard and Malhotra, 2006).

The Golgi vesiculates during interphase and mitosis. Protein trafficking through the generation of vesicles from the Golgi has been well documented (Warren and Malhotra, 1998, Emr *et al.*, 2009). Golgi vesiculation during mitosis has been extensively studied (Persico *et al.*, 2009). These findings are reminiscent of the vesicles identified in the vicinity of the NE gaps in the previous chapter. Furthermore, Golgi-derived vesicles (MV2α) are involved in the formation of the NE of male pronucleus in echinoderm cell-free assays (Collas and Poccia, 1996). Together, these findings suggest that the Golgi is a possible source of fusogenic vesicles.

Localised DAG production in Golgi vesicles may contribute to membrane fusion at the reforming NE. Therefore, we applied rapalogue-induced dimerisation tools that target DAG at the Golgi to determine the impact of Golgi-DAG depletion on NE reassembly during mitosis.

7.2 Acute Golgi-DAG depletion by rapalogue dimerisation tools

To deplete DAG at the Golgi, the rapalogue dimerisation tool described in Chapter 5 was used. The Golgi functions as a site for protein and polysaccharide modification. It contains three sub-compartments, which are classified as *cis*-, *medial*- and *trans*-Golgi according to their orientation relative to the ER and plasma membrane, and their biochemical profile. Numerous Golgi resident proteins are responsible for macromolecule modification and cargo trafficking, and many of them are transported to other cellular compartments. Therefore, many Golgi resident proteins are not desirable for use as organelle-specific markers. For instance, acute manipulation of phosphoinositides (PIs) in the Golgi was performed using a rapamycin-induced dimerisation tool conjugated to the TGN38 Golgi marker (Szentpetery *et al.*, 2010). However, TGN38 cycles between the *trans*-Golgi network and the plasma membrane (Stanley and Howell, 1993). Therefore, to specifically recruit lipid-modifying enzymes to the Golgi, proteins with a restrictive Golgi localisation are required. We constructed three rapalogue dimerisation tools conjugated with different Golgi resident proteins and tested their ability to recruit lipid-modifying enzymes.

7.2.1 GCNT1 (glucosaminyl (N-acetyl) transferase 1, core 2)

GCNT1 is responsible for the biosynthesis of branched oligosaccharides, and has been shown to be confined to the *cis*- and *medial*-Golgi (Skrincosky *et al.*, 1997). The cytosolic and transmembrane domains of GCNT1 are responsible for its Golgi localisation (Zerfaoui *et al.*, 2002). We incorporated GCNT1 into the rapalogue dimerisation tool to target *cis*- and *medial*-Golgi.

7.2.2 ST6GALNAC1 (ST6 (alpha-N-acetyl-neuraminyl-2,3-beta-galactosyl-1,3)-N-acetylgalactosaminide alpha-2,6-sialyltransferase 1)

ST6GALNAC1 is an enzyme that alters the O-glycan structures of polysaccharides by adding a sialic acid to GalNAc. It has a highly restricted localisation pattern in non-cancer cells (Ikehara *et al.*, 1999). Immunoelectron microscopy showed that ST6GALNAC1 is located throughout the Golgi (Sewell *et al.*, 2006). Therefore, ST6GALNAC1 was used to target the whole Golgi.

7.2.3 GRASP65 (Golgi reassembly stacking protein 65)

GRASP65 is a Golgi stacking protein that localises to the *cis*-Golgi (Barr *et al.*, 1997). It participates in mitotic Golgi fragmentation (Sutterlin *et al.*, 2005) and Golgi ribbon formation though the GRASP65-GM130 (Golgi matrix protein 130) complex (Puthenveedu *et al.*, 2006). The amino acids 1-201 of GRASP65, also known as the GRASP domain, contain a myristoylated site which allows Golgi membrane targeting (Tang *et al.*, 2010). Thus the GRASP domain was used as a *cis*-Golgi marker.

7.3 Optimisation of rapalogue dimerisation tools targeting the Golgi

7.3.1 Oligosaccharide transferases

Two oligosaccharide transferases targeting different Golgi subcompartments were cloned into the rapalogue dimerisation tool. Figure 7.1 shows the localisation of GFP-2FKBP-GCNT1 and GFP-2FKBP-ST6GALNAC1 in HeLa cells. Both rapalogue constructs were correctly expressed at the Golgi, indicated by the similar expression of the same oligosaccharide transferase solely fused to a GFP. High expressing cells transfected with the rapalogue dimerisation tools showed increase in cytoplasmic fluorescence, but the major fluorescent signal was concentrated at the Golgi.

However, lipid-modifying enzymes were not recruited to the Golgi using these oligosaccharide transferases rapalogue constructs. Figure 7.2-B shows the rapalogue-treated HeLa cells co-expressing GFP-2FKBP-GCNT1 and RFP-Flag-FRB-DGKεK/SKIP. DGK and SKIP are lipid-modifying enzymes that deplete DAG in our targeted membrane. DGK phosphorylates DAG to PtdOH and SKIP dephosphorylate PtdIns(4,5)P_2 to PtdIns(4)P limiting the DAG precursor (see Chapter 5). In the presence of rapalogue, DGKεK or SKIP was expected to be recruited to the Golgi within an hour but there was no recruitment after 3 h of rapalogue treatment. Although a slight increase in DGKεK or SKIP fluorescence was observed as time progressed, the fluorescence did not co-localise with that of GCNT1. Similarly, SKIP was not recruited to the Golgi using GFP-2FKBP-ST6GALNAC1. After 2 h of rapalogue treatment, there was no co-localisation between the ST6GALNAC1 and SKIP fluorescent signals (Figure 7.3-B).

A possible explanation for the failed recruitment may be that the interaction between the rapalogue and the FKBP domains was blocked. Figure 7.4-A illustrates the possibility that GFP may bind to the short cytosolic domain of the oligosaccharide transferase thus preventing rapalogue from binding to the 2FKBP. To verify this, the GFP could have been re-orientated on the lumenal side of the Golgi (Figure 7.4-B). However, due to time constraints, we focused on the optimisation of the rapalogue dimerisation tool using the GRASP Golgi marker.

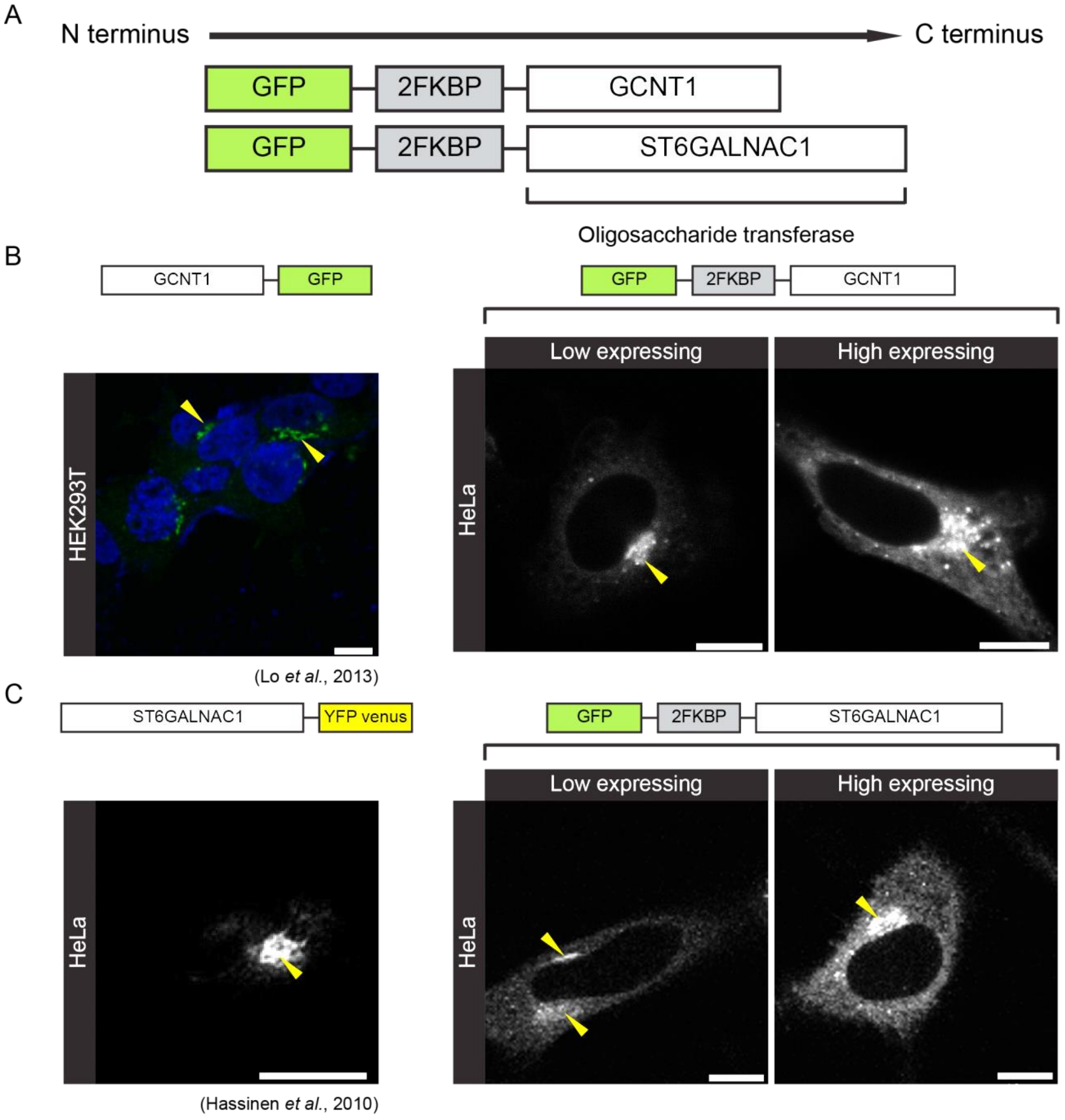

(Lo *et al.*, 2013)

(Hassinen *et al.*, 2010)

Figure 7.1 Rapalogue dimerisation tools based on oligosaccharide transferases localise correctly to the Golgi

(A) Schematics of oligosaccharide transferases fused to the rapalogue-binding 2FKBP domains and the fluorescent tag GFP; length of the domains is in scale with the number of base pairs. (B) Left panel: confocal image of HEK293T cells transduced with GCNT1-GFP (green) and probed by nuclear stain (blue), adapted from *Lo *et al.* (2013). Right panels: HeLa cells transfected with GFP-2FKBP-GCNT1. Confocal images of live transfected cells with different expression levels were acquired. (C) Left panel: HeLa cells transfected with ST6GALNAC1-YFP$_{\text{venus}}$, adapted from *Hassinen *et al.* (2010). Right panels: HeLa cells transfected with GFP-2FKBP-ST6GALNAC1. Confocal images of live transfected cells with different expression levels were acquired. (B – C), GCNT1 and ST6GALNAC1 rapalogue dimerisation tools localised to the Golgi (yellow arrows). Enhanced cytoplasmic fluorescence of the rapalogue dimerisation tools was observed in the high expressing cells. Scale bar, 10 µm.

*These researches were originally published in the cited journals (see references) © the American Society for Biochemistry and Molecular Biology

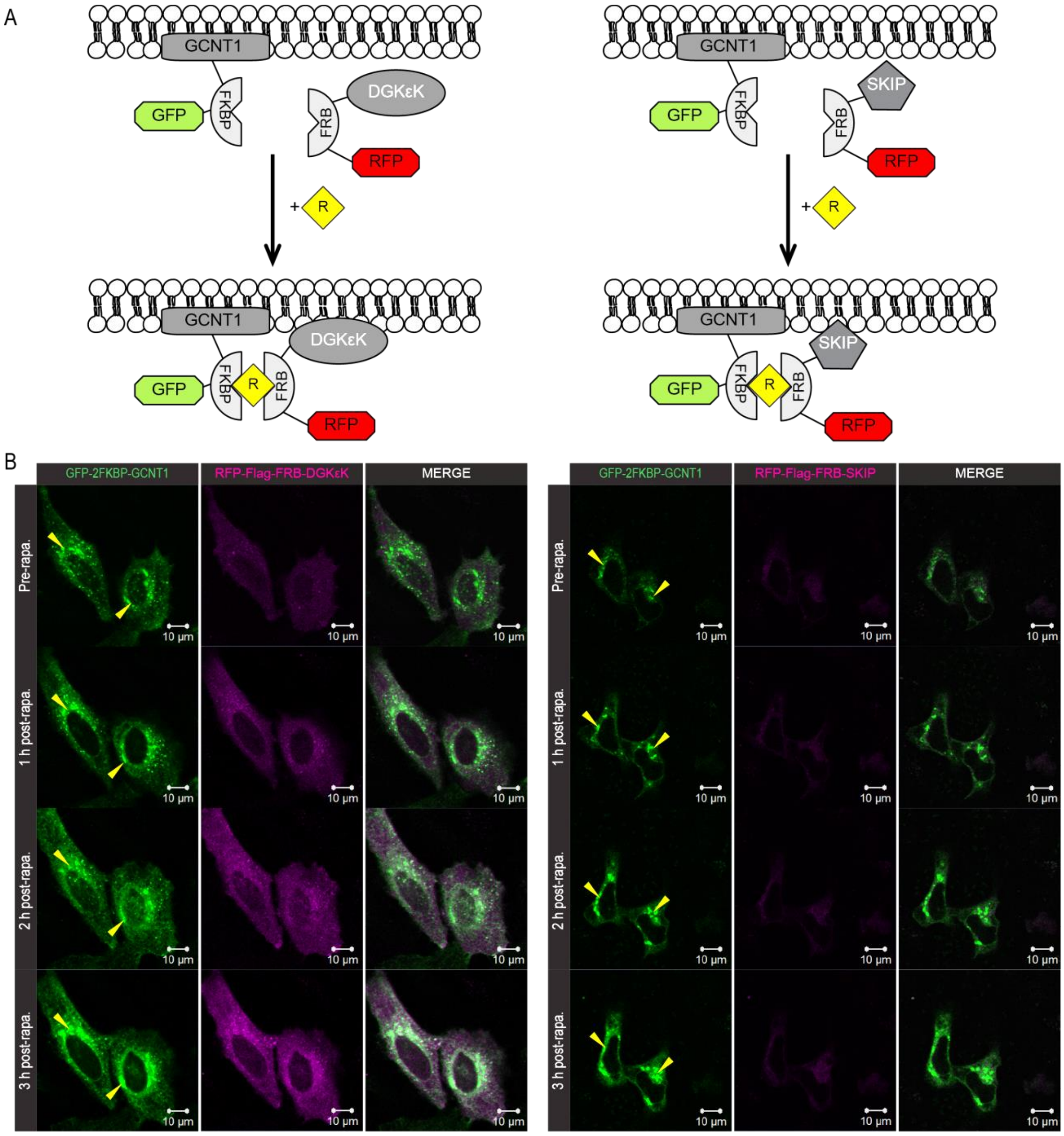

Figure 7.2 Lipid-modifying enzymes are not recruited to GFP-2FKBP-GCNT1 in the presence of rapalogue

(A) Diagram of GCNT1 rapalogue dimerisation tool. Upon addition of rapalogue, RFP-Flag-FRB-DGKεK (DGKεK) or RFP-Flag-FRB-SKIP (SKIP) is predicted to be recruited to GFP-2FKBP-GCNT1 (GCNT1) so that Golgi-DAG will be depleted by conversion to PtdOH, or by limitation of its precursor PtdIns(4,5)P_2. (B) HeLa cells double transfected with GCNT1 (green) and DGKεK/SKIP (magenta) were imaged live by confocal microscopy and followed for 3 h after addition of rapalogue. Yellow arrows indicate the Golgi localisation of GCNT1. No obvious recruitment of DGKεK/SKIP to GCNT1 was observed in the presence of rapalogue. Scale bar, 10 μm.

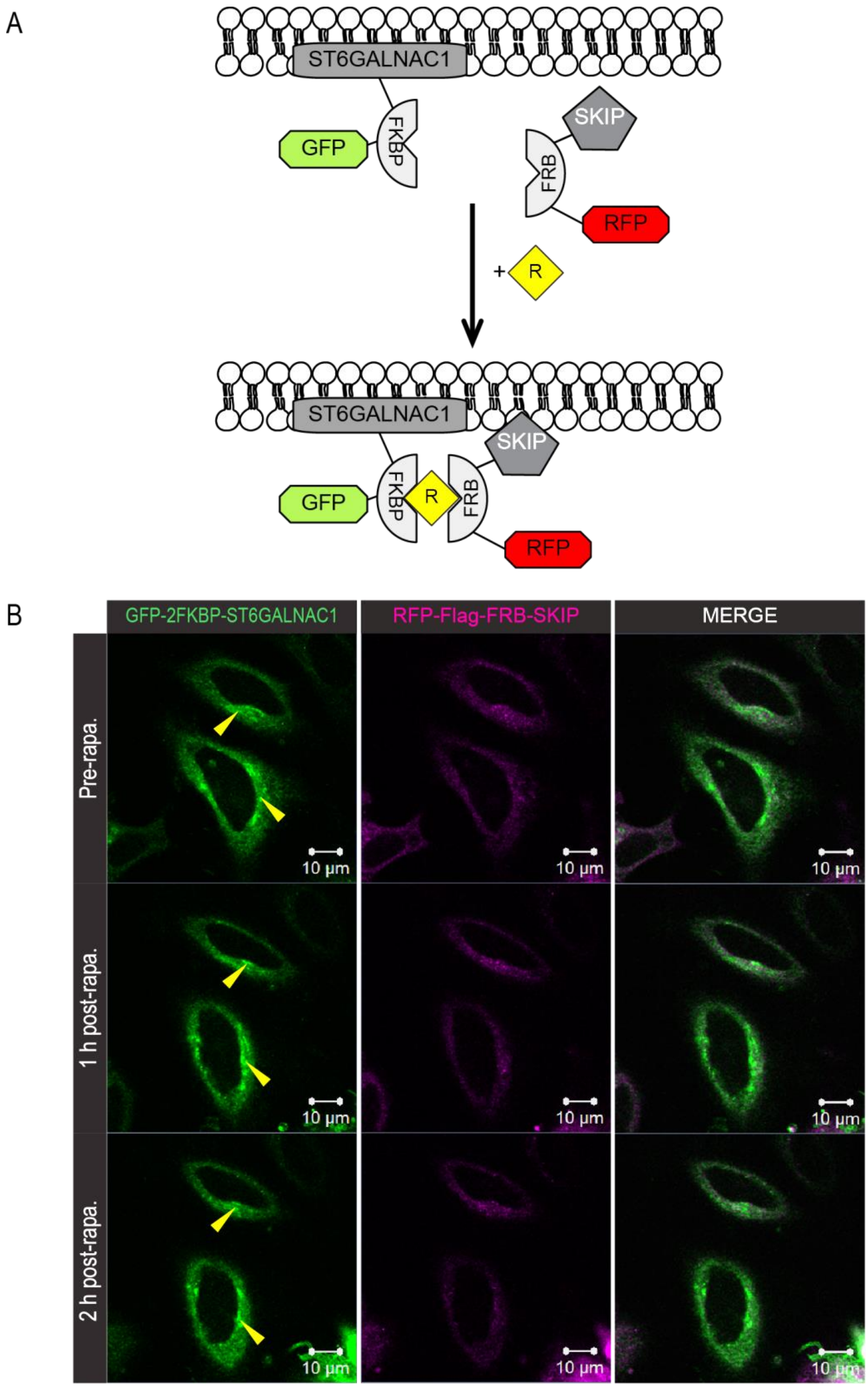

Figure 7.3 SKIP is not recruited to GFP-2FKBP-ST6GALNAC1 in the presence of rapalogue

(A) Diagram of ST6GALNAC1 rapalogue dimerisation tool. RFP-Flag-FRB-SKIP (SKIP) is predicted to be recruited to GFP-2FKBP-ST6GALNAC1 (ST6GALNAC1) in the presence of rapalogue so that Golgi-DAG will be depleted through conversion of its precursor PtdIns(4,5)P$_2$ to PtdIns4P. (B) HeLa cells double transfected with ST6GALNAC1 (green) and SKIP (magenta) were imaged live by confocal microscopy and followed for 2 h after addition of rapalogue. Yellow arrows indicate the Golgi localisation of ST6GALNAC1. No recruitment of SKIP to ST6GALNAC1 was observed in the presence of rapalogue. Scale bar, 10 μm.

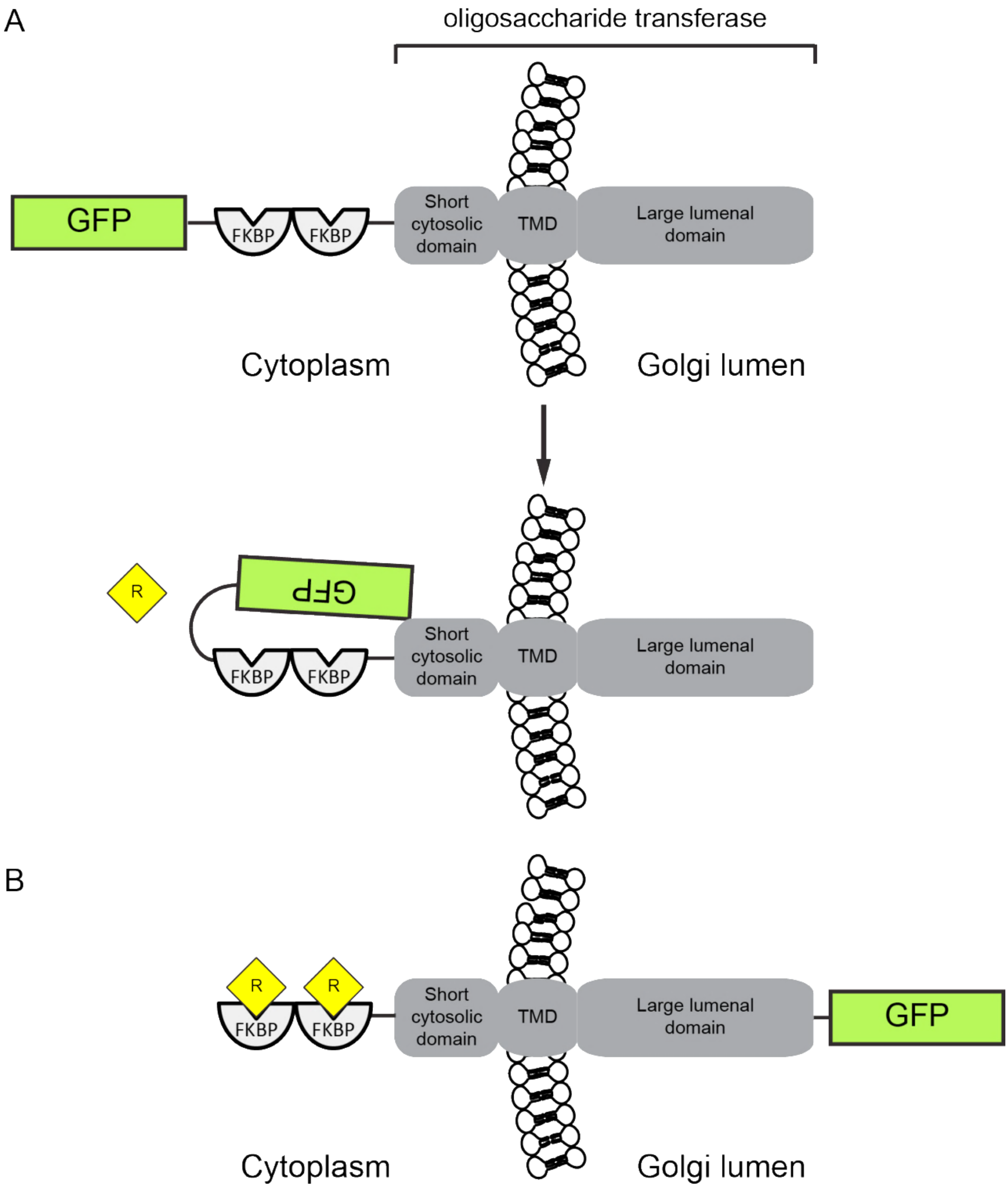

Figure 7.4 **Putative explanation for the failed recruitment by the oligosaccharide transferase rapalogue dimerisation tools**

(A) The typical structure of an oligosaccharide transferase contains three parts: a large lumenal domain, a transmembrane domain (TMD) and a short cytoplasmic domain. GFP may interact with the short cytosolic domain of the oligosaccharide transferases thus prohibiting rapalogue (yellow) from binding to the FKBP domains. (B) Construct with the GFP re-orientated to the Golgi lumen may recruit lipid-modifying enzymes to the Golgi.

7.3.2 GRASP65

Figure 7.5-A shows how the GRASP domain of GRASP65 was cloned into the rapalogue dimerisation tool. A non-Golgi-binding mutant GRASP.G2A was also cloned into the tool as a negative control. Localisation of GRASP65 has been studied and well documented (Barr *et al.*, 1997). COS7 and HeLa cells transfected with GRASP-GFP displayed distinctive Golgi fluorescence (yellow arrows) and a minimal NE fluorescence (white arrows) in the high expressing cells (Figure 7.5-B). GRASP.G2A however did not localise to any membrane structures, and was instead distributed homogeneously in the cytosol and the nucleus.

Initial GRASP rapalogue dimerisation tools mislocalised. COS7 cells transfected with 2FKBP-GRASP-GFP displayed a strong nuclear and a reduced Golgi fluorescence compared to the given GFP-tagged constructs. A similar result was observed in cells transfected with 2FKBP-GRASP.G2A-GFP (Figure 7.5-C). Since the first few amino acids of GRASP are responsible for its Golgi localisation, we suspected that the 2FKBP domains hindered the binding of GRASP to the Golgi in the initial GRASP rapalogue dimerisation tools. Therefore, the 2FKBP domains were re-orientated to the C terminus of the construct (Figure 7.6-A). COS7 and HeLa cells transfected with the modified GRASP rapalogue construct exhibited an identical Golgi localisation compared to the cells transfected with the given constructs (Figure 7.6-B). Hence, the modified GRASP rapalogue dimerisation tool was used to recruit DGKεK to the Golgi.

Live HeLa cells co-expressing GRASP-GFP-2FKBP and RFP-Flag-FRB-DGKεK were treated with rapalogue and followed for 3 h. In the presence of rapalogue, DGKεK was recruited to the Golgi after 1 h, supported by the co-localisation of DGKεK and GRASP-GFP-2FKBP (Figure 7.7-B, white arrows and merged images). Consistent and reproducible recruitment was observed in low and high expressing cells. Therefore, GRASP-GFP-2FKBP was used in the following experiments to deplete Golgi-DAG.

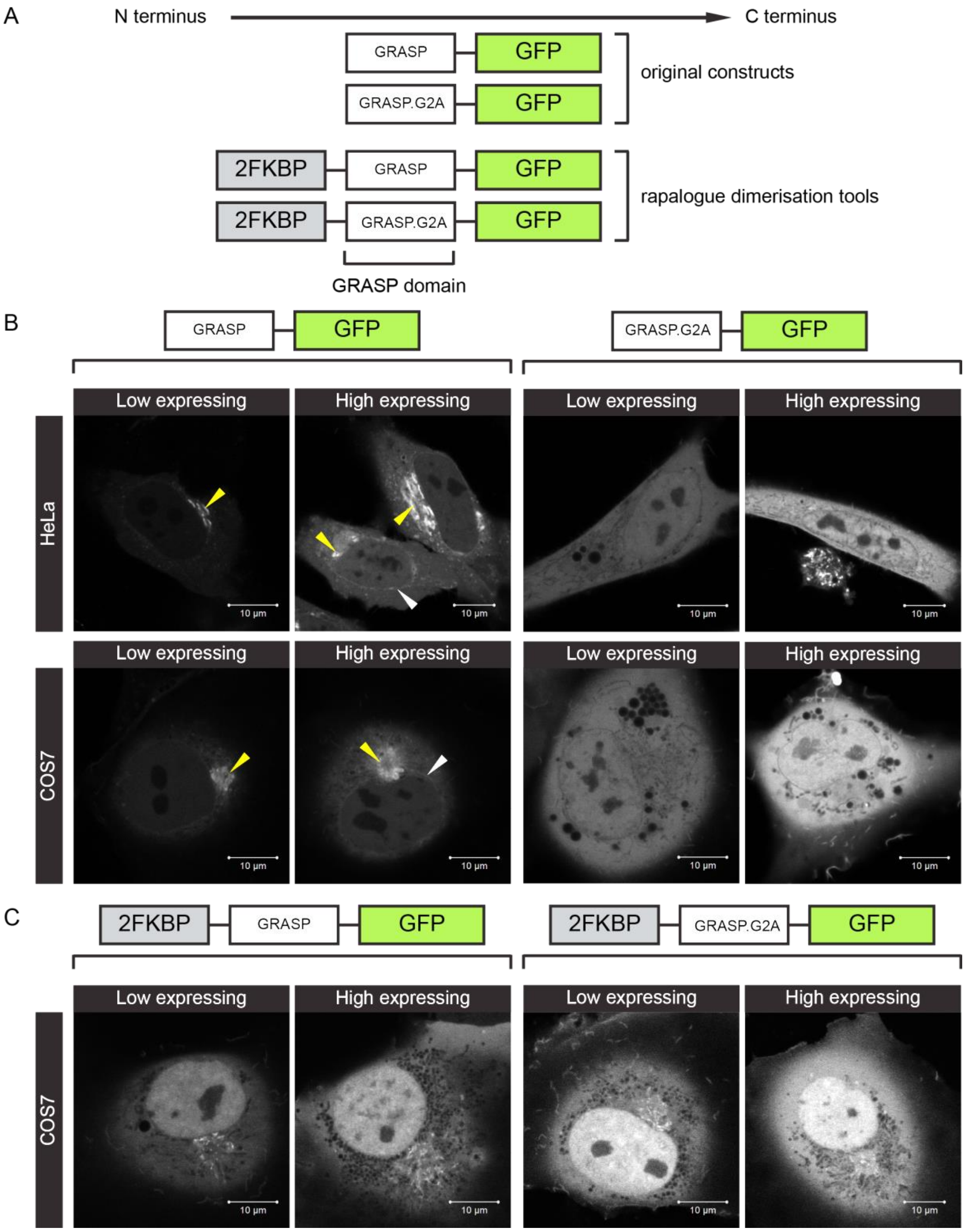

Figure 7.5 Mislocalisation of initial GRASP rapalogue dimerisation tools

(A) Schematics of the original GRASP constructs and GRASP domains fused to the rapalogue dimerisation tool; length of the domains is in scale with the number of base pairs. GRASP.G2A is non-myristoylatable and thus is a non-Golgi-binding mutant. (B) COS7 and HeLa cells were transfected with the WT and mutant GRASP domain fused to GFP. Live confocal images of transfected cells with different expression levels were acquired. Yellow arrows indicate the Golgi localisation of GRASP and white arrows indicate the minimal NE localisation of GRASP in the high expressing cells. GRASP.G2A localised homogenously in the nucleus and the cytosol. (C) COS7 cells were transfected with 2FKBP-GRASP-GFP or its mutant. In the 2FKBP-GRASP-GFP transfected cells, a strong nuclear fluorescence and a reduced Golgi fluorescence were observed compared to the original construct. Similar localisation patterns were observed in the 2FKBP-GRASP.G2A-GFP transfected cells. Scale bar, 10 μm.

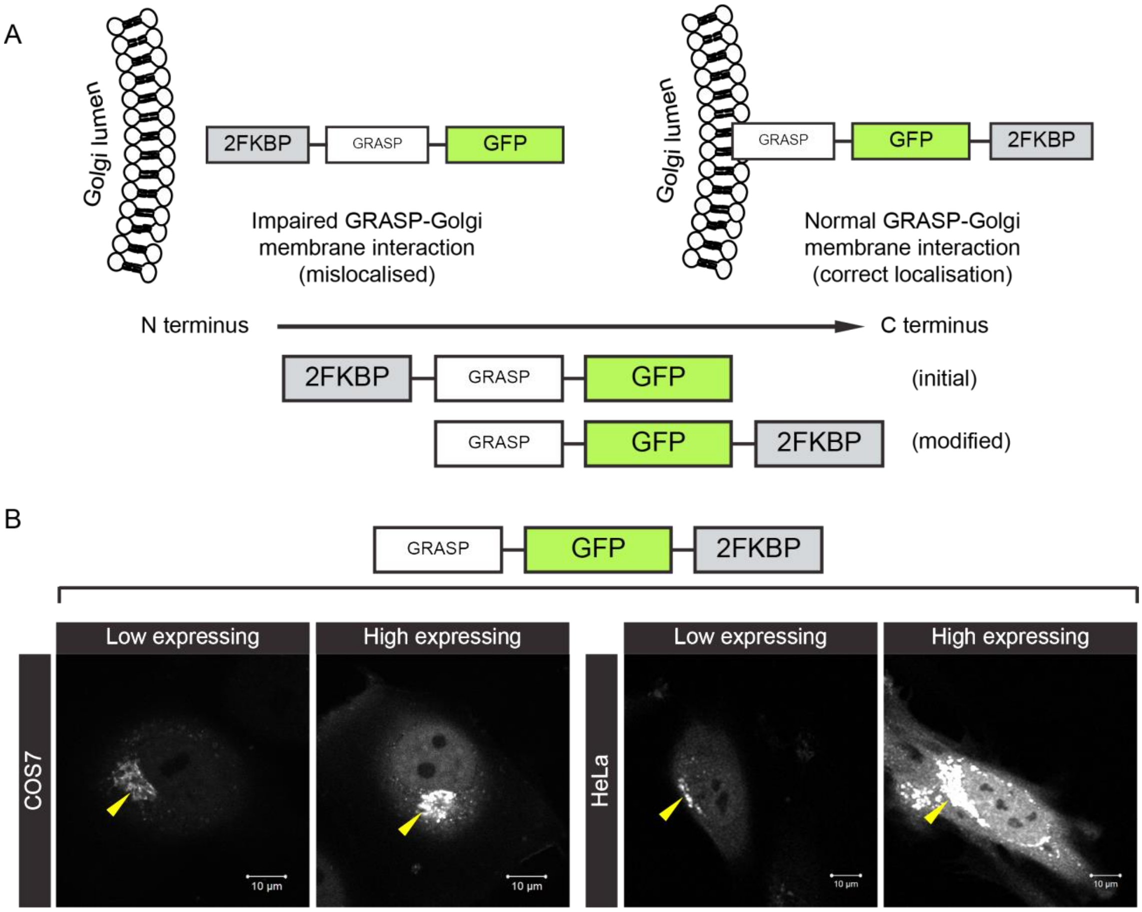

Figure 7.6 Modified GRASP rapalogue dimerisation tool correctly localise to the Golgi

(A) Putative explanation for the mislocalisation of initial GRASP rapalogue dimerisation tools. The 2FKBP domain may hinder the interaction between GRASP and the Golgi membranes thus resulting in the mislocalisation of 2FKBP-GRASP-GFP. A construct with 2FKBP re-orientated to the C terminus may restore the binding of GRASP to the Golgi. (B) COS7 and HeLa cells were transfected with GRASP-GFP-2FKBP. Live confocal images of transfected cells with different expression levels were acquired. Yellow arrows indicate the Golgi localisation of GRASP, identical to that of the original construct shown in Figure 7.5-B. Scale bar, 10 µm.

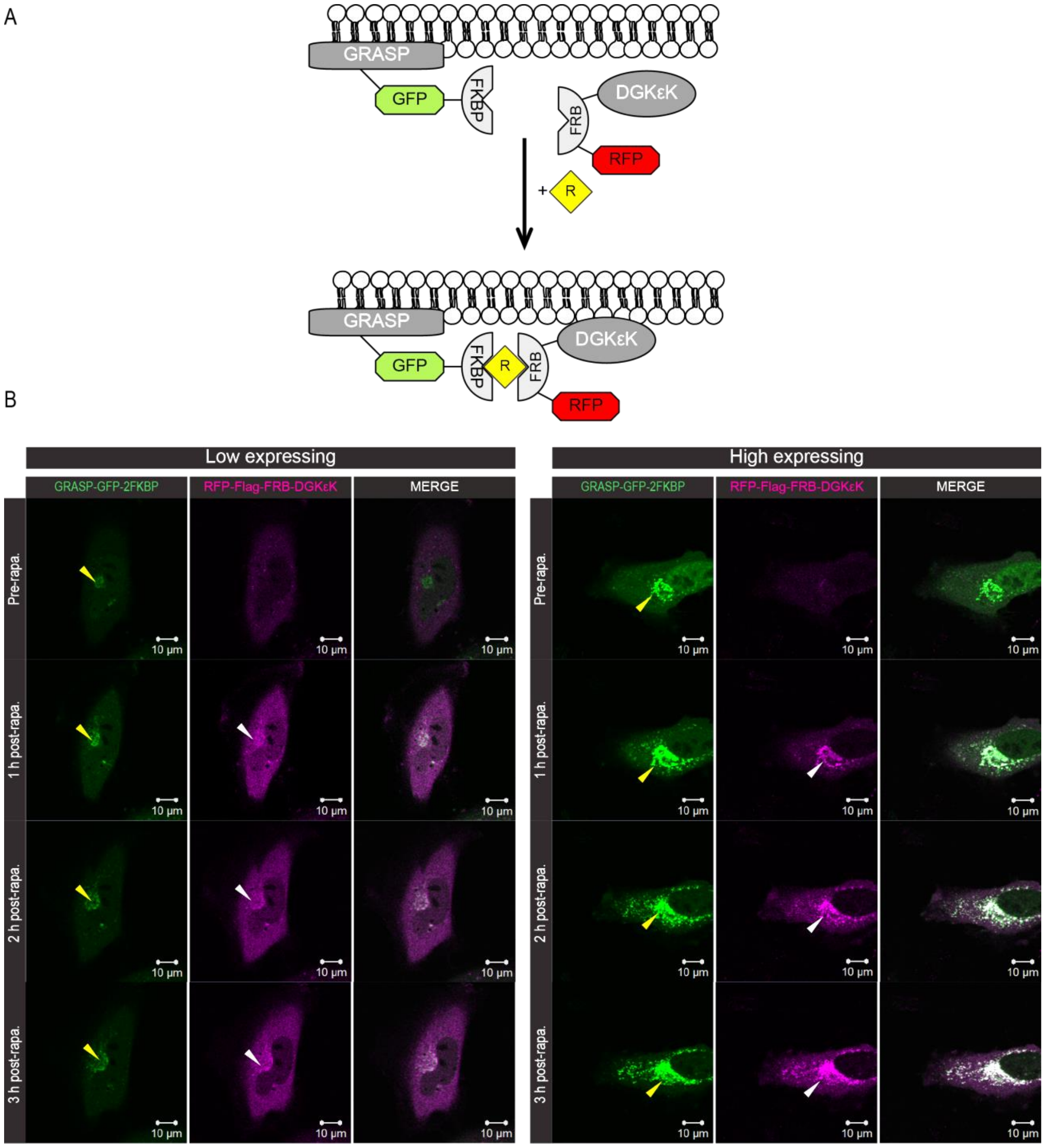

Figure 7.7 Modified GRASP rapalogue dimerisation tool recruits DGKεK to Golgi membranes

(A) Diagram of the modified GRASP rapalogue dimerisation tool. Upon addition of rapalogue, RFP-Flag-FRB-DGKεK (DGKεK) is expected to be recruited to GRASP-GFP-2FKBP (GRASP). DAG in the Golgi will be converted to PtdOH. (B) Live HeLa cells double transfected with GRASP (green) and DGKεK (magenta) were imaged by confocal microscopy and followed for 3 h after addition of rapalogue. Yellow arrows indicate the Golgi localisation of GRASP and white arrows indicate the recruitment of DGKεK to the Golgi. Scale bar, 10 µm.

7.4 Golgi-DAG depletion in mammalian cells

The GRASP rapalogue dimersiation tool was optimised for Golgi-DAG depletion. The next step was to follow the transfected cells though mitosis, and determine the impact of Golgi-DAG depletion on NE reassembly. To ensure DAG is specifically modified at the Golgi, cells with an excessive expression of GRASP were not selected. High expression of DGKεK may also cause cell death. Therefore, only the cells with the following two criteria were selected. First, the initial fluorescence of GRASP should be restricted to the Golgi. Second, the initial fluorescence of DGKεK should be homogenously distributed in the cytosol and the intensity should be just slightly higher than the background. The positions of these cells were recorded and checked every 30 min after addition of rapalogue until a cell entered mitosis.

Figure 7.8-A shows the recruitment of DGKεK or its catalytically inactive mutant DGKεK.D434N to the Golgi of HeLa cells. Before adding rapalogue, the cells were incubated with ER tracker. The ER tracker was used as an indicator for normal NE reassembly. Golgi-DAG-depleted cells were expected to have impaired NE reassembly whereas the unperturbed cells were expected to have a complete NE at cytokinesis. However, at the light microscopy level, we observed no difference in NE morphology between Golgi-DAG-depleted and unperturbed cells. In both conditions, signal from the ER tracker was detected at the reforming NE of the cells in every mid-section (Figure 7.8-B, white arrows). Since the resolution of light microscopy, approximately 200 nm, does not allow us to observe ultrastructure of the NE to determine if there are any gaps or abnormal phenotype, the Golgi-DAG-depleted and unperturbed cells were analysed using CLEM.

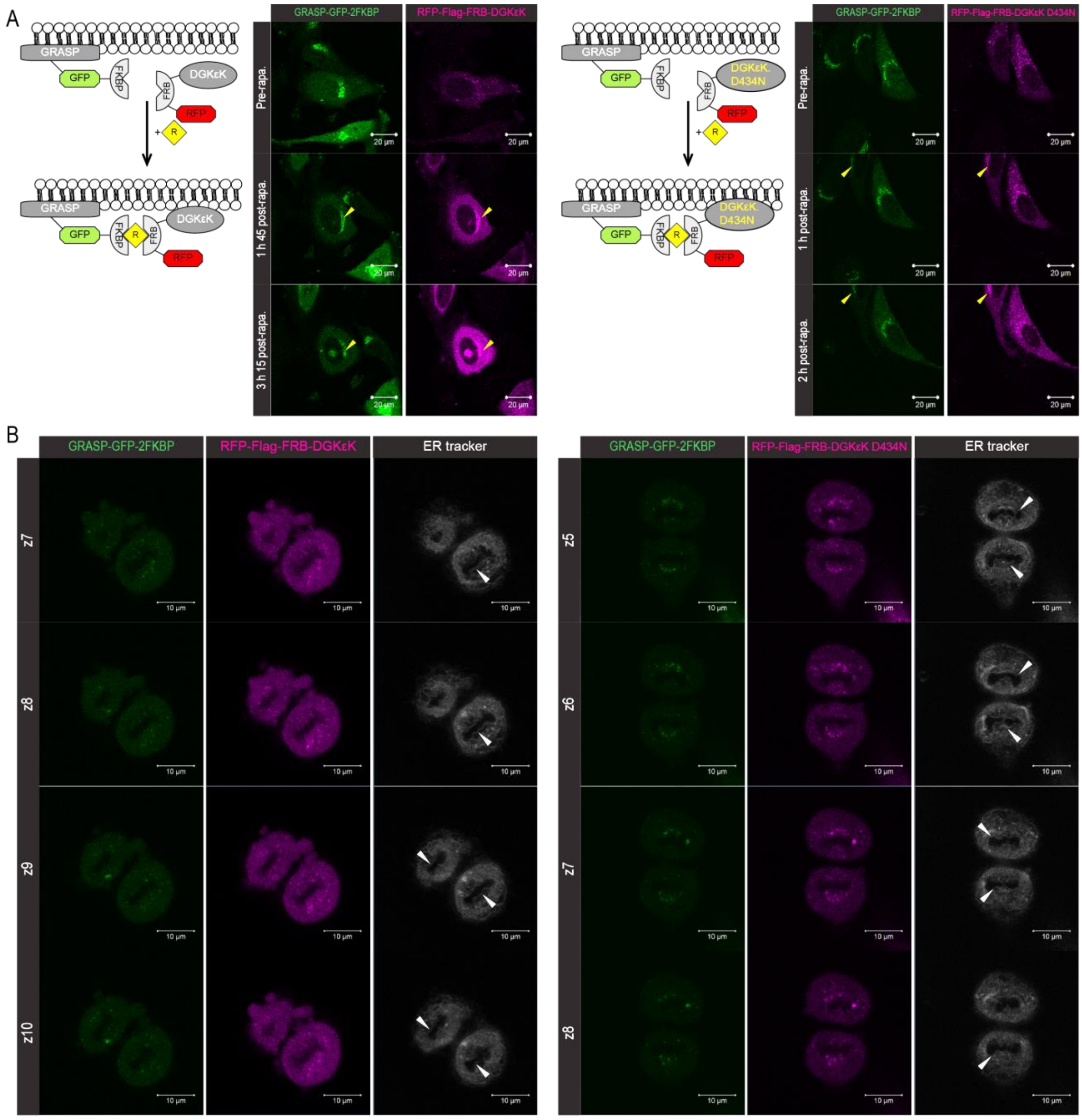

Figure 7.8 Light microscopy does not have adequate resolution to distinguish the morphological differences between Golgi-DAG-depleted and unperturbed cells

(A) RFP-Flag-FRB-DGKεK (DGKεK) or RFP-Flag-FRB-DGKεK.D434N (DGKεK.D434N) was recruited to GRASP-GFP-2FKBP (GRASP) in the presence of rapalogue. DGKεK (left panel) or DGKεK.D434N (right panel) co-localised with GRASP (yellow arrows) after 1 h of rapalogue treatment. GRASP, green; DGKεK or DGKεK.D434N, magenta. Scale bar, 20 µm. (B) Middle sections of DGKεK- & DGKεK.D434N-expressing cells shown in (A) were followed for 5 to 7 h till mitosis and fixed at cytokinesis (live images). Prior to the addition of rapalogue, cells were incubated with the ER tracker (grey) in order to determine a normal NE reassembly. In both Golgi-DAG-depleted (DGKεK-expressing) and unperturbed (DGKεK.D434N-expressing) cells, signals of the ER tracker were observed at the reforming NE (white arrows). No morphological differences were noted. The cytokinesis cells were fixed for subsequent CLEM analysis. Scale bar, 10 µm.

7.5 Serial block-face scanning electron microscopy (SBF SEM) analysis of Golgi-DAG-depleted mammalian cells

In conventional CLEM, electron micrographs are acquired using serial section TEM. A typical CLEM workflow was illustrated in Chapter 5. Using this approach, it can take months to obtain high resolution images and corresponding 3D reconstructions of the ultrastructure of a cell because manual serial-sectioning is skill- and experience-demanding. Moreover, although commercial algorithms are available to align micrographs automatically, the fine tuning of alignment is time consuming. Lost or broken sections, which are not uncommon during sample collection, result in missing information of volume data of the cells. To improve the speed of acquisition of high resolution images, SBF SEM was used to analyse the NE morphology of Golgi-DAG-depleted cells.

The principle of SBF SEM is illustrated in Figure 7.9. A heavily stained epoxy resin-embedded sample (the trapezoid block) is mounted on an in-chamber ultramicrotome. A SEM image is taken of the surface of the resinated sample by detection of backscattered electrons. After that, a diamond knife cut off the top of the trapezoid block and a successive SEM image is taken after retraction of the diamond knife. One major advantage of SBF SEM is the automated generation of a large number of serial images within a relatively short time. Moreover, since the resin block is very stable in the sectioning chamber, the images are already approximately aligned at the point of acquisition. These advantages maximise the throughput of high resolution information of cells of interest.

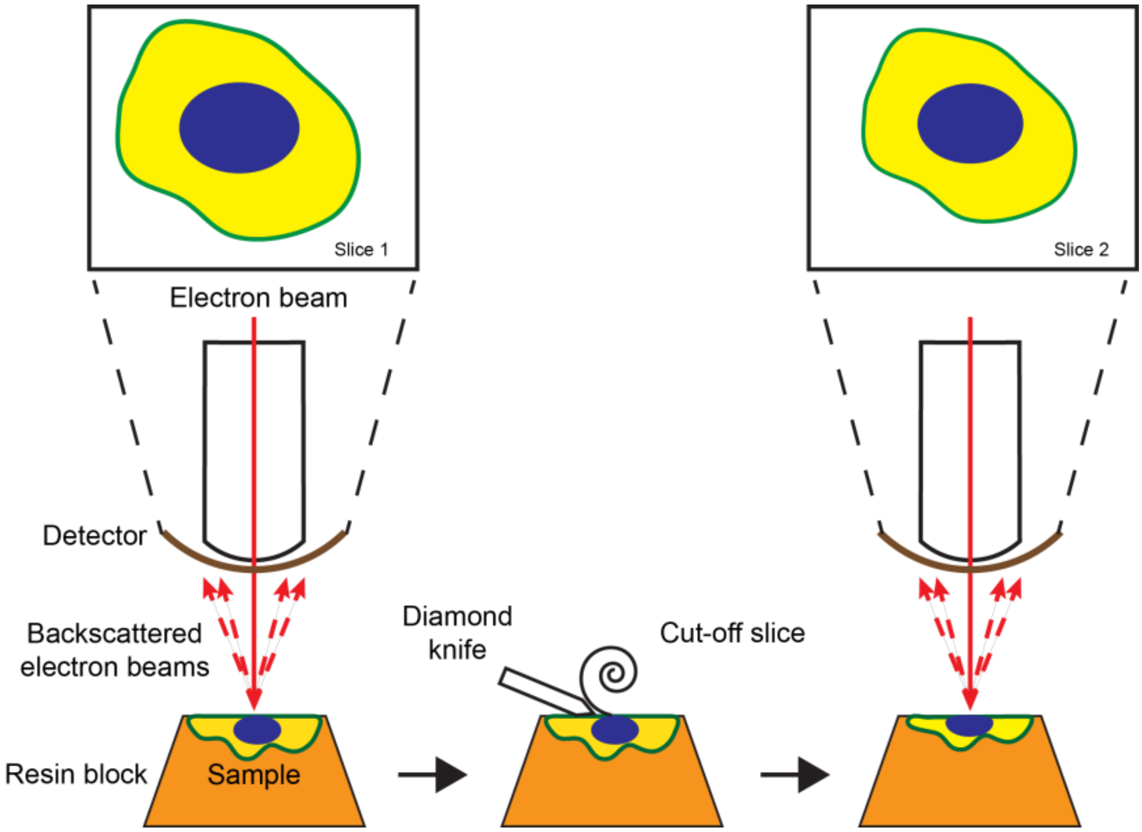

Figure 7.9 Principle of SBF SEM

An electron beam scans the surface of the resin-embedded sample (trapezoid) and the backscattered electron beams are collected by the detector to form SEM images. Then an ultrathin slice (50 nm in our experiments) is cut off the top of the trapezoid using a diamond knife associated with the automated ultramicrotome. This process repeats until the whole sample is cut through.

7.6 The impact of Golgi-DAG depletion on NE assembly

We are interested in the impact of Golgi-DAG depletion on NE assembly at late mitotic stages and we expected Golgi-DAG depletion would not affect the NE morphology in interphase cells. Figure 7.10 shows the NE morphology of interphase cells co-transfected with GRASP-GFP-2FKBP (GRASP) and RFP-Flag-FRB-DGKεK (DGKεK). In the presence of rapalogue, DGKεK was recruited to the Golgi (lower panel: + rapa). However, regardless of the absence or presence of rapalogue, the interphase cells appeared to have an intact NE in the electron micrographs, suggesting depletion of Golgi-DAG has no effect on NE morphology in interphase cells.

Figure 7.11 reveals the NE morphology of a NE-DAG-depleted and a Golgi-DAG-unperturbed cell at cytokinesis, which served as the positive and negative control for the Golgi-DAG depletion experiment respectively. When DGKεK was recruited to the NE/ER with LBR a fragmented NE was observed. This indicated our lipid-modifying enzyme DGKεK is catalytically active and able to cause the same phenotype as described in Chapter 5. As expected, when DGKεK was not recruited to the Golgi in the absence of rapalogue, the cytokinesis cell co-transfected with GRASP and DGKεK displayed a complete NE.

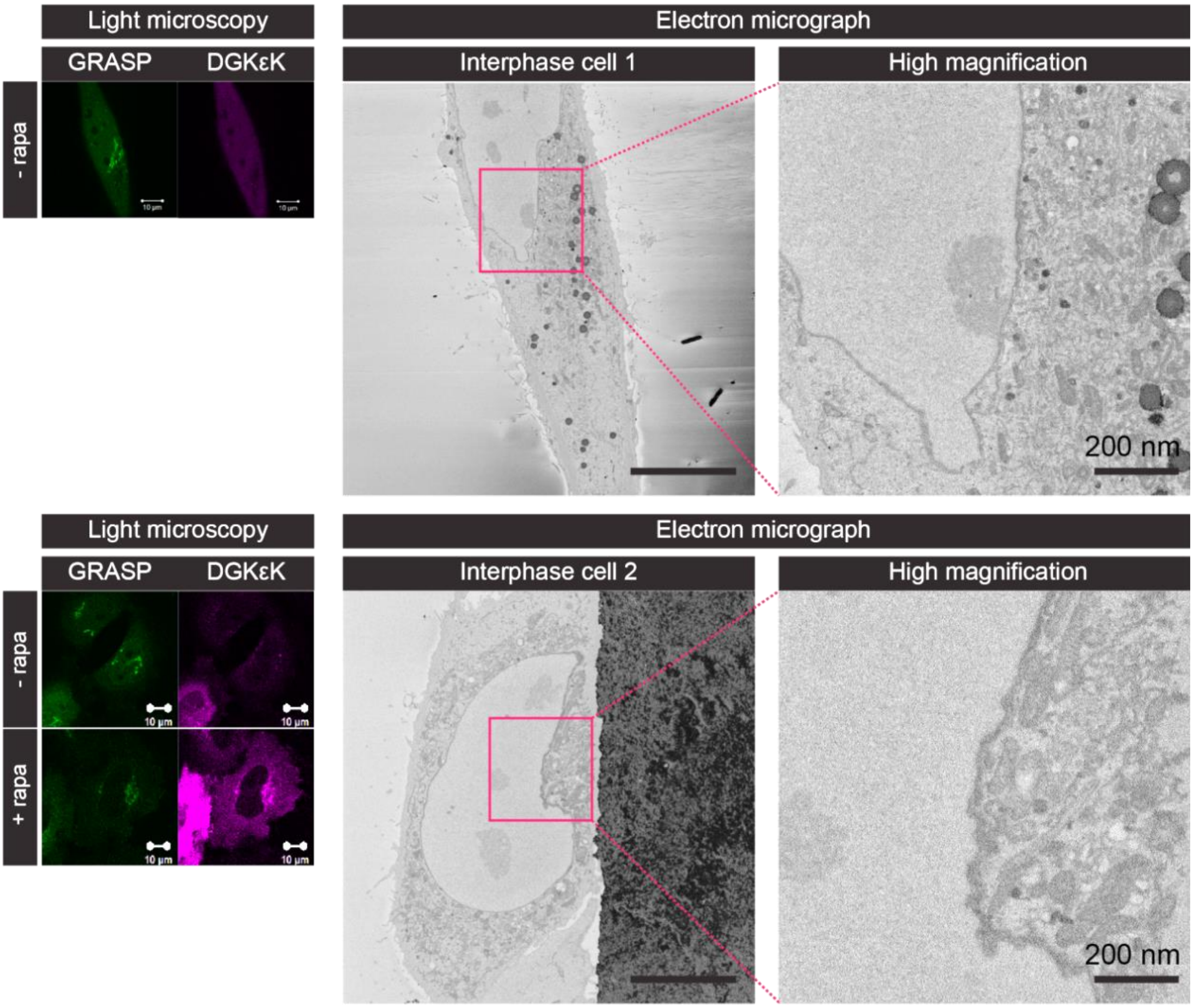

Figure 7.10 The NE is intact in interphase cells transfected with the Golgi rapalogue dimerisation tools

HeLa cells were co-transfected with GRASP-GFP-2FKBP (GRASP; green) and RFP-Flag-FRB-DGKεK (DGKεK; magenta), and were imaged live by confocal microscopy before fixation for SBF SEM analysis. Right panels display a selected electron micrograph near the base of the interphase cells of interest. In both the absence (interphase cell 1) and presence (interphase cell 2) of rapalogue, the interphase cells appeared to have an intact NE, showed in the micrographs at high magnification. Scale bar, 10 µm (fluorescence and low magnification electron micrographs); 200 nm (high magnification electron micrographs).

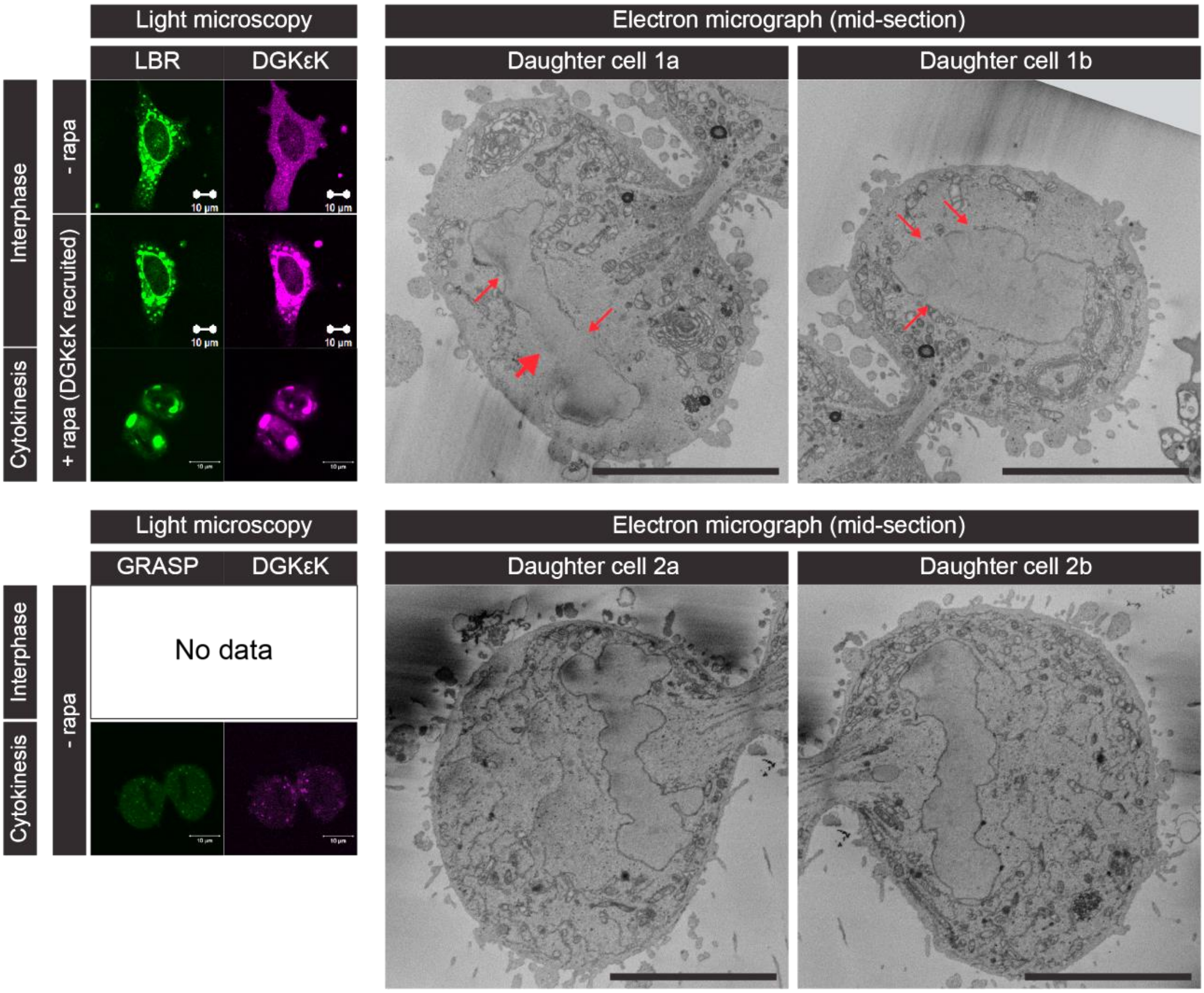

Figure 7.11 The NE morphology of NE-DAG-depleted and Golgi-DAG-unperturbed cytokinesis cells
HeLa cells under different treatments were followed through mitosis and imaged live by confocal microscopy. The cells of interest were fixed at cytokinesis and subjected to SBF SEM analysis. **Top panel:** In the presence of rapalogue, cells co-transfected with GFP-2FKBP-LBRΔTM2-8 (LBR; green) and RFP-Flag-FRB-DGKεK (DGKεK; magenta) showed a phenotype of fragmented NE, identical to the results showed in Chapter 5. Multiple NE gaps (red arrows) were observed and some of them have a length of over 5 µm (big red arrow). **Bottom panel:** In the absence of rapalogue, cells co-transfected with GRASP-GFP-2FKBP (GRASP; green) and DGKεK appeared to have an intact NE. Scale bar, 10 µm.

Then we analysed the impact of Golgi-DAG depletion on NE completion at cytokinesis. Figure 7.12 shows the NE morphology of the cytokinesis cells in which DGKεK was recruited to the Golgi. It is difficult to control the expression levels of the rapalogue dimerisation tools in these cells. Hence, we "qualified" the recruitment instead. For a robust recruitment, the fluorescent intensity of DGKεK should be equal or stronger than that of GRASP in most of the *z*-sections. Conversely in a weaker recruitment, the fluorescent intensity of DGKεK is weaker than that of GRASP in most of the *z*-sections. A detailed quantification of recruitment is in progress but is not included here due to time constraints. Out of five experiments, cell 1a & b (robust recruitment) displayed a fragmented NE phenotype (Video 7.1.1) whereas the other cells (weaker recruitment) showed an intact NE. Moreover, the fragmented NE phenotype in the Golgi-DAG-depleted cells appeared less severe compared to the NE-DAG-depleted cells. However, further quantification of the fragmented NE phenotype is required. This result suggests that Golgi-DAG is involved in NE assembly during mitosis.

Catalytically inactive DGKεK was recruited to the Golgi in the control experiments. We expected a complete NE in these cells. However, mixed NE phenotypes were observed (Figure 7.13). In both strong (cell 1a & b) and weaker (cell 4a &b) recruitments NE gaps were observed. These NE gaps appeared smaller compared to those in the Golgi-DAG-depleted cell. We are conducting a thorough quantification for better comparison. The mixed phenotypes in these control experiments may be related to the progression of mitosis. Since the cells are not synchronous we cannot expect them all to be at exactly the same stage in mitosis. Therefore if gaps are still perceived with the inactive mutant of DGKεK it is not indicative of the malfunctioning of the inactive kinase.

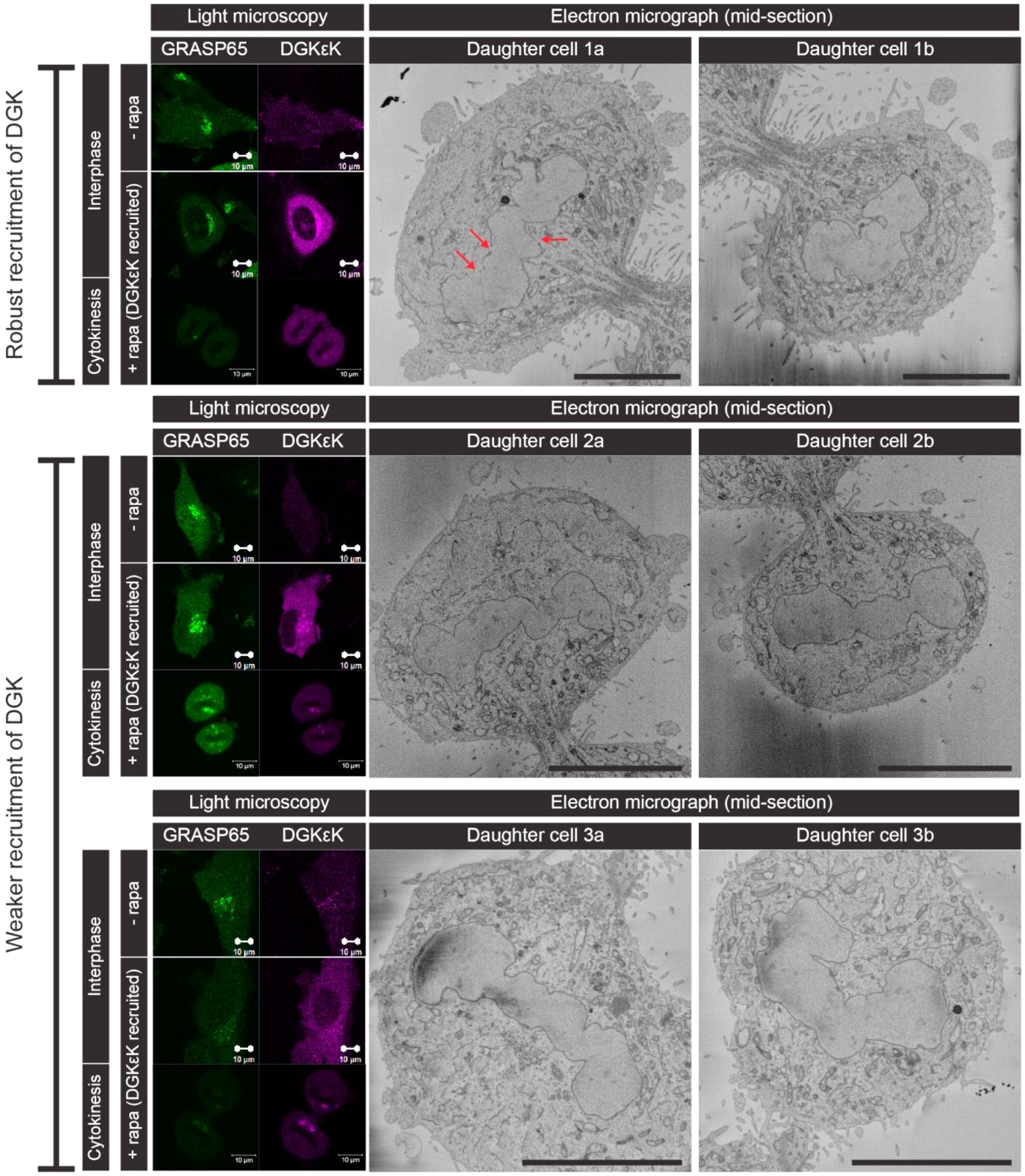
Light microscopy
Electron micrograph (mid-section)
GRASP65
DGKεK
Daughter cell 1a
Daughter cell 1b
Robust recruitment of DGK
Interphase
Cytokinesis
- rapa
+ rapa (DGKεK recruited)
10 µm
Light microscopy
Electron micrograph (mid-section)
GRASP65
DGKεK
Daughter cell 2a
Daughter cell 2b
Light microscopy
Electron micrograph (mid-section)
GRASP65
DGKεK
Daughter cell 3a
Daughter cell 3b
Weaker recruitment of DGK
Interphase
Cytokinesis
- rapa
+ rapa (DGKεK recruited)
10 µm

(Cont'd)

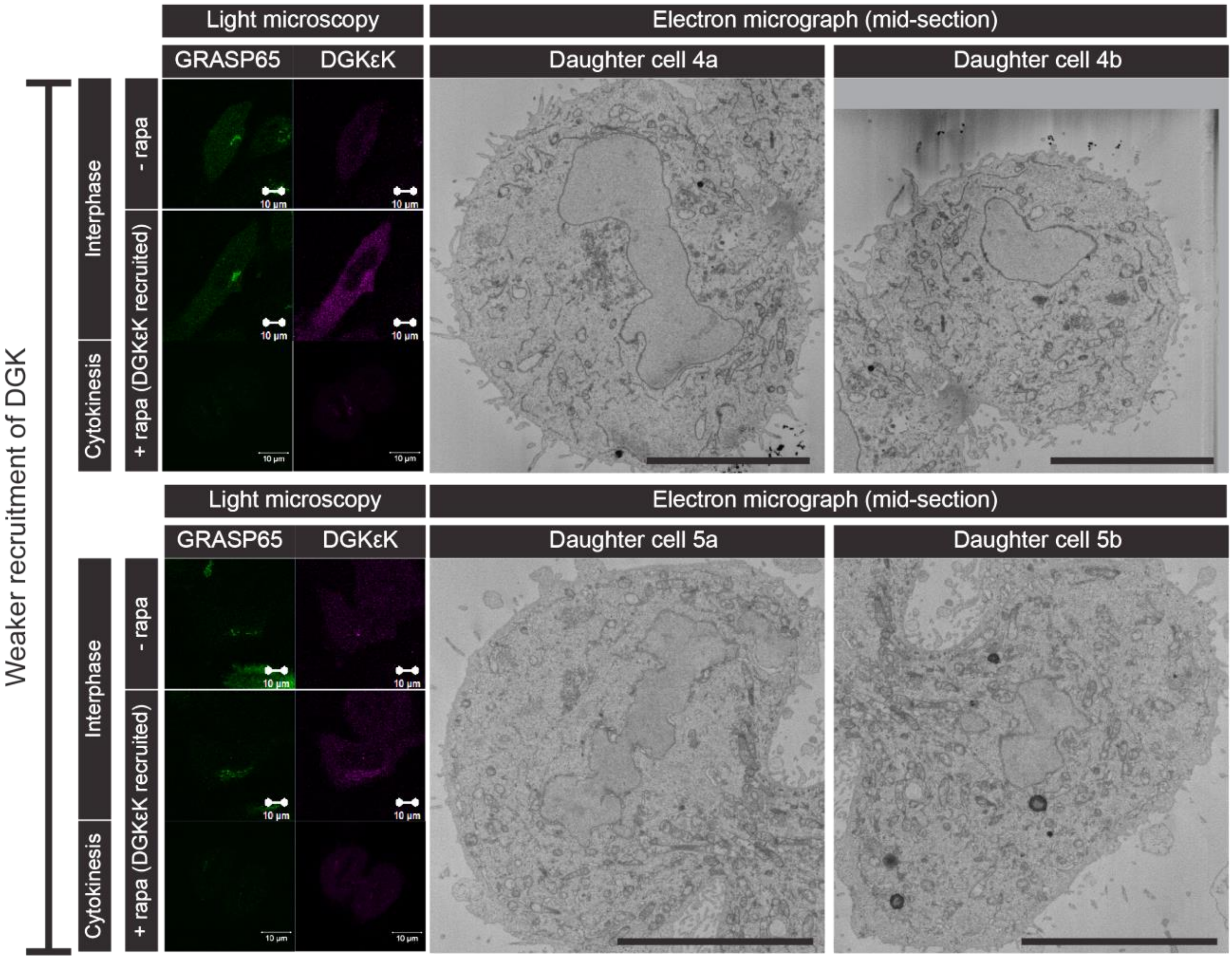

Figure 7.12 Golgi-DAG-depleted cells show fragmented NE

HeLa cells co-transfected with GRASP-GFP-2FKBP (GRASP; green) and RFP-Flag-FRB-DGKεK (DGKεK; magenta) were treated with rapalogue, followed through mitosis and fixed at cytokinesis for SBF SEM analysis. n = 5 experiments were performed and the results were grouped according to the robustness of enzyme recruitment to the Golgi. Cell 1a & b displayed a fragmented NE with multiple NE gaps (cell 1a, red arrows; also see Video 7.1.1) whereas other daughter cells (cell 2 – 5a & b) with weaker recruitment of DGKεK displayed an intact NE. Scale bar, 10 µm.

Video 7.1 Golgi-DAG-depleted cells show fragmented NE

Serial electron micrographs of daughter cells 1 – 5a & b were exported in .tiff format and converted into videos with QuickTime player. Video 7.1.1 – Video 7.1.5 represents the result of daughter cells 1 – 5a & b respectively. Videos are played at a speed of 6 frames per second.

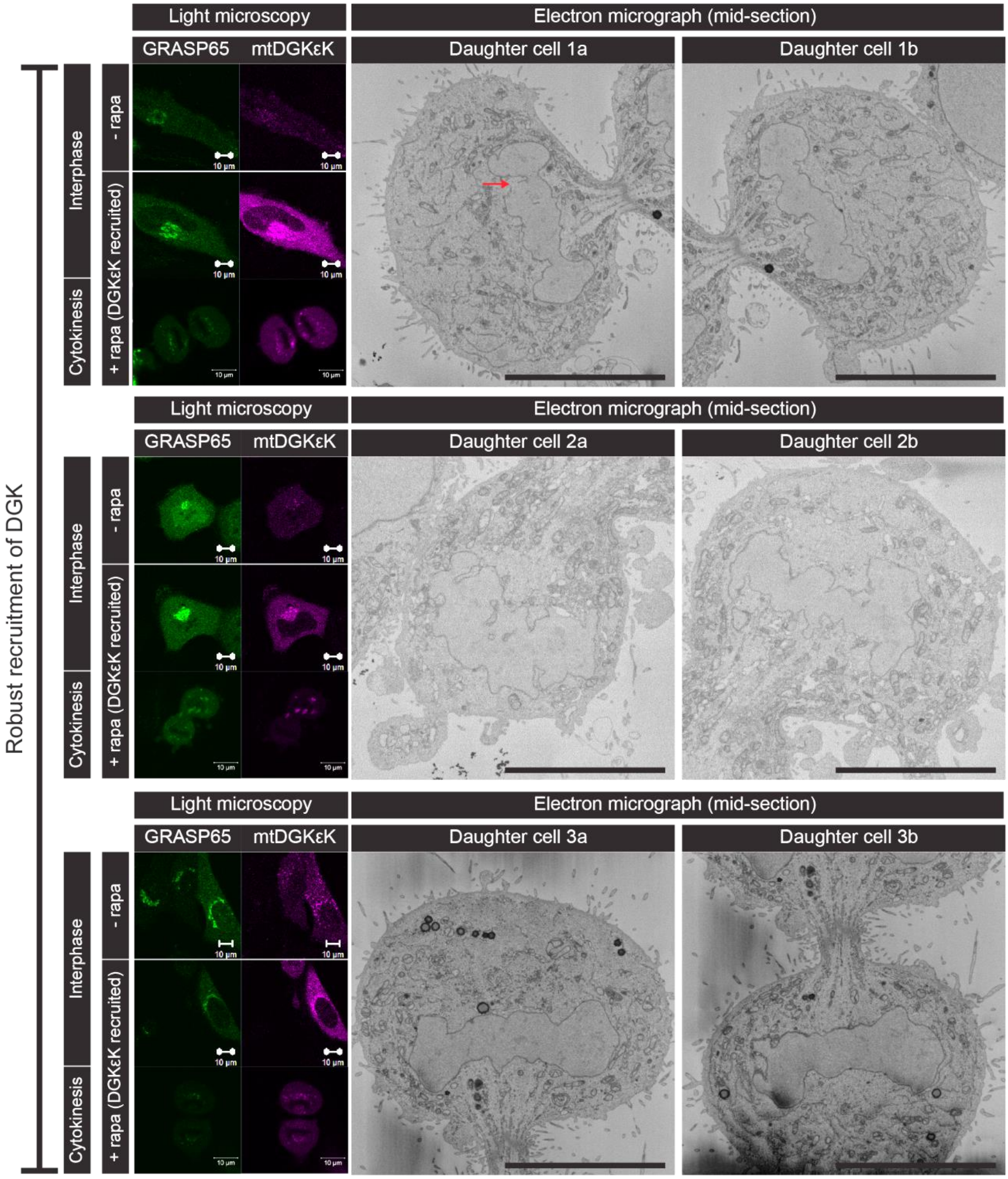
Robust recruitment of DGK
Light microscopy
Electron micrograph (mid-section)
GRASP65
mtDGKεK
Daughter cell 1a
Daughter cell 1b
Interphase
Cytokinesis
- rapa
+ rapa (DGKεK recruited)
10 µm
Light microscopy
Electron micrograph (mid-section)
GRASP65
mtDGKεK
Daughter cell 2a
Daughter cell 2b
Interphase
Cytokinesis
- rapa
+ rapa (DGKεK recruited)
10 µm
Light microscopy
Electron micrograph (mid-section)
GRASP65
mtDGKεK
Daughter cell 3a
Daughter cell 3b
Interphase
Cytokinesis
- rapa
+ rapa (DGKεK recruited)
10 µm

(Cont'd)

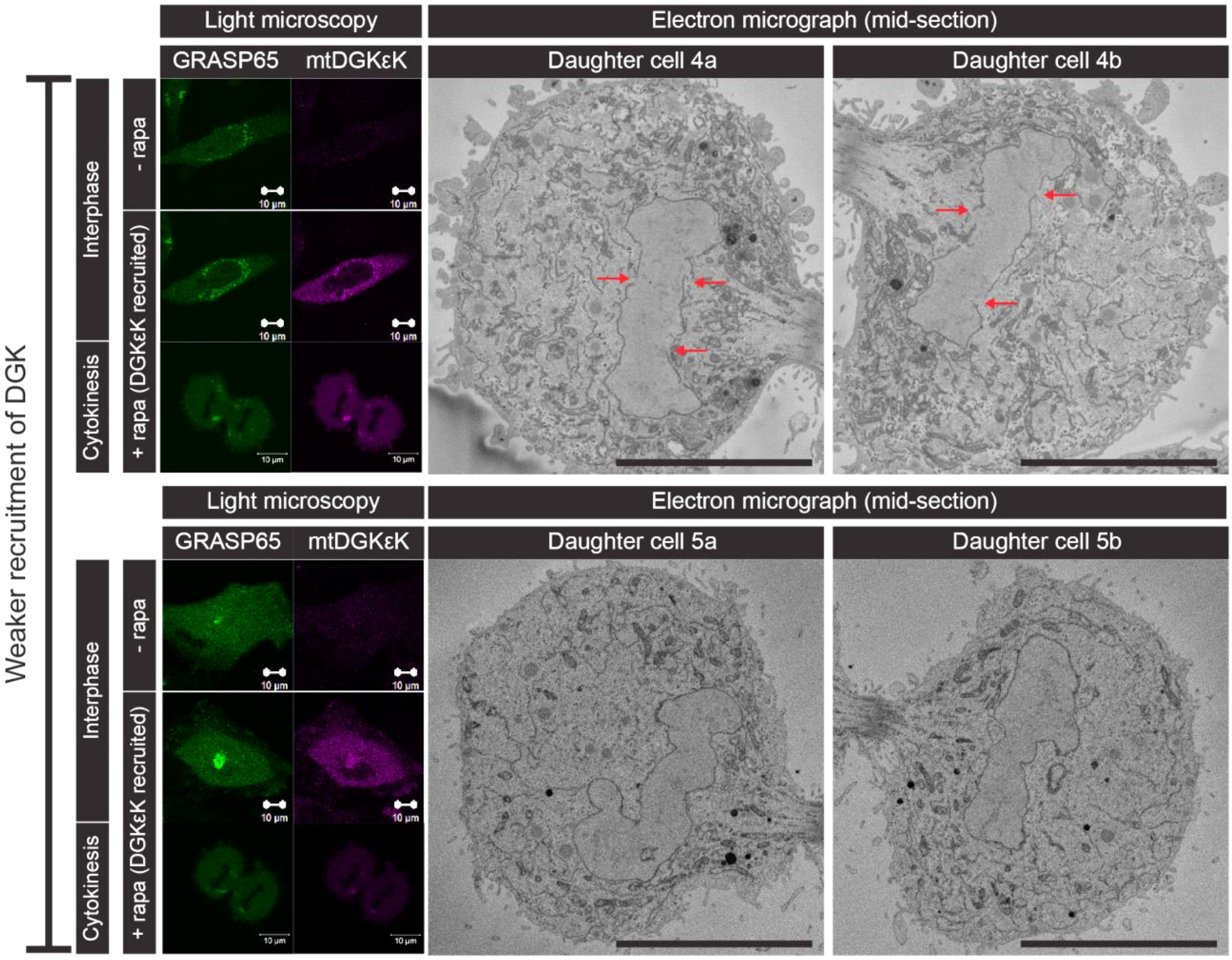

Figure 7.13 Mixed phenotypes are observed in cells with mutant DGKεK recruited to the Golgi
HeLa cells co-transfected with GRASP-GFP-2FKBP (GRASP; green) and RFP-Flag-FRB-DGKεK.D434N (mtDGKεK; magenta), a catalytic inactive DGKεK, were treated with rapalogue, followed through mitosis and fixed at cytokinesis for SBF SEM analysis. n = 5 experiments were performed and the results were grouped according to the robustness of enzyme recruitment to the Golgi. Cells 1, 2, 3a & b had a robust recruitment of mtDGK to the Golgi. NE gaps were observed in cell 1a & b (cell 1a, red arrow; Video 7.2.1). However, cells 2a & b and 3a & b appeared to have an intact NE (Video 7.2.2, Video 7.2.3). Cell 3 – 5a & b had a weaker recruitment of mtDGK to the Golgi. Cells 5a & b showed an intact NE but cells 4a & b displayed a fragmented NE with multiple NE gaps (cell 4a & b, red arrows; Video 7.2.4). Scale bar, 10 µm.

Video 7.2 Mixed phenotypes are observed in cells with mutant DGKεK recruited to the Golgi
Serial electron micrographs of daughter cells 1 – 5a & b described in Figure 7.13 were exported in .tiff format and converted into videos with QuickTime player. Video 7.2.1 – Video 7.2.5 represent the results of daughter cells 1 – 5a & b respectively. Videos are played at a speed of 6 frames per second.

To determine the correlation between completeness of the NE and progression of mitotic stage, we analysed the midbody of cytokinesis cells. As the cell progresses through cytokinesis, its midbody undergoes two obvious morphological changes. The midzone length of the midbody increases whereas the furrow diameter of the midbody decreases. Position of the cytokinesis furrow and its progression is a robust and highly regulated cellular process (Maddox *et al.*, 2007). Moreover, the furrow diameter has been shown to be regulated by a motor protein KIF-4 at a specific time point during cytokinesis (Hu *et al.*, 2011). Therefore, the furrow diameter of the midbody is a possible indication of the mitotic stage.

The midbody is a cylindrical structure in three-dimensions and a precise measurement of the furrow diameter will require 3D model reconstruction. Due to time limitation, the mid-section furrow diameter was measured and approximated as the true furrow diameter of the midbody. Table 7.1 summarises the measurement of furrow diameter in the Golgi-DAG-depleted and unperturbed cells. In the control experiments where the Golgi was recruited with catalytically inactive DGKεK. Cell 1a & b, and cell 4a & b have larger furrow diameter than the rest of the cells except for cell 2a & b. This suggests that cell 1a & b, and cell 4a & b were in an earlier mitotic time point in which small NE gaps may still exist.

Table 7.1 Mid-section furrow diameter in Golgi-DAG-depleted and unperturbed cells

Rapalogue tools: (GRASP/DGKεK)	Mid-section furrow diameter (μm)	Rapalogue tools: (GRASP/DGKεK.D434N)	Mid-section furrow diameter (μm)
Cell 1a & b	2.79	Cell 1a & b	3.08
Cell 2a & b	2.81	Cell 2a & b	5.72
Cell 3a & b	2.80	Cell 3a & b	2.39
Cell 4a & b	1.71	Cell 4a & b	3.36
Cell 5a & b	5.12	Cell 5a & b	2.72

GRASP/DGKεK: Golgi-DAG-depleted condition; GRASP/DGKεK.D434N: Golgi-DAG-unperturbed condition. Underlined cells displayed a fragmented NE phenotype.

7.7 Discussion

7.7.1 Optimisation of Golgi marker-based rapalogue dimerisation tools

Three markers were tested to recruit lipid-modifying enzymes to the Golgi. For the oligosaccharide transferases, although correctly localised to the Golgi, they failed to recruit the lipid-modifying enzymes. Interactions between the fluorescent protein and the cytosolic domain of the transferases may have obstructed the binding of rapalogue to the 2FKBP domains leading to such a result. Initially, the full length oligosaccharide transferases were fused to the rapalogue-binding domains. This was to avoid mislocalisation compared to fuse a domain that is never guaranteed to localise the same. However, Golgi N-glycosyltransferases such as ST6GALNAC1 have been shown able to form homo- and heterodimeric complexes (Hassinen *et al.*, 2010). The dimer may bring the 2FKBP domains into very close proximity and hinder rapalogue binding. Interestingly, the cytosolic and TMD of oligosaccharide transferases have been shown to be sufficient for Golgi localisation (Colley, 1997). Therefore, rapalogue dimerisation tools that fuse solely with the Golgi-localising domain of oligosaccharide transferase may be a better tool for lipid-modifying enzyme recruitment.

Initial GRASP rapalogue dimerisation tools mislocalised but the modified constructs were correctly localised to the Golgi, and were able to recruit lipid-modifying enzymes in the presence of rapalogue. These findings suggest that the construction of inducible dimerisation device is far from being a straightforward process and that the orientation of protein domains in the rapalogue dimerisation construct is critical. It is therefore necessary to understand the membrane binding mechanisms of the selected markers.

7.7.2 The impact of Golgi-DAG depletion on NE assembly

Similar to the experiments performed in Chapter 5, we modulated the DAG levels in the Golgi using the rapalogue dimerisation tools. A *cis*-Golgi targeting marker GRASP65 was used and depletion of Golgi-DAG resulted in NE gaps at cytokinesis. SBF SEM analysis indicated that the fragmented NE phenotype in the Golgi-DAG-depleted cells was less severe compared to that in the NE-DAG-depleted cells. This observation suggests that localised DAG production from the Golgi may be mainly involved in NE gap closure. Such suggestion can be supported by the fact that DGKεK recruitment does not affect the NE in interphase cell, and only cells with robust recruitment of DGKεK to the Golgi upon rapalogue treatment displayed a fragmented NE.

To obtain a dividing cell with optimal expression levels of both the Golgi marker and lipid-modifying enzyme is not a trivial task. DGKεK is recruited to the Golgi (a GRASP vs DGKεK titration) in the presence of rapalogue, and as time progresses excessive DGKεK may accumulate in the cytoplasm. In many cases, prolonged recruitment of DGKεK to the Golgi led to cell death. In addition, highly expressed GRASP65 mislocalised and those cells were not selected, limiting the number of cells we could study. Although synchronisation of cells is possible, addition of synchronising agents is not preferable in our case as they affect the NE reassembly as mentioned earlier.

7.7.3 Mixed phenotypes in Golgi-DAG-unperturbed cells

In Chapter 5, when DGKεK.D434N was recruited to the NE (n = 6 independent experiments), 1 out of 19 cells (5.3%) had a fragmented NE (Table 5.1). The fact that DGKεK.D434N did not give totally negative results suggests an incomplete penetrance of this catalytically inactive enzyme *in vivo*. Therefore, it is possible to see fragmented NE when DGKεK.D434N was recruited to the Golgi. The chance seeing fragmented NE appeared higher (2 out of 5 cells) when we modulated Golgi-DAG. However, without enough statistics, a definite conclusion could not be drawn. Alternative approaches to obtain statistically significant data will be discussed in the next chapter.

There is also a possibility that the mixed phenotypes are associated with mitotic progression. The furrow diameter was used as an indicator for mitotic progression, and the preliminary results indicated that those cells with a fragmented NE were at an earlier mitotic progression (Table 7.1). Although an exception was noticed (cell 2, GRASP/DGKεK.D434N recruitment), the midbody of this cell appeared asymmetrical (Video 7.2.2). Hence, this cell may not be the best representative in the furrow diameter analysis. The fragmented NE phenotypes given by DGKεK.D434N were likely because of the penetrance of DGKεK.D434N, or an observation of mixed cell cycle population, or both. A cell synchronisation protocol that does not affect NE reassembly could be a solution to verify such speculation.

In addition, to confirm whether the fragmented NE phenotype in these DGKεK.D434N expressing cells is DAG-dependent, we could rescue the cells with DAG-containing SUVs; a non-rescuable result would indicate that the NE gaps are caused by other factors. Nevertheless, this experiment would need to be done on synchronised cells or cells labelled with a marker which indicates mitotic progression. Super-resolution would be required because confocal microscopy does not have sufficient resolution to determine the gaps at the NE. In conclusion, this is the first study showing the possible involvement of the Golgi, and associated DAG localisation, in NE assembly.

7.8 **Summary**

We tested several Golgi markers for their ability to recruit DGKεK to the Golgi. A rapalogue construct using the *cis*-Golgi marker GRASP65 was optimised. Depletion of *cis*-Golgi-DAG resulted in fragmentation of the NE, suggesting the involvement of the Golgi and its localised DAG production in NE assembly during mitosis. Although a totally negative result was not observed in the experiments using a catalytically inactive DGKεK, such observation was likely because of a mixed cell cycle population. Statistically significant data will be required to distinguish if the NE gaps are caused by Golgi-DAG depletion.

Chapter 8 General discussion

8.1 Overview

The major objective of this thesis was to investigate the role of fusogenic vesicles in mammalian NE assembly. Our understanding of the mammalian NE assembly is dominated by the morphological observation of mitotic ER (quite often assumed by investigators as the only membrane compartment contributing to reforming the NE) and the localisation of NE proteins during mitosis. At least a single fusion event is required to fuse NE precursor membranes into a complete NE during an open mitosis. However, this critical fact is usually understated. Over the last thirty years, our group and collaborators focused on elucidating the NE fusion mechanism using the echinoderm cell-free assay and we demonstrated localised production of fusogenic lipid (DAG) as the critical molecular mechanism of NE assembly. Several key findings were discovered using the echinoderm model, including the requirement of MV1s to form a complete NE of the male pronucleus and where MV1s are compartments enriched in poly-phosphoinositides, PLCγ and a src kinase. Nevertheless, the NE fusion mechanism in mammalian cells remains uncharacterised. We hypothesised fusogenic vesicles similar to MV1 were conserved in mammalian cells and these MV1-like vesicles would be responsible for sealing the gaps of a reforming NE during mitosis.

8.1.1 The challenges and novel findings

The major challenge in this study is the limited biochemical information regarding mammalian NE assembly. Earlier studies have observed the presence of vesicles in mammalian NE assembly assay but mammalian fusogenic vesicles have not been isolated. Also, whether the observed vesicles are formed due to homogenisation or whether they are vesicular compartments similar to MV1 is unknown. Moreover, although the enrichment of PtdIns(4,5)P_2, PtdIns(3,4,5)P_3 in MV1 serves as an index to identify fusogenic vesicles in mammalian cells, probing phosphoinositides and their derivatives is a challenging task because the visualisation of these biomolecules is dependent on their specific-binding domains that usually participate in cell signalling. Furthermore, vesicles are small targets therefore conventional light microscopy lacks resolution to confirm the identity of candidate vesicles despite the fact that they can be labelled by phosphoinositide reporters. In addition, immuno-based EM is not the best method to label fusogenic vesicles since gold particles are relatively big compared to the vesicles and the use of detergent in permeabilisation will cause morphological changes in some cellular organelles. It is only recently that some alternative tools have become available to provide specific labelling of lipids/proteins and EM contrast simultaneously.

Using biochemical and cell biology approaches, the novel findings of this thesis are as follows:

- Membrane vesicles are found in the vicinity of the NE gaps during mitosis.
- The density (number of vesicles per area) of membrane vesicles is significantly higher in regions of large NE gap than in regions without gap, indicating a potential role of membrane vesicles in sealing NE gaps.
- Fusogenic vesicles in mammalian cells may have distinct features compared to MV1 and may originate from the ER or the Golgi.
- Localisation of PtdIns(3,4,5)P_3 and class I PI3 kinase at the ER, Golgi and perinuclear region suggests a population of PtdIns(3,4,5)P_3-enriched or MV1-like membrane vesicles in mammalian cells.
- DAG-enriched membrane vesicles are observed in interphase cells at EM resolution, these vesicles may participate in house-keeping membrane fusion events.
- Acute depletion of Golgi-DAG results in fragmented and incomplete NEs during mitosis, suggesting the involvement of Golgi in mammalian NE assembly.

8.2 The mammalian fusogenic vesicles that are responsible for NE gap closure

Lipid profile analysis of isolated membrane fractions requires complicated lipid mass-spectrometry protocols and large amounts of raw material. Hence, immunodetection of PLCγ, and Ran (MV1 features) was used as a relatively fast approach to determine membrane fractions analogous to MV1. Low density membrane fractions that are PLCγ- and Ran-positive were isolated from mammalian cells but these membrane fractions were very low in quantity and were not reproduced in all subcellular fractionations. At the same time, PLCγ and Ran were mainly enriched in medium density membrane fractions and were not separately from other endomembrane compartments. To confirm that these fractions were responsible for completing the NE, we tested if these fractions were also enriched in other fusion machineries.

Recent study from our group have confirmed the protein SFK1, a src kinase, as one of the fusion machineries that drives NE fusion event in the echinoderm model (Byrne *et al.*, 2014). However, a detailed protein profile of MV1 is missing. Protein profile analysis of MV1 may identify MV1-specific markers which help to isolate fusogenic vesicles in mammalian cells. Alternatively, since MV1 binds to demembranated sperm nuclei (Collas and Poccia, 1996), we can use this property as a tool to isolate MV1-like vesicles.

Mammalian fusogenic vesicles responsible for NE gap closure may originate from the ER, Golgi or other endomembranes. One of the fundamental criteria of membrane fusion is the localised production of DAG and DAG has been observed at the NE, ER and Golgi (Domart *et al.*, 2012, Peddie *et al.*, 2014). All these membrane compartments have been reported to vesiculate. Therefore, it will be a difficult task to isolate our target vesicles through a biochemical approach.

In the complementary cell biology approach, we confirmed the presence of MVs in the vicinity of the NE gaps using electron tomography. Quantitative analysis of these MVs indicated a putative consumption of them for NE gap closure but without further characterisation a precise conclusion cannot be drawn. Using the miniSOG constructs we detected DAG-enriched vesicles in interphase cells, the next step will be to determine if the MVs in the vicinity of the NE gaps are enriched in DAG and other fusion machineries. In this respect, we are developing polyphosphoinositide reporters that conjugated with miniSOG, a fusion protein provides EM contrast through photo-conversion. Some of our reporters could be used as recombinant probes for future works.

Furthermore, we speculate that the fusogenic vesicles required for NE gap closure are enriched in NE proteins such as LBR in addition to fusogenic lipids. Hence, co-localisation of these fusion machineries in the candidate vesicles will evidence our hypothesis. Co-localisation experiment at EM resolution has not been performed. However, the development of the next generation EM tags and their combination use will render possible the pursuit of this type of experiments (Chapter 6).

8.3 Visualisation of phosphoinositides and their derivatives

We demonstrated the presence of PtdIns(3,4,5)P_3 in endomembranes by both transfection (GFP-GRP1^{PH}) and recombinant (GST-GRP1^{PH}) probes. Since our targets are small vesicles (with an average diameter of approximately 55 nm), a GST-GFP-GRP1^{PH}-tSOG construct is being optimised in order to target PtdIns(3,4,5)P_3-enriched vesicles at cytokinesis at EM resolution. Apart from the PtdIns(3,4,5)P_3 reporters, a recombinant DAG probe (GST-GFP-C1aC1b) was also constructed in this study and will be used to determine if there is a difference in localisation of DAG using different probing approaches. Our next goal is to minimise the effect of reporters on lipid dynamics in order to obtain more precise information regarding the *in situ* localisation and quantity of target lipids. Alternative lipid reporter delivery techniques such as microinjection and protein transfection (Oba and Tanaka, 2012) are some possible ways to achieve the above objectives.

8.4 The duality of DAG

DAG has a well-documented second messenger role in various cellular functions (Toker, 2005) including the regulation of NE morphology (Larijani *et al.*, 2014). By acutely depleting DAG in the NE/ER using the rapalogue dimerisation device, we identified the role of DAG in mammalian NE assembly. At the same time, the incomplete NE phenotype caused by acute DAG depletion was rescued by both 1,2-DAG (second messenger) and 1,3-DAG (non-second messenger), indicating both the signalling and structural role of DAG in NE assembly. Lipid mass-spectrometry data indicated that the NE/ER contains mainly polyunsaturated DAG and early studies also support the fact that there is a variety of DAG species in mammalian cells (Hodgkin *et al.*, 1998). There is more than one pathway to generate DAG (Becker and Hannun, 2005, Oude Weernink *et al.*, 2007) in mammalian cells. For instance, hydrolysis of phosphatidylinositol by phospholipase C and phosphatidylcholine by phospholipase D and a phosphatase can generate DAG. It will be an interesting question to ask whether, as in the formation of the male pronucleus, a specific DAG species is enriched in the mammalian fusogenic vesicles required for NE gap closure. There may be different pools of DAG responsible for the spatial-temporal-specific fusion events, and these DAG pools may originate from different membrane compartments.

8.5 High throughput techniques to bridge light microscopy and electron microscopy

Confocal microscopy allows tracing of specific lipid by fusion protein but lacks resolution to observe vesicles and NE gaps; electron microscopy provides ultrastructure information but specific labelling in this context is difficult. CLEM was used in this study to take the best of both techniques. However, the complexity of EM and related sample preparation often limits the throughput of our study. To generate statistically significant data, super resolution microscopy can be used.

There are different techniques in super-resolution imaging but the basic principle is to overcome the diffraction limit of light microscopy. For instance, the structured illumination microscopy (SIM) enhance resolution by collecting frequency space information (Gustafsson *et al.*, 2008) and the stimulated emission depletion (STED) microscopy achieves super-resolution by selectively deactivating fluorophores. (Yamanaka *et al.*, 2014). Details of other super-resolution microscopy can be seen at a recent review by Fornasiero and Opazo (2015). However, these techniques usually require strong illumination of samples and specific fluorophores; live cell imaging is also difficult (Cox, 2014). Recently, the combination of Bessel beam and light sheet fluorescence microscopy allows fast and low phototoxicity imaging of molecules beyond the diffraction limit (Chen *et al.*, 2014). It is possible to perform live colocalisation experiments to characterise fusogenic vesicles. Furthermore, we can repeat the rapalogue-dimerisation experiments on this setup to obtain statistically significant data.

8.6 A refined fusion model of mammalian NE assembly

We depleted the Golgi-DAG with the rapalogue dimerisation device using GRASP65 as the Golgi membrane targeting marker. In a cytokinesis cell that highly express the DAG kinase, an incomplete NE was observed, characterised by multiple NE gaps. Although compared to the NE/ER-DAG depleted cells the fragmented phenotype was less severe, such observation implies the involvement of Golgi in NE reassembly. Indeed, Golgi-derived vesicles (MV2α) are required to form a complete NE in the male pronucleus formation. This is the first study to demonstrate the involvement of the Golgi (*cis*-Golgi) in NE assembly of live cells. The next step will be to validate the hypothesis that the MVs in the vicinity of the NE gaps are originated from the Golgi.

Based on our findings, we propose a refined model for mammalian NE assembly (Figure 8.1). During mitosis, mitotic ER forms cisternae at anaphase and makes contact with the separating chromosomes. The ER cisternae envelope the chromosomes and contribute to most of the reforming NE. In parallel, Golgi and ER vesicles that are enriched in DAG and possibly PtdIns(3,4,5)P_3 related fusion machineries seal the NE gaps through heterotypic and homotypic fusion respectively.

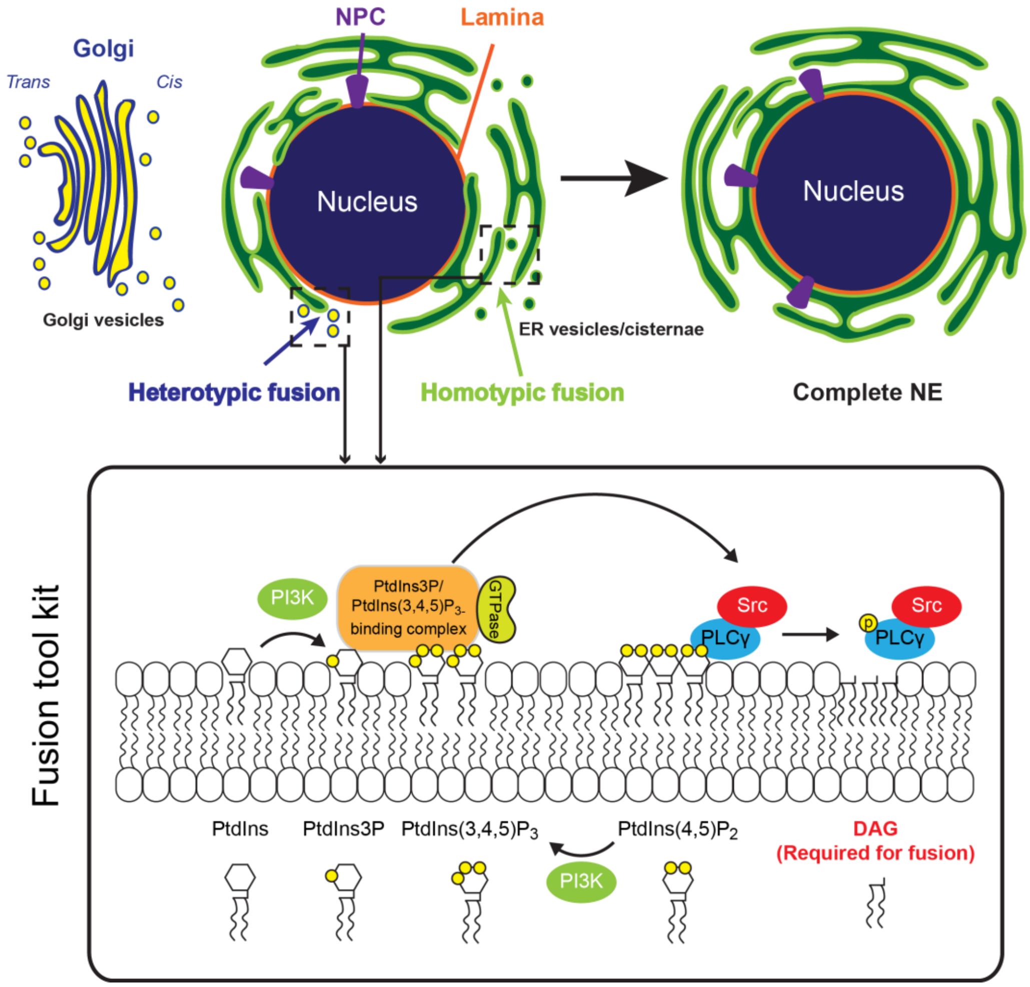

Figure 8.1 Schematic summary of the NE assembly fusion model in mammalian cells

8.7 Future prospective

This thesis has achieved several novel findings and initiated a link between the structural role of phospholipids, in particular the phosphoinositides, and membrane morphology in addition to their signalling role. Yet, how phosphoinositide dynamics is regulated and the influence of their dynamics on NE assembly and membrane organelle morphology will require further dissection. The future directions of this study will be as follows.

Firstly, the MVs in the vicinity of the NE are uncharacterised. To confirm these MVs are participating in membrane fusion we will need to determine if they are enriched in DAG. It is likely that the MVs in the vicinity of the NE are enriched in DAG due to their elevated quantity in the regions of gaps. We can draw this parallel from the formation of the male pronucleus. However, the presence of DAG does not provide information regarding their ultimate fusion site. To confirm any DAG-enriched MVs are responsible for NE gaps closure, the presence of NE transmembrane proteins (NETs) such as LBR is likely and can be tested. At the moment we cannot perform co-localisation experiments at EM resolution. Nevertheless, we can probe DAG and LBR individually in the candidate MVs. If the DAG-enriched and LBR-positive MVs have similar distribution pattern during mitosis it is possible that they are the fusogenic vesicles responsible for NE gaps closure. Using a similar approach, we can determine the membraneous origin of the fusogenic vesicles. For instance, similar distribution pattern of DAG-enriched and Golgi marker-positive MVs can validate the Golgi origin of the fusogenic vesicles. Super-resolution techniques mentioned above also will allow us to characterise fusogenic vesicles.

Depletion of *cis*-Golgi-DAG resulted in fragmented NE in mammalian cells in our study and trafficking of Golgi vesicles has been shown required for maintenance of NE shape in yeast (Webster *et al.*, 2010). Together, we can infer that membrane trafficking from the Golgi to the NE/ER is critical for NE assembly during mitosis. NE reassembly may involve the input from COPI-coated vesicles, which transport fusion machineries from the *cis*-Golgi to the ER. Therefore, modulation of COPI-associated membrane trafficking is a functional assay to test the potential role of Golgi-to-ER trafficking in NE assembly. In addition, defects in ER-to-Golgi transport have been reported to cause abnormal nuclear morphology (Kimata *et al.*, 1999). Hence, COPII- and clathrin-coated vesicles may also participate in NE assembly. Our study opens a window to explore the role of Golgi as a “mediator” to maintain membrane morphology of different organelles or as a “buffering organelle” to provide precursor membranes to maintain the proper formation of the nuclear envelope.

References

ADAMS, J. C. 1981. Heavy metal intensification of DAB-based HRP reaction product. *J Histochem Cytochem,* 29**,** 775.

ALESSI, D. R. & COHEN, P. 1998. Mechanism of activation and function of protein kinase B. *Curr Opin Genet Dev,* 8**,** 55-62.

ALLAN, D., THOMAS, P. & MICHELL, R. H. 1978. Rapid transbilayer diffusion of 1,2-diacylglycerol and its relevance to control of membrane curvature. *Nature,* 276**,** 289-90.

AMON, A. 2002. Synchronization procedures. *Methods Enzymol,* 351**,** 457-67.

ANDERSEN, J. S., LAM, Y. W., LEUNG, A. K., ONG, S. E., LYON, C. E., LAMOND, A. I. & MANN, M. 2005. Nucleolar proteome dynamics. *Nature,* 433**,** 77-83.

ANDERSON, D. J. & HETZER, M. W. 2007. Nuclear envelope formation by chromatin-mediated reorganization of the endoplasmic reticulum. *Nat Cell Biol,* 9**,** 1160-6.

ANDERSON, D. J. & HETZER, M. W. 2008. Reshaping of the endoplasmic reticulum limits the rate for nuclear envelope formation. *J Cell Biol,* 182**,** 911-24.

ANTONIN, W., ELLENBERG, J. & DULTZ, E. 2008. Nuclear pore complex assembly through the cell cycle: regulation and membrane organization. *FEBS Lett,* 582**,** 2004-16.

ANTONIN, W., FRANZ, C., HASELMANN, U., ANTONY, C. & MATTAJ, I. W. 2005. The integral membrane nucleoporin pom121 functionally links nuclear pore complex assembly and nuclear envelope formation. *Mol Cell,* 17**,** 83-92.

BAI, J. & PAGANO, R. E. 1997. Measurement of spontaneous transfer and transbilayer movement of BODIPY-labeled lipids in lipid vesicles. *Biochemistry,* 36**,** 8840-8.

BALCH, W. E., DUNPHY, W. G., BRAELL, W. A. & ROTHMAN, J. E. 1984. Reconstitution of the transport of protein between successive compartments of the Golgi measured by the coupled incorporation of N-acetylglucosamine. *Cell,* 39**,** 405-16.

BALLA, T., BONDEVA, T. & VARNAI, P. 2000. How accurately can we image inositol lipids in living cells? *Trends Pharmacol Sci,* 21**,** 238-41.

BARALDI, E., DJINOVIC CARUGO, K., HYVONEN, M., SURDO, P. L., RILEY, A. M., POTTER, B. V., O'BRIEN, R., LADBURY, J. E. & SARASTE, M. 1999. Structure of the PH domain from Bruton's tyrosine kinase in complex with inositol 1,3,4,5-tetrakisphosphate. *Structure,* 7**,** 449-60.

BARD, F. & MALHOTRA, V. 2006. The formation of TGN-to-plasma-membrane transport carriers. *Annu Rev Cell Dev Biol,* 22**,** 439-55.

BARON, C. L. & MALHOTRA, V. 2002. Role of diacylglycerol in PKD recruitment to the TGN and protein transport to the plasma membrane. *Science,* 295**,** 325-8.

BARONA, T., BYRNE, R. D., PETTITT, T. R., WAKELAM, M. J., LARIJANI, B. & POCCIA, D. L. 2005. Diacylglycerol induces fusion of nuclear envelope membrane precursor vesicles. *J Biol Chem,* 280**,** 41171-7.

BARR, F. A., PUYPE, M., VANDEKERCKHOVE, J. & WARREN, G. 1997. GRASP65, a protein involved in the stacking of Golgi cisternae. *Cell,* 91**,** 253-62.

BASANEZ, G., NIEVA, J. L., RIVAS, E., ALONSO, A. & GONI, F. M. 1996. Diacylglycerol and the promotion of lamellar-hexagonal and lamellar-isotropic phase transitions in lipids: implications for membrane fusion. *Biophys J,* 70**,** 2299-306.

BAUMEISTER, W., GRIMM, R. & WALZ, J. 1999. Electron tomography of molecules and cells. *Trends Cell Biol,* 9**,** 81-5.

BAUR, T., RAMADAN, K., SCHLUNDT, A., KARTENBECK, J. & MEYER, H. H. 2007. NSF- and SNARE-mediated membrane fusion is required for nuclear envelope formation and completion of nuclear pore complex assembly in Xenopus laevis egg extracts. *J Cell Sci,* 120**,** 2895-903.

BECKER, K. P. & HANNUN, Y. A. 2005. Protein kinase C and phospholipase D: intimate interactions in intracellular signaling. *Cell Mol Life Sci,* 62**,** 1448-61.

BELAZI, D., SOLE-DOMENECH, S., JOHANSSON, B., SCHALLING, M. & SJOVALL, P. 2009. Chemical analysis of osmium tetroxide staining in adipose tissue using imaging ToF-SIMS. *Histochem Cell Biol,* 132**,** 105-15.

BERRIDGE, M. J. & IRVINE, R. F. 1984. Inositol trisphosphate, a novel second messenger in cellular signal transduction. *Nature,* 312**,** 315-21.

BEVERS, E. M., COMFURIUS, P., DEKKERS, D. W. & ZWAAL, R. F. 1999. Lipid translocation across the plasma membrane of mammalian cells. *Biochim Biophys Acta,* 1439**,** 317-30.

BLOM, T., SOMERHARJU, P. & IKONEN, E. 2011. Synthesis and biosynthetic trafficking of membrane lipids. *Cold Spring Harb Perspect Biol,* 3**,** a004713.

BORLAND, R. N., PARTIN, A. W., EPSTEIN, J. I. & BRENDLER, C. B. 1993. The use of nuclear morphometry in predicting recurrence of transitional cell carcinoma. *J Urol,* 149**,** 272-5.

BOTELHO, R. J., TERUEL, M., DIERCKMAN, R., ANDERSON, R., WELLS, A., YORK, J. D., MEYER, T. & GRINSTEIN, S. 2000. Localized biphasic changes in phosphatidylinositol-4,5-bisphosphate at sites of phagocytosis. *J Cell Biol,* 151**,** 1353-68.

BROERS, J. L., RAMAEKERS, F. C., BONNE, G., YAOU, R. B. & HUTCHISON, C. J. 2006. Nuclear lamins: laminopathies and their role in premature ageing. *Physiol Rev,* 86**,** 967-1008.

BROWN, W. J., CHAMBERS, K. & DOODY, A. 2003. Phospholipase A2 (PLA2) enzymes in membrane trafficking: mediators of membrane shape and function. *Traffic,* 4**,** 214-21.

BRUNGER, A. T. 2001. Structural insights into the molecular mechanism of calcium-dependent vesicle-membrane fusion. *Curr Opin Struct Biol,* 11**,** 163-73.

BURGER, K. N. 2000. Greasing membrane fusion and fission machineries. *Traffic,* 1**,** 605-13.

BURKE, B. 2001. The nuclear envelope: filling in gaps. *Nat Cell Biol,* 3**,** E273-4.

BURKE, B. & GERACE, L. 1986. A cell free system to study reassembly of the nuclear envelope at the end of mitosis. *Cell,* 44**,** 639-52.

BURKE, B., GRIFFITHS, G., REGGIO, H., LOUVARD, D. & WARREN, G. 1982. A monoclonal antibody against a 135-K Golgi membrane protein. *EMBO J,* 1**,** 1621-8.

BURKE, B. & STEWART, C. L. 2002. Life at the edge: The nuclear envelope and human disease. *Nature Reviews Molecular Cell Biology,* 3**,** 575-585.

BYRNE, R. D., BARONA, T. M., GARNIER, M., KOSTER, G., KATAN, M., POCCIA, D. L. & LARIJANI, B. 2005. Nuclear envelope assembly is promoted by phosphoinositide-specific phospholipase C with selective recruitment of phosphatidylinositol-enriched membranes. *Biochem J,* 387**,** 393-400.

BYRNE, R. D., GARNIER-LHOMME, M., HAN, K., DOWICKI, M., MICHAEL, N., TOTTY, N., ZHENDRE, V., CHO, A., PETTITT, T. R., WAKELAM, M. J., POCCIA, D. L. & LARIJANI, B. 2007. PLCgamma is enriched on poly-phosphoinositide-rich vesicles to control nuclear envelope assembly. *Cellular Signalling,* 19**,** 913-22.

BYRNE, R. D., LARIJANI, B. & POCCIA, D. L. 2009. Tyrosine kinase regulation of nuclear envelope assembly. *Adv Enzyme Regul,* 49**,** 148-56.

BYRNE, R. D., VEERIAH, S., APPLEBEE, C. J. & LARIJANI, B. 2014. Conservation of proteo-lipid nuclear membrane fusion machinery during early embryogenesis. *Nucleus,* 5.

BYRNE, R. D., ZHANDRE, V., LARIJANI, B. & POCCIA, D. 2008. Nuclear Envelope Formation In Vitro: A Sea Urchin Egg Cell-Free System. *In:* HANCOCK, R. (ed.) *The Nucleus: Physical Properties and Imaging Methods, Principles and Protocols, Methods in Molecular Biology.* Humana Press.

CAMERON, L. A. & POCCIA, D. L. 1994. In vitro development of the sea urchin male pronucleus. *Dev Biol,* 162**,** 568-78.

CAMPELO, F., MCMAHON, H. T. & KOZLOV, M. M. 2008. The hydrophobic insertion mechanism of membrane curvature generation by proteins. *Biophys J,* 95**,** 2325-39.

CAZZOLLI, R., SHEMON, A. N., FANG, M. Q. & HUGHES, W. E. 2006. Phospholipid signalling through phospholipase D and phosphatidic acid. *IUBMB Life,* 58**,** 457-61.

CELIS, J. E. 1998. *Cell biology: A laboratory handbook, Vol. 2*, Academic Press, San Diego.

CHEN, B. C., LEGANT, W. R., WANG, K., SHAO, L., MILKIE, D. E., DAVIDSON, M. W., JANETOPOULOS, C., WU, X. S., HAMMER, J. A., 3RD, LIU, Z., ENGLISH, B. P., MIMORI-KIYOSUE, Y., ROMERO, D. P., RITTER, A. T., LIPPINCOTT-SCHWARTZ, J., FRITZ-LAYLIN, L., MULLINS, R. D., MITCHELL, D. M., BEMBENEK, J. N., REYMANN, A. C., BOHME, R., GRILL, S. W., WANG, J. T., SEYDOUX, G., TULU, U. S., KIEHART, D. P. & BETZIG, E. 2014. Lattice light-sheet microscopy: imaging molecules to embryos at high spatiotemporal resolution. *Science,* 346**,** 1257998.

CHEN, R., KANG, V. H., CHEN, J., SHOPE, J. C., TORABINEJAD, J., DEWALD, D. B. & PRESTWICH, G. D. 2002. A monoclonal antibody to visualize PtdIns(3,4,5)P(3) in cells. *J Histochem Cytochem,* 50**,** 697-708.

CHEN, S. Y. & CHENG, K. H. 1990. Infrared and time-resolved fluorescence spectroscopic studies of the polymorphic phase behavior of phosphatidylethanolamine/diacylglycerol lipid mixtures. *Chem Phys Lipids,* 56**,** 149-58.

CHERNOMORDIK, L. V. & KOZLOV, M. M. 2005. Membrane hemifusion: crossing a chasm in two leaps. *Cell,* 123**,** 375-82.

CHERNOMORDIK, L. V. & ZIMMERBERG, J. 1995. Bending membranes to the task: structural intermediates in bilayer fusion. *Curr Opin Struct Biol,* 5**,** 541-7.

CHI, Y. H., CHEN, Z. J. & JEANG, K. T. 2009. The nuclear envelopathies and human diseases. *J Biomed Sci,* 16**,** 96.

CHRISTIANSON, H. C., SVENSSON, K. J. & BELTING, M. 2014. Exosome and microvesicle mediated phene transfer in mammalian cells. *Semin Cancer Biol*.

COLANZI, A., DEERINCK, T. J., ELLISMAN, M. H. & MALHOTRA, V. 2000. A specific activation of the mitogen-activated protein kinase kinase 1 (MEK1) is required for Golgi fragmentation during mitosis. *J Cell Biol,* 149**,** 331-9.

COLLAS, P., COURVALIN, J. C. & POCCIA, D. 1996. Targeting of membranes to sea urchin sperm chromatin is mediated by a lamin B receptor-like integral membrane protein. *J Cell Biol,* 135**,** 1715-25.

COLLAS, P. & POCCIA, D. 1996. Distinct egg membrane vesicles differing in binding and fusion properties contribute to sea urchin male pronuclear envelopes formed in vitro. *J Cell Sci,* 109 (Pt 6)**,** 1275-83.

COLLAS, P. & POCCIA, D. 2000. Membrane fusion events during nuclear envelope assembly. *Subcell Biochem,* 34**,** 273-302.

COLLEY, K. J. 1997. Golgi localization of glycosyltransferases: more questions than answers. *Glycobiology,* 7**,** 1-13.

CORBIN, J. A., DIRKX, R. A. & FALKE, J. J. 2004. GRP1 pleckstrin homology domain: activation parameters and novel search mechanism for rare target lipid. *Biochemistry,* 43**,** 16161-73.

COX, S. 2014. Super-resolution imaging in live cells. *Dev Biol*.

CRONIN, T. C., DINITTO, J. P., CZECH, M. P. & LAMBRIGHT, D. G. 2004. Structural determinants of phosphoinositide selectivity in splice variants of Grp1 family PH domains. *EMBO J,* 23**,** 3711-20.

CURRIE, R. A., WALKER, K. S., GRAY, A., DEAK, M., CASAMAYOR, A., DOWNES, C. P., COHEN, P., ALESSI, D. R. & LUCOCQ, J. 1999. Role of phosphatidylinositol 3,4,5-trisphosphate in regulating the activity and localization of 3-phosphoinositide-dependent protein kinase-1. *Biochem J,* 337 (Pt 3)**,** 575-83.

D'AMICO, F., SKARMOUTSOU, E. & STIVALA, F. 2009. State of the art in antigen retrieval for immunohistochemistry. *J Immunol Methods,* 341**,** 1-18.

DAI, J., TING-BEALL, H. P. & SHEETZ, M. P. 1997. The secretion-coupled endocytosis correlates with membrane tension changes in RBL 2H3 cells. *J Gen Physiol,* 110**,** 1-10.

DAS, S. & RAND, R. P. 1984. Diacylglycerol causes major structural transitions in phospholipid bilayer membranes. *Biochem Biophys Res Commun,* 124**,** 491-6.

DAVIS, L. I. & BLOBEL, G. 1986. Identification and characterization of a nuclear pore complex protein. *Cell,* 45**,** 699-709.

DE CAMILLI, P., EMR, S. D., MCPHERSON, P. S. & NOVICK, P. 1996. Phosphoinositides as regulators in membrane traffic. *Science,* 271**,** 1533-9.

DE LAS HERAS, J. I., BATRAKOU, D. G. & SCHIRMER, E. C. 2013. Cancer biology and the nuclear envelope: a convoluted relationship. *Semin Cancer Biol,* 23**,** 125-37.

DE MATTEIS, M., GODI, A. & CORDA, D. 2002. Phosphoinositides and the golgi complex. *Curr Opin Cell Biol,* 14**,** 434-47.

DE MATTEIS, M. A. & GODI, A. 2004. Protein-lipid interactions in membrane trafficking at the Golgi complex. *Biochim Biophys Acta,* 1666**,** 264-74.

DE PAUL, A. L., MUKDSI, J. H., PETITI, J. P., GUTIÉRREZ, S., QUINTAR, A. A., MALDONADO, C. A. & TORRES, A. I. 2012. Immunoelectron microscopy: a reliable tool for the analysis of cellular processes. *Applications of immunocytochemistry***,** 65-96.

DE SOUZA, C. P., OSMANI, A. H., HASHMI, S. B. & OSMANI, S. A. 2004. Partial nuclear pore complex disassembly during closed mitosis in Aspergillus nidulans. *Curr Biol,* 14**,** 1973-84.

DEERINCK, T. J., BUSHONG, E. A., THOR, A. & ELLISMAN, M. H. 2010. NCMIR methods for 3D EM: a new protocol for preparation of biological specimens for serial block face scanning electron microscopy. *Microscopy***,** 6-8.

DEITCH, J. S., SMITH, K. L., SWANN, J. W. & TURNER, J. N. 1990. Parameters affecting imaging of the horseradish-peroxidase-diaminobenzidine reaction product in the confocal scanning laser microscope. *J Microsc,* 160**,** 265-78.

DELLAIRE, G., KEPKAY, R. & BAZETT-JONES, D. P. 2009. High resolution imaging of changes in the structure and spatial organization of chromatin, gamma-H2A.X and the MRN complex within etoposide-induced DNA repair foci. *Cell Cycle,* 8**,** 3750-69.

DOMART, M. C., HOBDAY, T. M., PEDDIE, C. J., CHUNG, G. H., WANG, A., YEH, K., JETHWA, N., ZHANG, Q., WAKELAM, M. J., WOSCHOLSKI, R., BYRNE, R. D., COLLINSON, L. M., POCCIA, D. L. & LARIJANI, B. 2012. Acute manipulation of diacylglycerol reveals roles in nuclear envelope assembly & endoplasmic reticulum morphology. *PLoS One,* 7**,** e51150.

DRUMMOND, S., FERRIGNO, P., LYON, C., MURPHY, J., GOLDBERG, M., ALLEN, T., SMYTHE, C. & HUTCHISON, C. J. 1999. Temporal differences in the appearance of NEP-B78 and an LBR-like protein during Xenopus nuclear envelope reassembly reflect the ordered recruitment of functionally discrete vesicle types. *J Cell Biol,* 144**,** 225-40.

DUMAN, J. G. & FORTE, J. G. 2003. What is the role of SNARE proteins in membrane fusion? *Am J Physiol Cell Physiol,* 285**,** C237-49.

DUMAS, F., BYRNE, R. D., VINCENT, B., HOBDAY, T. M., POCCIA, D. L. & LARIJANI, B. 2010. Spatial regulation of membrane fusion controlled by modification of phosphoinositides. *PLoS One,* 5**,** e12208.

ELLENBERG, J. 2002. Dynamics of nuclear envelope proteins during the cell cycle in mammalian cells. *Nuclear envelope dynamics in embryos and somatic cells,* 23**,** 15.

ELLENBERG, J., SIGGIA, E. D., MOREIRA, J. E., SMITH, C. L., PRESLEY, J. F., WORMAN, H. J. & LIPPINCOTT-SCHWARTZ, J. 1997. Nuclear membrane dynamics and reassembly in living cells: targeting of an inner nuclear membrane protein in interphase and mitosis. *J Cell Biol,* 138**,** 1193-206.

EMR, S., GLICK, B. S., LINSTEDT, A. D., LIPPINCOTT-SCHWARTZ, J., LUINI, A., MALHOTRA, V., MARSH, B. J., NAKANO, A., PFEFFER, S. R., RABOUILLE, C., ROTHMAN, J. E., WARREN, G. & WIELAND, F. T. 2009. Journeys through the Golgi--taking stock in a new era. *J Cell Biol,* 187**,** 449-53.

ENGLISH, A. R. & VOELTZ, G. K. 2013. Rab10 GTPase regulates ER dynamics and morphology. *Nat Cell Biol,* 15**,** 169-78.

EPAND, R. M., STAFFORD, A., WANG, J. & EPAND, R. F. 1992. Zwitterionic amphiphiles that raise the bilayer to hexagonal phase transition temperature inhibit protein kinase C. The exception that proves the rule. *FEBS Lett,* 304**,** 245-8.

EYSTER, K. M. 2007. The membrane and lipids as integral participants in signal transduction: lipid signal transduction for the non-lipid biochemist. *Adv Physiol Educ,* 31**,** 5-16.

FAGONE, P. & JACKOWSKI, S. 2009. Membrane phospholipid synthesis and endoplasmic reticulum function. *J Lipid Res,* 50 Suppl**,** S311-6.

FARGE, E. & DEVAUX, P. F. 1992. Shape changes of giant liposomes induced by an asymmetric transmembrane distribution of phospholipids. *Biophys J,* 61**,** 347-57.

FARSAD, K. & DE CAMILLI, P. 2003. Mechanisms of membrane deformation. *Curr Opin Cell Biol,* 15**,** 372-81.

FILI, N., CALLEJA, V., WOSCHOLSKI, R., PARKER, P. J. & LARIJANI, B. 2006. Compartmental signal modulation: Endosomal phosphatidylinositol 3-phosphate controls endosome morphology and selective cargo sorting. *Proc Natl Acad Sci U S A,* 103**,** 15473-8.

FISCHER, A. H., TAYSAVANG, P., WEBER, C. J. & WILSON, K. L. 2001. Nuclear envelope organization in papillary thyroid carcinoma. *Histol Histopathol,* 16**,** 1-14.

FORD, M. G., MILLS, I. G., PETER, B. J., VALLIS, Y., PRAEFCKE, G. J., EVANS, P. R. & MCMAHON, H. T. 2002. Curvature of clathrin-coated pits driven by epsin. *Nature,* 419**,** 361-6.

FORNASIERO, E. F. & OPAZO, F. 2015. Super-resolution imaging for cell biologists: Concepts, applications, current challenges and developments. *Bioessays,* 37**,** 436-51.

FOTIN, A., CHENG, Y., SLIZ, P., GRIGORIEFF, N., HARRISON, S. C., KIRCHHAUSEN, T. & WALZ, T. 2004. Molecular model for a complete clathrin lattice from electron cryomicroscopy. *Nature,* 432**,** 573-9.

FRANCIS, G., KEREM, Z., MAKKAR, H. P. & BECKER, K. 2002. The biological action of saponins in animal systems: a review. *Br J Nutr,* 88**,** 587-605.

FROLOV, V. A., SHNYROVA, A. V. & ZIMMERBERG, J. 2011. Lipid polymorphisms and membrane shape. *Cold Spring Harb Perspect Biol,* 3**,** a004747.

FULLER, N., BENATTI, C. R. & RAND, R. P. 2003. Curvature and bending constants for phosphatidylserine-containing membranes. *Biophys J,* 85**,** 1667-74.

GANT, T. M., HARRIS, C. A. & WILSON, K. L. 1999. Roles of LAP2 proteins in nuclear assembly and DNA replication: truncated LAP2beta proteins alter lamina assembly, envelope formation, nuclear size, and DNA replication efficiency in Xenopus laevis extracts. *J Cell Biol,* 144**,** 1083-96.

GEORGATOS, S. D., PYRPASOPOULOU, A. & THEODOROPOULOS, P. A. 1997. Nuclear envelope breakdown in mammalian cells involves stepwise lamina disassembly and microtubule-drive deformation of the nuclear membrane. *J Cell Sci,* 110 (Pt 17)**,** 2129-40.

GIEPMANS, B. N. G. 2008. Bridging fluorescence microscopy and electron microscopy. *Histochemistry and Cell Biology,* 130**,** 211-217.

GOLDENTHAL, K. L., HEDMAN, K., CHEN, J. W., AUGUST, J. T. & WILLINGHAM, M. C. 1985. Postfixation detergent treatment for immunofluorescence suppresses localization of some integral membrane proteins. *J Histochem Cytochem,* 33**,** 813-20.

GONCZY, P. 2002. Nuclear envelope: torn apart at mitosis. *Curr Biol,* 12**,** R242-4.

GONI, F. M. 2014. The basic structure and dynamics of cell membranes: an update of the Singer-Nicolson model. *Biochim Biophys Acta,* 1838**,** 1467-76.

GONI, F. M. & ALONSO, A. 2000. Membrane fusion induced by phospholipase C and sphingomyelinases. *Biosci Rep,* 20**,** 443-63.

GRAHAM, T. R. 2004. Flippases and vesicle-mediated protein transport. *Trends Cell Biol,* 14**,** 670-7.

GRAHAM, T. R. & KOZLOV, M. M. 2010. Interplay of proteins and lipids in generating membrane curvature. *Curr Opin Cell Biol,* 22**,** 430-6.

GRAY, A., VAN DER KAAY, J. & DOWNES, C. P. 1999. The pleckstrin homology domains of protein kinase B and GRP1 (general receptor for phosphoinositides-1) are sensitive and selective probes for the cellular detection of phosphatidylinositol 3,4-bisphosphate and/or phosphatidylinositol 3,4,5-trisphosphate in vivo. *Biochem J,* 344 Pt 3**,** 929-36.

GRIMES, M. L., ZHOU, J., BEATTIE, E. C., YUEN, E. C., HALL, D. E., VALLETTA, J. S., TOPP, K. S., LAVAIL, J. H., BUNNETT, N. W. & MOBLEY, W. C. 1996. Endocytosis of activated TrkA: evidence that nerve growth factor induces formation of signaling endosomes. *J Neurosci,* 16**,** 7950-64.

GROSSHANS, B. L., ORTIZ, D. & NOVICK, P. 2006. Rabs and their effectors: achieving specificity in membrane traffic. *Proc Natl Acad Sci U S A,* 103**,** 11821-7.

GRUENBERG, J. & HOWELL, K. E. 1989. Membrane traffic in endocytosis: insights from cell-free assays. *Annu Rev Cell Biol,* 5**,** 453-81.

GRUNER, S. M. 1985. Intrinsic curvature hypothesis for biomembrane lipid composition: a role for nonbilayer lipids. *Proc Natl Acad Sci U S A,* 82**,** 3665-9.

GUILLOU, H., LECUREUIL, C., ANDERSON, K. E., SUIRE, S., FERGUSON, G. J., ELLSON, C. D., GRAY, A., DIVECHA, N., HAWKINS, P. T. & STEPHENS, L. R. 2007. Use of the GRP1 PH domain as a tool to measure the relative levels of PtdIns(3,4,5)P3 through a protein-lipid overlay approach. *J Lipid Res,* 48**,** 726-32.

GUSTAFSSON, M. G., SHAO, L., CARLTON, P. M., WANG, C. J., GOLUBOVSKAYA, I. N., CANDE, W. Z., AGARD, D. A. & SEDAT, J. W. 2008. Three-dimensional resolution doubling in wide-field fluorescence microscopy by structured illumination. *Biophys J,* 94**,** 4957-70.

GUTTINGER, S., LAURELL, E. & KUTAY, U. 2009. Orchestrating nuclear envelope disassembly and reassembly during mitosis. *Nat Rev Mol Cell Biol,* 10**,** 178-91.

HAN, X. & GROSS, R. W. 1992. Nonmonotonic alterations in the fluorescence anisotropy of polar head group labeled fluorophores during the lamellar to hexagonal phase transition of phospholipids. *Biophys J,* 63**,** 309-16.

HARAGUCHI, T., KOUJIN, T., HAYAKAWA, T., KANEDA, T., TSUTSUMI, C., IMAMOTO, N., AKAZAWA, C., SUKEGAWA, J., YONEDA, Y. & HIRAOKA, Y. 2000. Live fluorescence imaging reveals early recruitment of emerin, LBR, RanBP2, and Nup153 to reforming functional nuclear envelopes. *J Cell Sci,* 113 (Pt 5)**,** 779-94.

HASSINEN, A., RIVINOJA, A., KAUPPILA, A. & KELLOKUMPU, S. 2010. Golgi N-glycosyltransferases form both homo- and heterodimeric enzyme complexes in live cells. *J Biol Chem,* 285**,** 17771-7.

HELMS, J. B., DE VRIES, K. J. & WIRTZ, K. W. 1991. Synthesis of phosphatidylinositol 4,5-bisphosphate in the endoplasmic reticulum of Chinese hamster ovary cells. *J Biol Chem,* 266**,** 21368-74.

HETZER, M., GRUSS, O. J. & MATTAJ, I. W. 2002. The Ran GTPase as a marker of chromosome position in spindle formation and nuclear envelope assembly. *Nat Cell Biol,* 4**,** E177-84.

HINSHAW, J. E. & SCHMID, S. L. 1995. Dynamin self-assembles into rings suggesting a mechanism for coated vesicle budding. *Nature,* 374**,** 190-2.

HOBDAY, T. M. C. 2012. *The involvement of phosphoinositides and their derivatives in nuclear envelope assembly.* PhD thesis, University College London.

HODGKIN, M. N., PETTITT, T. R., MARTIN, A., MICHELL, R. H., PEMBERTON, A. J. & WAKELAM, M. J. 1998. Diacylglycerols and phosphatidates: which molecular species are intracellular messengers? *Trends Biochem Sci,* 23**,** 200-4.

HOLMBERG, K. 2003. *Surfactants and polymers in aqueous solution,* Chichester, Wiley.

HOWE, C. L., VALLETTA, J. S., RUSNAK, A. S. & MOBLEY, W. C. 2001. NGF signaling from clathrin-coated vesicles: evidence that signaling endosomes serve as a platform for the Ras-MAPK pathway. *Neuron,* 32**,** 801-14.

HOWELL, K. E., DEVANEY, E. & GRUENBERG, J. 1989. Subcellular fractionation of tissue culture cells. *Trends Biochem Sci,* 14**,** 44-7.

HU, C. K., COUGHLIN, M., FIELD, C. M. & MITCHISON, T. J. 2011. KIF4 regulates midzone length during cytokinesis. *Curr Biol,* 21**,** 815-24.

HURLEY, J. H. & GROBLER, J. A. 1997. Protein kinase C and phospholipase C: bilayer interactions and regulation. *Curr Opin Struct Biol,* 7**,** 557-65.

HUTCHISON, C. J. 2014. Do lamins influence disease progression in cancer? *Adv Exp Med Biol,* 773**,** 593-604.

HUYNH, H., WANG, X., LI, W., BOTTINI, N., WILLIAMS, S., NIKA, K., ISHIHARA, H., GODZIK, A. & MUSTELIN, T. 2003. Homotypic secretory vesicle fusion induced by the protein tyrosine phosphatase MEG2 depends on polyphosphoinositides in T cells. *J Immunol,* 171**,** 6661-71.

IKEHARA, Y., KOJIMA, N., KUROSAWA, N., KUDO, T., KONO, M., NISHIHARA, S., ISSIKI, S., MOROZUMI, K., ITZKOWITZ, S., TSUDA, T., NISHIMURA, S. I., TSUJI, S. & NARIMATSU, H. 1999. Cloning and expression of a human gene encoding an N-acetylgalactosamine-alpha2,6-sialyltransferase (ST6GalNAc I): a candidate for synthesis of cancer-associated sialyl-Tn antigens. *Glycobiology,* 9**,** 1213-24.

IMAI, A. & GERSHENGORN, M. C. 1987. Independent phosphatidylinositol synthesis in pituitary plasma membrane and endoplasmic reticulum. *Nature,* 325**,** 726-8.

IRINO, Y., TOKUDA, E., HASEGAWA, J., ITOH, T. & TAKENAWA, T. 2012. Quantification and visualization of phosphoinositides by quantum dot-labeled specific binding-domain probes. *J Lipid Res,* 53**,** 810-9.

IVANKIN, A., KUZMENKO, I. & GIDALEVITZ, D. 2012. Cholesterol mediates membrane curvature during fusion events. *Phys Rev Lett,* 108**,** 238103.

JESCH, S. A. & LINSTEDT, A. D. 1998. The Golgi and endoplasmic reticulum remain independent during mitosis in HeLa cells. *Mol Biol Cell,* 9**,** 623-35.

JETHWA, N. 2014. *The role of polyphosphoinositides in Akt/PKB activation dynamics in subcellular compartments.* UCL (University College London).

KARANASIOS, E., HAN, G. S., XU, Z., CARMAN, G. M. & SINIOSSOGLOU, S. 2010. A phosphorylation-regulated amphipathic helix controls the membrane translocation and function of the yeast phosphatidate phosphatase. *Proc Natl Acad Sci U S A,* 107**,** 17539-44.

KATSO, R., OKKENHAUG, K., AHMADI, K., WHITE, S., TIMMS, J. & WATERFIELD, M. D. 2001. Cellular function of phosphoinositide 3-kinases: implications for development, homeostasis, and cancer. *Annu Rev Cell Dev Biol,* 17**,** 615-75.

KEENAN, T. W., BEREZNEY, R. & CRANE, F. L. 1972. Lipid composition of further purified bovine liver nuclear membranes. *Lipids,* 7**,** 212-5.

KIM, Y. J., GUZMAN-HERNANDEZ, M. L. & BALLA, T. 2011. A highly dynamic ER-derived phosphatidylinositol-synthesizing organelle supplies phosphoinositides to cellular membranes. *Dev Cell,* 21**,** 813-24.

KIMATA, Y., LIM, C. R., KIRIYAMA, T., NARA, A., HIRATA, A. & KOHNO, K. 1999. Mutation of the yeast epsilon-COP gene ANU2 causes abnormal nuclear morphology and defects in intracellular vesicular transport. *Cell Struct Funct,* 24**,** 197-208.

KLARLUND, J. K., TSIARAS, W., HOLIK, J. J., CHAWLA, A. & CZECH, M. P. 2000. Distinct polyphosphoinositide binding selectivities for pleckstrin homology domains of GRP1-like proteins based on diglycine versus triglycine motifs. *Journal of Biological Chemistry,* 275**,** 32816-21.

KLEINIG, H. 1970. Nuclear membranes from mammalian liver. II. Lipid composition. *J Cell Biol,* 46**,** 396-402.

KLOSE, C., SURMA, M. A. & SIMONS, K. 2013. Organellar lipidomics--background and perspectives. *Curr Opin Cell Biol,* 25**,** 406-13.

KNIGHT, J. D., LERNER, M. G., MARCANO-VELAZQUEZ, J. G., PASTOR, R. W. & FALKE, J. J. 2010. Single molecule diffusion of membrane-bound proteins: window into lipid contacts and bilayer dynamics. *Biophys J,* 99**,** 2879-87.

KOMANDER, D., FAIRSERVICE, A., DEAK, M., KULAR, G. S., PRESCOTT, A. R., PETER DOWNES, C., SAFRANY, S. T., ALESSI, D. R. & VAN AALTEN, D. M. 2004. Structural insights into the regulation of PDK1 by phosphoinositides and inositol phosphates. *EMBO J,* 23**,** 3918-28.

KONING, A. J., LUM, P. Y., WILLIAMS, J. M. & WRIGHT, R. 1993. DiOC6 staining reveals organelle structure and dynamics in living yeast cells. *Cell Motil Cytoskeleton,* 25**,** 111-28.

KOOIJMAN, E. E., CHUPIN, V., FULLER, N. L., KOZLOV, M. M., DE KRUIJFF, B., BURGER, K. N. & RAND, P. R. 2005. Spontaneous curvature of phosphatidic acid and lysophosphatidic acid. *Biochemistry,* 44**,** 2097-102.

KORFALI, N., WILKIE, G. S., SWANSON, S. K., SRSEN, V., BATRAKOU, D. G., FAIRLEY, E. A., MALIK, P., ZULEGER, N., GONCHAREVICH, A., DE LAS HERAS, J., KELLY, D. A., KERR, A. R., FLORENS, L. & SCHIRMER, E. C. 2010. The leukocyte nuclear envelope proteome varies with cell activation and contains novel transmembrane proteins that affect genome architecture. *Mol Cell Proteomics,* 9**,** 2571-85.

KOZLOV, M. M., CAMPELO, F., LISKA, N., CHERNOMORDIK, L. V., MARRINK, S. J. & MCMAHON, H. T. 2014. Mechanisms shaping cell membranes. *Curr Opin Cell Biol,* 29C**,** 53-60.

KOZLOVSKY, Y., CHERNOMORDIK, L. V. & KOZLOV, M. M. 2002. Lipid intermediates in membrane fusion: formation, structure, and decay of hemifusion diaphragm. *Biophys J,* 83**,** 2634-51.

KOZLOVSKY, Y. & KOZLOV, M. M. 2002. Stalk model of membrane fusion: solution of energy crisis. *Biophys J,* 82**,** 882-95.

KREMER, J. R., MASTRONARDE, D. N. & MCINTOSH, J. R. 1996. Computer visualization of three-dimensional image data using IMOD. *J Struct Biol,* 116**,** 71-6.

LARIJANI, B., BARONA, T. M. & POCCIA, D. L. 2001. Role for phosphatidylinositol in nuclear envelope formation. *Biochem J,* 356**,** 495-501.

LARIJANI, B. & DUFOURC, E. J. 2006. Polyunsaturated phosphatidylinositol and diacylglycerol substantially modify the fluidity and polymorphism of biomembranes: a solid-state deuterium NMR study. *Lipids,* 41**,** 925-32.

LARIJANI, B., HAMATI, F., KUNDU, A., CHUNG, G. C., DOMART, M. C., COLLINSON, L. & POCCIA, D. L. 2014. Principle of duality in phospholipids: regulators of membrane morphology and dynamics. *Biochem Soc Trans,* 42**,** 1335-42.

LARIJANI, B. & POCCIA, D. L. 2009. Nuclear envelope formation: mind the gaps. *Annu Rev Biophys,* 38**,** 107-24.

LARIJANI, B. & POCCIA, D. L. 2012. Effects of phosphoinositides and their derivatives on membrane morphology and function. *Curr Top Microbiol Immunol,* 362**,** 99-110.

LEE, A. G. 2004. How lipids affect the activities of integral membrane proteins. *Biochim Biophys Acta,* 1666**,** 62-87.

LI, G., D'SOUZA-SCHOREY, C., BARBIERI, M. A., ROBERTS, R. L., KLIPPEL, A., WILLIAMS, L. T. & STAHL, P. D. 1995. Evidence for phosphatidylinositol 3-kinase as a regulator of endocytosis via activation of Rab5. *Proc Natl Acad Sci U S A,* 92**,** 10207-11.

LINDSAY, Y., MCCOULL, D., DAVIDSON, L., LESLIE, N. R., FAIRSERVICE, A., GRAY, A., LUCOCQ, J. & DOWNES, C. P. 2006. Localization of agonist-sensitive PtdIns(3,4,5)P3 reveals a nuclear pool that is insensitive to PTEN expression. *J Cell Sci,* 119**,** 5160-8.

LISCOVITCH, M., CHALIFA, V., PERTILE, P., CHEN, C. S. & CANTLEY, L. C. 1994. Novel function of phosphatidylinositol 4,5-bisphosphate as a cofactor for brain membrane phospholipase D. *J Biol Chem,* 269**,** 21403-6.

LIU, J., PRUNUSKE, A. J., FAGER, A. M. & ULLMAN, K. S. 2003. The COPI complex functions in nuclear envelope breakdown and is recruited by the nucleoporin Nup153. *Dev Cell,* 5**,** 487-98.

LIU, J., ZUO, X., YUE, P. & GUO, W. 2007. Phosphatidylinositol 4,5-bisphosphate mediates the targeting of the exocyst to the plasma membrane for exocytosis in mammalian cells. *Mol Biol Cell,* 18**,** 4483-92.

LO, C. Y., ANTONOPOULOS, A., GUPTA, R., QU, J., DELL, A., HASLAM, S. M. & NEELAMEGHAM, S. 2013. Competition between core-2 GlcNAc-transferase and ST6GalNAc-transferase regulates the synthesis of the leukocyte selectin ligand on human P-selectin glycoprotein ligand-1. *J Biol Chem,* 288**,** 13974-87.

LOHKA, M. J., HAYES, M. K. & MALLER, J. L. 1988. Purification of maturation-promoting factor, an intracellular regulator of early mitotic events. *Proc Natl Acad Sci U S A,* 85, 3009-13.

LONGO, F. J. 1972. An ultrastructural analysis of mitosis and cytokinesis in the zygote of the sea urchin, Arbacia punctulata. *J Morphol,* 138, 207-38.

LONGO, F. J. & ANDERSON, E. 1969. Sperm differentiation in the sea urchins Arbacia punctulata and Strongylocentrotus purpuratus. *J Ultrastruct Res,* 27, 486-509.

LU, L., LADINSKY, M. S. & KIRCHHAUSEN, T. 2009. Cisternal Organization of the Endoplasmic Reticulum during Mitosis. *Molecular Biology of the Cell,* 20, 3471-3480.

LU, L., LADINSKY, M. S. & KIRCHHAUSEN, T. 2011. Formation of the postmitotic nuclear envelope from extended ER cisternae precedes nuclear pore assembly. *J Cell Biol,* 194, 425-40.

LU, Q., LU, Z., LIU, Q., GUO, L., REN, H., FU, J., JIANG, Q., CLARKE, P. R. & ZHANG, C. 2012. Chromatin-bound NLS proteins recruit membrane vesicles and nucleoporins for nuclear envelope assembly via importin-alpha/beta. *Cell Res,* 22, 1562-75.

LUCOCQ, J. 1992. Mimicking mitotic Golgi disassembly using okadaic acid. *J Cell Sci,* 103 (Pt 4), 875-80.

LUCOCQ, J., BERGER, E. & HUG, C. 1995. The pathway of Golgi cluster formation in okadaic acid-treated cells. *J Struct Biol,* 115, 318-30.

LUMB, C. N. & SANSOM, M. S. 2012. Finding a needle in a haystack: the role of electrostatics in target lipid recognition by PH domains. *PLoS Comput Biol,* 8, e1002617.

LYMAN, S. K., GUAN, T., BEDNENKO, J., WODRICH, H. & GERACE, L. 2002. Influence of cargo size on Ran and energy requirements for nuclear protein import. *J Cell Biol,* 159, 55-67.

MACKINNON, R. 2004. Structural biology. Voltage sensor meets lipid membrane. *Science,* 306, 1304-5.

MADDOX, A. S., LEWELLYN, L., DESAI, A. & OEGEMA, K. 2007. Anillin and the septins promote asymmetric ingression of the cytokinetic furrow. *Dev Cell,* 12, 827-35.

MAEDA, Y., BEZNOUSSENKO, G. V., VAN LINT, J., MIRONOV, A. A. & MALHOTRA, V. 2001. Recruitment of protein kinase D to the trans-Golgi network via the first cysteine-rich domain. *EMBO J,* 20, 5982-90.

MAIOLINO, P., RESTUCCI, B., PAPPARELLA, S. & DE VICO, G. 2002. Nuclear morphometry in squamous cell carcinomas of canine skin. *J Comp Pathol,* 127, 114-7.

MALHAS, A., GOULBOURNE, C. & VAUX, D. J. 2011. The nucleoplasmic reticulum: form and function. *Trends Cell Biol,* 21, 362-73.

MARTELL, J. D., DEERINCK, T. J., SANCAK, Y., POULOS, T. L., MOOTHA, V. K., SOSINSKY, G. E., ELLISMAN, M. H. & TING, A. Y. 2012. Engineered ascorbate peroxidase as a genetically encoded reporter for electron microscopy. *Nature Biotechnology,* 30, 1143-+.

MAUGER, J. P. 2012. Role of the nuclear envelope in calcium signalling. *Biol Cell,* 104, 70-83.

MAYORGA, L. S., COLOMBO, M. I., LENNARTZ, M., BROWN, E. J., RAHMAN, K. H., WEISS, R., LENNON, P. J. & STAHL, P. D. 1993. Inhibition of endosome fusion by phospholipase A2 (PLA2) inhibitors points to a role for PLA2 in endocytosis. *Proc Natl Acad Sci U S A,* 90, 10255-9.

MCMAHON, H. T. & GALLOP, J. L. 2005. Membrane curvature and mechanisms of dynamic cell membrane remodelling. *Nature,* 438, 590-6.

MEYER, N. L. & LONGO, F. J. 1979. Cytological events associated with in vitro aged and fertilized rabbit eggs. *Anat Rec,* 195, 357-74.

MILNE, J. L., BORGNIA, M. J., BARTESAGHI, A., TRAN, E. E., EARL, L. A., SCHAUDER, D. M., LENGYEL, J., PIERSON, J., PATWARDHAN, A. & SUBRAMANIAM, S. 2013. Cryo-electron microscopy--a primer for the non-microscopist. *FEBS J,* 280, 28-45.

MORAVEC, T. 1999. *Spector, D.L., Goldman, R.D., Leinwand L.A. (ed.): Cells: A Laboratory Manual. Volume 2: Light Microscopy and Cell Structure,* Kluwer Academic Publishers.

MORRELL, C. N., MATSUSHITA, K. & LOWENSTEIN, C. J. 2005. A novel inhibitor of N-ethylmaleimide-sensitive factor decreases leukocyte trafficking and peritonitis. *J Pharmacol Exp Ther,* 314**,** 155-61.

MURAI, T. 2012. The role of lipid rafts in cancer cell adhesion and migration. *Int J Cell Biol,* 2012**,** 763283.

NEUMANN, S. & SCHMID, S. L. 2013. Dual role of BAR domain-containing proteins in regulating vesicle release catalyzed by the GTPase, dynamin-2. *J Biol Chem,* 288**,** 25119-28.

NEWPORT, J. 1987. Nuclear reconstitution in vitro: stages of assembly around protein-free DNA. *Cell,* 48**,** 205-17.

OANCEA, E., TERUEL, M. N., QUEST, A. F. & MEYER, T. 1998. Green fluorescent protein (GFP)-tagged cysteine-rich domains from protein kinase C as fluorescent indicators for diacylglycerol signaling in living cells. *J Cell Biol,* 140**,** 485-98.

OBA, M. & TANAKA, M. 2012. Intracellular internalization mechanism of protein transfection reagents. *Biol Pharm Bull,* 35**,** 1064-8.

OUDE WEERNINK, P. A., HAN, L., JAKOBS, K. H. & SCHMIDT, M. 2007. Dynamic phospholipid signaling by G protein-coupled receptors. *Biochim Biophys Acta,* 1768**,** 888-900.

PATEL, N., RUDICH, A., KHAYAT, Z. A., GARG, R. & KLIP, A. 2003. Intracellular segregation of phosphatidylinositol-3,4,5-trisphosphate by insulin-dependent actin remodeling in L6 skeletal muscle cells. *Mol Cell Biol,* 23**,** 4611-26.

PAYRASTRE, B., MISSY, K., GIURIATO, S., BODIN, S., PLANTAVID, M. & GRATACAP, M. 2001. Phosphoinositides: key players in cell signalling, in time and space. *Cell Signal,* 13**,** 377-87.

PEDDIE, C. J., BLIGHT, K., WILSON, E., MELIA, C., MARRISON, J., CARZANIGA, R., DOMART, M. C., O'TOOLE, P., LARIJANI, B. & COLLINSON, L. M. 2014. Correlative and integrated light and electron microscopy of in-resin GFP fluorescence, used to localise diacylglycerol in mammalian cells. *Ultramicroscopy,* 143**,** 3-14.

PEEL, N., LARIJANI, B. & PARKER, P. J. 2013. Localised interventions in cellular processes. *Biochim Biophys Acta,* 1834**,** 1364-70.

PERRY, R. J. & RIDGWAY, N. D. 2005. Molecular mechanisms and regulation of ceramide transport. *Biochim Biophys Acta,* 1734**,** 220-34.

PERSICO, A., CERVIGNI, R. I., BARRETTA, M. L. & COLANZI, A. 2009. Mitotic inheritance of the Golgi complex. *FEBS Lett,* 583**,** 3857-62.

PETER, B. J., KENT, H. M., MILLS, I. G., VALLIS, Y., BUTLER, P. J., EVANS, P. R. & MCMAHON, H. T. 2004. BAR domains as sensors of membrane curvature: the amphiphysin BAR structure. *Science,* 303**,** 495-9.

PETTITT, T. & WAKELAM, M. 1999. Diacylglycerol kinase epsilon, but not zeta, selectively removes polyunsaturated diacylglycerol, inducing altered protein kinase C distribution in vivo. *The Journal of biological chemistry,* 274**,** 36181.

PINHEIRO, P. S., JANSEN, A. M., DE WIT, H., TAWFIK, B., MADSEN, K. L., VERHAGE, M., GETHER, U. & SORENSEN, J. B. 2014. The BAR Domain Protein PICK1 Controls Vesicle Number and Size in Adrenal Chromaffin Cells. *J Neurosci,* 34**,** 10688-700.

PLONNE, D., CARTWRIGHT, I., LINSS, W., DARGEL, R., GRAHAM, J. M. & HIGGINS, J. A. 1999. Separation of the intracellular secretory compartment of rat liver and isolated rat hepatocytes in a single step using self-generating gradients of iodixanol. *Anal Biochem,* 276**,** 88-96.

POCCIA, D. & COLLAS, P. 1997. Nuclear envelope dynamics during male pronuclear development. *Dev Growth Differ,* 39**,** 541-50.

POCCIA, D. & LARIJANI, B. 2009. Phosphatidylinositol metabolism and membrane fusion. *Biochem J,* 418**,** 233-46.

POTERYAEV, D., SQUIRRELL, J. M., CAMPBELL, J. M., WHITE, J. G. & SPANG, A. 2005. Involvement of the actin cytoskeleton and homotypic membrane fusion in ER dynamics in Caenorhabditis elegans. *Mol Biol Cell,* 16**,** 2139-53.

PUTHENVEEDU, M. A., BACHERT, C., PURI, S., LANNI, F. & LINSTEDT, A. D. 2006. GM130 and GRASP65-dependent lateral cisternal fusion allows uniform Golgi-enzyme distribution. *Nat Cell Biol,* 8**,** 238-48.

RAFIKOVA, E. R., MELIKOV, K. & CHERNOMORDIK, L. V. 2010. Cytosol-dependent membrane fusion in ER, nuclear envelope and nuclear pore assembly: Biological implications. *Nucleus,* 1**,** 487-491.

RAMEH, L. E. & CANTLEY, L. C. 1999. The role of phosphoinositide 3-kinase lipid products in cell function. *J Biol Chem,* 274**,** 8347-50.

RANDAZZO, P. A. & KAHN, R. A. 1994. GTP hydrolysis by ADP-ribosylation factor is dependent on both an ADP-ribosylation factor GTPase-activating protein and acid phospholipids. *J Biol Chem,* 269**,** 10758-63.

RAUCHER, D. & SHEETZ, M. P. 2000. Cell spreading and lamellipodial extension rate is regulated by membrane tension. *J Cell Biol,* 148**,** 127-36.

RAWICZ, W., OLBRICH, K. C., MCINTOSH, T., NEEDHAM, D. & EVANS, E. 2000. Effect of chain length and unsaturation on elasticity of lipid bilayers. *Biophys J,* 79**,** 328-39.

RAWYLER, A. J., ROELOFSEN, B., WIRTZ, K. W. & OP DEN KAMP, J. A. 1982. (poly) Phosphoinositide phosphorylation is a marker for plasma membrane in Friend erythroleukaemic cells. *FEBS Lett,* 148**,** 140-4.

REDDY, K. L., ZULLO, J. M., BERTOLINO, E. & SINGH, H. 2008. Transcriptional repression mediated by repositioning of genes to the nuclear lamina. *Nature,* 452**,** 243-7.

RISSELADA, H. J. & GRUBMULLER, H. 2012. How SNARE molecules mediate membrane fusion: recent insights from molecular simulations. *Curr Opin Struct Biol,* 22**,** 187-96.

RIZO, J. & ROSENMUND, C. 2008. Synaptic vesicle fusion. *Nat Struct Mol Biol,* 15**,** 665-74.

RONG, S. B., HU, Y., ENYEDY, I., POWIS, G., MEUILLET, E. J., WU, X., WANG, R., WANG, S. & KOZIKOWSKI, A. P. 2001. Molecular modeling studies of the Akt PH domain and its interaction with phosphoinositides. *J Med Chem,* 44**,** 898-908.

ROSNER, M., SCHIPANY, K. & HENGSTSCHLAGER, M. 2013. Merging high-quality biochemical fractionation with a refined flow cytometry approach to monitor nucleocytoplasmic protein expression throughout the unperturbed mammalian cell cycle. *Nat Protoc,* 8**,** 602-26.

ROUSSEL, G. & NUSSBAUM, J. L. 1982. Surface labelling of oligodendrocytes with anti-myelin serum in cell cultures from the rat brain. Light- and electron-microscopic immunocytochemical studies. *Cell Tissue Res,* 225**,** 581-94.

RUIZ-GONZALEZ, R., CORTAJARENA, A. L., MEJIAS, S. H., AGUT, M., NONELL, S. & FLORS, C. 2013. Singlet oxygen generation by the genetically encoded tag miniSOG. *J Am Chem Soc,* 135**,** 9564-7.

SACKMANN, E. 2014. Endoplasmatic reticulum shaping by generic mechanisms and protein-induced spontaneous curvature. *Adv Colloid Interface Sci,* 208**,** 153-60.

SAITO, K., SCHARENBERG, A. M. & KINET, J. P. 2001. Interaction between the Btk PH domain and phosphatidylinositol-3,4,5-trisphosphate directly regulates Btk. *Journal of Biological Chemistry,* 276**,** 16201-16206.

SANCHEZ-PINERA, P., MICOL, V., CORBALAN-GARCIA, S. & GOMEZ-FERNANDEZ, J. C. 1999. A comparative study of the activation of protein kinase C alpha by different diacylglycerol isomers. *Biochem J,* 337 (Pt 3)**,** 387-95.

SATO, M., UEDA, Y., TAKAGI, T. & UMEZAWA, Y. 2003. Production of PtdInsP3 at endomembranes is triggered by receptor endocytosis. *Nat Cell Biol,* 5**,** 1016-22.

SCHIRMER, E. C., FLORENS, L., GUAN, T., YATES, J. R., 3RD & GERACE, L. 2003. Nuclear membrane proteins with potential disease links found by subtractive proteomics. *Science,* 301**,** 1380-2.

SCHMID, A. C., WISE, H. M., MITCHELL, C. A., NUSSBAUM, R. & WOSCHOLSKI, R. 2004. Type II phosphoinositide 5-phosphatases have unique sensitivities towards fatty acid composition and head group phosphorylation. *FEBS Lett,* 576**,** 9-13.

SCOTT, C. C., VACCA, F. & GRUENBERG, J. 2014. Endosome maturation, transport and functions. *Semin Cell Dev Biol*.

SCOTT, M. C., CHEN, C. C., MECKLENBURG, M., ZHU, C., XU, R., ERCIUS, P., DAHMEN, U., REGAN, B. C. & MIAO, J. 2012. Electron tomography at 2.4-angstrom resolution. *Nature,* 483**,** 444-7.

SEEMANN, J., PYPAERT, M., TAGUCHI, T., MALSAM, J. & WARREN, G. 2002. Partitioning of the matrix fraction of the Golgi apparatus during mitosis in animal cells. *Science,* 295**,** 848-51.

SEKER, H., ODETAYO, M. O., PETROVIC, D., NAGUIB, R. N., BARTOLI, C., ALASIO, L., LAKSHMI, M. S. & SHERBET, G. V. 2002. Assessment of nodal involvement and survival analysis in breast cancer patients using image cytometric data: statistical, neural network and fuzzy approaches. *Anticancer Res,* 22**,** 433-8.

SEWELL, R., BACKSTROM, M., DALZIEL, M., GSCHMEISSNER, S., KARLSSON, H., NOLL, T., GATGENS, J., CLAUSEN, H., HANSSON, G. C., BURCHELL, J. & TAYLOR-PAPADIMITRIOU, J. 2006. The ST6GalNAc-I sialyltransferase localizes throughout the Golgi and is responsible for the synthesis of the tumor-associated sialyl-Tn O-glycan in human breast cancer. *J Biol Chem,* 281**,** 3586-94.

SHIBATA, Y., HU, J., KOZLOV, M. M. & RAPOPORT, T. A. 2009. Mechanisms shaping the membranes of cellular organelles. *Annu Rev Cell Dev Biol,* 25**,** 329-54.

SHORTER, J. & WARREN, G. 2002. Golgi architecture and inheritance. *Annu Rev Cell Dev Biol,* 18**,** 379-420.

SHU, X., LEV-RAM, V., DEERINCK, T. J., QI, Y., RAMKO, E. B., DAVIDSON, M. W., JIN, Y., ELLISMAN, M. H. & TSIEN, R. Y. 2011. A genetically encoded tag for correlated light and electron microscopy of intact cells, tissues, and organisms. *PLoS Biol,* 9**,** e1001041.

SINGER, S. J. & NICOLSON, G. L. 1972. The fluid mosaic model of the structure of cell membranes. *Science,* 175**,** 720-31.

SKRINCOSKY, D., KAIN, R., EL-BATTARI, A., EXNER, M., KERJASCHKI, D. & FUKUDA, M. 1997. Altered Golgi localization of core 2 beta-1,6-N-acetylglucosaminyltransferase leads to decreased synthesis of branched O-glycans. *J Biol Chem,* 272**,** 22695-702.

SMITH, S. & BLOBEL, G. 1993. The first membrane spanning region of the lamin B receptor is sufficient for sorting to the inner nuclear membrane. *J Cell Biol,* 120**,** 631-7.

STANLEY, K. K. & HOWELL, K. E. 1993. TGN38/41: a molecule on the move. *Trends Cell Biol,* 3**,** 252-5.

SUNDARAMOORTHY, S., GOH, J. B., RAFEE, S. & MURATA-HORI, M. 2010. Mitotic Golgi vesiculation involves mechanisms independent of Ser25 phosphorylation of GM130. *Cell Cycle,* 9**,** 3100-5.

SUTTERLIN, C., POLISHCHUK, R., PECOT, M. & MALHOTRA, V. 2005. The Golgi-associated protein GRASP65 regulates spindle dynamics and is essential for cell division. *Mol Biol Cell,* 16**,** 3211-22.

SZENTPETERY, Z., VARNAI, P. & BALLA, T. 2010. Acute manipulation of Golgi phosphoinositides to assess their importance in cellular trafficking and signaling. *Proc Natl Acad Sci U S A,* 107**,** 8225-30.

TANG, D., YUAN, H. & WANG, Y. 2010. The role of GRASP65 in Golgi cisternal stacking and cell cycle progression. *Traffic,* 11**,** 827-42.

THYBERG, J. & MOSKALEWSKI, S. 1992. Reorganization of the Golgi complex in association with mitosis: redistribution of mannosidase II to the endoplasmic reticulum and effects of brefeldin A. *J Submicrosc Cytol Pathol,* 24**,** 495-508.

TOKER, A. 2005. The biology and biochemistry of diacylglycerol signalling. Meeting on molecular advances in diacylglycerol signalling. *EMBO Rep,* 6**,** 310-4.

TOOZE, S. A. 2006. Subcellular Fractionation Procedures and Metabolic Labeling Using [35S] Sulfate to Isolate Dense Core Secretory Granules from Neuroendocrine Cell Lines. *In:* JULIO, E. C. (ed.) *Cell biology: a laboratory handbook.* New York, USA: Elsevier Science

TOOZE, S. A., FLATMARK, T., TOOZE, J. & HUTTNER, W. B. 1991. Characterization of the immature secretory granule, an intermediate in granule biogenesis. *J Cell Biol,* 115**,** 1491-503.

TRESSET, G. 2009. The multiple faces of self-assembled lipidic systems. *PMC Biophys,* 2**,** 3.

ULBERT, S., ANTONIN, W., PLATANI, M. & MATTAJ, I. W. 2006. The inner nuclear membrane protein Lem2 is critical for normal nuclear envelope morphology. *FEBS Lett,* 580**,** 6435-41.

ULITZUR, N. & GRUENBAUM, Y. 1989. Nuclear envelope assembly around sperm chromatin in cell-free preparations from Drosophila embryos. *FEBS Lett,* 259**,** 113-6.

UNWIN, N. 2005. Refined structure of the nicotinic acetylcholine receptor at 4A resolution. *J Mol Biol,* 346**,** 967-89.

VAILLANT, D. C. & PAULIN-LEVASSEUR, M. 2008. Evaluation of mammalian cell-free systems of nuclear disassembly and assembly. *J Histochem Cytochem,* 56**,** 157-73.

VAN MEER, G. & DE KROON, A. I. 2011. Lipid map of the mammalian cell. *J Cell Sci,* 124**,** 5-8.

VANHAESEBROECK, B., LEEVERS, S. J., AHMADI, K., TIMMS, J., KATSO, R., DRISCOLL, P. C., WOSCHOLSKI, R., PARKER, P. J. & WATERFIELD, M. D. 2001. Synthesis and function of 3-phosphorylated inositol lipids. *Annu Rev Biochem,* 70**,** 535-602.

VARNAI, P., ROTHER, K. I. & BALLA, T. 1999. Phosphatidylinositol 3-kinase-dependent membrane association of the Bruton's tyrosine kinase pleckstrin homology domain visualized in single living cells. *J Biol Chem,* 274**,** 10983-9.

VARNAI, P., THYAGARAJAN, B., ROHACS, T. & BALLA, T. 2006. Rapidly inducible changes in phosphatidylinositol 4,5-bisphosphate levels influence multiple regulatory functions of the lipid in intact living cells. *J Cell Biol,* 175**,** 377-82.

VENKATESWARLU, K., GUNN-MOORE, F., OATEY, P. B., TAVARE, J. M. & CULLEN, P. J. 1998a. Nerve growth factor- and epidermal growth factor-stimulated translocation of the ADP-ribosylation factor-exchange factor GRP1 to the plasma membrane of PC12 cells requires activation of phosphatidylinositol 3-kinase and the GRP1 pleckstrin homology domain. *Biochem J,* 335 (Pt 1)**,** 139-46.

VENKATESWARLU, K., OATEY, P. B., TAVARE, J. M. & CULLEN, P. J. 1998b. Insulin-dependent translocation of ARNO to the plasma membrane of adipocytes requires phosphatidylinositol 3-kinase. *Curr Biol,* 8**,** 463-6.

VIDUGIRIENE, J. & MENON, A. K. 1993. Early lipid intermediates in glycosyl-phosphatidylinositol anchor assembly are synthesized in the ER and located in the cytoplasmic leaflet of the ER membrane bilayer. *J Cell Biol,* 121**,** 987-96.

VIEIRA, O. V., BUCCI, C., HARRISON, R. E., TRIMBLE, W. S., LANZETTI, L., GRUENBERG, J., SCHREIBER, A. D., STAHL, P. D. & GRINSTEIN, S. 2003. Modulation of Rab5 and Rab7 recruitment to phagosomes by phosphatidylinositol 3-kinase. *Mol Cell Biol,* 23**,** 2501-14.

VILLANI, M., SUBATHRA, M., IM, Y. B., CHOI, Y., SIGNORELLI, P., DEL POETA, M. & LUBERTO, C. 2008. Sphingomyelin synthases regulate production of diacylglycerol at the Golgi. *Biochem J,* 414**,** 31-41.

VILLAR, A. V., ALONSO, A. & GONI, F. M. 2000. Leaky vesicle fusion induced by phosphatidylinositol-specific phospholipase C: observation of mixing of vesicular inner monolayers. *Biochemistry,* 39**,** 14012-8.

VILLAR, A. V., GONI, F. M. & ALONSO, A. 2001. Diacylglycerol effects on phosphatidylinositol-specific phospholipase C activity and vesicle fusion. *FEBS Lett,* 494**,** 117-20.

VINES, C. M. 2012. Phospholipase C. *Adv Exp Med Biol,* 740**,** 235-54.

VOELTZ, G. K., PRINZ, W. A., SHIBATA, Y., RIST, J. M. & RAPOPORT, T. A. 2006. A class of membrane proteins shaping the tubular endoplasmic reticulum. *Cell,* 124**,** 573-86.

WANG, A. S., KUNDU, A., FONG, B., FITZGERALD, J., LARIJANI, B. & POCCIA, D. 2013. A structural role for lipids in organelle shaping. *Biol Bull,* 224**,** 218-26.

WARREN, G. 1993. Membrane partitioning during cell division. *Annu Rev Biochem,* 62**,** 323-48.

WARREN, G. & MALHOTRA, V. 1998. The organisation of the Golgi apparatus. *Curr Opin Cell Biol,* 10**,** 493-8.

WATT, S. A., KIMBER, W. A., FLEMING, I. N., LESLIE, N. R., DOWNES, C. P. & LUCOCQ, J. M. 2004. Detection of novel intracellular agonist responsive pools of phosphatidylinositol 3,4-bisphosphate using the TAPP1 pleckstrin homology domain in immunoelectron microscopy. *Biochem J,* 377**,** 653-63.

WATTON, S. J. & DOWNWARD, J. 1999. Akt/PKB localisation and 3' phosphoinositide generation at sites of epithelial cell-matrix and cell-cell interaction. *Curr Biol,* 9**,** 433-6.

WEBSTER, M. T., MCCAFFERY, J. M. & COHEN-FIX, O. 2010. Vesicle trafficking maintains nuclear shape in Saccharomyces cerevisiae during membrane proliferation. *J Cell Biol,* 191**,** 1079-88.

WEI, J. H. & SEEMANN, J. 2009. Spindle-dependent partitioning of the Golgi ribbon. *Commun Integr Biol,* 2**,** 406-7.

WEIXEL, K. M., BLUMENTAL-PERRY, A., WATKINS, S. C., ARIDOR, M. & WEISZ, O. A. 2005. Distinct Golgi populations of phosphatidylinositol 4-phosphate regulated by phosphatidylinositol 4-kinases. *J Biol Chem,* 280**,** 10501-8.

WICKNER, W. & SCHEKMAN, R. 2008. Membrane fusion. *Nat Struct Mol Biol,* 15**,** 658-64.

WIESE, C., GOLDBERG, M. W., ALLEN, T. D. & WILSON, K. L. 1997. Nuclear envelope assembly in Xenopus extracts visualized by scanning EM reveals a transport-dependent 'envelope smoothing' event. *J Cell Sci,* 110 (Pt 13)**,** 1489-502.

WILKIE, G. S., KORFALI, N., SWANSON, S. K., MALIK, P., SRSEN, V., BATRAKOU, D. G., DE LAS HERAS, J., ZULEGER, N., KERR, A. R., FLORENS, L. & SCHIRMER, E. C. 2011. Several novel nuclear envelope transmembrane proteins identified in skeletal muscle have cytoskeletal associations. *Mol Cell Proteomics,* 10**,** M110 003129.

WOODBURY, D. J. & HALL, J. E. 1988. Vesicle-membrane fusion. Observation of simultaneous membrane incorporation and content release. *Biophys J,* 54**,** 345-9.

WOODS, A. J., ROBERTS, M. S., CHOUDHARY, J., BARRY, S. T., MAZAKI, Y., SABE, H., MORLEY, S. J., CRITCHLEY, D. R. & NORMAN, J. C. 2002. Paxillin associates with poly(A)-binding protein 1 at the dense endoplasmic reticulum and the leading edge of migrating cells. *J Biol Chem,* 277**,** 6428-37.

WRIGHT, R. & RINE, J. 1989. Transmission electron microscopy and immunocytochemical studies of yeast: analysis of HMG-CoA reductase overproduction by electron microscopy. *Methods Cell Biol,* 31**,** 473-512.

WYMANN, M. P. & SCHNEITER, R. 2008. Lipid signalling in disease. *Nat Rev Mol Cell Biol,* 9**,** 162-76.

YAMANAKA, M., SMITH, N. I. & FUJITA, K. 2014. Introduction to super-resolution microscopy. *Microscopy (Oxf),* 63**,** 177-92.

YANG, L., GUAN, T. & GERACE, L. 1997a. Integral membrane proteins of the nuclear envelope are dispersed throughout the endoplasmic reticulum during mitosis. *J Cell Biol,* 137**,** 1199-210.

YANG, M., ELLENBERG, J., BONIFACINO, J. S. & WEISSMAN, A. M. 1997b. The transmembrane domain of a carboxyl-terminal anchored protein determines localization to the endoplasmic reticulum. *J Biol Chem,* 272**,** 1970-5.

ZAAL, K. J., SMITH, C. L., POLISHCHUK, R. S., ALTAN, N., COLE, N. B., ELLENBERG, J., HIRSCHBERG, K., PRESLEY, J. F., ROBERTS, T. H., SIGGIA, E., PHAIR, R. D. & LIPPINCOTT-SCHWARTZ, J. 1999. Golgi membranes are absorbed into and reemerge from the ER during mitosis. *Cell,* 99**,** 589-601.

ZERFAOUI, M., FUKUDA, M., LANGLET, C., MATHIEU, S., SUZUKI, M., LOMBARDO, D. & EL-BATTARI, A. 2002. The cytosolic and transmembrane domains of the beta 1,6 N-acetylglucosaminyltransferase (C2GnT) function as a cis to medial/Golgi-targeting determinant. *Glycobiology,* 12**,** 15-24.

ZERIAL, M. & MCBRIDE, H. 2001. Rab proteins as membrane organizers. *Nat Rev Mol Cell Biol,* 2**,** 107-17.

ZHANG, B. & ZHAI, Z. H. 1995. The roles of two kinds of membrane vesicles in the formation of annulate lamellae and nuclear envelopes in a cell-free system from Xenopus egg extracts. *Shi Yan Sheng Wu Xue Bao,* 28**,** 41-53.

ZHENDRE, V., GRELARD, A., GARNIER-LHOMME, M., BUCHOUX, S., LARIJANI, B. & DUFOURC, E. J. 2011. Key role of polyphosphoinositides in dynamics of fusogenic nuclear membrane vesicles. *PLoS One,* 6**,** e23859.

ZIEMBA, B. P., PILLING, C., CALLEJA, V., LARIJANI, B. & FALKE, J. J. 2013. The PH domain of phosphoinositide-dependent kinase-1 exhibits a novel, phospho-regulated monomer-dimer equilibrium with important implications for kinase domain activation: single-molecule and ensemble studies. *Biochemistry,* 52**,** 4820-9.

ZIEVE, G. W., TURNBULL, D., MULLINS, J. M. & MCINTOSH, J. R. 1980. Production of large numbers of mitotic mammalian cells by use of the reversible microtubule inhibitor nocodazole. Nocodazole accumulated mitotic cells. *Exp Cell Res,* 126**,** 397-405.

ZIMMERBERG, J. & KOZLOV, M. M. 2006. How proteins produce cellular membrane curvature. *Nat Rev Mol Cell Biol,* 7**,** 9-19.

ZINK, D., FISCHER, A. H. & NICKERSON, J. A. 2004. Nuclear structure in cancer cells. *Nature Reviews Cancer,* 4**,** 677-687.